ANNUAL·REPORT·90

# Institute FOR Transuranium Elements

JOINT RESEARCH CENTRE

COMMISSION OF THE EUROPEAN COMMUNITIES

EUR 13815 EN

COMMISSION OF THE EUROPEAN COMMUNITIES

Joint Research Centre

INSTITUTE
FOR TRANSURANIUM ELEMENTS
KARLSRUHE

# Annual Report 1990

TUAR-90



1991

Published by the
COMMISSION OF THE EUROPEAN COMMUNITIES
Directorate-General
Telecommunications, Information Industries and Innovation
Bâtiment Jean Monnet
LUXEMBOURG



Luxembourg: Office for Official Publications of the European Communities, 1990

Catalogue nummer: CD-NA-13815-EN-C

ECSC-EEC-EAEC, Brussels Luxembourg, 1990

Printed in the Federal Republic of Germany

## Abstract

Basic *Safety Research on Nuclear Fuels* in 1990 centered on studies of the interrelation between structure, fission gas release and operating conditions of high burn-up LWR fuel.
Basic mechanisms of fission product release were clarified in so-called single-effect studies.
As an input parameter for safety studies, the specific heat capacity of molten $UO_2$ was measured up to 8000 K.

The investigations of *Safety Aspects of Fuel Operation* revealed that structural and chemical changes limit the operation of mixed nitride fuels to centre temperatures below 2000 K.
Studies on the Safe Handling of Fuel Materials concentrated on the spread of airborne contamination in accident situations.

Of primary concern in the field of *Actinide Determination and Recycling* was the nuclear transmutation of long-lived radioactive waste constituants and the recycling of self- generated Pu.

Progress in the *Characterisation of Waste Forms and of High Burn-Up Fuel* was achieved by simulating the effects of long- term storage on leachibility and mechanical stability of waste glasses.
An electrochemical study is helping to better understand $UO_2$ corrosion in aqueous solutions, an important asset in the evaluation of spent fuel storage possibilities.
An instrument for the non-destructive characterisation of spent fuel in terms of minor actinide and fission product inventory was developed and undergoes testing.

In the field of *Actinide Research*, especially 1:1:1 and 1:2:2 neptunium and plutonium compounds were prepared and characterised for solid state measurements.
Band structures of actinide intermetallics were calculated.
Photoelectron spectroscopy was performed with PuSe and UAlNi. and high-pressure phases as well as compressibilities were determined by X-ray diffraction for $PuO_2$, PuSe, Pm, and a Pm-Sm alloy.
The pressure dependence of the optical reflectivity was measured for several pnictides and chalcogenides of U and Th, and equipment for the determination of the electrical resistivity of actinides under pressure was set up.

The effectiveness of acoustic aerosol agglomeration under static conditions with different sound sources and under various geometries was confirmed in an *Exploratory Research* project. An extension to a dynamic environment as a first step to open air applications is under study.

As scientific-technical *Support to Community Policies*, the Institute for Transuranium Elements has continued to perform analytical work for the Commission's Safeguards Directorate.

The development of a high-speed optical pyrometer for temperature measurements in an industrial environment as well as experiments to enhance the efficiency of industrial filters by ultrasonic techniques are being pursued in the context of Commission programmes for Technology Transfer and Innovation.

In support to the Commission's Directorate General for External Relations and in collaboration with the IAEA and the Radium Khlopin Institute, a robotized system for the preparation and conditioning of samples from a reprocessing plant for mass spectrometry was installed at the Radium Institute in Gatchina, near Leningrad.

Major contract *Work for Third Parties* in 1990 dealt with the study of dissolution characteristics of high burn-up fuel, with the preparation of minor actinide alloys, with the production of alpha-emitting nuclides for radio-therapy, and with the transfer of fuel pin codes to national research institutions and licencing authorities. A project to analyse fuel rods from commercial power reactors was under preparation.

# Table of Contents

## ANNEXES

# Foreword

to the Annual Progress Report 1990
of the European Institute for Transuranium Elements
by J. van Geel, Director

As the previous Annual Report TUAR 89, the present document covers not only progress made in Nuclear Fuels and Actinide Research, but describes all major activities of the Institute for Transuranium Elements in 1990. The principal chapter, Main Achievements, is organized in such a way, that it reflects the organizational structure of the Institute with its five scientific-technical units. This leads to situations where, for example, work dealing with the characterisation of radioactive waste is reported in two different sections: one deals with more basic aspects while the other one is concerned with investigations on industrial-type waste matrices.

The work load on Institute staff due to contractual obligations has again increased. In order to cope with new problems arising in this context, it became necessary to install new radio-analytical equipment and to modify the entrance cell to our hot laboratory, so that we are now in a position to accomodate also fuel elements from commercial power reactors and subject them to extensive post-irradiation examinations with sophisticated instrumentation.

The following pages should demonstrate that the increase in work for third parties has, up to now, no detrimental effects either on the quality, or on the quantity of work done for the execution of our multiannual specific research programme, which remained primarily concerned with problems of nuclear safety, with studies on the chemistry of high burn-up fuel, with investigations on possibilities of nuclear transmutation of long-lived waste constituants, with the characterisation of radioactive waste forms, especially spent fuel, and with efforts to reduce the dangers arising from the spread of nuclear aerosols.

A fraction of about 15% of the Institute's research potential was devoted to fundamental studies in the field of actinide crystal chemistry and solid state physics.

The four-year period of the present multiannual research programme of the Commission's Joint Research Centre comes to an end in December 1991. Preparations for a new programme are under way.

Karlsruhe, in May 1991

# Executive Summary

As in the preceding years, the principal theme of research work carried out at the European Institute for Transuranium Elements in 1990 was **Nuclear Safety.**

Specific, Community-funded activities dealt with Basic Safety Research on Nuclear Fuels, with Safety Aspects of Fuel Operation and Handling, with Actinide Determination and Recycling, with the Characterisation of Nuclear Waste Forms and of High Burn-Up Fuel, and with Basic Actinide Research.

Possibilities of acoustic aerosol scavenging were studied under the heading "Exploratory Research", while work in support of Community policies was carried out essentially in the field of nuclear safeguards and, to a lesser extent, in the frame of Commission programmes on Technology Transfer and Innovation. Finally, about 7% of the Institute's research potential were devoted to contract work for third parties.

The results of this work in 1990 were published (or submitted for publication) in 92 articles in scientific- technical journals and presented in 85 contributions to various conferences. In addition, 14 Topical Reports and 13 Technical Notes were issued. Three patents were applied for during the reporting period.

In the pursuit of its tasks, the Institute collaborated in 1990 closely with 88 external laboratories, in Europe and overseas.

Under the heading *Basic Safety Research on Nuclear Fuels*, characteristic features of fuel structure were studied by electron microscopy and electron microprobe and related to the ability of the fuel to release fission gases under steady state and transient conditions. Basic mechanisms of fission product release were clarified in so-called single effect studies, where the release of selectively introduced volatile fission products (e.g. by ion implantation) into $UO_2$ with different simulated burn-ups was measured under well controlled conditions. FP release studies were also of interest for our collaboration with the international reactor safety project PHEBUS PF.

New information on characteristic fuel parameters under extreme operating and/or accident conditions was obtained by measurements of the specific heat of molten $UO_2$ (at temperatures up to 8000 K) and by determining the oxygen potential of mixed oxide fuel at very high burn-up (up to 13% FIMA).

Post-irradiation examination of debris from the Three Mile Island reactor and of fuel from the Silène safety experiment brought to light interesting relations between structural phenomena observed after irradiation and the conditions to which the fuel was exposed.

New experimental evidence made it possible to further develop and test the mathematical fuel performance codes TRANSURANUS, FUTURE and MITRA.

The study of *Safety Aspects of Fuel Operation* led to the conclusion that the use of uranium-plutonium nitrides as nuclear fuel has limitations with respect to the central fuel temperature. Above 2000 K, restructuring and decomposition of the nitrides accompanied with the appearance of a metallic phase will result in important changes in structure, composition and fuel pin behaviour.

Investigations into the *Safety of Handling Radioactive Materials* increased our knowledge about the spreading of radioactive particles in case of fire in a nuclear installation: In the case of "wet" contamination, the percentage of heavy metal carried away into the ventilation outlet was found to be considerably lower than in situations where material exposed to a fire is contaminated with powder-like products.

In the same context, a study was launched on the transport of large (radioactive) particles in ducts and chimneys in order to understand why the observed release of radioactive resin particles from the exhaust stack of a BWR power station was not detected by the normal sampling and monitoring lines in the stack.

Activities in the field of *Actinide Determination and Recycling* dealt primarily with the nuclear transmutation of long-lived radioactive waste constituents and the recycling of self-generated plutonium from high burn-up PWR fuel. From a detailed study of the possibilities to recycle plutonium in pressurized water reactors in repeated cycles at burn-ups of the order of 50 GWd/t it appeared that most parameters approached an equilibrium value after 6 cycles. The higher actinides, americium and curium, are built up to relatively high levels, and the total increase in neutron emission would necessitate remote handling for fuel processing.

As a follow-up of discussions in a Workshop on Partitioning and Transmutation of Minor Actinides which was held at the Institute in October 1989, the technical feasibility of various transmutation procedures was assessed. In particular, possibilities for system-immanent recycling of long-lived radionuclides, including $^{99}Tc$ and $^{129}I$, were evaluated and the status of research in the field of system-immanent recycling of minor actinides was summarized. It was concluded that system-immanent recycling would require less research and development effort than more advanced transmutation procedures such as employing a dedicated minor actinide burner, but that the needs for partitioning remain unchanged.

Minor actinide oxide fuel samples had been irradiated in the Karlsruhe KNK fast flux test facility and in the French PHENIX reactor. While in the KNK fuel samples all nuclides of interest have by now been analysed and the results are being compared with calculated data, 4 PHENIX pins containing Np and Am will have been shipped from Marcoule to Karlsruhe by the end of the year and will undergo post-irradiation analysis in 1991.

Phase diagram studies on candidate fuels for MA transmutation, i.e. $(U_{1-x}Np_x)N$ with $0<x<1$ and $(U_{0.8}Am_{0.2})O_2$ were continued.

A previously described actinide separation scheme with high pressure cation exchange was successfully tested, and the suitability of trialkyl phosphine oxide (TRPO) for the removal of actinides from waste was demonstrated.

The characterisation of non-processed *spent fuel and of high level vitrified waste* with respect to properties of relevance for their behaviour under conditions of long-term storage is another topic of concern for the Institute.

In 1990, experiments on Cm-doped waste glasses to produce realistic (long-term) radiation damage were terminated. From the effects on fracture behaviour, density changes and leachability it was concluded, that alpha-decay damage does not present a problem for long-term storage of the various glasses studied.

A detailed study of the incorporation of transuranium elements in titanate nuclear waste ceramics has yielded new partitioning data for waste forms containing PUREX waste simulant in combination with oxides of neptunium, plutonium, or americium.

Understanding the mechanisms of $UO_2$ corrosion in aqueous solutions is essential to evaluate the long-term behaviour of unprocessed spent fuel in an underground repository which may be flooded with ground water. Therefore an electrochemical study was launched to pinpoint key species or rate determining steps in the corrosion process. Preliminary results showed that the $UO_2$ oxidation state is very sensitive to the $O_2$ content of the corroding agent, particularly at low levels.

This observation was confirmed in continued corrosion tests with irradiated $UO_2$ and MOX fuel in SOXHLET extractors.

A new activity was launched in 1990 to model mathematically the consequences of underground water intrusion into a spent fuel repository by defining the problems, adapting existing ITU software to the particular needs of this project and by specifying additional software requirements for the analytical treatment of the problem.

Leaching studies with highly active industrial waste glasses (from CEA Marcoule) led to similar results as previously reported investigations with ESTER glass.

In an effort to non-destructively characterise spent fuel in terms of minor actinide and fission product inventory, and, consequently, its radiotoxicity, cooling time, burn-up and fissile material content, a neutron counting unit has been developed for the passive interrogation of individual fuel rods. The unit will be calibrated with a 10 MBq $^{252}Cf$ source for counting efficiency and field of view. Isotope correlation techniques will then be used to obtain the desired information from neutron and photon measurements.

Activities in 1990 in the field of *Actinide Research* comprised the preparation, single crystal growth, characterisation and encapsulation of different classes of neptunium and plutonium compounds for measurement of physical properties. Accent was on ternary 1:1:1 and 1:2:2 compounds, solid solutions of NaCl type compounds, and certain intermetallics. Single crystals were prepared for the first time, by new methods, or of particularly high purity or large size, for the compounds $PuNi_2$, $NpSn_3$, $PuPt_2$, $PuAl_2$, NpBi, $Pu_4Sb_3$, and $U_5Sb_4$. Splat-cooled samples of ceramic materials were obtained. Setup of new facilities for single crystal growth, for preparing compounds from very high purity Np and $^{242}Pu$ was started.

Density functional theory for orbital magnetism was developed. Work on a general theory of magnetic anisotropy is in progress. New computer codes were developed for calculations on large unit cells ("supercells") and for positron wave functions. Band structure calculations were performed for intermetallics, especially Laves phases, and, as a prerequisite to the study of the corresponding uranium compound, for $Nd_2Fe_{14}B$.

An XPS/UPS study was performed on PuSe and UAlNi. PuSe was found to behave like a highly correlated 5f metal. A helium cooling device for the active photoelectron spectrometer was developed.

High-pressure phases and compressibilities were determined by X-ray diffraction for $PuO_2$, PuSe, NpSe, Pm and a Pm-Sm alloy in our laboratories in Karlsruhe. Similar high-pressure studies with synchrotron X-rays were performed at DESY Hamburg on

halides, borides, sulfides, pnictides and carbides of uranium and/or thorium, and on a high-pressure phase of plutonium. $PuO_2$ turned out to be much less compressible than other actinide dioxides. Possible shifts of the $L_{III}$ x-ray absorption edge under pressure were studied in $UCl_4$, $UO_2$ and U(P,S) with synchrotron radiation at LURE, Orsay.

The pressure dependence of optical reflectivity was investigated for several pnictides and chalcogenides of uranium and thorium. Band structure and density of states of some of these compounds were calculated as a prerequisite for reflectivity calculations. Equipment for the measurement of electrical resistivity under high pressure was set up.

Technology transfer discussions are under way with a private company for commercialising a crystal growth furnace developed in our laboratories. Work in project *Actinide Research* was published, during 1990, in about 25 publications in international scientific journals and in about 50 contributions to international scientific conferences.

Close collaboration with about 40 external scientific institutions involved exchange of staff and of samples. These collaborations included magnetic and electrical measurements, neutron scattering, and use of synchrotron radiation for diffraction, absorption, and magnetic scattering of x-rays. Samples prepared in the Institute were used for most of these measurements.

The capabilities of the ITU *Actinide Information Centre* were extended by the data bank system THERSYST to the storage and handling of thermophysical property data of heavy elements. In 1990, 1029 data sets from 147 publications concerning 72 actinide metals and compounds have been processed and stored in THERSYST.

*Exploratory Research* on acoustic aerosol agglomeration has clearly demonstrated its effectiveness on solid, liquid, and solid/liquid mixtures of aerosols under static conditions in small (0.6 $m^3$) and medium size (15 $m^3$) enclosures with 400 W piezo-electric transducers producing sound pressure levels of up to 160 dB at 21 kHz. Agglomeration of fog aerosols was also observed in a 170 $m^3$ test chamber at sound pressure levels of 140 dB produced by a pulsed chemical combustion engine (pulse jet) working at a fundamental frequency of 200 Hz. Projects are under way to extend the frequency range of the piezo-electric devices down to 1 kHz and, as a first step to open air applications, to study possibilities of acoustic aerosol scavenging in a dynamic test rig with flowing air as a carrier.

As scientific-technical *support to Community policies*, the Institute for Transuranium Elements has continued to perform analytical work for the Commission's Safeguards Directorate. In the frame of this activity, new analytical techniques are under development using inductively-coupled plasma mass spectrometry (ICP-MS). ICP-MS was found to be the method of choice for the determination of neptunium in uranium or plutonium solutions. The fines (0.1 - 15 μm) from a fuel solution are analysed by ICP-MS, and the same analytical technique is being used in conjunction with a short-pulse infrared Nd:YAG laser on particles ablated from the surface of irradiated solid fuel samples.

Increasing demands for gamma-spectrometric analyses made it necessary to install new counting equipment. Test runs for the determination of Pu isotope ratios were made, using the so-called MGA program. The program demands stable counting conditions, this is why the equipment had to be installed in a remote room in the basement far from laboratory background radiation and stray fields.

The Institute has participated in a multi-laboratory experiment to use lutetium for calibrating the volume of reprocessing tanks for safeguards purposes. The results of the exercise in which 5 laboratories took part is presently under evaluation.

In 1990, work was started to design and equip laboratories with automatic analytical instruments for the analysis of nuclear fuel samples taken under routine nuclear materials safeguards inspections on-site, i.e. directly at nuclear fuel reprocessing plants. The laboratories are to be installed in Cap de la Hague (France) and in Sellafield (UK). Three possibilities for the bulk analysis of Pu and MOX samples (titration, K-edge densitometry, and passive neutron counting) are being considered. During the reporting period, the possibilities for robotized conditioning of solutions for isotope dilution and the sytem for automatic data collection, reduction and evaluation were adapted to conditions in on-site laboratories while the expert system to work out the necessary parameters for sample preparation has been further refined. An improved quality control system is under development.

In the same context, an analytical technique was developed for the measurement of the plutonium concentration in high burn-up fuel solutions by intrinsic densitometry.

In support to the Directorate General for External Relations (DG I) and in collaboration with the International Atomic Energy Agency and the Radium Khlopin Institute a robotized system for the preparation and conditioning for mass spectrometry of samples from a reprocessing plant was installed at the Radium Institute in Gatchina, near Leningrad, in October 1990. First comparative results of ongoing field tests are expected in the spring of 1991.

In support of the Commission's Directorate for Technology Transfer and Innovation (DG XIII/C) efforts are being continued to develop a laboratory-type ultra-fast multi-colour pyrometer into a product for industrial applications.

With the same perspective, experiments are under way to enhance the efficiency of industrial electrostatic filters, cyclones, and Venturi scrubbers by acoustic techniques. For this purpose, a new test rig for aerosol preconditioning under dynamic flow conditions was designed and installed.

Major contract work in 1990 dealt with the study of the dissolution characteristics of high burn-up fuel, with the preparation of minor actinide alloys, with the production of alpha-emitting nuclides for radio-therapy, and with the transfer of fuel pin codes to national research institutions and licencing authorities.


# MAIN ACHIEVEMENTS AND MILESTONES

# 1 Specific Programmes

## 1.1 Basic Safety Research on Nuclear Fuels

### Introduction

The aim of improving the safety of nuclear fuels was approached with a broad and comprehensive experimental investigation and with modelling activities using different computer codes to better understand processes and mechanisms operative in LWR oxide fuels up to very high burn-ups reaching ~ 60 GWd/tU, and by studying the behaviour of the fuel at very high temperatures of up to 8000 K. Thus, properties and mechanisms were measured and investigated which are relevant for the fuel behaviour under both steady state operation, under operational transients and in accident situations at intermediate and high burn-up. The working philosophy followed was that practized successfully at ITU before, i.e. to perform well-planned laboratory experiments providing basic fuel data in parallel with careful post-irradiation analysis of fuel which has been irradiated under steady state, transient or accident conditions up to high burn-up, and to use the results thus obtained to develop and validate computer codes which can then be used to predict the fuel behaviour over a wide range of conditions. A large number of actions was taken and important milestones were achieved, comprising

- a very detailed examination of a large number of fuels with electron optical means of the international fission gas release project Risø III, providing an extensive data base for fuel structure and fission gas release under steady state and transient conditions

- cooperation in the international reactor safety project Phebus PF

- determination of important physical properties up to very high temperatures. For instance, the heat capacity of liquid $UO_2$ was successfully measured up to 8000 K. Also, the oxygen potential of LMFBR fuel was measured at very high burn-ups of up to 13 % FIMA

- further post-irradiation examination work was done on debris from the Three Mile Island reactor and on fuel from the Silène Safety experiment

- so-called "single effect studies" were performed in the laboratory whereby the release of selectively introduced interesting volatile fission products (e.g. by ion implantation) into $UO_2$ with different simulated burn-ups (so-called SIMFUEL) is measured under well-controlled conditions. Also, a number of properties of this SIMFUEL was studied, and different nuclear techniques were used to determine the kinetics of fuel oxidation during leaching in water for the concept of direct storage of spent fuel

- the fuel performance codes TRANSURANUS, FUTURE and MITRA were further developed and tested. International interest in using the TRANSURANUS code was large, the code is now being used by a number of organisations including licensing bodies. It constitutes also an important contribution to the development of the European Accident Code for fast breeder reactors.

### Structural Investigations and Basic Studies on Fuels - Oxide Fuel Transients

The cooperation with the International Fission Gas Release Project Risø III was continued. This project was officially terminated at the end of 1990, but some replica and transmission electron microscope investigations and a few electron microprobe analyses will be performed in early 1991. In parallel laboratory work, simulated high burn-up fuel was produced, characterized and used for fission gas release studies and measure-

ments of physical properties. This latter activity is performed in cooperation with Chalk River, AECL, Canada. In addition, studies on radiation damage in $UO_2$ were continued. For the first time, damage formation was investigated in-situ at 5 K and recovery was followed up to 2000 K.

## Fission product behaviour in transient tested LWR fuel samples studied by transmission, scanning, and replica electron microscopy

### Introduction

A very comprehensive study of the behaviour of the fission gas products in transient-tested LWR fuel samples has been made using Replica Electron Microscopy (REM), Scanning Electron Microscopy (SEM) and Transmission Electron Microscopy (TEM). A large proportion of the work falls within the reporting period for TUAR 90.

A full list of all the specimens examined by REM is given in Tab. 1.1, and totals eighteen samples, of which three were base-irradiated and fifteen transient-tested fuels. Of the transient-tested fuel pins, eight had been refabricated with thermocouples prior to the test. Two base-irradiated fuels were studied by TEM and SEM, and further observations were made on a transient-tested fuel which had previously been examined. Details of these sections are given in Tab. 1.2.

*Tab. 1.1 Table of samples examined by REM.*

| Sample | Burn-up (%FIMA) | Transient |
|---|---|---|
| B1 | 4.6 | Base Irradiation |
| B2 | 2.3 | Base Irradiation |
| B3 | 4.7 | Base Irradiation |
| T1 | 4.5 | Transient Max. Power = 350 W/cm |
| T2 | 4.6 | Transient Max. Power = 450 W/cm |
| T3 | 4.6 | Transient Max. Power = 410 W/cm |
| T4 | 4.6 | Transient Max. Power = 175 W/cm |
| T5 | 4.5 | Transient Max. Power = 390 W/cm |
| T6 | 4.4 | Transient Max. Power = 205 W/cm |
| T7 | 4.5 | Transient Max. Power = 384 W/cm |
| TR1 | 4.6 | Transient Max. Power = 410 W/cm Refabricated pin. |
| TR2 | 4.7 | Transient Max. Power = 410 W/cm Refabricated pin. |
| TR3 | 4.7 | Transient Max. Power = 360 W/cm Refabricated pin. |
| TR4 | 4.5 | Transient Max. Power = 410 W/cm Refabricated pin. |
| TR5 | 4.8 | Transient Max. Power = 410 W/cm Refabricated pin. |
| TR6 | 2.4 | Transient Max. Power = 442 W/cm Refabricated pin. |
| TR7 | 4.6 | Transient Max. Power = 397 W/cm Refabricated pin. |
| TR8 | 4.7 | Transient Max Power = 415 W/cm Refabricated pin. |

*Tab. 1.2 Table of samples examined by TEM/SEM.*

| Sample | Burn-up (%FIMA) | Transient |
|---|---|---|
| B1(1) | 4.6 | Base Irradiation, Specimen from fuel periphery |
| B1(2) | 4.6 | Base Irradiation, Specimen from fuel centre |
| B3(1) | 4.7 | Base Irradiation, Specimen from fuel periphery |
| B3(2) | 4.7 | Base Irradiation, Specimen from fuel centre |
| TR2 | 4.7 | Transient Tested Refabricated pin |

### Sample preparation and examination

#### *Transmission electron microscopy*

Two techniques have been used to prepare fuel samples suitable for TEM. Both of these start from a polished cross sectional slice of a fuel pin which has first been examined by optical microscopy, and in chosen cases also by Electron Probe Microanalysis (EPMA). Such sections are cut in the hot cell facility of the Institute and polished down to a thickness of about 0.3 mm.

The fuel sections are almost invariably heavily cracked, and the cladding is removed so that the fuel breaks into small pieces defined by the pattern of cracks. At this stage the optical micrographs are required so that each piece can be related from its shape back to its original position on the pin fuel cross section. Two different methods are now used to complete the preparation depending on the primary aim of the examination.

In the first method a chosen piece of fuel is electropolished by remote manipulation in a lead shielded glovebox until a small hole is formed. The areas around the periphery of the hole are usually thin enough ( < 150nm ) for TEM. The electropolishing is performed in a double jet apparatus using Lenoir's solution at a polishing potential of 40 V. After perforation the samples are

usually treated for one hour in an ion-beam thinning apparatus to clean the surfaces, which are frequently covered with a thin contamination layer from the polishing.

The advantage of this method of preparation is that very high positional accuracy can be obtained for the areas examined by TEM, enabling reliable estimates of the fuel temperature to be made. The disadvantage is that the bulk of the sample, and thus its activity, are relatively high which complicates specimen handling and prevents the local chemical composition from being determined in the microscope using Energy Dispersive X-ray Analysis (EDAX). In addition a proportion of any metallic precipitates formed in the fuel is lost during the electropolishing.

The second method of preparation involves taking a small piece of the fuel from a chosen radial position, and crushing this to a fine powder. The crushing is performed under methanol, and drops of the resulting suspension are allowed to dry on carbon-film coated copper support grids. The small fuel fragments remaining supported on the film are usually thin enough for TEM. This method has the advantages of low specimen activity, enabling easy handling and the application of EDAX analysis, but does not have the high positional accuracy of the electropolishing technique. Any precipitates of the metallic fission products are, however, retained and can be analysed by EDAX.

The specimens were examined in a 200 kV Hitachi H700 HST Transmission Electron Microscope specially modified for handling radioactive materials by direct connection to a glovebox system, and equipped with secondary electron imaging facilities and a Tracor Northern TN5500 energy dispersive X-ray analysis system. With this microscope a resolution of better than 1 nm by TEM and 5 nm by SEM could be attained on samples with activities up to 3 Rem/h at 10 cm.

### *Replica electron microscopy*

This technique also starts from a fuel cross section which has been cut, polished and then lightly etched to reveal the grain boundary structure and any large fission gas bubbles which may be present. A plastic replica is made of the full cross section using a plastic film (Triafol) lightly wetted with acetone. The resulting negative plastic replicas are decontaminated, then a germanium shadowed carbon/formvar positive replica is prepared from each by vacuum deposition.

The carbon replicas are photographed to enable positional information to be obtained, and small pieces are then carefully cut and mounted on support grids for examination in the TEM.

Being an indirect replication technique the resolution of detail which can be obtained is limited to about 30 nm, but the method complements the TEM technique in enabling bubbles in the size range 30 nm up to 500 nm to be imaged and measured, with the big advantage that the full fuel pin diameter of approximately 9 mm can be examined instead of just a limited area. In addition the samples have a very low activity and can be handled easily outside a glovebox.

The replicas were examined in a Siemens Elmiskop IA TEM, at an accelerating voltage of 60 kV.

## Experimental results:

Although all the experimental work has been completed on the samples listed, only the transmission electron microscopy results have been fully evaluated and reported at this stage. The evaluation of the very large number of replicas examined is in progress, but will not be completed until March 1991 when the remaining three replicas necessary to finish the project have been examined. The final report on this work will be produced in March 1991, and for this reason detailed results from the REM analysis will not be given here.

### *Characterisation of the base-irradiated non-transiented fuel samples by TEM and SEM*

For each of the base-irradiated non-transiented samples two specimens were examined by TEM, one from the periphery of the fuel and one from the centre. Both fuels showed effectively the same microstructural characteristics.

#### The peripheral specimens

The microstructure at the periphery was characterised by the following features:

i) A high density dislocation network.

ii) A high density of very small fission gas bubbles and solid fission product precipitates.

These were the only significant features of the micro-structure at the periphery and there was no development of a population of large fission gas bubbles.

A mean dislocation density of 2.2 x $10^{10}$ cm.cm$^{-3}$ was determined within the grains. This value was relatively constant. The dislocation lines were frequently jogged and were characteristic of networks formed by climb-induced growth in the high point defect flux. An example of the typical dislocation structure is shown in Fig. 1.1. The very high density of small dislocation loops as seen in this micrograph was also a characteristic feature of the microstructure at the periphery.

Extensive dislocation networks forming low angle grain boundaries were also frequently observed. The dislocation density in these boundaries reached local high values of up to 1.4 x $10^{11}$ cm.cm$^{-3}$.

At the periphery a very high density of small fission gas bubbles appeared, with an average diameter of 8 nm, and a narrow size distribution. The bubbles were homogeneously distributed with an average density of 1.2 x $10^{16}$ cm$^{-3}$. The small fission gas bubbles were almost always linked to small precipitates of approximately the same size distribution.

An example of this fission gas bubble population is shown in Fig. 1.2 from fuel sample B1(1). The local microswelling value due to this population of small fission gas bubbles is negligibly small at about 0.1%.

**The central specimens**

In contrast to specimens from fuel pins which had been transient tested the central and peripheral microstructures of the base-irradiated fuel were very similar, the main difference being the occasional presence of a low density of rather larger fission gas bubbles.

Both the dislocation density and character were

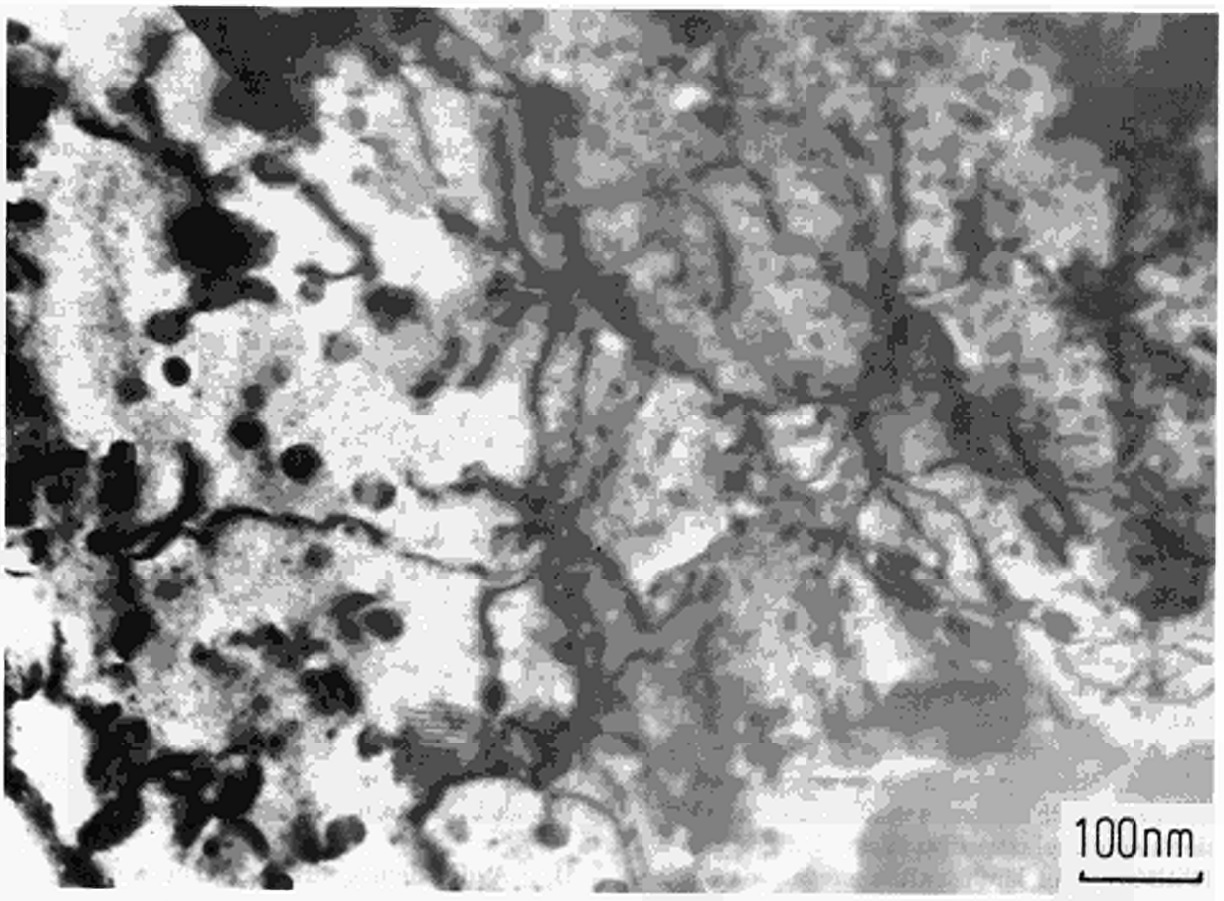


*Fig. 1.1* *Typical dislocation structure as observed at the periphery of the base-irradiated fuel (B1(1))*

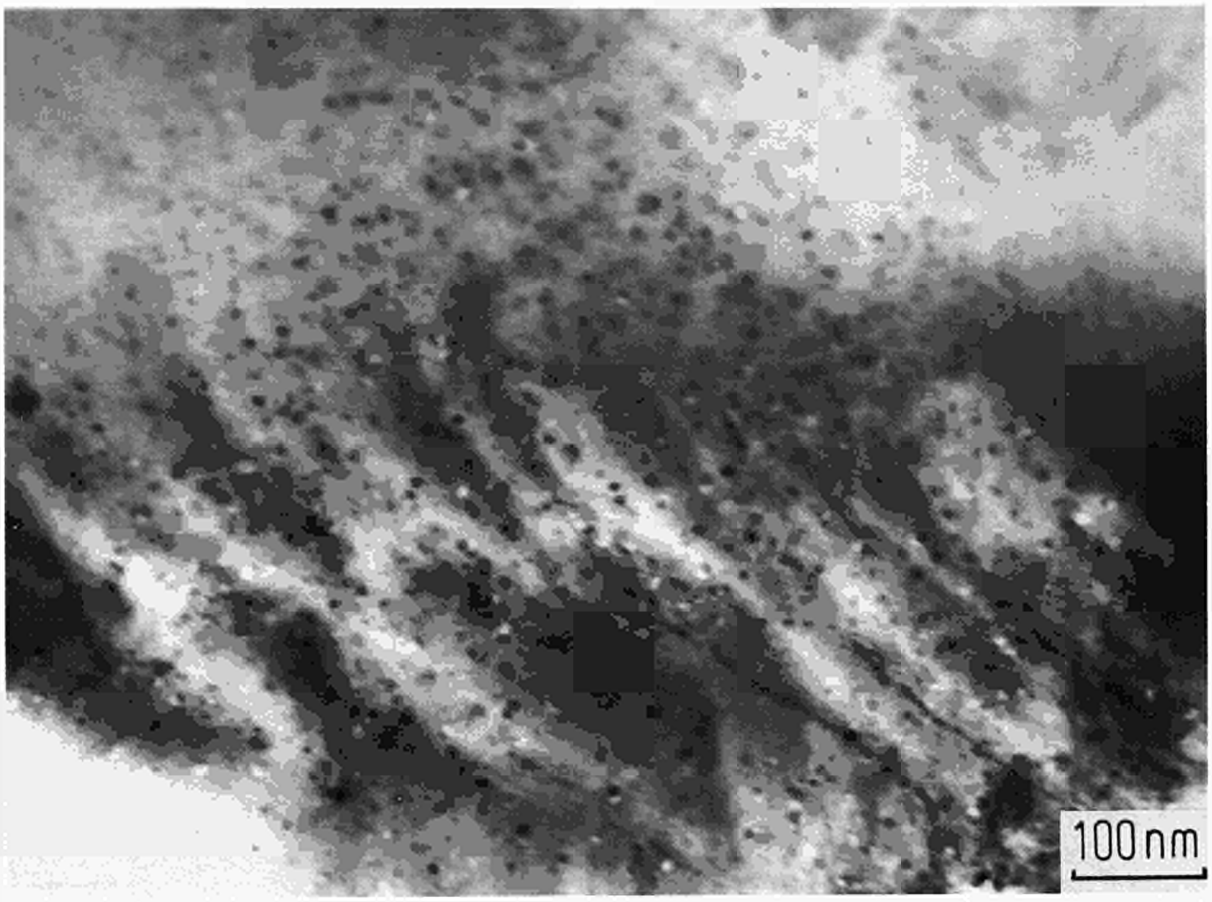


*Fig. 1.2* *Micrograph showing the population of very small fission gas bubbles as observed at the periphery of the base-irradiated fuel B1(1)*

very similar to those observed at the periphery, the measured density being equal at 2.2 x $10^{10}$ cm.cm$^{-3}$.

A population of very small fission gas bubbles exists at the centre of the fuel, again almost invariably associated with small precipitates of approximately the same size. The size distribution is narrow with a mean diameter of 7.5 nm, and the density is uniform with an average value of 1.9 x $10^{16}$ cm$^{-3}$.

Rather unexpectedly areas showing larger fission gas bubbles in the size range 7 nm to 27 nm were found in the central regions of the fuel. The distribution of these areas was inhomogeneous and the bubbles were always linked to dislocation networks. The local density of this bubble population reached a value of 2.4 x $10^{15}$ cm$^{-3}$, but the overall density is very low because the population was completely absent over 90% of the area examined. An example of this bubble population is shown in Fig. 1.3, taken from the fuel sample B3(2).

## *Comparison of the microstructures of the transient-tested and base-irradiated fuel samples*

The experimental results obtained on the transient-tested samples have been reported previously. The main differences in the microstructure of the transient-tested fuels are the development of a population of fission gas bubbles in the size range 30 nm to 400 nm, leading to local swelling of the fuel, and the growth of large precipitates of the solid fission products.

The comparison of the base-irradiated fuel with the transient-tested fuel can be summarised as follows:

i). The microstructure of the base irradiated fuels is characterised by a uniform dislocation density, on average 2.2 x $10^{10}$ cm.cm$^{-3}$, largely climb induced, and a high density of very small fission gas bubbles. There is very

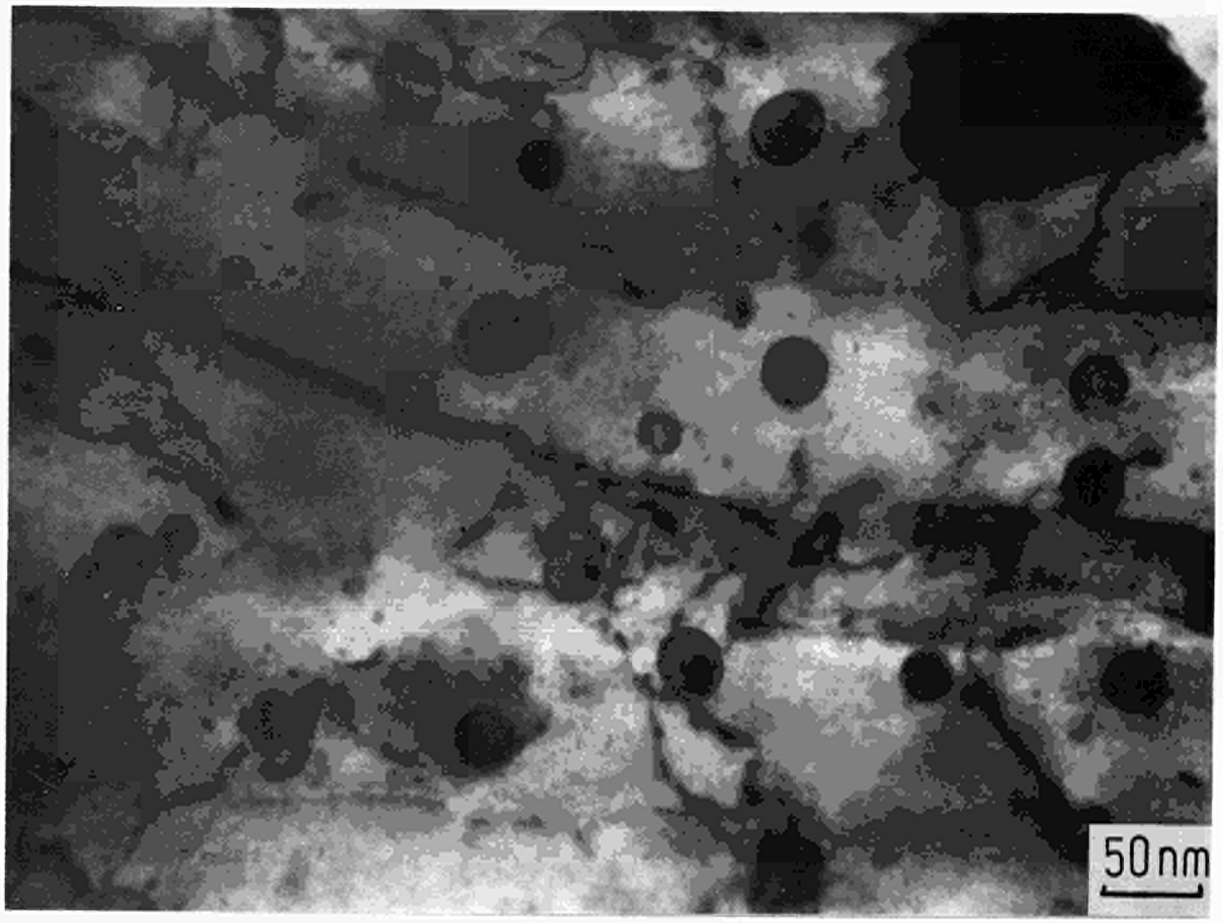


*Fig. 1.3* *An example of an area of larger fission gas bubbles as found with a very low inhomogeneous distribution in the base-irradiated fuel sample B3(2)*

little variation in microstructure between the periphery and the centre of the fuel.

ii) The nature of the dislocation structures observed in the transiented samples indicates that plastic deformation has occurred during the transient, particularly towards the centre of the fuel. The dislocation density at the fuel centre is lower than at the periphery, and extensive network and low angle grain boundary formation is observed.

iii) The population of small fission gas bubbles observed in the base-irradiated sample had the same density and size distribution at the periphery of the transiented samples, but was absent at the centre of the fuel.

iv) A population of large fission gas bubbles grows during the transient associated with the dislocation networks, and leads to local microswelling. The large bubbles are often surrounded by dense dislocation tangles, probably resulting from dislocation loop punching to relieve bubble overpressure. The density of these bubbles is low at the periphery and centre of the fuels, and peaks at a radial position around R/Ro = 0.4 to 0.5. The microswelling contribution from this bubble population reaches values of about 1.5% averaged over the total fuel cross section. An example of this bubble population imaged by TEM is shown in Fig. 1.4 taken from the specimen TR2.

### *Results of the REM analysis of the transient-tested fuel samples*

The evaluation of the results obtained by REM on the fuel samples listed in Tab.1.1 is still in progress, and only a brief indication of the results obtained will be presented here.

The primary microstructural difference between the base-irradiated and the transiented samples was the growth of a population of large fission gas bubbles (> 50nm) during the transient. The dis-

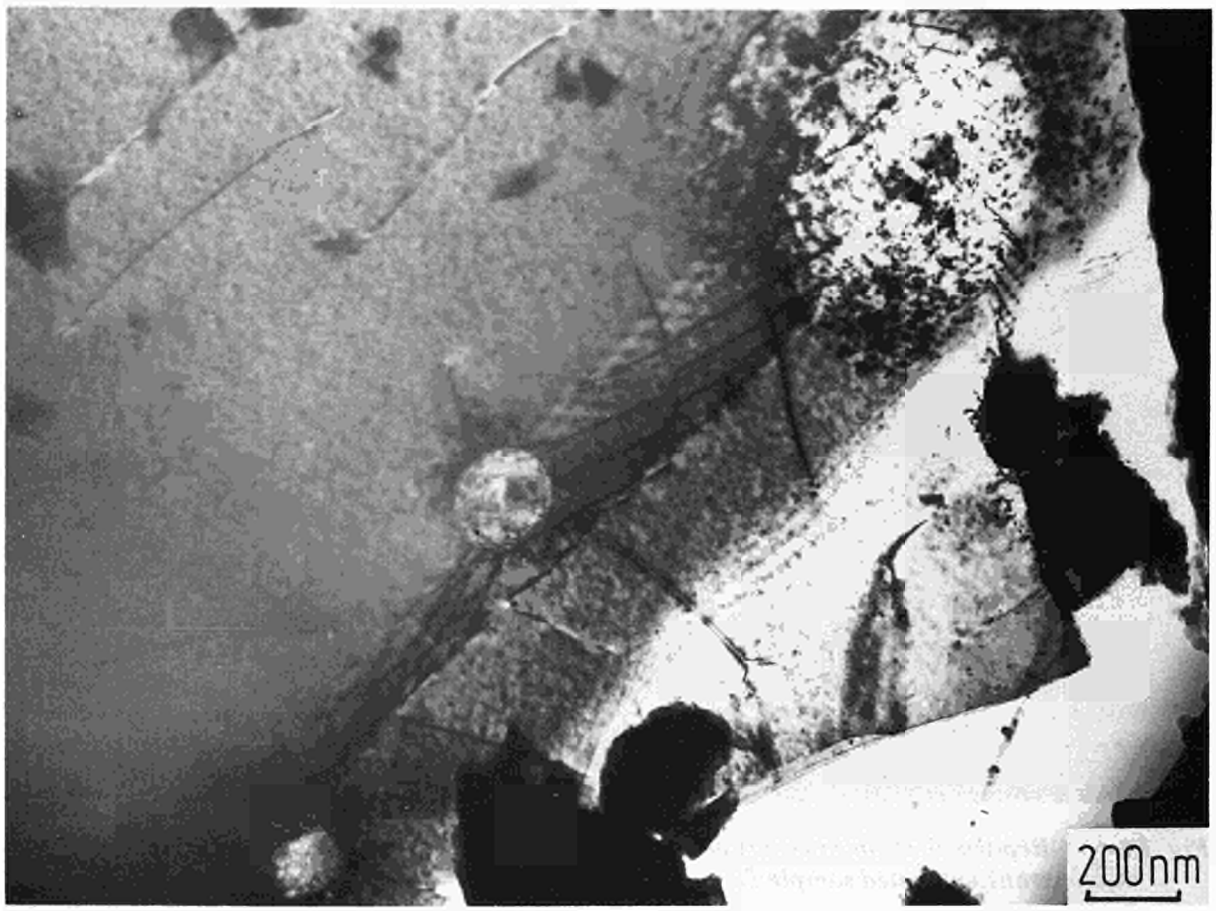


*Fig. 1.4* *Micrograph showing an example of the large fission gas bubble population which is created during the transient. These bubbles are almost invariably linked to the dislocation networks ( TR2 )*

tribution of this bubble population is most conveniently analysed as a function of radius using the REM technique. Figs. 1.5, 1.6, 1.7, 1.8 show a series of REM micrographs taken at various radial positions showing the development of the population of large fission gas bubbles at various radial positions for the a typical transient-tested fuel sample ( T5 ). The following features can be seen typically on the replicas:

Periphery

$R/R_0 = 1.0$ - Grain boundaries visible from the etching. No grain boundary bubbles or intragranular bubbles visible. Zone of increased porosity in the immediate vicinity of the periphery.

$R/R_0 = 0.71$ - Start of grain boundary decoration by small fission gas bubbles. No intra-granular bubbles.

$R/R_0 = 0.70$ - Strong grain boundary decoration. Start of intragranular bubble formation.

$R/R_0 = 0.40$ - Peak position for intragranular swelling. Denuded zones visible adjacent to grain boundaries.

Centre

$R/R_0 = 0$ - Very low density of large grain boundary and intragranular bubbles.

The resulting microswelling due to this fission gas bubble population averaged over the full fuel radius amounted to about 1.5 %. All the transient tested fuels showed a peak in the radial microswelling profile at a position of about $R/R_0 = 0.4$ - 0.5.

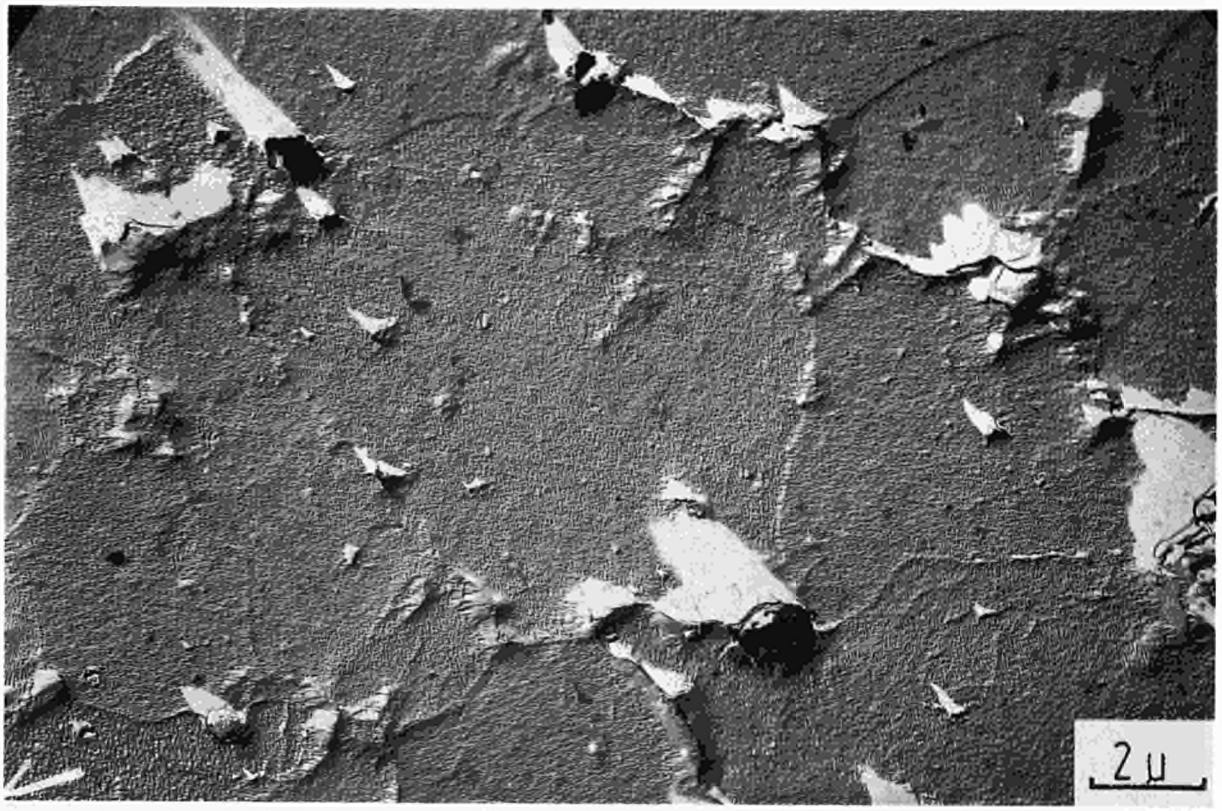


*Fig. 1.5* *Replica electron micrograph showing the highly porous zone at the periphery of the transient-tested sample T5*

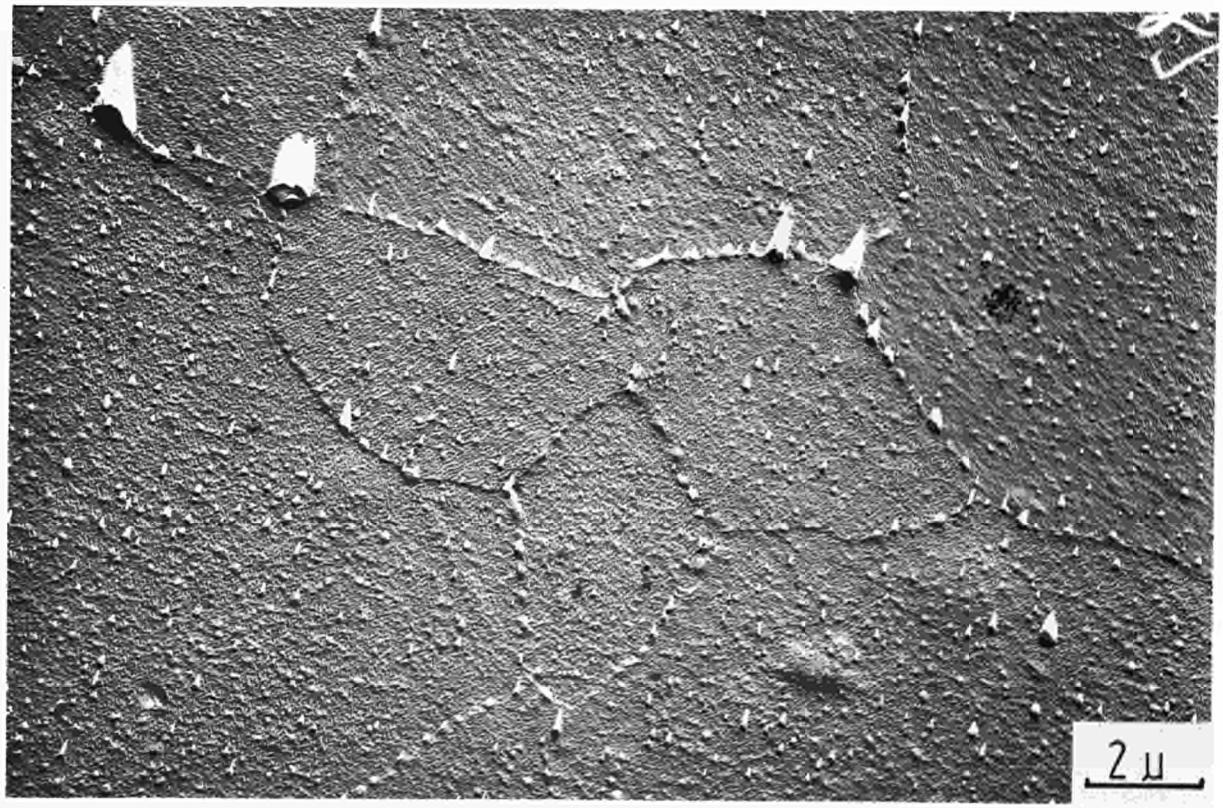


*Fig. 1.6* *Replica electron micrograph taken at the radial position R/Ro = 0.70, showing bubbles on the grain boundaries and the onset of intragranular fission gas bubble formation (Sample T5)*

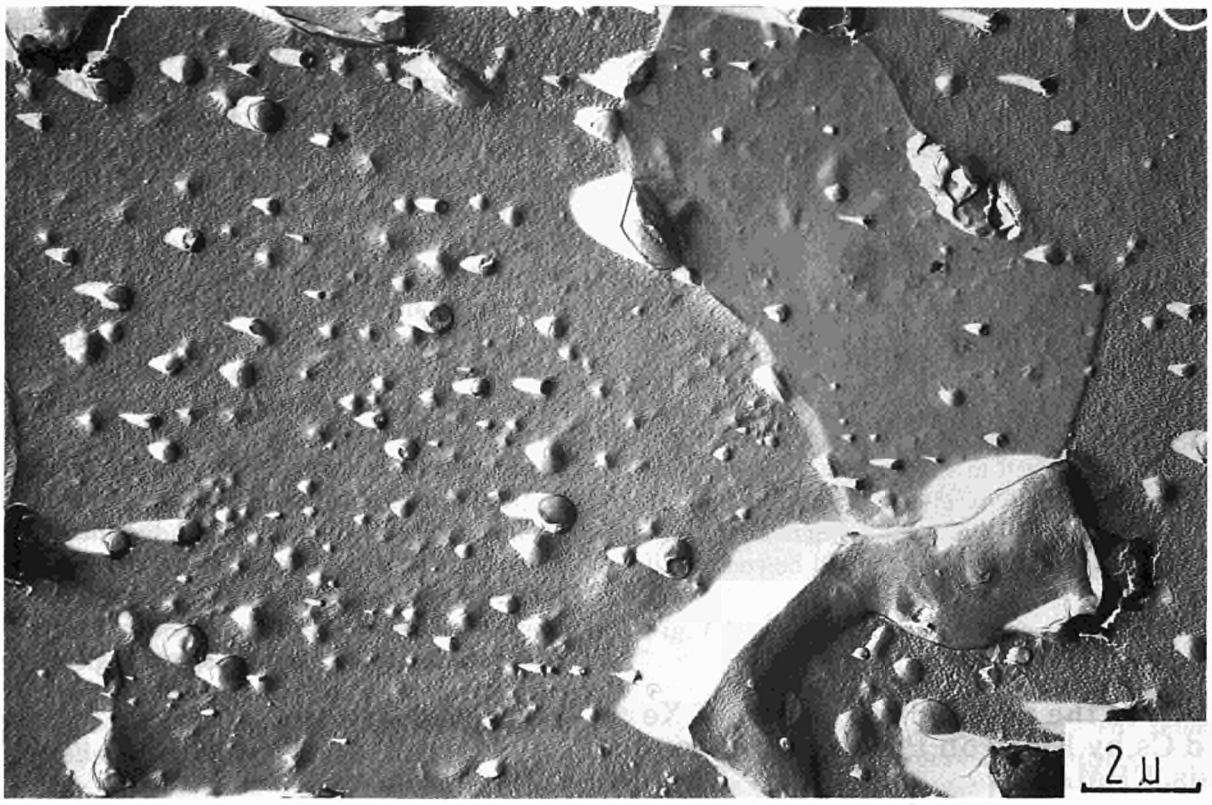


*Fig. 1.7* *Replica electron micrograph taken at the radial postion R/Ro = 0.40 showing high local intra granular swelling due to the growth of fission gas bubbles (Sample T5)*

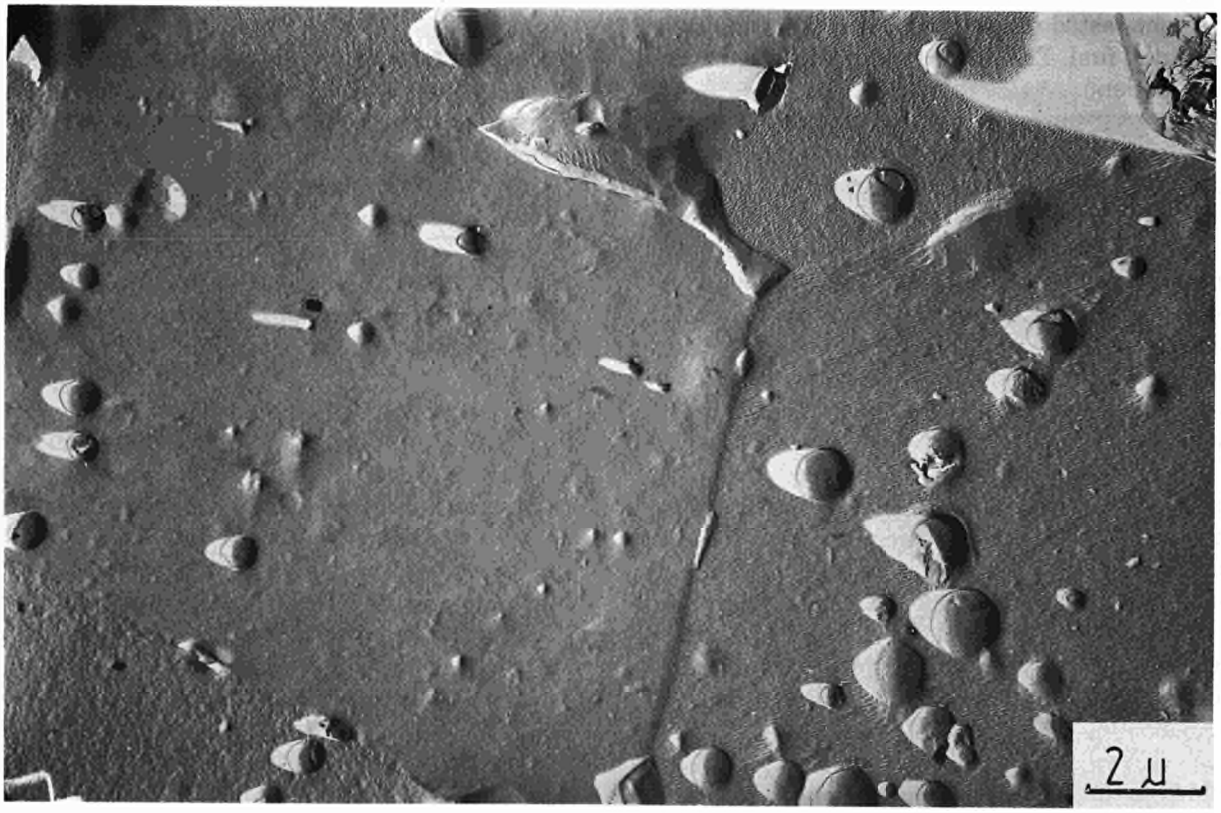


*Fig. 1.8* *Replica electron micrograph taken at the radial position R/Ro = 0.06, close to the fuel centre, showing a strong reduction in the density of the large fission gas bubble population (Sample T5)*

The preliminary results of the evaluation of the replicas which are already available indicate that a consistent picture is emerging of the properties and growth of the fission gas bubble populations as a function of temperature, burn up and the type and extent of the transient. In addition the results demonstrate that the fission gas behaviour does not appear to be affected by the process of refabrication.

## Conclusions

Very significant progress has been made during the reporting period in the analysis of transient-tested fuel samples by electron microscopy, and the understanding of the micro-structural changes and effects. This work will be concluded during 1991.

## Study of the radial distribution of Xe and Cs by Electron Probe Micro Analysis, EPMA

The radial distributions of Xe and Cs in 20 sections of fuel have been measured by EPMA. Fuel sections were taken from all the successfully transient-tested rod segments and from the base-irradiated fuel. The latter sections fulfilled a control function.

Most of the sections analysed were cut from rod segments that had been refabricated and fitted with a thermocouple and/or a pressure transducer. Five different types of transient test were employed each of which fall into the category of either a "staircase" ramp in which the terminal power was reached stepwise and slowly or a fast ramp in which the terminal power was reached in two leaps. Some of the tests incorporated one or more power dips.

The transient test conditions were wide ranging. The terminal power (pin average) varied from 29.8 to 44.7 $kWm^{-1}$ and the hold time from 2 to 140 h. Further, both Xe and He fill gas was used at different pressures (1 at. min., 25 at. max.). The fuel investigated came from four different sources and had burn-ups which ranged from 2.8 to 5.3 at%.

EPMA is used to obtain detailed information about the amount of fission gas released from the $UO_2$ grains. It is expected that comparison of the radial concentration profiles for the different fuel sections will provide important information about the effects of the main test parameters: terminal power, hold time and fill gas. It will also be possible, for the first time, to directly relate local gas release values to the fuel temperature. This will enable precise determination of the apparent gas diffusion coefficent and will be invaluable in furthering our understanding of the mechanism of fission gas release. Furthermore, by comparing the EPMA results for the fuels from different sources the effect of fuel specification and fabrication route should be seen. At present it can be stated that the level of gas release in the transient tests was not affected by refabrication.

In all except two cases X-ray fluorescence analysis (XRF) has been carried out at the Risø National laboratory on fuel sections adjacent to those taken for EPMA. Differences between the XRF and EPMA data point to gas retention on grain boundaries and in closed pores. Such information is required in order to establish the importance of mechanical pressure in delaying gas release under transient conditions.

## Characterization of simulated high burn-up fuel (SIMFUEL) and Kr-release measurements

To replicate the complex microstucture of high burn-up fuel, it is necessary to achieve uniform dispersion of all added fission products and to reach phase equilibrium during SIMFUEL preparation. This implies that the SIMFUEL constituents must be mixed homogeneously on a submicrometer scale and then heated to a sufficiently high temperature to achieve diffusion rates which ensure homogeneity on an atomic level. To this end, vacuum-dried, high purity additives (99.999 % purity oxides) were dry mixed with small particle-size $UO_2$ powder. High-energy, wet, stirred-ball milling was used to achieve a uniform submicrometer dispersion of the entire composition. The resulting slurry was kept suspended until it was spray dried. This served to lock the selected composition (corresponding to burn-ups of 3 or 6 at.%) into granules. Conventional pre-compaction, granulation, pressing and sintering at 1650 °C for 2 hours under flowing $H_2$ yielded a structure typical of a fuel that has operated at high temperature where solid phases precipitate and gas bubbles form.

The phases present and the fission products in solution were analysed by a large number of techniques: X-ray diffraction, scanning electron microscopy (SEM), electron-probe microanalysis

(EPMA) in energy- (EDX) and wavelength-dispersive (WDX) mode, transmission electron microscopy (TEM), selected-area electron diffraction (SAED), extractive replica-electron microscopy (REM), secondary ion mass spectrometry (SIMS) and X-ray photoelectron spectroscopy (XPS) were all used. As expected, Y, Zr, Sr, La, Nd, Ca were fully or partially dissolved in the matrix. Spherical metallic Mo-Ru-Pd-Rh precipitates were found uniformly dispersed throughout the matrix (Fig. 1.9) and a finely precipitated perovskite phase of the type (BaSr) · $ZrO_3$ (Fig. 1.10) was observed decorating the matrix grain boundaries, thus fully replicating irradiated fuel. Compared with previous fabrication campaigns (TUAR 1988, p. 42), the final material contained less "fabrication impurities" (mainly Si and Fe). Therefore, the previously observed formation of Ba-silicate scales interferring with gas release measurements was avoided. As before, Kr was introduced by controlled ion implantation using the Chalk River electromagnetic mass separator. The details of fabrication and characterization have been published in the reporting period [1].

The release of Kr was, for the first time, measured isochronally and isothermally under oxidizing conditions and in the temperature range of

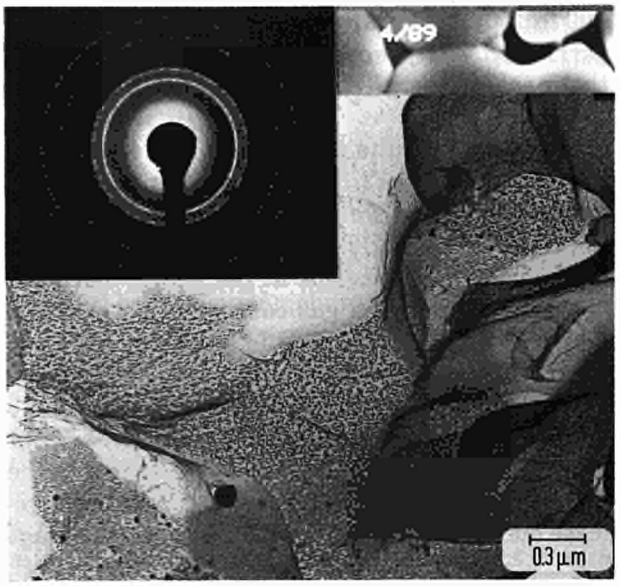


*Fig. 1.10* *Extraction replica electron micrograph and electron diffraction pattern. A grain boundary area of a fracture surface is seen showing small perovskite crystallites*

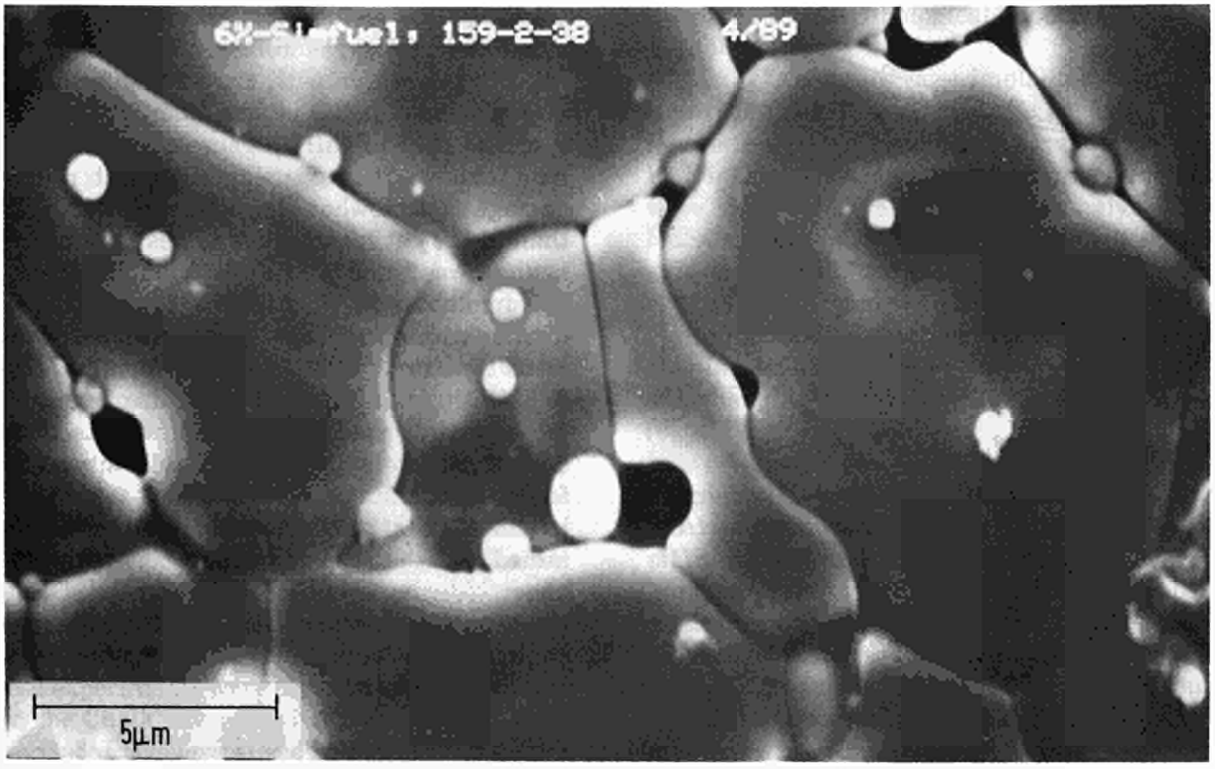


*Fig. 1.9* *Scanning electron micrograph of SIMFUEL showing noble metal precipitates*

300 to 1500 °C. Parallel experiments were always performed with reactor-grade $UO_2$ pellets. A further parameter was the gas concentration.

Some typical results on Kr-release are shown in Figs. 1.11 and 1.12. Fig. 1.11 gives results for isothermal anneals at 1500 °C and under reducing conditions ($Ar/H_2$) for a rather small gas concentration. $10^{12}$ ions/cm$^2$ at the energy used (40 keV) correspond to a gas concentration of about $10^{-3}$ at.% at which gas bubble formation does not occur but gas trapping at radiation-induced lattice defects is already causing most of the gas to diffuse more slowly than single gas atoms would move in a perfect $UO_2$ lattice [2]. As shown in the lowest part of the figure for $UO_2$, composite release curves are obtained with a fast release stage

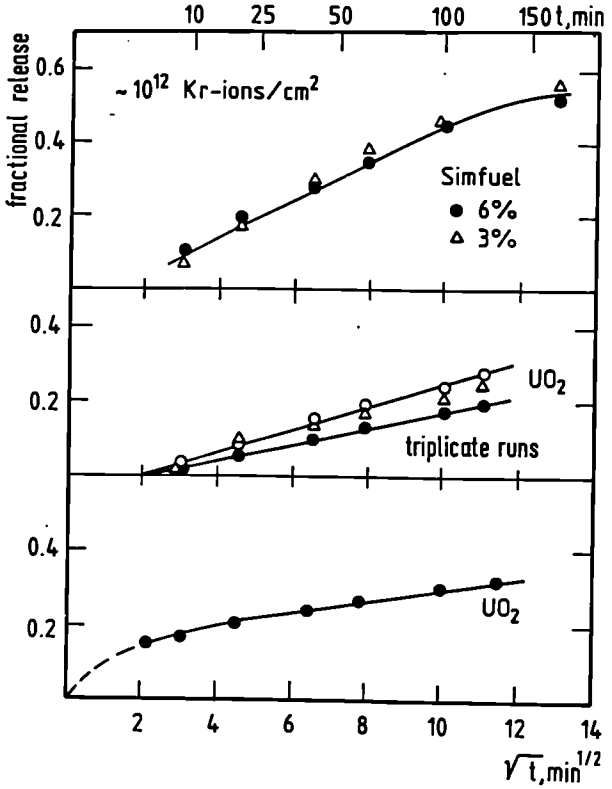


*Fig. 1.11* *Isothermal release of Kr-85 at a small gas concentration from $UO_2$, and from 3 % b.u. and 6 % b.u. SIMFUEL at 1500 °C under reducing conditions. The lower part shows a typical as-measured release curve for $UO_2$. The two upper parts show results following subtraction of the fast release in the first anneal stage of 5 min duration (see dashed curve in the lower part)*

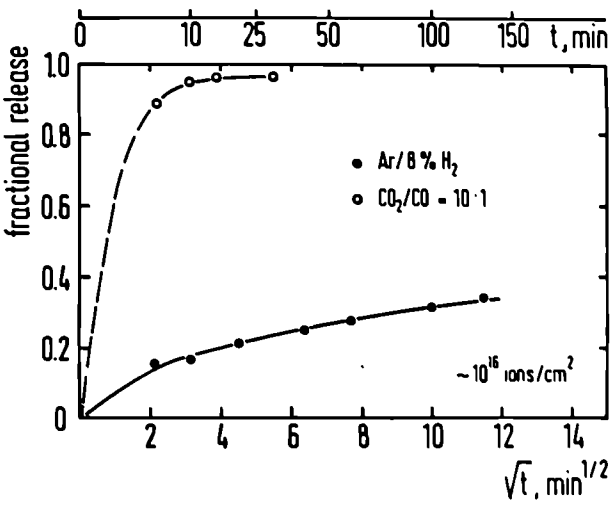


*Fig. 1.12* *Isothermal release of Kr-85 at a high gas concentration at 1500 °C under either reducing or oxidizing conditions*

occurring during some or all of the first 5 min anneal corresponding to the high diffusion coefficient representative of single gas atom diffusion without trapping. Such a stage is typical for ion-implanted $UO_2$ since a fraction of the gas located near to the surface can be released without becoming trapped. The second part of the release curves represents gas diffusion in the presence of trapping. This yields the effective diffusion coefficients describing gas diffusion in operating fuel [2]. It is constant with time as shown by the straight lines in the middle and upper parts of Fig. 1.11. The slightly higher release from SIMFUEL shows that trapping of gas at radiation damage is somewhat less efficient in SIMFUEL than in $UO_2$ at high temperatures. A similar behaviour was found in isochronal anneals. Because the implantation distances are small, release fractions are much larger for ion-implanted specimens than for similar experiments on irradiated fuel. With the diffusion coefficients obtained, the corresponding percentages of gas release for the anneal conditions of Fig. 1.11 would only be 1.1 % for reactor irradiated $UO_2$ and 1.5 % for reactor irradiated SIMFUEL. Similar results were obtained for other gas concentrations and anneals under reducing conditions. The presence of non-volatile fission products in $UO_2$ is thus predicted not to cause a dramatic increase in gas release at high temperatures.

Such a dramatic increase is, however, observed if either $UO_2$ or SIMFUEL are annealed in oxidizing $CO/CO_2$ mixtures during the release experi-

ment. Since the oxygen potentials of $UO_{2+x}$ and of given $CO/CO_2$ mixtures have different temperature dependences, annealing in a given $CO/CO_2$ mixture causes different x-values in $UO_{2+x}$ at different temperatures. The data of Fig. 1.12 are thus for $UO_2$ oxidized to $UO_{2.04}$ in the first anneal stage, whereas the data of Fig. 1.13 are for different x-values. A very pronounced increase in release rate is seen for oxidized fuel.

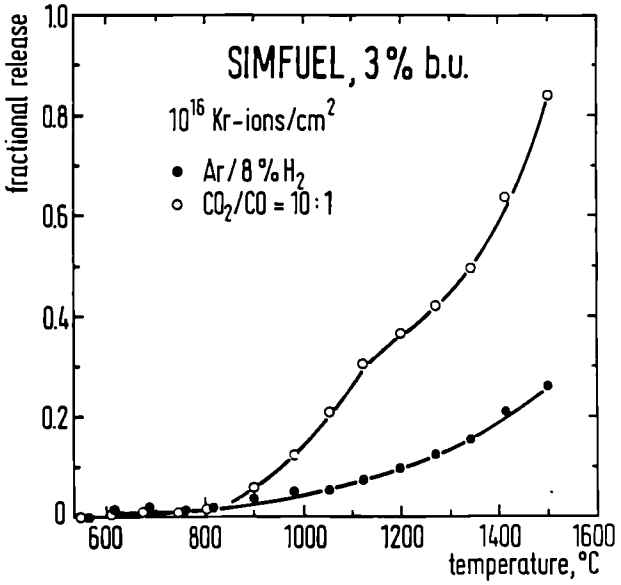


*Fig. 1.13 Isochronal release of Kr-85 from 3 % SIMFUEL under either reducing or oxidizing conditions*

More data of this type at different gas concentrations have been and are being collected to provide a data base for the three-parameter field of temperature T, deviation from stoichiometry x and gas concentration c. For all parameters used so far, trapping of Kr was significantly reduced in $UO_{2+x}$ as well as in oxidized SIMFUEL as compared with stoichiometric fuel. More data will be reported in the next annual report. Confirming results were also obtained on the mixed oxide $(U,Th)O_2$ with 3 % U-content where annealing in air also caused significantly reduced trapping and thus considerably increased gas release values. These experiments were performed in cooperation with the Chalk River Laboratories, AECL, Canada and JAERI, Japan and were reported at the Int. Conf. on Nonstoichiometric Compounds in Tokyo, Dec. 1990 [3].

## Radiation damage in $UO_2$: Damage production and recovery in the U-sublattice of ion implanted $UO_2$ between 5 K and 2000 K

In much of the existing literature on damage (point defect) ingrowth and recovery of $UO_2$, changes in the defect state of the $UO_2$ lattice were followed by measuring changes in physical properties that are *not specific* for a given sublattice, hence which do not unequivocally differentiate between oxygen and uranium defects. Such measured properties are electrical resistivity and lattice parameter. Also, damage was always produced at 293 K or at some (often estimated) temperature above room temperature (e.g. [4]): radiation damage consists, however, of defects in *both* the oxygen and the uranium sublattice: interstitials, vacancies and their clusters in both sublattices, as well as extended defects (dislocation lines and loops, stacking faults) are all formed.

The Rutherford backscattering (RBS)/channeling technique was used here, which allows separate measurements in the U-sublattice. U-ions are the less mobile species in $UO_2$. A typical ratio of diffusion coefficients is $D^O/D^U \sim 10^8$ at 1400 °C [5]. Mobility of U-atoms is therefore rate-controlling for technologically interesting processes such as grain growth, sintering, creep etc., and knowledge on U defect mobility is thus not only of scientific but also of technological importance.

$UO_2$ single crystals were implanted with Kr- or Xe-ions in the dose range of $5x10^{14}$ to $1 \times 10^{16}$ ions/cm$^2$ at either room temperature or at 77 or 5 K. For the low temperature implants the crystals were implanted and in situ analyzed with RBS/channeling with 2 MeV He-ions using the 2-axis cryostatic goniometer at INFP, KfK. This set-up is connected with an ion implanter and a van de Graaff accelerator which allows for performing implantation and RBS/channeling without changing the temperature and the vacuum [6].

Aligned and random spectra were measured before and after ion implantation. The crystals implanted at low temperature were slowly warmed-up to room temperature, and the aligned spectra were measured at different temperatures. To measure recovery at temperatures above 293 K, the crystals were furnace-annealed and subsequently analyzed.

Fig. 1.14 shows the comparison of random and channeling spectra obtained for an unimplanted

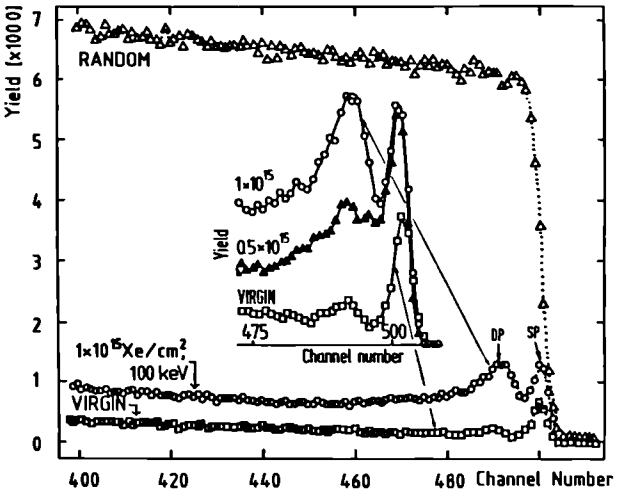


*Fig. 1.14* *Random and aligned backscattering spectra for a <100> $UO_2$ single crystal implanted with Xe-ions at 5 K. The aligned spectrum for the unimplanted crystal is also shown. The inset shows aligned spectra for $UO_2$ single crystals implanted with two different doses of Xe-ions at 5 K*

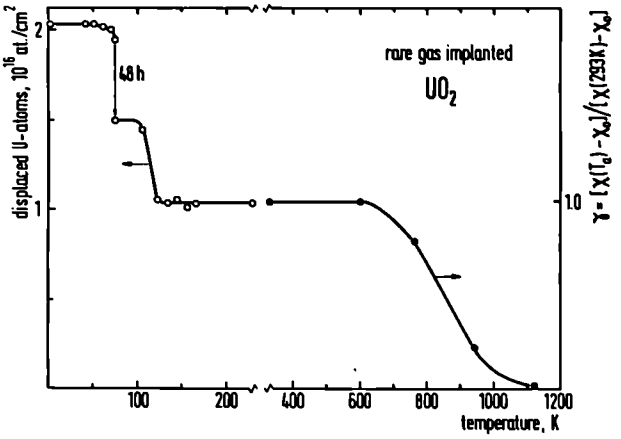


*Fig. 1.15* *Damage recovery of ion-bombarded $UO_2$ ($1x10^{15}$ rare-gas ions/cm²) as a function of temperature, expressed as number of displaced U-atoms for $T \leq 293$ K, and as dechanneling parameter $\gamma$ for higher temperatures*

$UO_2$ single crystal and for the same crystal after in-situ implantation with 100 keV Xe-ions at 5 K. Two well distinguished peaks are present for the aligned crystal: the usual surface peak (SP) due to the surface atoms not being shielded on atomic rows and a damage peak (DP) at a greater depth (lower energy or smaller channel number). The inset shows the evolution of the damage ingrowth as a function of the implantation fluence: a steady growth of DP is observed. For clarity, the results obtained for doses between $1x10^{15}$ and $1x10^{16}$ ions/cm² and at bombardment temperatures of 77 and 293 K are not included in Fig. 1.14.

During in-situ warming up, only very small changes were observed in the spectra until a temperature of 77 K (liquid nitrogen temperature) was reached. At this temperature, the specimen was stored for 48 h and then it was further warmed up to room temperature.

The analysis of the spectra has to separate changes in the thermal vibrations of U-and O-atoms from recovery of damage. Fig. 1.15 shows the result of the analysis. Two recovery stages below room temperature are clearly visible. The first one, located at 77K appeared only after prolonged (48h) storage at this temperature. Its location at 77 K is somewhat ambiguous because of the very slow kinetics of defect transformation. The second low temperature recovery stage occurs at 110 K.

The further recovery at $T \geq 600$ K in Fig. 1.15 is given as dechanneling parameter $\gamma$ [7]. $\gamma$, as shown on the right ordinate, is essentially determined by $X_2$ ($T_a$) where $T_a$ = anneal temperature, and $X_0$ = minimum aligned yield of a virgin crystal behind the surface peak. Fig. 1.16 shows that temperatures of damage annealing are shifted to higher values if higher ion doses are used [7].

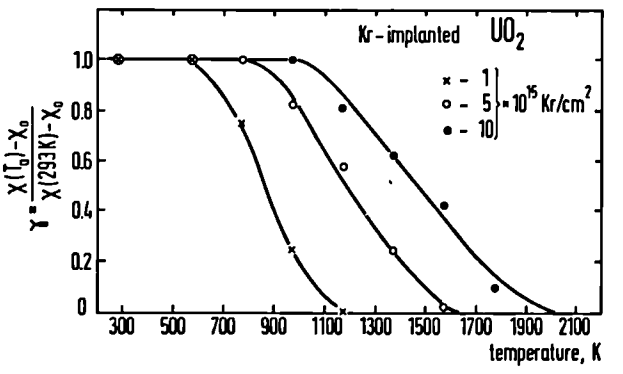


*Fig. 1.16* *Damage recovery of $UO_2$ implanted with increasing doses of Kr-ions at 293 K*

## Discussion

Recovery stages in radiation damaged solids are usually attributed to different defect reactions. The simplest of these are annihilation of interstitials (i) and vacancies (v). This leads to the necessity of measuring and explaining at least 4 stages in a compound like $UO_2$ (stages for $O_i$, $O_v$, $U_i$, $U_v$). Previous work did not yield convincing evidence for the behavior of $U_i$, and no data existed for damage formation and recovery below room temperature.

In the present work, the first recovery stage located at ~ 77 K is clearly due to U-defect mobility. It is generally agreed that for $UO_2$, $U_v$ mobility causes the stage centered around 870 K [8]. We can therefore attribute the stage at ~ 77 K to $U_i$. Recovery begins with correlated recombinations of close Frenkel pairs. With increasing temperature, long range migration of $U_i$ starts allowing recombinations with alien vacancies, hence uncorrelated recombinations occur. At the end of the stage, interstitials survive only in small clusters.

The stage at 110 K can accordingly be explained as being caused by release of $U_i$ from shallow traps. This can lead to the growth of larger clusters and dislocation loops. Loop formation at low temperatures (20 to 200°C) has indeed been seen in transmission electron microscopy in $UO_2$ irradiated with 1.8 MeV electrons or in a reactor [9].

The next broad recovery stage at 700 to 900 K is then attributed to the mobility of single (or clustered) U-vacancies, in agreement with results on quenched $UO_2$ and on diffusion data. With increasing ion dose, this stage is shifted to higher temperatures, as one would expect for cluster formation. At a dose of $1x10^{16}$ ions/cm$^2$, recovery is not complete before 2000 K are reached. These data contribute to our knowledge on lattice defects in $UO_2$, and they point to a deficiency of calculating defect energies for $U_i$ with a fully ionic model of $UO_2$. These calculations had yielded rather high migration energies (and thus recovery temperatures) for $U_i$ [10]. On the other hand, the results help to explain the measured rather high diffusion coefficients D* for radiation-enhanced U-diffusion in $UO_2$ during fission: fission rate-dependent values of up to $D^* \sim 10^{-16}$ cm$^2$s$^{-1}$ were observed even at the lowest temperatures used (~ 100°C). The mobility of $U_i$ away from the centre of the fission spike, due to the biasing force of the hydrostatic pressures formed within the spike can explain the observed values [11].

**References**


[1] P.G. Lucuta, R.A. Verrall, Hj. Matzke and B.J. Palmer, J. Nucl. Mater., 178 (1991) 48

[2] Hj. Matzke "Gas Release Mechanisms in $UO_2$ - A Critical Review", UK-Report AERE-R 9733 (1980) 345 and Radiation Effects 53 (1980) 219

[3] T. Ogawa, R.A. Verrall, Hj. Matzke and P.G. Lucuta, Int. Conf. on Non-stoichiometric Compounds, Tokyo, Dec. 1990, in print in Solid State Ionics

[4] N. Nakae, A. Harada, T. Kirihara and S. Nasu, J. Nucl. Mater. 71 (1978) 314

[5] Hj. Matzke , J. Chem. Soc., Faraday Trans. 86 (1990) 1243

[6] R. Kaufmann, J. Geerk and F. Ratzel, Nucl. Instrum. Methods 205 (1983) 293

[7] Hj. Matzke. and A. Turos, Nucl. Instrum. Methods Phys. Res. B46 (1990) 117

[8] Hj. Matzke, J. Chem. Soc., Faraday Trans. 2, 83 (1987) 1121

[9] J. Soullard, J. Nucl. Mater. 135 (1985) 139

[10] R.A. Jackson, A.D. Murray, J.H. Harding and C.R.A. Catlow, Phil. Mag. 53 (1986) 27

[11] Hj. Matzke , Radiation Effects 64 (1982) 3 and 75 (1983) 317


## Leaching, hydration and surface analysis of unirradiated $UO_2$

This study aims at providing the necessary basic data needed for any model of leaching spent fuel. First results were reported in TUAR 1988, p. 179 and TUAR 1989, p. 39. Sensitive nuclear methods are used to determine extent, depth and kinetics of surface layers formed on $UO_2$ during exposure to water with different pH-values and to Q-brine. In particular, Rutherford backscattering (RBS) and the channeling technique are used to measure thickness and U-content of surface layers, and elastic recoil detection analysis (ERDA) is applied to measure the hydrogen content of the surface layers affected by leaching. For these measurements, He-beams of 2 to 2.3 MeV energy are used obtained from van de Graaff accelerators (KfK and University of Padova).

## Experimental

The material used was either single-crystalline $UO_2$ or sintered pellets of reactor grade $UO_2$. All materials were pre-annealed to adjust the oxygen to metal, O/M, ratio to the stoichiometric value of 2.

Leaching was performed in distilled water with three different pH-values (pH = 4, 7 and 10) or in Q-brine in autoclaves with a Teflon lining at temperatures between room temperature and 200 °C and for times between 1 h and 1000 h. The ratio of solution volume to surface area of $UO_2$ was 10:1 or 20:1 $cm^3/cm^2$. Before and following leaching, the specimens were weighed. RBS spectra were measured before and following leaching. The single crystals were also investigated with the channeling technique, i.e. RBS spectra were measured in random and aligned mode before and following leaching. The RBS/channeling technique enables one to measure the displacements of U-atoms from their sites in the fluorite structure in the spectra of aligned crystals, and it gives information on the O/U-ratio in the spectra for random orientation. In this way, both, layer thickness and layer composition, can be determined following leaching.

Some representative specimens were analysed for possible hydrogen (water) pick-up due to leaching by applying elastic recoil detection analysis (ERDA) with 2.2 MeV He-ions. An angle of incidence of 75° was chosen and the beam intensity was kept small (0.2 $\mu A/cm^2$) to minimize H loss due to energy deposition. Calibration of ERDA was made with standards of hydrogenated amorphous silicon with constant H concentrations of 5.6 or $12.3 \times 10^{21}$ $H/cm^2$ [1].

## Results

The <100> single crystals used showed a very good channeling behavior with a minimum aligned yield, $\chi_{min}$, of about 0.03, in agreement with theoretical prediction [2].

Leaching at temperatures up to 100 °C, even for relatively long time (i.e. about 1000 h) did not produce any noticeable change in the channeling spectra, independent of the pH-value. Also, no change in weight was observed. An effect of leaching was first measured after prolonged treatment at 130 °C. Fig. 1.17 shows the time dependence of the thickness of the oxidized layers formed by leaching for the case of pH = 10. For this pH-value and for the rather high temperatures, a parabolic time law is observed, compatible with a growth mechanism controlled by oxygen diffusion through the layers. For lower temperatures and neutral leaching conditions, layer growth was rather linear with time, indicating that under these conditions, growth is controlled by the oxidation reaction taking place at the interface between the distorted and the undistorted parts of the crystal. For pH = 4, very thin layers were found even for long leaching times, probably due to increased U-solubility.

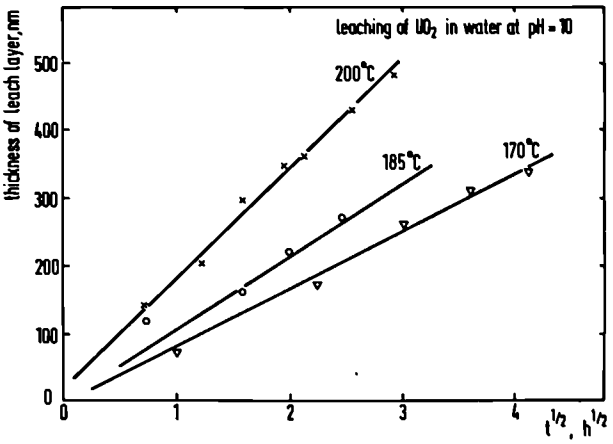


*Fig. 1.17 Thickness of oxidized layers on $UO_2$ leached at 170, 185, or 200 °C in water at pH = 10, as a function of time*

Additional information on the disording mechanism can be obtained from an analysis of the random spectra (see TUAR 1988, p. 181). A rough evaluation shows that the approximate composition of the near-surface layers is about $UO_{2.3}$. This would correspond to the formation of a $U_3O_7$ layer. A more careful analysis of different specimens has been started. It shows that the oxygen content varies often with depth within the layer and usually is in the range of O/U-ratios corresponding to $U_2O_5$ or $U_3O_7$.

For long leaching times at the highest temperature used, i.e. 200 °C and times of 600 to 1000 h, a small hydrogen content was detected [1]. Scanning electron micrographs (see Fig. 2.36 in TUAR 87, p. 111 for an example) showed local growth of basalt-type uranium oxide crystals. EDAX analysis confirmed that these crystals contain only U atoms as metal atoms.

## Discussion

The present study provides quantitative data on the thickness of layers which form on $UO_2$ when exposed to water. Such data are needed to understand and to model direct storage of spent nuclear fuels. The study also provides information on the concentration of U-atoms displaced from their original sites within the fluorite structure of $UO_2$,

and on the O/U-ratio. Layer thicknesses between about 100 and 500 nm were measured, depending on temperature T, time t and pH-value of the water. The time dependence could be measured between 130 and 200 °C. Below 130 °C, no surface change could be detected for the t-range used.

$UO_2$ itself has a very low solubility in water; however, following surface oxidation to a higher oxide, often postulated to be $U_3O_7$, the solubility increases [e.g. 4] . The chemistry of $UO_2$ as a function of redox conditions has been studied before [e.g. 5] indicating an oxidation to $UO_{2+x}$ under rather reducing conditions and showing that the oxidation can proceed beyond $UO_{2.33}$ (or $U_3O_7$) under more oxidizing conditions. The present study shows that both rate-law and composition of the layers depend on T and pH-value. The data, for instance, exhibit a $t^{\frac{1}{2}}$ law indicating rate-control by oxygen diffusion through the oxidized layer of (approximate) composition of $UO_{2.33}$. The indicated activation enthalpy of 0.9 eV and the diffusion coefficients calculated from the curves are compatible with this suggestion. Oxygen interstitials are the mobile species in $UO_{2+x}$, the most probable range of experimental values of their migration energy is 0.8 to 1.0 eV [6] and the D-values calculated from layer growth fall roughly into the range extrapolated from high-temperature measurements of chemical diffusion of oxygen in $UO_{2+x}$ [6]. As another example, in neutral water and at lower temperatures, layer growth was indicated to proceed linearly with t, pointing to a reaction-controlled growth rather than a diffusion-controlled one.

ERDA analysis confirms the absence of any hydrogen in the above layers, within the detection limit of this method. We thus deal with layers of higher uranium oxides with O/U-ratios in the range corresponding to about $U_3O_7$ and $U_2O_5$. A very careful surface analysis including simulation calculations has been started to better determine the indicated gradients in oxygen content through the oxidized layers.

Uptake of hydrogen was only observed for the highest temperature of 200 °C and long leaching times. Under these conditions, a complex solution-reprecipitation process causes the surface to become covered with new oxide crystals such as basaltic crystals mentioned above. Random RBS spectra are compatible with $UO_3$ formation under these conditions. ERDA yields hydrogen contents significantly smaller than those thermodynamically postulated for the equilibrium (at room temperature) compound $UO_3 \cdot 2H_2O$, known as schoepite in mineralogy [7]. Schoepite is the stable $U^{6+}$ hydroxide at low temperatures and is believed to be formed as weathering product of uraninite under oxidizing conditions. At 200 °C, n in $UO_3 \cdot nH_2O$ decreases from 2 to about 0.8. The value found by ERDA is still lower, i.e. ~ 0.2. This indicates either a nonequilibrium composition of the schoepite formed, or a surface coverage of only 25 %; this latter possibility is compatible with the SEM results.

**References**


[1] Hj. Matzke, G. Della Mea, F.L. Freire, jr. and V. Rigato, Nucl. Instrum. Methods Phys. Res. B45 (1990) 194

[2] Hj. Matzke and A. Turos, Solid State Ionics, in press. Presented at Int. Conf. Nonstoichiometric Compounds, Tokyo, Dec. (1990)

[3] Hj. Matzke and A. Turos, Nucl. Instrum. and Methods Phys. Res. B 46 (1990) 117

[4] K. Ollila, Mater. Res. Proc. 127 (1989) 337

[5] D.W. Shoesmith, S. Sunder, B.M. Ikeda and F. King, Mater. Res. Proc. 127 (1989) 279

[6] Hj. Matzke, J. Chem. Soc., Faraday Transactions 86 (1990) 1243

[7] P.B. Hostetler and R.M. Garrels, Econ. Geolog. 57 (1962) 137


## Determination of oxygen potential of FBR oxide fuel at very high burn-ups

A new series of measurements of oxygen potential, $\Delta G(O_2)$ of high burn-up $(U,Pu)O_2$ from fast breeder irradiations was performed. The miniature emf-cell used previously [1] was employed successfully to measure oxygen potentials of fuel up to the very high burn-up of 13.6 at.% (see Fig. 1.18). This work was done in cooperation with CEN Cadarache, as the previous work [1]. As is seen in Fig. 1.18, $\Delta G(O_2)$ increases significantly with the burn-up, due to the oxidative nature of fission and due to fission products dissolved in the fuel matrix. The present data are the first ones at such high burn-ups, and they indicate a saturation of this increase at ~ 10 at.% burn-up.

**Reference**


[1] Hj. Matzke, J. Ottaviani, D. Pellottiero and J. Rouault, J. Nucl. Mater. 160 (1988) 142

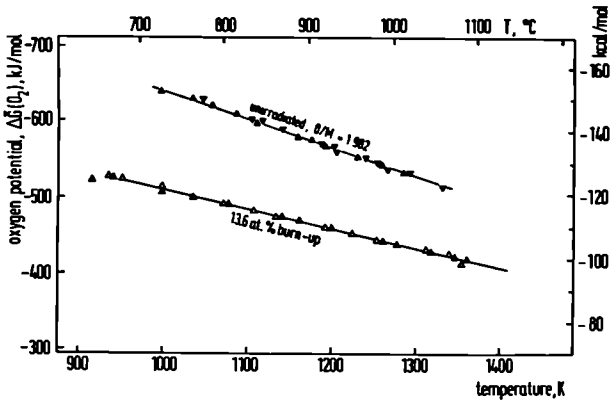


*Fig. 1.18 Oxygen potential measurements with the miniature emf-cell of unirradiated $(U_{0.8}Pu_{0.2})O_{1.982}$ and oxide irradiated to 13.6 at.% burn-up*

# Study of Problems related to Reactor Safety

## Introduction

A number of investigations were performed in direct relation to reactor safety programmes concerned with destructive accidents. The cooperation with the Phebus PF Project [1] was intensified with modification and production of ultrasonic thermometers for the first in-pile test, with specification for the analysis of fuel rods and with an examination of a double-density $ZrO_2$-insulator after contact with liquid $UO_2$. Further work dealt with a post-irradiation examination of the fuel of the Silène fission gas experiment and final examinations of samples from the reactor core of TMI-2 were performed.

### Reference

[1] E.F. Scott de Martinville, Ph. Delchambre and P. von der Hardt, "The Phebus FP Project, Status Report 1989/90", EUR-12926 EN (1990)

## Examination of a dual-density $ZrO_2$ thermal insulator after contact with liquid $UO_2$

### Introduction

A stabilised dual-density $ZrO_2$ specimen is to be used as an insulation material in the fuel bundle section of the Phebus PF project facility. It is composed of a dense $ZrO_2$ layer plasma-sprayed onto a porous $ZrO_2$ layer (50% porosity) that has a CoCrAlY coating to provide adhesion between the two layers. A sample of the zirconia had been placed in a stainless steel vat and held in position against the bottom by a metal rod. The vat was then rapidly filled with a 100 kg of superheated liquid $UO_2$ at 3050°C and allowed to cool. The specimen was then removed and mounted ready for metallographic examination, along with a control specimen of double density zirconia. The following examination was made in collaboration with JRC Ispra who provided the ready mounted samples.

### Optical and SEM/EDAX examination

Both optical and SEM/EDAX examinations were carried out. The structure of the double density zirconia before testing can be seen in Fig. 1.19. The plasma-sprayed $ZrO_2$ grains in the dense layer have a flattened shape, while the porosity and grain of the porous $ZrO_2$ are rounded.

By contrast, examination of the tested $ZrO_2$ specimen showed the interaction of the liquid $UO_2$ with the $ZrO_2$ layers (Fig. 1.20). An outer $UO_2$ layer is seen above a one-phase, mixed oxide (U, Zr)$O_2$ layer (approx. 250-300µm deep), which sits upon the lower half of the dense $ZrO_2$ layer. The interfacial CoCrAlY layer is now dispersed into separate melted spheres. Some of the components such as Al and Y appear, from EDAX analysis, to have diffused into the $ZrO_2$ matrix. The lower half of the dense $ZrO_2$ structure is also very changed with larger rounded grains replacing the flattened grain structure and a eutectic structure evident at the grain boundaries composed of Al-Zr oxides and Y-U oxides. This rounded structure indicates a fusing of this layer during the heating. There is also deep cracking evident in the lower half of the dense $ZrO_2$ indicating severe stresses as a result of the high thermal gradients. There was a significant increase in the thickness of the dense layer. There is no completely clear explanation for this increase. The Ispra report [1] sug-

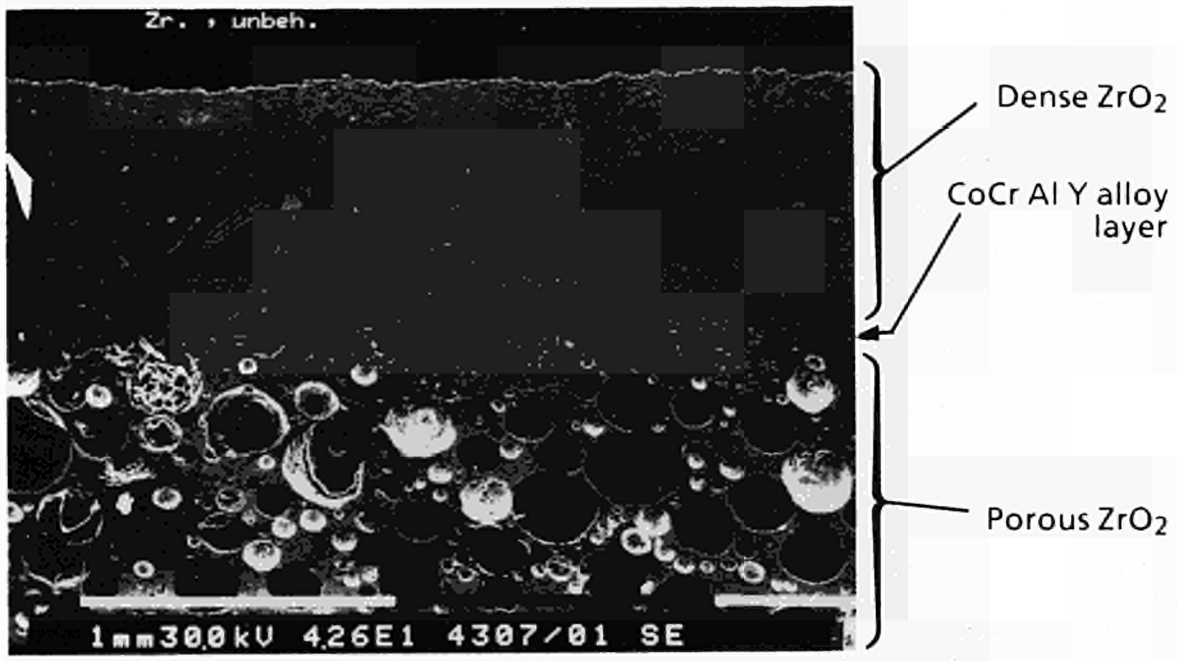


*Fig. 1.19 SEM micrograph of double density $ZrO_2$ sample prior to testing (46x)*

gests that this may be due to melting and densification of the upper region of the porous $ZrO_2$ directly below. This should be tested in further experiments with the material, as the porous $ZrO_2$ layer appears to have only been slightly affected by the heating at the interface.

## Discussion of time-temperature profiles

The single phase (Zr, U)$O_2$ oxide sometimes shows a constant U/Zr ratio across its depth. This implies a local melting of the upper layers of the dense $ZrO_2$ in contact with the liquid $UO_2$ at 3050°C, and indicates that the surface 250-300 µm depth reached up to 2000 to 2500°C and then rapidly solidified as a single phase oxide, as did the chill zone of $UO_2$ crystals at the interface with the $ZrO_2$. There was clearly substantial melting of the lower half of the dense $ZrO_2$ layer, while the subjacent porous $ZrO_2$ appeared to have been only superficially affected.

On the basis of the $ZrO_2$ and (U, Zr)$O_2$ melting points, estimated thermal conductivities and diffusivities, and the liquid $UO_2$ temperature, it has been assessed that the heating to form the single phase mixed oxide was completed within milliseconds, while the cooling to the final structure (i.e. below 1800°C) occurred within several seconds.

The zone of greatest thermal stresses during the test appears to have been in the lower regions of the dense $ZrO_2$ layer (as evidenced by cracking).

## Concluding remarks

It can be stated that despite some thermal cracking, the double density zirconia material successfully withstood the weight of molten $UO_2$ against it, and from the point of compatibility with liquid $UO_2$ it seems to be suitable for its intended use as a thermal shield around the Phebus PF bundle.

**Reference**

[1] P. Bottelier, G. Buscaglia, M. Cambini, M. Della Roma and R. Zeyen, Compatibility of Liquid $UO_2$ with Dual-Density $ZrO_2$ Insulator Sample, Ispra, Technical Note 1.89.107 (1989).

## Post-irradiation examination of a Silène specimen

Silène is a series of experiments carried out by CEN - Cadarache intended principally to determine the effect of fission gas pressure build up on the melting fuel under very fast power ramp conditions.

The (U,Pu)$O_2$ fuel (containing 25 wt% Pu) was irradiated under steady-state conditions for 90 days (~2 at.% burn-up) before being ground up and repacked as a powder into open-ended mini-pins and ramped first at 729 J/g and then again at 1393 (±70) J/g (the latter being sufficient to melt the fuel).

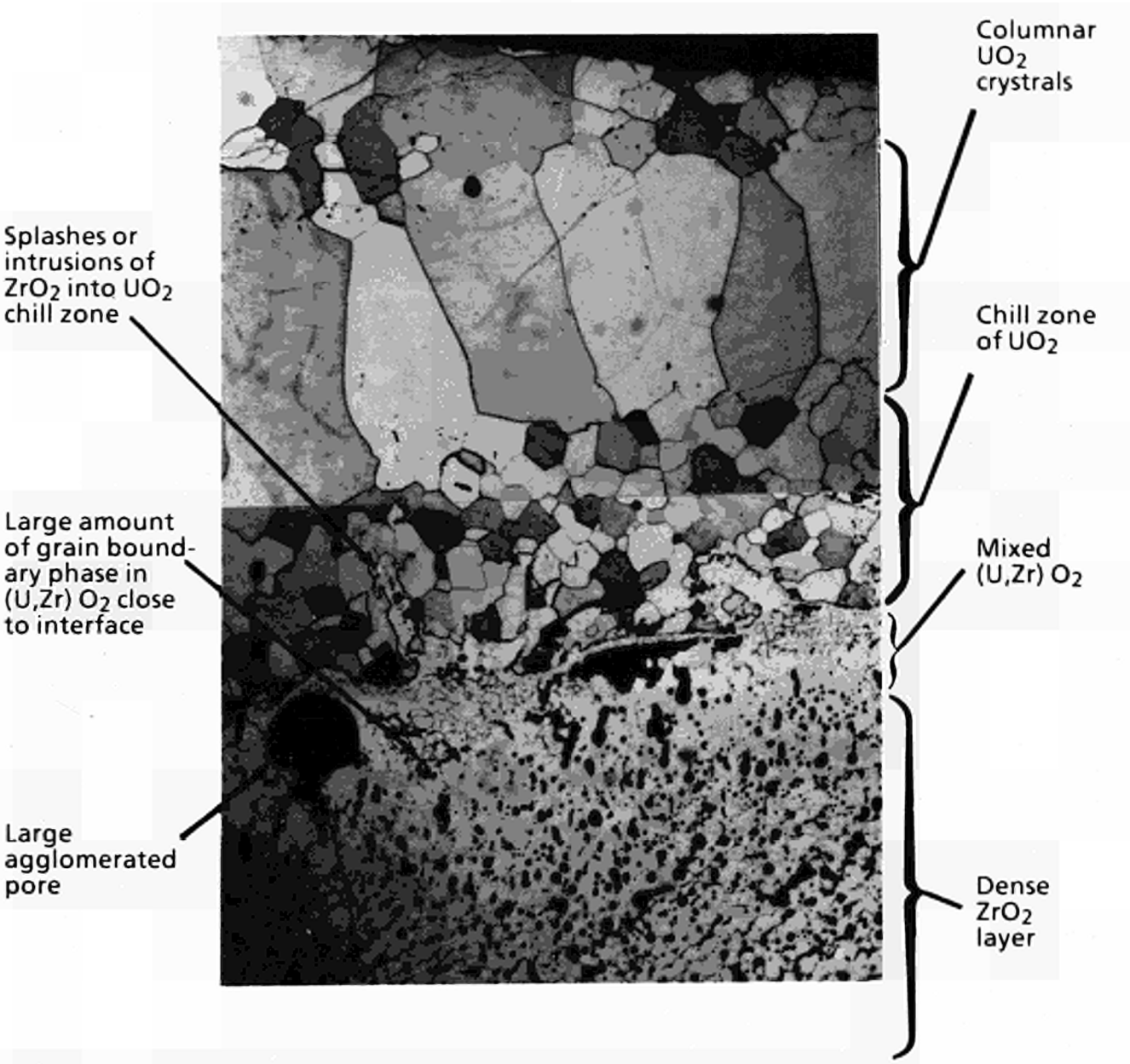


*Fig. 1.20 Optical micrograph of etched $UO_2$-tested sample showing $UO_2$ grains (50x)*

A mini-pin from after the first ramp only (TP36) and a pin exposed to both ramps (TP29) were then examined at ITU as part of the collaboration with CEN Cadarache.
The ramping had an explosive effect and had compacted the powder in an outer ring against the steel cladding (see Fig. 1.21), as well as blowing fuel out into the free volume above the pin.
The twice-ramped TP29 had noticeably less fuel left than TP36 because of the additional ramping as well as ruptures in the cladding. The hollow ring of fuel had large ellipsoidal pores oriented radially with reduced porosity at the outer edges. These pores may have been formed either by fission gas release or by trapping of He filling gas during the impaction of the fuel against the cladding. The grain size also appeared to be considerably larger and with more pores than the starting material, and there may have been melting in some zones.
SEM/EDAX examination also noted metallic phases linked to these pores that were rich in Mo and Ru fission products (Fig.1.22).

EMPA (Microprobe) measurements detected Xe or Cs in the solid (or in micropores up to approx. 500 Å diameter), at or below the limits of detection (~200 ppm (wt.) for Xe and ~170 ppm (wt.) for

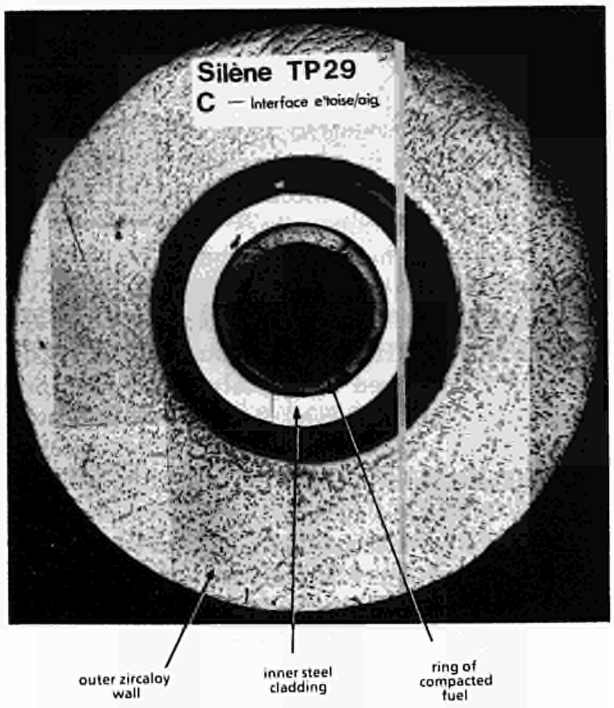


*Fig. 1.21 Silène TP29 - Interface (27x)*

*Tab. 1.3 Microprobe analyses of Silène specimens (parts per million)[1]*

| | TP29 | | TP36 | | Ref. Matl. No.2 | |
|---|---|---|---|---|---|---|
| | Xe | Xe | | Cs | Xe | Cs |
| Point 1 | 155±28 | < 100 | | 270 | 2770 | 2370 |
| Point 2 | 230±86 | < 100 | | 180 | 2700 | 2380 |
| Point 3 | 250±93 | < 100 | (3) | 330 | 2700 | 2270 |
| Point 4 | 210±78 | < 100 | | 150 | - | - |
| Point 5 | - | (2) 110 | | 170 | - | - |
| Point 6 | - | (2) 100 | | 180 | - | - |
| Average | 210 ppm | < 100ppm | | 230ppm | 2700ppm | 2300ppm |

Limits of Detection: 190 - 200 ppm Xe
170 ppm Cs

Note:
(1) each point an average of ten values
(2) pieces found between cladding and zircaloy
(3) confidence limits: ±130 ppm Cs

Cs). This compares with ~2700 ppm Xe and ~2300 ppm Cs found in unramped control material (see Tab. 1.3).
The TEM examination revealed some occasional fine intragranular porosity in which slight amounts of Xe (or Cs) may be retained, but the above measurements indicate that 90-95% of the Xe and Cs has been released from the fuel during either of the ramps.
This lack of retained Xe found here is not unexpected in view of the gross microstructural changes observed during the ramping.
The comparison between the ramped and unramped fuels shows how ramping at these very high power densities converts a powder fuel into a fused, porous ring impacted against the cladding with at least 90% of the Xe and Cs released from the fuel, even at 50% melt power levels (730 J/g).

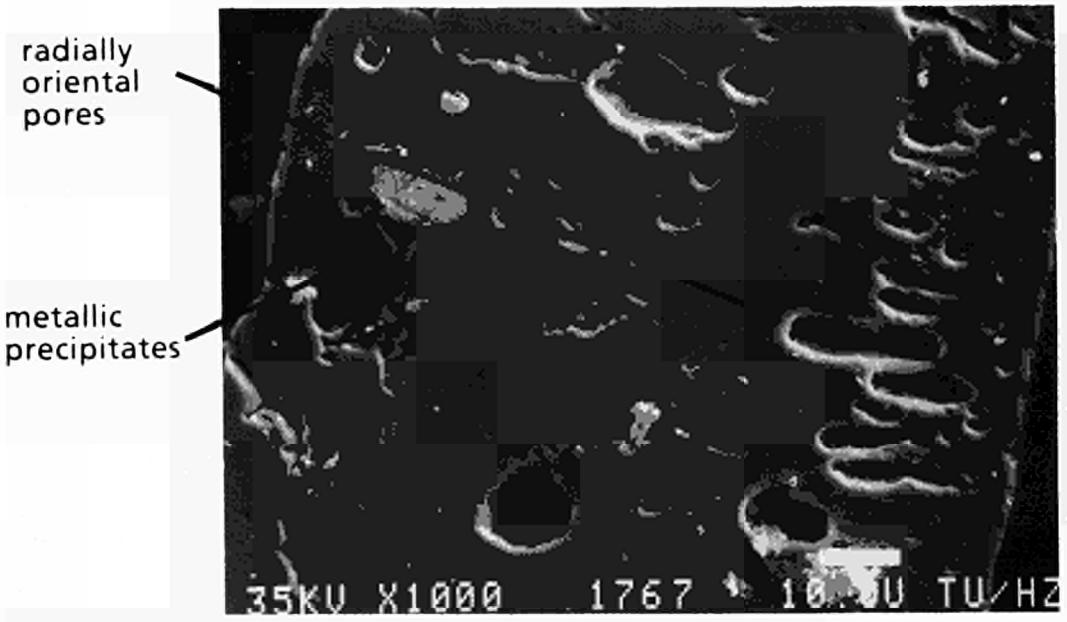


*Fig. 1.22 Silène TP36 - Interface - fuel showing porosity and precipitates (1000x)*

## Examination of samples from the reactor core of TMI-2

The Institute has participated during the last 3 years via the OECD in a programme sponsored by the US Department of Energy to examine samples taken from the severely damaged core of the TMI-2 reactor.
In this time the results of the investigation of

i) the completely molten inner core
ii) the surrounding crust
iii) the particulate debris lying above the upper crust
iv) fuel rod remnants from the reactor's edge

have already been reported in previous annual reports (see TUAR 88, p.34; TUAR 89, p.181); final aspects were examined in 1990 concerning the quantitative and qualitative γ-spectroscopy analysis of a melted core rock sample (G12-P9-B) and an unaffected pellet from a fuel rod sample (C7 3-35) from the reactor's edge.

The G12-P9-B sample has been shown by previous optical and electron-optical examination to be composed of a $UO_2$ phase, $ZrO_2$ phase, and a dispersed ferrous (Fe, Ni, Cr, Al) oxide phase. This composition seems to have resulted from the fusion of the $UO_2$ fuel, the zircaloy cladding and the stainless steel or inconel structural components; the aluminium comes from the $Al_2O_3$ present in the burnable poison rods.

The specimen were refluxed in 10M $HNO_3$+0.01M $NH_4F$ for 18 hours at 95°C; the fuel pellet dissolved completely while the core sample left an undissolved residue that consisted mostly of $ZrO_2$; both the solutions and the residue were analysed by γ-spectroscopy (see Fig. 1.23).

The most important nuclide in the fuel was $^{137}Cs$, and thereafter there were small peaks due to $^{134}Cs$, $^{125}Sb$, $^{155}Eu$, $^{154}Eu$. Similar analyses on fuel samples at CEA Saclay revealed the same isotopes in similar concentrations. In the soluble fraction of the core sample, although $^{137}Cs$ was the strongest peak, $^{134}Cs$, $^{125}Sb$, $^{154}Eu$, $^{155}Eu$ were much more in evidence along with non-volatile fission products such as $^{144}Pr$, $^{144}Ce$, $^{106}Rh$, and the irradiation product $^{60}Co$ (the latter probably originating from the Zircaloy cladding).

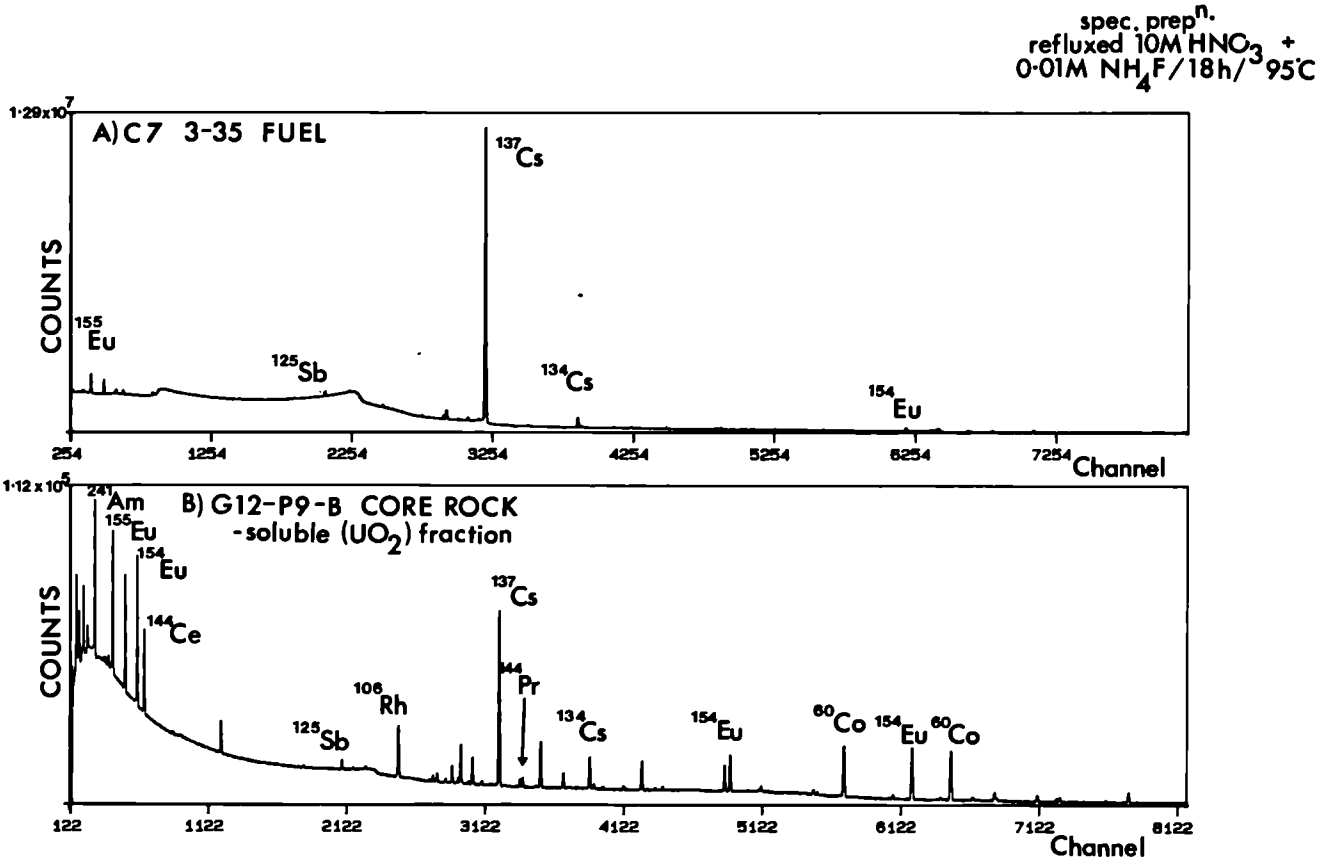


*Fig. 1.23* *γ-spectra of TMI-2 samples from A) unaffected fuel rod from the reactor's edge and B) molten core rock sample (soluble fraction)*

The insoluble fraction of the G12-P9-B core sample contained mostly $^{60}Co$, along with $^{137}Cs$, $^{106}Rh$ and also $^{241}Am$; in comparison with the soluble fraction there was an enhanced concentration of $^{60}Co$ but lowered $^{137}Cs$ levels in the finely-divided residual $ZrO_2$ phase. Analyses by CEA, Saclay of core and agglomerate samples showed the same range of isotopes (excepting $^{241}Am$) but in widely differing concentrations which underlines the heterogeneity of the samples, especially the agglomerates.

Considering the likely conditions sustained by the core sample of up to 2500°C (the eutectic temperature of the $ZrO_2$ -$UO_2$ system) during the accident it is very surprising to find a volatile product $^{137}Cs$ as a major nuclide, particularly in the insoluble phase. The concentration of the $^{60}Co$ in a $ZrO_2$-rich phase is also surprising as $^{60}Co$ would have been expected to separate into the ferrous phase, which would be in the soluble fraction.

These results clearly show that despite very high temperatures (~2500°C or higher) volatile fission products $^{134}Cs$, $^{137}Cs$, $^{125}Sb$ are still retained within the molten core.
This serves as an indication of the complexity of the core chemistry in these conditions and further implies that fission product release codes should not assume a 100% release for volatiles.
In a broader context the investigation has indicated how and at what temperatures the reactor can melt down. Different mechanisms are operative at different locations and temperatures. The inner core was a completely molten $ZrO_2$-$UO_2$ mixture at 2500°C, the outer crust (a heterogeneous metallic/ceramic structure) had a more variable temperature in the region of 1500°C, when eutectic interactions between the stainless steel control rod cladding and zircaloy cladding are possible (between 1200°C and 1400°C). However if the silver control rod alloy (m.p. 800°C) is released then dissolution processes could start below 1000°C.

# Study of High Temperature Properties of Nuclear Materials

## Introduction

In the reporting year, an important milestone has been reached with the measurement of the specific heat of liquid $UO_2$ at temperatures up to 8000. K. With the successful conclusion of this project, the next high temperature measurement in progress is that of the thermal expansion coefficient of liquid $UO_2$.

The new research line, concerning the behavior of radioactive fission products and actinides in reactor accidents and in spent-fuel repositories, is going to take up the largest part of our investments both in manpower and equipment. Besides the construction of a system of shielded Knuden-cells with mass spectrometers for the measurements of FP transpiration from irradiated LWR fuel, substantial analytical work is being carried out by updating existing computer codes for the characterization of the irradiated fuel and the prediction of the primary source term in a variety of hypothetical accident situations. Furthermore, new codes describing the chemical equilibrium of the system fuel-water-fission products are being developed.

Studies of high temperature thermophysical properties of non-radioactive materials are continuing. Thanks to the availability of sophisticated equipment, substantial results have been achieved with minimum effort.

Our studies on graphite melting under high pressure inert gas provided an important contribution to the better definition of the carbon phase diagram.

A subject of particular importance for advanced pyrometric applications is the so called X-point phenomena in the high temperature emissivity of refractory transition metals. This effect has been long debated in recent years, and our latest measurements, carried out with improved experimental techniques, provide a solid experimental background for the interpretation of this phenomenon. In this context, an explanation of the spectral emissivity isotherm crossing ($\lambda_x$-point) has been given, based on a simple quantum-mechanical model.

## Specific heat of urania up to 8000 K

In reactor safety analysis dealing with very rapid reactivity excursions, the thermodynamic properties of the fuel at very high temperatures play an essential role. A long effort has been made during the last decade in order to assess a reliable equation of state for $UO_2$ up to the critical point. In this context ITU has provided a substantial experimental and theoretical contribution [1,2]. However, though the available thermodynamic models could in part be validated [3] and are now able to predict with sufficient accuracy primary quantities like equilibrium vapour pressures and thermodynamic potentials, differential quantities, as for instance the specific heat $C_p$, are still subjected to large uncertainties.

The construction of a high pressure autoclave was started at the Institute with the intent of measuring $C_p$ from the cooling curve of $UO_2$ spherical samples simultaneously heated by four symmetrically oriented laser beams in an inert gas atmosphere with pressures up to 1000 bar.
A number of serious experimental and analytical difficulties have been encountered during the setting up of this experiment, which have been surmounted by developing and implementing original and innovative techniques [4].

The experiment, based on the accurate measurement of the sample temperature during and after the laser shot and on the subsequent evaluation of the energy loss rates, requires a careful study of the cooling mechanisms (radiation and convection) as well as of the heat transport phenomena occurring in the sample. The long test and calibration work of the apparatus was concluded in summer 89', thereafter, in three experiment campaigns, $UO_2$ spheres of approximately 1mm diameter were heated up to 4000, 5000 and 8500 K, respectively, under conditions suitable for a significant analysis. More than one hundred tests have been carried out and analyzed, but only in less than 20 experiments the heating conditions were sufficiently homogeneous. Actually, the temperature evolution on the surface was used to calculate the heat penetration and the time evolution of the sample radial temperature profiles with a computer code. These have then been compared with ceramographic sections of the sample and only the shots where the position of the melting front agreed with that calculated were considered for the analysis.

The analysis started from the energy rate balance in all the virtually isothermal radial shells which were subdivided into two classes, those below the temperature where the specific heat was previously determined, and those whose specific heat was unknown. By increasing the peak temperature step by step from the melting temperature upwards, the shells with unknown specific heat were kept in the vicinity of the surface where the experimental error in temperature was small. The value of $C_p$ in each shell was obtained by solving the local heat rate balance equation. A large number of points was available for the analysis, so that for the final evaluation of $C_p$ only the outer shells were used in order to minimize the influence of the heat transport on the results.

Fig.1.24 shows the specific heat as a function of temperature; the results have been obtained from the analysis of approximately 200 experimental points. The full dots are the $C_p$ values below the melting point, which have been obtained by a critical review of the published data. The squares are the new measurements grouped in intervals of 100 K (which is a generous estimate of the temperature error). The scatter of the points is not surprising if one considers that five independent parameters are intervening in the analysis with their respective errors (temperature, temperature rate, emissivity, convective losses and thermal conductivity).

The analysis of the trend of $C_P(T)$ is in progress.

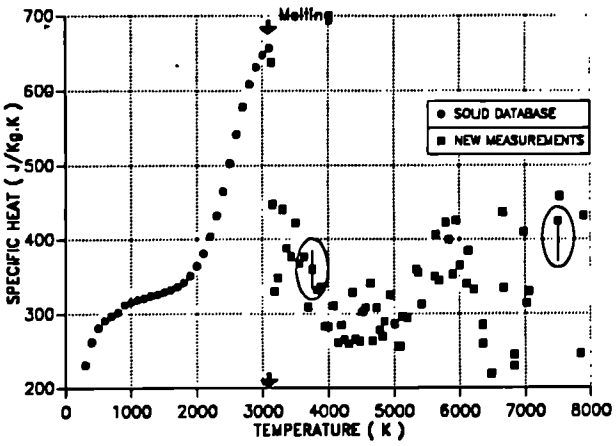


*Fig. 1.24* *Specific Heat of Urania: Symmetrical and asymmetrical error bars are indicated for the medium and high temperature region, respectively*

**References**

[1] R.W. Ohse et al, Equation of State of Uranium Dioxide, J. Nucl. Mater. 130 (1985) 165

[2] E.A. Fischer, Evaluation of the Urania Equation of State Based on Recent Vapour Pressure Measurements, Rep. KFK 4084 (1987) Karlsruhe, Germany

[3] W. Breitung , S.A. Wright, Measurements of the Total Pressure from Irradiated (U,Pu)-Mixed Oxide, Nucl. Sci. Eng. (in print)

[4] J.P. Hiernaut, C. Ronchi, Calorimetric Measurements with Acoustic Levitation in High-Temperature Heating Experiments with Pulsed Laser Beams, High. Temp.-High Press. 21 (1989) 119

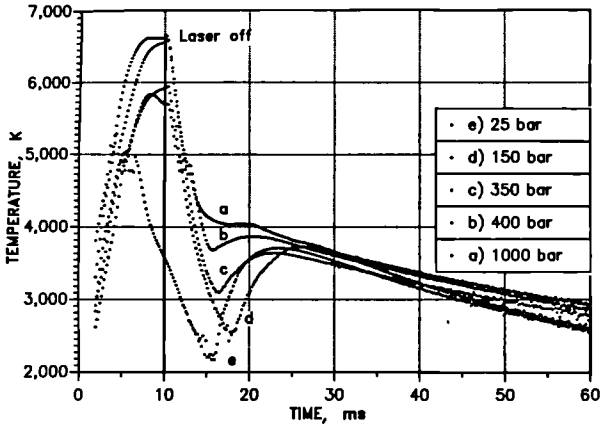


*Fig. 1.25* *Temperature evolution in pulses at various pressures*

*At low buffer gas pressures, the temperature during cooling attains a minimum, due to formation of carbon soot from vaporized graphite. The effect decreases by increasing gas pressure and is effectively absent at 1000bar, when the freezing plateau is clearly detected*

## Graphite melting at high pressure

From the beginning of this century, the solid/liquid/vapor triple point of graphite has been a subject of debate and, despite the progress in experimental techniques , the uncertainties became even greater in the last few years.

In our experiments spherical graphite specimens were heated by four tetrahedrally oriented laser beams to produce a fairly uniform temperature on the surface. A sufficiently large amount of molten graphite was produced to make it possible to identify the liquid/solid transition by a conventional thermoanalytical method. With the chosen experimental method most of the uncertainty factors have been minimized and, particularly, the experimental conditions were suitably selected to produce unambiguous and directly detectable melting effects. The temperature was measured by multichannel pyrometry, which enabled a detailed analysis of the perturbations and errors to be carried out. The triple point of graphite was found to be in the interval (see Figs 1.25, 1.26):

$T_t = 4100 \pm 50\,K$ and $p_t = 110 \pm 10\,bar$

The expansion upon melting is very large (up to 70%); this indicates, according to the Clausius-Clapeyron equation that the slope of the melting line as a function of pressure is positive. This, and the location of the triple point, imply a sequence of corollaries on the nature of the graphite/liquid transition and on the properties of the liquid phase. Contrarily to predictions based on corresponding states (e.g. in analogy with Ge) liquid graphite near the triple point should have a low coordination number and the dense tetravalent liquid should only be formed at higher pressures.

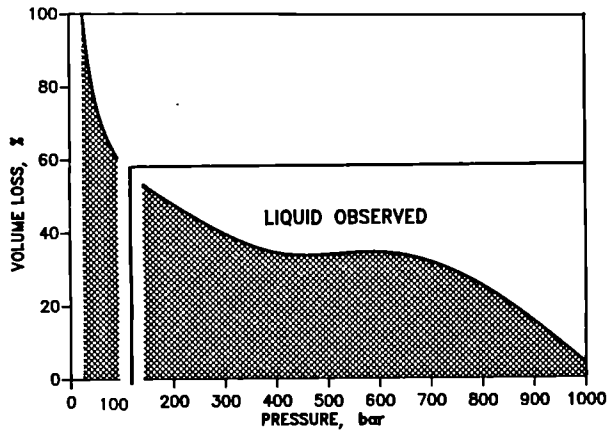


*Fig. 1.26* *Fractional graphite mass evaporated or sublimated from the sample at constant energy input as a function of gas pressure. The observed existence range of the liquid phase is indicated*

## Emissivity behavior in refractory metals and oxides

The spectral emissivities of a number of refractory metals and ceramic oxides have been measured from about 2500 K up to temperatures above the melting point $T_m$. The experimental method adopted is based on multiwavelength pyrometry , where the determination of the spectral emissivity is implicitly related to the evaluation of temperature through the radiation emission law and an assumed relationship between spectral emissivity $\varepsilon$ and wavelength $\lambda$. Heating was done with a pulsed laser in times of the order of 100 ms. The spectral emissivities in the range 500-1000 nm were obtained for temperatures up to 4000 K. The error of the measurements of $\varepsilon_\lambda$ is lower than 10% and decreases with increasing temperature.

Our experiments on refractory metals (Hf,Mo,Nb, Re,Rh,Ta,V, W and Zr)

1. confirm the existence of a unique wavelength, $\lambda_x$, for each metal (already well established in the solid state where $\partial\varepsilon_\lambda / \partial\lambda \leq 0$) to which different $\varepsilon_\lambda$-isotherms converge for $\lambda<\lambda_x$ and from which they diverge for $\lambda>\lambda_x$ and at which $\varepsilon_\lambda$ is independent of T - and thus equal, in particular, to its value at $T_m$.

2. indicate that $\lambda_x$ is preserved through $T_m$ and

3. reveal that at $T_m$, the emissivity is independent of $\lambda$ ($\partial\varepsilon_\lambda / \partial\lambda = 0$), whilst for $T > T_m$ $\partial\varepsilon_\lambda / \partial\lambda > 0$ - opposite to its behavior at $T < T_m$. Equivalently, our findings can be summarized by the statement that the temperature $T_x$ at which different emissivity isochromates intersect coincides with $T_m$.

In some cases (V,Nb) the isochromates are really linear in T at $< T_m$, for which the equality $T_x = T_m$ could be readily anticipated simply by extrapolation. In other metals (Ta, Mo, W) the emissivity isochromates display a strong bending as $T \rightarrow T_m$ and the $T_x$ point is here produced by the variation in $\partial\varepsilon_\lambda / \partial T$.

The newly discovered equality of $T_x$ with $T_m$ is of great technological importance in that it provides an extremely useful reference point for ratio- and multichannel pyrometers.

Detailed theoretical investigations reveal that the occurrence of $\lambda_x$ and $T_x$ points is intimately connected with the particular T- and $\lambda$- dependences of the inter-band contribution to the imaginary part of the complex dielectric function entailed by specific features of the electronic band-structure of the transition metals concerned (see Figs 1.27, 1.28); in addition, the occur-

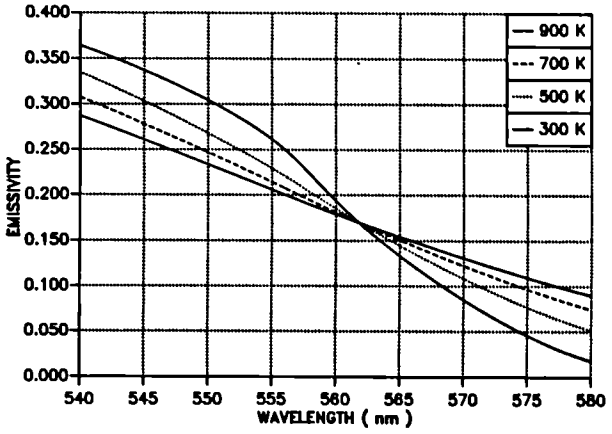


*Fig. 1.27* *Interband contribution to the spectral emissivity at four different temperatures in copper. The contributions have been calculated by assuming a Fermi energy $E_F = 2.2$ eV and $E_0 = 1.6$ eV. The curves intersect at a wavelength of energy $E_F$*

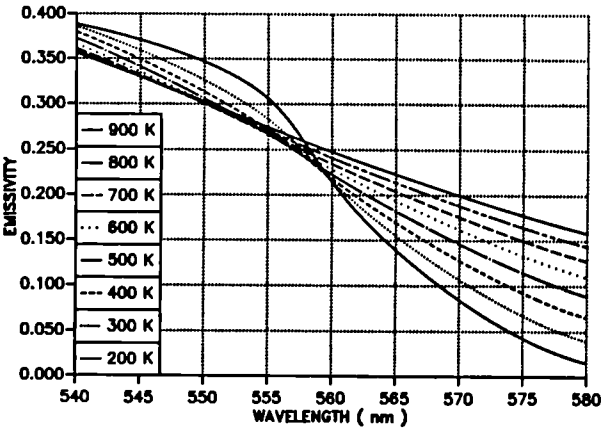


*Fig. 1.28* *Entire spectral emissivity at different temperatures in copper calculated as the sum of an interband and an intraband (Drude) contribution. The X-point is seen to be spread into a small region in the $\varepsilon$ - $\lambda$ space*

rence of $T_x$ points at $T_m$ would appear to be peculiar to the transition metals on account of quantitative differences in their band structure from that which characterizes, for instance, the noble metals, which exhibit only $\lambda_x$ points.

The behavior of the emissivity in ceramics oxides ($UO_2$, $ThO_2$ and $ZrO_2$) was studied up to temperatures above the melting point by heating the samples in a high pressure buffer-gas atmosphere in order to minimize vaporization and stoichiometry variations during the measurements. The spectral emissivities in the examined wavelength interval increase monotonously with temperature. The isochromates of $\varepsilon_\lambda(T)$ do not cross each other and no X-points are observed. It is worthwhile noting that during the fast cool-down these oxides exhibit significant supercooling. In this phase the emissivity increases with decreasing temperature. During the following crystallization stage the emissivity rapidly achieves the value of the equilibrium phase, producing a discontinuity (Y-point) on the observed curve of $\varepsilon = \varepsilon(T)$. The effect was observed with good reproductibility both in the same and in different samples.

## Laser-flash equipment for thermal diffusivity measurements

As a consequence of requests for thermal diffusivity measurements at temperatures substantially below the presently implemented minimum of 1050 K, the possibility of optical detection of small temperature variations down to 600-700 K was investigated. The quality of such data as well as the minimum attainable temperature depend crucially on the signal-to-noise ratio. The signal depends on the efficiency of light collection and on the size of the detector, whereas the noise is determined by the type,size and mode of operation (cooling, bias) of the detector as well as by the noise of the amplifier. The planned installation in a shielded cell practically limits the minimum detector temperature to thermo-electrically attainable - 30° C.

The optics must be designed in such a way, that on the one hand as much light as possible is guided from the object onto the detector, whereas on the other hand the image should be so well defined that the detector itself limits the object field. For operation at 5 µm these goals are attainable with simple meniscus lenses made of Ge or ZnSe, for 1.5 to 2 µm with glass aspheric lenses or even standard achromats.

The detector tested comprises photoconductive PbSe elements and photovoltaic (Hg,Cd)Te diodes (for 5 µm), as well as photovoltaic Ge or InGaAs diodes (for 1.5 to 2 µm) and Si photodiodes (<1.05 µm).

Amplifier noise depends on the parallel impedance of the detector. The amplifier must be designed in accordance with the type of detector used. Measurements at 5 µm appear to be justified only below 550 K, and require high aperture optics and/or additional noise reduction through averaging - if detector cooling is limited to thermoelectrically attainable temperatures. The best performance in the temperature range 550 to 850 K is obtained with InGaAs detectors, whereby cooling at -30° C only results in a modest improvement (1.5-3.5 dB) in the range 550-600 K.

# Theoretical Activities

## Participation in the Phebus source term modeling

The partners of the PHEBUS-PF project are now engaged in a program of calculation which should lead in February 1991 to a proposal to the SAWG of a reference case for test FPT-0.

Besides its work of characterisation and measurements on the PHEBUS fuel, the Institute has been requested to do analytical work in the field of source term evaluation. The aim is to give a prediction of the amount and the nature of the released nuclides and, if possible, all chemical species all along the transient stages.

TUI became involved in this work since its analytical tools are able to provide an original way of computing the released fission products. Indeed, instead of calculating the released nuclides as a function of temperature (as is done in the widely used CORSOR model making use of experimental data which cover a reduced range of nuclides), the TUI model is based on a detailed description of the fuel structure evolution followed by a description of the nuclide displacements and transmutations.

The interest of this analytical work is the following:

- It provides an independent way of source term calculation that enables a comparison to be made with other models.

- It gives detailed descriptions of the mechanical and chemical fuel status which in many aspects can be compared with experimental observations and measurements.

- It gives the inventory of the released radionuclides and the local partition of the retained amounts, which may prove to be of great interest for those nuclides whose release rate cannot be measured satisfactorily.

## Code implementation work

The software which calculates the detailed fuel structural and mechanical behavior is FUTURE [1], [2]. The one which calculates the nuclide birth, decay and redistribution is MITRA [3]. The formation of chemical species from the several nuclides can be calculated with SOLGASMIX-AUT [4] which is an improved version of the original SOLGASMIX software.

FUTURE is constructed to calculate all the relevant local effects occurring in the irradiated fuel pin during temperature excursions. These effects are analyzed on a microscopic scale (involving lattice and subgranular elementary volume elements), on a structural scale (involving the features of the sintered medium), and on a geometrical scale (regarding the pin design parameters). The thread of the analysis is the migration and precipitation of the volatile fission products with the consequent fuel deformation and dilatation processes occurring within a realistically structured environment.

Though FUTURE has already been validated on several experiments, some enhancements were to be made in the year 1990: implementation of the delay factor in the model that describes the precipitation of the dissolved volatile fission products in gas bubbles, reduction of the computing time (factor 2 to 3), correction of remaining errors, writing of chart output, implementation of the stochiometry computing per fuel zone, completion of an interface with the MITRA software, preparation of a user's manual [2] and, on OECD's request, of a delivery of FUTURE to the NEA data bank.

The code MITRA was constructed with the aim of calculating the release of radioactive fission products by taking into account all the processes which, as far as we know, affect the long range matter transport in the fuel, that is: the birth and decay process, the precipitation in bubbles of volatile fissions products, the several thermal diffusion processes, the radiation enhanced resolution process. The information on the fuel microscopic structure comes either from experimental data or from a previous run of FUTURE. The nuclides libraries and data-bases are obtained from ORIGEN. It has to be checked if they are still relevant for a fuel irradiated in BR3.

Due to the number of species that should be accounted for and to the several degrees of precision in the fuel sections description, a suitable and user friendly output had to be made in such a way that only the nuclides and fuel zones of interest be, on request, outlisted. The necessary work on the output environment was performed in the reporting year.

The software SOLGASMIX calculates equilibrium compositions in systems containing one gaseous phase, condensed mixtures and condensed phases of invariant or variable stoechiometry. In the frame of the PHEBUS calculations, the compositions are to be found from the given nuclides of a former MITRA run. Owing to the large number of nuclides and, presumably, of runs, a new input procedure had to be created. A thermodynamic data bank was therefore constructed and an interface program between that database and SOLGASMIX as well. The work was made in the year 1990 and the corresponding software is now refered as SOLGASMIX-AUT. At the moment the database contains approximately 150 species. A crucial problem remains the modelling of the various mixtures which could represent in an adequate way the complex systems. The treatment of the various phases that can occur in accident temperature con-ditions can be made only through a pertinent choice of the constituents and a reasonably precise knowledge of the thermochemical properties of the involved compounds.

## Results

- The main enhancements of FUTURE are completed. The limiting cases in connexion with high temperature conditions have to be carefully checked.
- The output organisation of MITRA fullfills the required users friendly conditions.
- SOLGASMIX-AUT is ready in its organisation but should be tested on measurements to

be found either in the literature or among the TUI experiments.

## Prospectives

The following steps of the present study will be focused on:

- Highlighting of the limiting transient step subdivision with respect to the capabilities of FUTURE in order to reduce as much as possible computation costs.
- Calculations of the FPT-0 stage of thePHEBUS project.
- Calculations of the following tests - including the characterisation of the BR-3 test rods - (when the test conditions will be fixed).
- Definition of the MITRA output to be generated for the specific purposes (collection of nuclides in families, radial and axial fuel subdivision) and pre-calculation of the various PHEBUS tests.
- Collection and analysis of experimental data in order to simplify as far as possible the description of the chemical state of the system in SOLGASMIX-AUT and to improve its associated database.

**References**


[1] C. Ronchi, J. van de Laar, The fuel performance code FUTURE. EUR 11387 EN

[2] C. Messainguiral, The fuel performance code FUTURE. User's manual. EUR report (to be issued)

[3] C. Ronchi, M. Gardani, MITRA, an advanced code to calculate radionuclide release from nuclear fuels under general irradiation conditions. EUR 12375 EN.

[4] C. Ronchi, F. Turrini, Thermochemical data for reactor materials. EUR 12819 EN.


# Modelling of the chemistry of irradiated fuel

The chemical behavior of the fission products in irradiated LWR nuclear fuel is being investigated. The chemical constitution of the fuel is calculated by means of equilibrium models in order to analyse and predict the release rates of the relevant fission-product species, under normal and accident conditions.
Scope of this work is to give a realistic representation of the irradiated fuel, i.e. to pre-select the most likely chemical systems and species which are believed to be stable in the various phases of the fuel in the considered temperature range and calculate the chemical equilibrium in the fuel matrix and in the various separate structural pockets.

The oxygen partial pressure is an extrinsic model parameter which governs the complex set of the important chemical reactions that can occur across the wide gamut of conditions. In order to predict the evolution of the spatial distribution of the oxygen potential in the fuel during irradiation, several oxide systems and solid solutions of fission products (viz. Ln, Ce, Ba, Sr, Zr) have been considered.
In our calculations, the chemical system representing the irradiated fuel, is characterised by the radial distributions of oxygen, actinides and fission products (input data set), provided by a package of codes (FUTURE,MITRA) which calculate the diffusion kinetics of the elemental species and the evolution of the fuel structure. Oxygen potential, vapour partial pressures in the gas phase and compound concentrations in the solid/liquid solutions represent the output set.

## Development of the work

Different levels of investigation were required, involving:

- Identification and characterization of the possible chemical forms of the released fission products and actinides.

- Provision of a suitable database of the thermodynamic quantities for the relevant fission-product compounds/systems. We extended and organized in a computer database [1] the set of thermochemical data for reactor materials and fission products collected by Cordfunke and Potter [2] in the framework of a research contract supported by the Commission of the European Communities. In this context, at the JRC Karlsruhe a work was started in order to construct a computer file to be accessed by existing codes (MITRA, SOLGASMIX). The data presented there, pertaining to compounds formed by actinides, oxygen, fission products, coolant and bundle structural materials, were obtained from available large databases or reviews (the sources being mostly JANAF, NISTTHERMO, Baring and Knacke (B.K.) [3] and Kubaschewski and Alcock (K.A.) [4].

  The data reported in ref. [1] and [2] have been stored in a new database (BANCA.DIR). In

order to avoid storing a large number of tabulated values which involve in any case temperature interpolations, the free energy of formation of the various compounds, $\Delta G_f$, was expressed as a linear function of temperature in distinct T-intervals. The slope and the y-intercept of each line is indicated for the various segments. These may be visualized, when it is wished, as interpolating graphs, followed by the original tables.

- Development of the necessary software to handle and manipulate the collected data.

- Development of new subroutines to be used as an interface between the existing chemical equilibrium code (SOLGASMIX) and the thermochemical data bank, in order to make the complex input procedures automatic.

- Use of an equilibrium thermodynamic representation to describe the irradiated fuel matrix and obtain the real variation of the oxygen activity in the fuel. This method, [5], [6], assumes that the thermodynamic activities of the actinide and oxygen ions can be described by a solid solution of two or more components, which are chosen so that the experimental thermodynamic behavior is reproduced in terms of free energies of formation. Some of the oxide systems have been formulated starting from literature data and inserted into the global model:
  Binary oxide $UO_{2\pm y}$
  Ternary oxide $U_{1-z}Pu_z O_{2\pm y}$
  Ternary oxides : $U_{1-z}Ce_zO_{2+y}$
  $(U, Ln, Ce)O_{2+y}$
  Ternary oxide $(U,Ln,Pu, Ce)O_{2+y}$

- Treatment of the thermodynamic description of liquid non-ideal phases, based on the numerical reproduction of experimental phase diagrams. The liquid solution considered so far are:
  Binary system (Cs - I)
  Binary system (Cs - Te)
  Bynary system (Cs - O)

The work is obviously in continuous progress as additional significant compounds may still be devised, which could entail a revision of the system representation.

**References**


[1] C. Ronchi, F. Turrini, EUR 12819 en (1990).
[2] E.H.P. Cordfunke, R.J.M. Konigs, G. Prins, P.E. Potter, M.H. Rand, EUR Contract ETSN 0005 NL (1988).
[3] I. Barin and O. Knacke, Springer Publ. (1977) ."Inorganic Properties of Inorganic Substances", Berlin.
[4] O. Kubaschewski and C.B. Alcock, "Metallurgical Thermo-chemistry", 5th Edition (1979), Pergamon Press, New York.
[5] T.B. Lindemer, CALPHAD: Comput. Coupling Phase Diag. Thermochem. 10, (1986) 129.
[6] R.G.J. Ball (1989). AERE-R 13395.
[7] M. Gardani, C. Ronchi (1989), EUR 12375 en.
[8] G. Eriksson, Chem Scr. 8 (1975), 100.


# Thermodynamic Property Studies

## Thermodynamic properties of (U,Pu)N

The aim of this work is to measure the equilibrium vapour partial pressure of U-Pu mixed nitrides with high and low oxygen content. The equipment - constructed at TUI - consists of a Knudsen cell with a quadrupol mass spectrometer, heated by induction up to 3200 K. The furnace operates at $5 \cdot 10^{-8}$ *torr* vacuum. Facilities for the collection of the effused vapour on a system of targets are also available, making it possible to obtain an absolute calibration for the vapour pressure evalution. Calibration tests have been carried out on different metals (Au, Ag, Pt, Pd) enabling the optimisation of the mass spectrometer settings to be achieved. Palladium (with melting temperature = 1825 K) has been eventually chosen as a calibration standard. The accuracy of the thermodynamic calculations was increased by improving the temperature measurement technique and by extending the mass spectrometer sensitivity down to the order of $10^{-8}$ bar.

In the next step of the work UN will be investigated with the aim of establishing the detection limit of $N_2$ which is mainly affected by the amount of $CO_2$ present in the rest- and spurious gases. The measurements on mixed nitrides will immediately follow.

# Industrial Applications

## Acoustic levitation techniques

Tests have been performed in order to implement acoustic levitation in laboratory furnaces for containerless heat treatments.

The first experimental setup consists of an induction heated furnace in a quarz cylindrical vessel, equipped with a 20 kHz levitator. The furnace can be operated at steady state temperatures up to 1200° C with an inert gas atmosphere at room pressure. The transducer is made of a special titanium alloy. Both tranducer and reflector are located in the vicinity of the HF susceptor, so that watercooling had to be adapted to these components in order to keep their temperature below 300° C. Samples of approximately 5 mm size can be levitated in the center of the heated zone. The device is not yet performing as expected, for at high temperatures the pre-stressed transducer is subjected to impedence instabilities with marked losses in acoustic power. However, up to temperatures of approximately 600° C, the sample could be kept in levitation for long times without large unstabilities.
In a second experiment, tests were performed with laser heating, where the levitated sample was irradiated with continuous laser beams. Previous experiments with four, tetrahedrally oriented, pulsed Nd-YAG lasers, lead to a mediocre levitation stability even during millisecond pulses. With continous laser heating, the sample could be better maintained in position for longer times. However, since only two continous laser beams were available, the very high heat losses produced by the sonic field, caused remarkable thermal heterogeneities in the sample. Better heating conditions will be obtained with a lay-out consisting of four continuous beams.

# Modelling Work

## General fuel pin code development (TRANSURANUS)

TRANSURANUS is a computer program for the thermal and mechanical analysis of fuel rods in nuclear reactors and was developed at the European Institute for Transuranium Elements (ITU). Besides its flexibility for the fuel rod design (all reactor types), the TRANSURANUS code can deal with very different situations, as given, for instance, in an experiment under normal, off-normal and accident conditions. The time scale of the problems to be treated may range from milliseconds to years. The code has a comprehensive material data base for oxide, mixed oxide, carbide and nitride fuels (partially still under development) Zircaloy and steel claddings and different coolants.

At the beginning of the development the code was principally used in-house, i.e. as a tool to analyse and understand experimental results. In recent years, however, the interest to use this code in other organizations grew and the code is now used in the following places:
- KfK, Germany
- TÜV - Baden, Germany
- TÜV - Bayern, Germany
- PSI, Switzerland
- C.I.E.M.A.T., Spain
- EdF, France
- JRC - Ispra, Italy

Since the TRANSURANUS Code is incorporated in the EAC II Code, all groups having access to EAC II are also TRANSURANUS users. In the following, new developments are outlined, and the analyses of various experiments are discussed.

### New formulation for all strain components

Volume changes are treated in the TRANSURANUS code via strains (e.g. thermal strains, creep strains, strains due to plastification, densification or swelling etc.). The subroutines calculating these strains were rewritten and their programming structure reorganized. All strains are now called from the driver STRNDR ("strain driver") which calls the different strain contributions (subroutines STRN05 - STRN12). This reorganization enables the users to include new strain cor-

relations more easily. It is important to note that a user can implement a new correlation either explicitly or implicitly just by setting the variable IMPLIC to 0 or 1 in this new correlation. The option IMPLIC = 1 organizes a fully implicit treatment, i.e. a calculation in the innermost thermal-mechanical iteration loop automatically.

## New LWR models

The LWR models were extended to high burn-up according to the broad Risø database available to TUI. However, since none of the models for the gaseous fission product behaviour was able to predict the observed burst release during power variations (even during a decrease of the reactor power), a new model is under development which is able to describe the diffusion of gas along the grain boundaries to the free pin volume. This model is based on the assumption that the transport of volatile fission gas products (vfp) through the fuel can be modelled by the diffusion of gas through a porous medium. Under reactor conditions, both steady state and transient, the parameters of the model, (temperature, gas source) vary strongly in space and time. All of this is described by a diffusion equation with a source term to represent the release of vfp's from grain boundaries. The diffusion parameter is not a constant but is a function of the concentration and thus the equation is nonlinear. A three level implicit method was used to solve this equation numerically. It was found that this method results in a stable convergent solution in contrast to simpler implicit or explicit methods (which are almost always unconditionally unstable). For the case of a central void the existence of a stable solution can be proved rigorously.

Under some conditions there are simple analytic solutions of the diffusion equation: perfect agreement was shown between these and the numerical solutions, Fig. 1.29. A numerical method was developed by Hofmann and Meek for this problem. Agreement was demonstrated between their solution and the numerical technique, Fig. 1.30. The three step implicit method has the added advantage of guaranteeing a convergent stable solution in many cases and it is easier to implement.

We believe that only such a model is able to correctly describe how the gas is collected on grain boundaries and then suddenly released when microcracks open during shut-down periods. It should be kept in mind that most of the detailed gas release models treat only the behaviour of the fission gas on one single grain. However, the whole diffusion path to the free volume consists of several hundreds of grains which have to be passed under strongly varying conditions such as temperature, stress level or porosity.

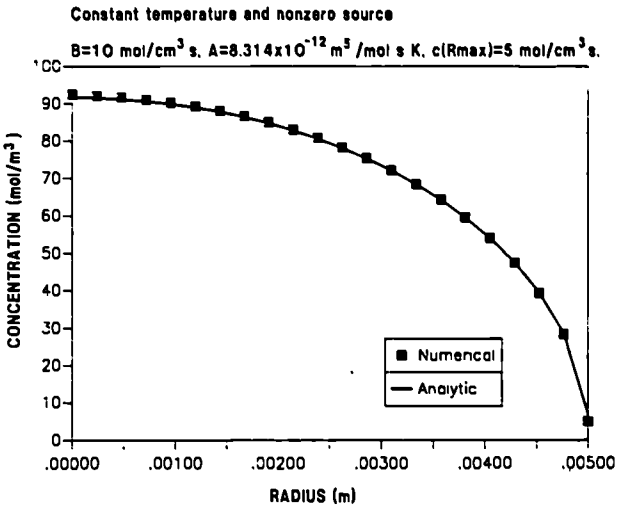


*Fig. 1.29* *Plot of the volatile fission product concentration as a function of radius in the case of constant temperature and nonzero source (cylindrically symmetric pin geometry)*

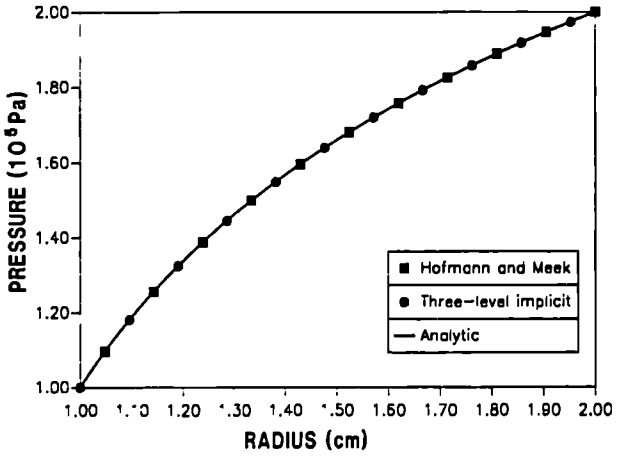


*Fig. 1.30* *Plot of the volatile fission product pressure as a function of radius in the case of no source and constant temperature*

It is planned to incorporate the new model in 1991 in the TRANSURANUS code and perform the first tests. Since experimentally different burst-releases for different fuels were observed no time schedule can be given for the planned release of this model.

## New TRANSURANUS models for use with the EAC code

In agreement with the EAC user group several extensions are under preparation:

- incorporation of the new Harwell FBR failure model
- incorporation of a new, simplified crack model
- incorporation of models to handle a partially destroyed fuel pin
- permanent improvements according to the EAC user's needs.

### *Outer corrosion of the cladding*

The models for the outer corrosion of different cladding materials have been revised and extended. Subroutine OUTCOR ("outer corrosion") is the driver for the submodels OCCOCO, OCECEK and OCTOEB. A new input option for the selection of the outer cladding corrosion model is available (input variable ICORRO). In total 14 correlations are optional.

### *Grain growth models*

Subroutine GRNSZE calculating the grain growth has been completely rewritten. A new input option for the selection of grain growth models is available (input variable IGRNSZ).

### *Calculation of structural zones in the fuel*

The subroutines calculating the structural zones in the fuel have been completely rewritten. Subroutines STRUDR ("structural zones - driver") is the driver for the subroutines STRUOX ("structural zones of oxide and mixed oxide fuel") and STRUCA ("structural zones of carbide and mixed carbide fuel"). Subroutines STRUOX calls the submodels GRNSZE, STZN01, STZN02, STZN03, STZN04, STZN05 and STZN06. A new input option for the selection of models to predict the formation of structural zones is available (input variable ISTZNE). The basic options are:

- the original Olander model; in this model the boundaries between the structural zones depend on temperatures $T_{2,3}$ and $T_{3,4}$ which are time dependent.
- fuel restructuring zones are calculated from pore migration lengths.
- fuel restructuring zones are defined by constant temperatures.
- fuel restructuring zones are defined consistently with a grain growth model.

### *Transient thermal analysis*

The previous options for the thermal analysis were

INSTA = 0 for a purely steady-state analysis and

INSTA = 1 for a transient analysis.

If transient thermal effects can be neglected, (i.e. $\Delta t >> \tau$, where $\Delta t \equiv$ timestep and $\tau \equiv$ the thermal time constant) the analysis is switched automatically to a steady state analysis for that particular time step.

As a new option, INSTA = 2 has been introduced. With this option a purely steady-state thermal analysis is performed for all times $t \leq t_{trans}$ ($t_{trans}$ = time where the transient starts) whereas for $t > t_{trans}$ the thermal analysis is treated transiently. With this new option a long base irradiation followed by a fast transient is treated more effectively than using the previous method (INSTA = 1 for base irradiation and for the transient).

### *Power density form factor f(r)*

Two new options for the selection of the power density form factor f(r) (IFORM = 3 and 4) have been introduced. Both options give the local power density as a function of the neutron flux distribution, the density and the concentration of fissile material for FBR conditions.

### *TRANSURANUS training course*

Fuel rod behaviour codes should never be used as "black boxes". To make an optimum use of the TRANSURANUS code users must be familiar with the basic mathematical-mechanical concepts, the models and the general code structure. In particular, users must be familiar with

- the basic assumptions and their consequences (limitations of the code),
- the various input options,
- the structure and the programming of the ma-

terial data base (just in case a user wants to use his own data).

Special TRANSURANUS training courses were held to fill that gap. Experience with these courses showed that such a condensed ITU training course is very effective in that it helps a user to get familiar with these important details. It is planned to offer a similar course in 1991 for new TRANSURANUS users.

## New TRANSURANUS pre- and postprocessors

With an increasing number of users, the development of pre- and postprocessors started which help the user to avoid errors in the input data and to correctly interpret the results of an analysis. Basically, the TRANSURANUS input dataset consists of two parts:

1. input of pin geometry and options
2. input of time depending quantities.

Most of the input errors in part one are monitored, TRANSURANUS tries either to continue with default values or stops. In both cases detailed error messages are printed out. Input errors in part 2 cannot be detected automatically. Consequently a special preprocessor program AXORDER has been developed which automatically generates the second part of the TRANSURANUS input. The input for AXORDER is very simple (e.g. a table format for the power history, a separate table format for the coolant input temperature etc.).

The AXORDER preprocessor program is very user- friendly and simplifies significantly the TRANSURANUS input which depends on time and which may be very lengthy for complicated analyses.

The TRANSURANUS postprocessor is the plot program URPLOT, which has been extended to satisfy specific users need. URPLOT gives many variables as a function

of time,
of the radius and
of the axial coordinate.

At the end of 1990 work started to extend the URPLOT program to plot the many distributions of statistical results at different times (TRANSURANUS - Statistic version).

## TRANSURANUS handbook

Besides the training course and the various publications in journals or reports the TRANSURANUS handbook is the main source of information for users. Its input flow diagram and input description are continuously updated. Both parts are consistent with the latest version of TRANSURANUS. The handbook also includes a detailed description of all commonblock variables, which is very important for users who want to modify programs, and an increasing number of detailed model descriptions. The TRANSURANUS handbook is written in the IBM GML text mark-up language and consists presently of 300 pages.

## Implementation of the TRANSURANUS code on a workstation

The TRANSURANUS Code has been successfully implemented on an IBM RT Workstation and was also transferred successfully to the new IBM RISC/6000 work station of the TUI Modelling Group. Since the code was written consequently in standard FORTRAN 77 no problems arose with its transfer to the workstation. Presently, the whole program development is performed on a workstation using the UNIX operating system which offers distinct advantages by special commands such as the grep, the diff and the make command.

For potential users it is important to note that TRANSURANUS should run without any difficulties on all machines which provide a standard FORTRAN 77 software package. Up to now no problems were encountered when the code was transferred to various computer sites.

# Analysis of experiments using the TRANSURANUS code

## LWR analyses

Two different sets of analyses using the TRANSURANUS code were performed for LWR rods:

- Analyses of 8 ABB-Atom fuel rods from the "High Burn-up Effects Programme", i.e. rods from the TVO reactor
- Analyses of 3 selected fuel rods from the "Tribulation Programme".

Both analyses were performed in cooperation with PSI. It has to be stressed that the detailed design and irradiation reports were not made available to TUI for proprietary reasons (ABB-Atom) or project restrictions (Tribulation Programme).

The TUI Modelling Group performed several fuel rod analyses for PSI, transferred the TRANSURANUS Code to PSI and helped with its installation on the PSI computers.

The analyses of ABB-Atom high burn-up BWR fuel rods cannot be reported in detail since it is classified information. In total 8 different rods with complicated power histories were analysed using different options for model selection available in the TRANSURANUS code. Fig. 1.31 gives a typical example of a power history and the corresponding centre line temperature as calculated by the TRANSURANUS code. Other results of interest such as e.g.

- deformation of the cladding (radially and axially)
- fission gas release
- pin pressure
- gap size and fuel-cladding interaction
- fuel cladding heat transfer coefficient

are reported in Reference [7].

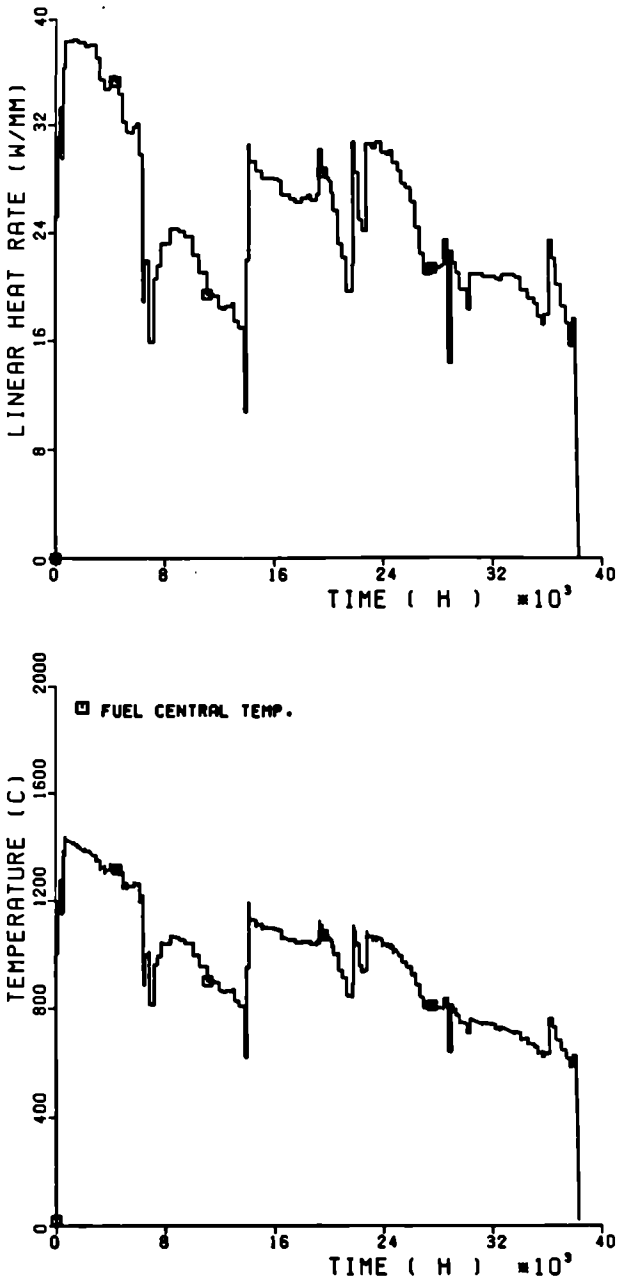


*Fig. 1.31* *Example of a typical power history of a rod from the "High Burn-up Effects Programme" and the corresponding centre line temperature as calculated by the TRANSURANUS code*

It is well known that this type of BWR fuel rod shows a high sensitivity regarding thermal feed back effects. This means that the data for each specific rod must be known very accurately. Of high relevance is the position of an individual rod in a fuel element. The conclusion of the study was that uncertainties of the linear rating for specific rods with correction factors between 0.95 and 1.2 of the average bundle rod power need further investigation.

Fig. 1.32 shows the power histories for the Tribulation rods considered. The TRIBULATION rods

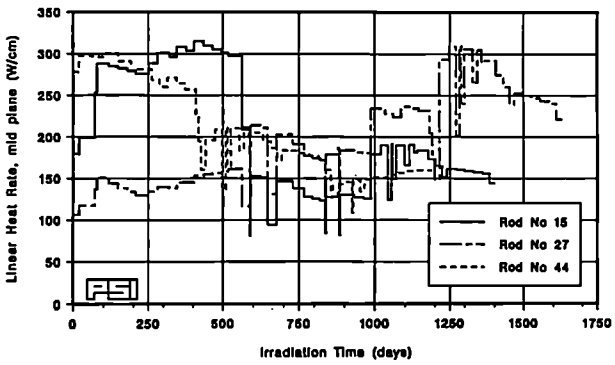


*Fig. 1.32* *Power history for the 3 Tribulation rods considered; this figure was taken from ref. [2]*

were selected since they were very well documented, and were irradiated in the same test reactor [BR3 PWR]. None of the three rods chosen had been ramped although TRIBULATION was basically a group of ramping experiments. The rods are referred to by their programme test matrix numbers i.e. 15, 27 and 44. The main fuel properties and rod characteristics are listed in Tab. 1.4.

The conclusions were:

The comparison exercise using COMETHE IV-A, INTERPIN (89.01) and TRANSURANUS com-

*Tab. 1.4* *Main input data of the fuel rods 15, 27 and 44 from the tribulation program; this table was taken from reference [2].*

| | | Rod 15 | Rod 27 | Rod 44 |
|---|---|---|---|---|
| | | Belgonucleaire | Westinghouse | Brown-Boveri Reactor |
| **Fuel** | | | | |
| Type | - | UO2 / ADU | UO2 / ADU | UO2 / AUC |
| Enrichment | % U 235 | 5.75 | 8.26 | 3.187 |
| Fuel to Clad Radial Gap | microns | 100 | 83 | 99 |
| Length of the Fuel Column | cm | 99.56 | 98.68 | 99.9 |
| Grain Size | microns | 11.7 | 10.5 | 7.1 |
| Pellet Density | % TD | 95.04 | 94.16 | 93.61 |
| Open Porosity | % | ? | ? | 64.5 |
| Densification | % TD | 0.27 | 0.32 | 0,82 a) |
| Dish Volume | % | 1.5 | 1.15 | 1.2 |
| **Cladding** | | | | |
| Type | - | Zircaloy-4 | Zircaloy-4 | Zircaloy-4 |
| Outer Radius | mm | 4.75 | 4.756 | 4.815 |
| Inner Radius | mm | 4.12 | 4.178 | 4.214 |
| Heat treatment | C / hours | 540 / 2,5 | 475 / 6,0 | 460 / 2,5 |
| **Plenum** | | | | |
| Length | cm | 9.52 | 11.11 | 6.65 |
| Filling Gas | - | He | He | He |
| Filling Pressure | MPa | 0.1 | 1.38 | 1.42 |

a) up to 1,46 % was measured

puter codes on rods 15, 27 and 44 of the TRIBULATION programme has shown quite a good agreement between calculated and measured values. A series of comparative calculations based only on three selected rods from a single program cannot be used to draw broad conclusions on the comparative accuracies and the power of prediction of the codes in general use. However observed deviations between the code results and measured values seem to correspond to differences in input values needed for each code or their differing default values when no measured input data was available. Here it can be mentioned that the lack of adequate open porosity values, fuel swelling and sintering data and of the actual cladding creep properties significantly influence the code results. This shows the importance of the availability of full and accurate data on the actual materials properties, the actual fabrication data, the design data and the power histories for a reliable code prediction.

The exercise has shown the tendency of all three codes, in their standard versions, to overestimate the pellet/clad mechanical interaction at high burn-up probably due to the fuel swelling rate being too high. Comparisons have shown large differences in the FGR curves produced by INTERPIN and those generated by COMETHE and TRANSURANUS. COMETHE and TRANSURANUS FGR curves are similar while INTERPIN shows an unexpected high athermal release component. In one case (rod 27) the Halden threshold model in COMETHE is overpredicted resulting in an underprediction of the EOL fission gas release value.

## FBR analysis

FBR analyses were performed in order to demonstrate the capabilities of the European Accident Code EAC-2 both under steady state preirradia-

tion conditions and for transient low-probability whole-core accident calculations. It is important to note that by coupling the TRANSURANUS code with its steady state and transient capabilities to the EAC Code full coherency is reached between the base irradiation and the transient in particular in the thermo-mechanical behaviour of the fuel rod. Contributions of the ITU Modelling Group were made towards the validation of various physical models. This was done on the basis of an international benchmark calculation or through simulations of experiments like the French CABRI - 1 in- pile or the Belgian - German MOL 7C/7 tests [1, 2, 4, 5, 6].

Besides these analyses, detailed precalculations for the CEA "Lambda" experiment were performed.

## CABRI-1 analyses

It is generally accepted that the state of the fuel pin prior to the accident (the so-called $t_0$ state) is one of the key parameters defining the sequence of events in the accident. In particular, the fission product behaviour (is the gas inside the grain, on the grain boundaries or was it released?), the mechanical behaviour (open gap or pellet-cladding interaction, the formation of a central void etc.) have a strong influence on a number of quantities. Those are the temperature level, i.e. the stored energy, the pressure build-up in the molten cavity, in the remaining solid fuel and consequently the loading on the cladding. This means that failure time, failure mode and location, which are further key parameters in the development of an accident, are largely influenced by the $t_0$ state of the pin.
The failure position is especially important because a near-mid-core failure position may lead to a positive reactivity feedback due to the in-pin fuel motion towards the failure site. On the contrary, a failure at the core top will result in a negative feedback, contributing to the reactor shutdown, because of the fuel movement out of the active core. For this reason, large efforts have been made to investigate both experimentally and theoretically, the fuel pin behaviour under accident situations.
Consequently, both items, i.e.
- the $t_0$ state and
- cladding failure

were studied in more detail.
Validation efforts for steady state irradiations concentrated on the CABRI Rig 1 preirradation where the $t_0$ state is precisely known through various experimental investigations. However, it has to be stressed that these results were not made available to us prior to the theoretical analyses. This means that the analysis of the CABRI Rig 1 base irradiation in the French PHENIX reactor was performed as a truly blind prediction.

The key quantities to be computed were
- the size of the central void formed due to pore migration processes,
- the restructuring process, that is: the formation of the columnar grain, the equiaxed grain and the unrestructured zone, respectively, along the fuel radius,
- the thermal effect of the fuel-cladding gap behaviour, which has a major impact on the gap conductance coefficient (low heat transfer in the presence of xenon or high heat transfer in the case of gap closure with strong contact pressure),
- the fission gas behaviour (production, release, distribution within the grains and on the grain boundaries), which depends basically on the loading of the pin during the irradiation.

## $T_0$ state

The detailed results of these TRANSURANUS blind predictions are reported in reference [4]. In addition, these results were discussed during an EAC Specialist Meeting and compared with the complete experimental evidence. The overall agreement was very satisfactory. For example, the fission gas release as predicted with the TRANSURANUS URGAS model and the KfK LAKU model are shown in Fig. 1.33. Fig. 1.34 gives the structure of the fuel. It can be seen that the radius of the central void and the radii of the columnar and the equiaxed grain zones are in excellent agreement with the data.

## Cladding failure

The TRANSURANUS Code offers several options for a wide variety of pin failure models: the simplest ones are just design dependent empirical correlations and the most sophisticated models perform a complete thermo-mechanical analysis of the fuel-cladding system during the preirradiation and the transient period, taking into account the damage accumulated in the pin.

In accident situations, after the pretransient period of irradiation, the fuel and the cladding under-

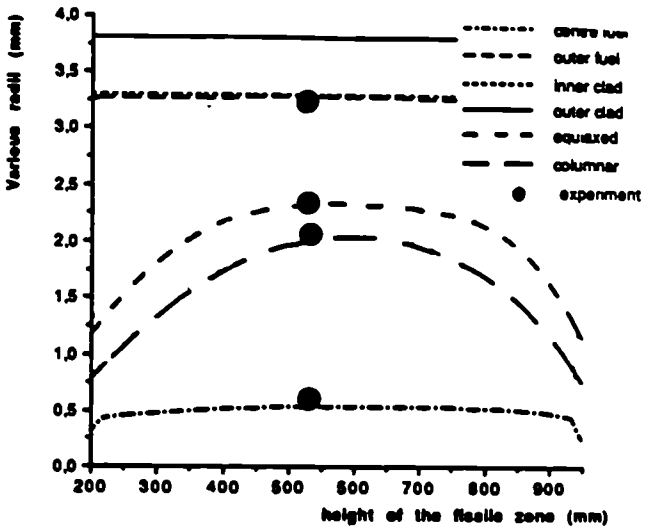


*Fig. 1.33* *Fission gas release of the CABRI-1 Rig1 preirradiation; the TRANS-URANUS-URGAS model and the KfK LAKU model are compared with the experimental values*

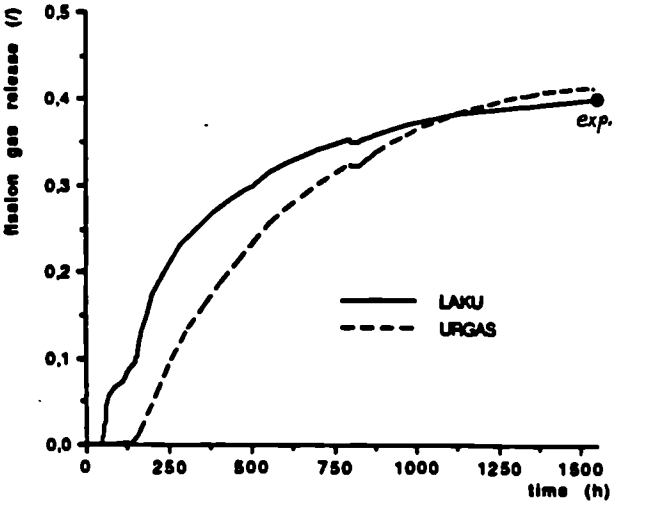


*Fig. 1.34* *Fuel rod geometry and radii of structural zones of the CABRI-1 Rig1 preirradiation; compared are the TRANSURANUS predictions with the experimental evidence*

go a complex series of thermo-chemical processes which may generate dynamic loading patterns far beyond the operational reactor conditions. In addition to the radiation level and the instantaneous values of stresses, strains and temperatures, which are steady state parameters, one has to consider the time rates of these quantities. Processes such as stress relaxation by creep play an important role if the time constants are favourable. The HEDL-TREAT experiments, for example, have shown that changes in the heating rate between 6 K/s and 111 K/s alter considerably the strength (UTS) and the ductility ($E_R$) of both the fuel and the cladding.

More generally three main mechanisms may be identified for the cladding loading:

- The thermal stresses arising from the temperature difference between cladding inner- and outer surface,
- the internal gas pressure, which acts directly on the cladding when the fuel-cladding gap is open, or which may even reopen this gap when its value exceeds the Pellet-Cladding-Mechanical Interaction (PCMI) pressure,
- the PCMI or contact pressure when the gap is closed: this interaction is due to thermal differential strains, fuel swelling, fuel volume increase due to the melting (drastic effect when the central cavity is closed and pressurized), or other effects like cracking, relocation ... etc.

Analyses showed that the results of the pin failure criteria incorporated into the TRANSURANUS Code (in principle all criteria which are available from the open literature) gave a wide variety of failure times for a specific transient loading history. It was therefore decided to follow a new approach to model pin failure based on microphysical processes. A first version of this model, at present under development at Harwell, was incorporated into the TRANSURANUS Code. This new model consists of a series of 3 primary microphysical failure mechanisms, which were identified for the standard cold-worked AISI 316 steel below the melting temperature. However, indications have been given on how to extend this new failure model to other cladding materials. These three mechanisms are transgranular failure, intergranular creep fracture and grain boundary cavity growth fracture. Being based on a microphysical analysis rather than on empirical design-dependent criteria, this new mechanistic model should be appropriate for nearly any failure situation, even for rapid transients far beyond the usual calibration dataset of the standard pin failure criteria.
The new version of this Harwell failure model will be tested with CABRI-1 data in 1991.

## Lambda experiment

The main objectives of the pre-test fuel behaviour calculations for the CEA-LAMBDA test using the TRANSURANUS code were:

- to check whether the test conditions are appropriate to determine the thermal conductivity of molten $UO_2$ and what uncertainty margins have to be considered,
- to calculate the central fuel temperatures for specific assumptions,
- to analyse whether the fuel/cladding gap will be closed at any location in the fissile zone,
- to analyse whether the fuel/cladding gap will be open at any location in the fertile zone,
- and to estimate the axial expansion of the fuel for various conditions.

The following conclusions result from the analyses performed:

### *Temperature*

As expected, the temperature strongly depends on the thermal conductivity of the molten fuel. The standard value of $\lambda$ leads to a maximum temperature in the range of 3900 K, whereas 5300 K is obtained using the lower value.

### *Gap size*

Because of the high temperatures the radial gap closes over the whole fissile length within the second ramp, i.e. prior to the final transient. It is important to note that the gap in both fertile zones remains open. Consequently, an axial blockage of the molten fuel to PCI of the fertile zone seems to be improbable.

### *Elongation*

The axial elongation of the fuel depends largely on the mode of the axial interaction. From theoretical considerations it can be concluded that

1. for the present situation the sticking friction option will almost certainly underpredict the axial expansion and overpredict the radial deformation.
2. the sliding friction option will probably overpredict the axial expansion and probably slightly underpredict the radial deformation.

The results clearly confirm these statements. From a closer analysis it is argued that the results obtained by the sticking friction option are highly unrealistic. The results further indicate that the interpretation of the LAMBDA experiment will largely depend on detailed knowledge of the thermal strains of molten fuel.

## Radioactive waste modelling

As a result of a management decision the Modelling Group has begun investigations in the area of High Level Radioactive Waste Disposal. The object is to identify specific problem areas to which we can apply our expertise. It is clear that this is not an easy task due to the vast amount of work already done in this field. In recent months an extensive literature survey has been carried out. As a result of this study proposals have already been put forward. We are continuing this work in order to define further topics for research.

**References**


[1] H.U. Wider, J.J. Devos, K. Lassmann, et al.,The European Accident Code-2: Overview on the Modelling, Seminar on the Commission Contribution to Reactor Safety Research, Nov. 1989, Varese (Italy)

[2] G. Van Goethem, H.U. Wider, K. Lassmann, et al.,Applications of the European Accident Code-2 EAC-2 in LMFBR Whole Core Safety Analysis and Pretest Calculations, Seminar on the Commission Contribution to Reactor Safety Research, Nov. 1989, Varese (Italy)

[3] C.T. Walker, K. Lassmann, R. Ronchi, M. Coquerelle, M. Mogensen, The D-COM Blind Problem in Fission Gas Release: The Predictions of the TRANSURANUS and FUTURE Codes, Nucl. Eng. Design, 117 (1989) 211-233

[4] G. Van Goethem, H.U. Wider, G. Peter, K. Lassmann, Mechanical Fuel Element Loading and Pin Failure Thresholds in EAC- 2, International Conference on Fast Reactor Core and Fuel Structural Behaviour, 4-6 June 1990, Inverness, UK

[5] G. Peter, K. Lassmann, H.U. Wider,Improved Treatment of Molten Fuel Inside LMFBR Pins and its Effect on the Pin Mechanics Calculation, International Conference on Fast Reactor Core and Fuel Structural Behaviour, 4-6 June 1990, Inverness, UK

[6] H.U. Wider, ..., K. Lassmann, et al., The European Accident Code EAC-2: Overview and Status, International ANS Topical Fast Reactor Safety Meeting, 12-16 August 1990, Snowbird, UT (USA)

[7] C. Ott, L.A. Nordstrôm, H.K. Kohl, M. Billaux, K. Lassmann, A Comparison of Measured and Calculated Results Using Three Rods of the Tribulation Programme and the Codes COMETHE, INTERPIN and TRANSURANUS, Topical Meeting on LWR Fuel Performance, 21-24 April 1991, Avignon, France (accepted paper)

# 1.2 Safety Aspects of Fuel Operation and Handling

## Introduction

One of the uncertainties which may limit the use of uranium-plutonium nitrides as nuclear fuel is their stability at elevated temperatures. An in-depth study has shown, that (U,Pu)N will probably not support fuel central temperatures above 2000 K. The details of this investigation are given below.

The programme on the formation and dispersion of radioactive aerosols in case of fire in a laboratory where uranium-plutonium oxide fuels are handled, has been brought to an end by studying release rates from different types of "contaminated" substrates and summarizing the results.

A new series of tests is under preparation to investigate the transport of "large" aerosol particles in ducts and chimneys.

## Investigation of the Operational Limits of Uranium-Plutonium Nitride Fuels

During irradiation nuclear fuels undergo important changes in structure and composition. These processes, unfortunately, occur under conditions which are not well known and, moreover, pure thermal effects and irradiation effects cannot be separated. The aim of this work is, therefore, to investigate the thermal effects only, i.e. the stability of mixed nitrides in a temperature gradient, and to evaluate their operational limits. To do this, out-of-pile experiments were made using an apparatus which enables a radial temperature gradient to be generated in fuel pellets.

### Starting material and experimental conditions

Uranium-plutonium nitride was synthesized by carbothermic conversion of oxides in flowing nitrogen at 1870 K. Depending on the fabrication route the pellets were either called type C (for conventional preparation) or type P (for directly pressed). The lowest residual carbon and oxygen contents in the final product were about 300 ppm, and less than 500 ppm, respectively, and this was obtained by carbothermic conversion with excess carbon and subsequent decarburisation with nitrogen-hydrogen gas mixtures. Pellets with an oxygen content up to 7600 ppm were also prepared in order to compare different types of fuel. The main characteristics of the starting materials used for this investigation are summarized in Tab. 2.1. The specimens were homogeneous solid solutions characterized by similar pore shape, low density, high values of open porosity and by different levels of oxygen impurity. The porosity values determined by quantitative ceramography do not include cracks and holes, and generally were lower than those derived from geometrical density measurements. Typical microstructures are shown in Fig. 2.1. Most of the pores had a pseudo-ellipsoidal shape, they were located on the grain boundaries and formed a network of channels connected to the surface of the pellets. Mercury porosimetry showed that about 50% of the mercury forced to penetrate into the open pores could not escape when the pressure was released. This clearly indicates that the pores were interconnected via small channels (bottle-neck type porosity).

Uranium-plutonium oxide type precipitates were detected in polished cross-sections of samples containing oxygen in amounts greater than 1500 ppm, specimens C3 and C4 in Fig. 2.1. These oxides are able to dissolve oxygen to form oxinitrides at temperatures above 1300 K. Microstructural analysis was carried out by light and electron microscopy. An electronic image analyser and software QMA[1] were used for the quantitative investigation of the pore and grain populations. The shape factor for each pore was calculated by dividing the maximum by the minimum chord length (a sphere has a shape factor 1). The open porosity of the material was measured by penetration techniques using a Carlo Erba mercury porosimeter working at pressures up to 4000 bars. The grains were revealed by chemical etching.

*Tab. 2.1* *Characterics of uranium-plutonium nitride starting material.*

| | Fuel Type: | | | | |
|---|---|---|---|---|---|
| | C | | | | P |
| | C1 | C2 | C3 | C4 | |
| Pu/(U + Pu) | 0.23 | | | | |
| Carbon, ppm | ≈300 | | | | |
| Oxygen, ppm | ≈500 | ≈1500 | ≈3760 | ≈7600 | ≈500 |
| Oxide type incl., % | | | 3 | 5.6 | |
| Geom. density, % TD | 83 | 81 | 81 | 81 | 84 |
| Total porosity, % (+) | 14-17 | 16-17 | 17-18 | 17-18 | 13-15 |
| Porosity on grain boundaries, % of total | >90 | | | | |
| Open porosity, % of total | >90 | | | | |
| Pore shape factor | 1.60 | 1.55 | 1.62 | 1.79 | 1.53 |
| Mean pore size, micron | 3.5 + -3 | 2.8 + -3 | 3.6 + -8 | 3.4 + -7 | 2.5 + -2 |
| Mean grain size, micron | 12 | 7 | 9 | 8.5 | 7.5 |

(+) Determined by quantitative ceramography

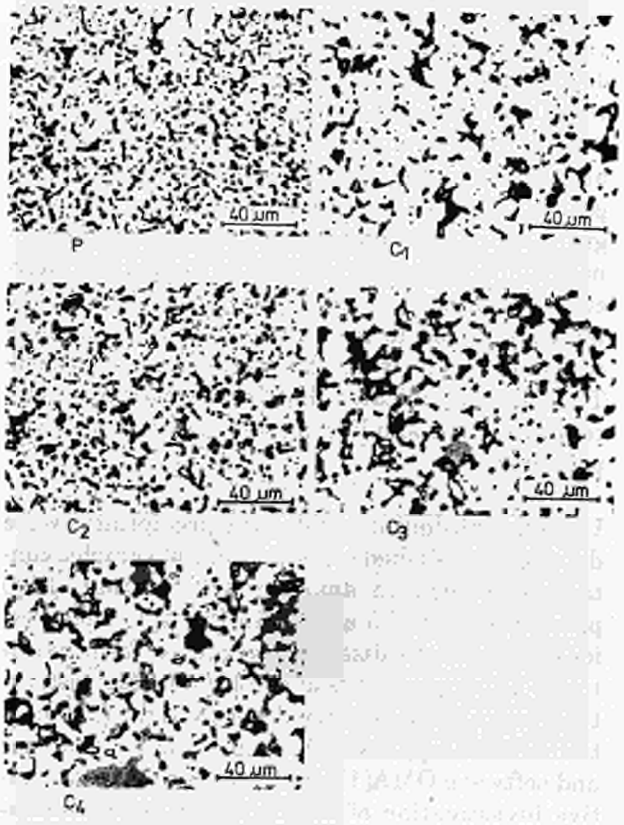


*Fig. 2.1* *Typical microstructures of as-sintered uranium-plutonium nitrides type C and P (see also Tab. 2.1). Note the oxide type inclusions (grey phase) in the specimens C3 and C4 containing 3700 and 7600 ppm oxygen, respectively*

The experiments were carried out using a DEH (direct electrical heating) apparatus [2,3] in which radial temperature gradients were generated in cylindrical pellets by an electrical current flowing in the axial direction. Stationary heating in this apparatus leads to a temperature distribution across the fuel radius, which can be computed using the values of the radially dissipated power, the surface temperature and the thermal and electrical conductivities. The temperature at the surface of the pellets was measured by optical pyrometry with an accuracy of ±40 K. The duration of the experiments varied between a few minutes and 100 hours. The working atmosphere was helium and nitrogen.

## Results and discussion

During the early heat treatment periods in a temperature gradient all nitride pellets fractured by a mechanism common to all ceramic fuels and dependent on the thermal gradient. However, only one radial or diametral crack, with a few microcracks and small pieces broken off at the pellet periphery, were observed in most of the cross-sections analyzed, Fig. 2.2. In spite of this cracking the pellets preserved their cylindrical shape and could be easily handled and even re-used for further experiments. The results in Tab. 2.2 show that at temperatures below 2000 K the initial porosity and grain pattern of the nitride fuels did not change under the influence of the thermal

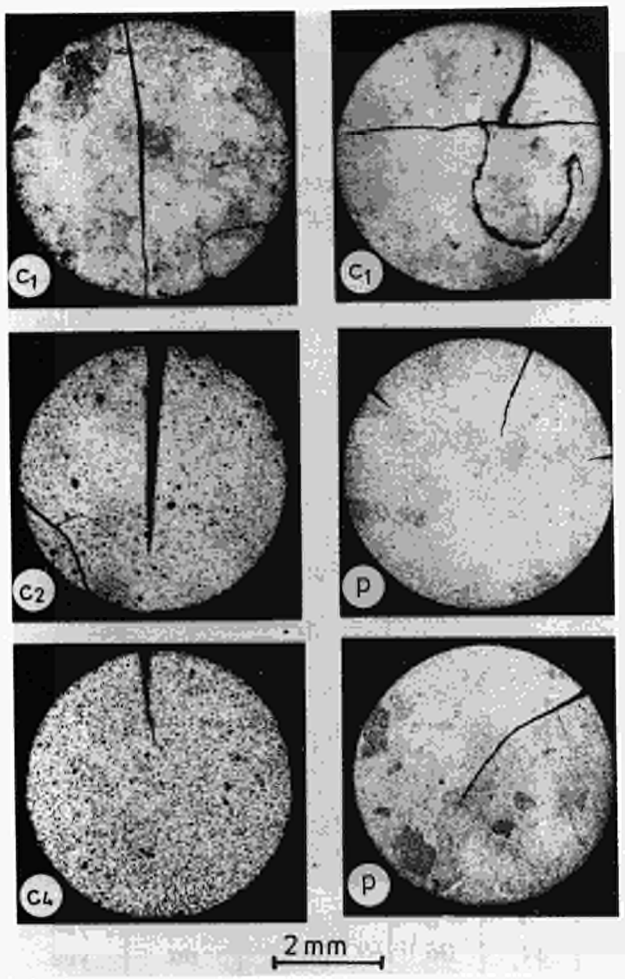


*Fig. 2.2* *Cross-sections of mixed nitrides type C and P after heat treatment in a temperature gradient. Typical radial and diametral cracks*

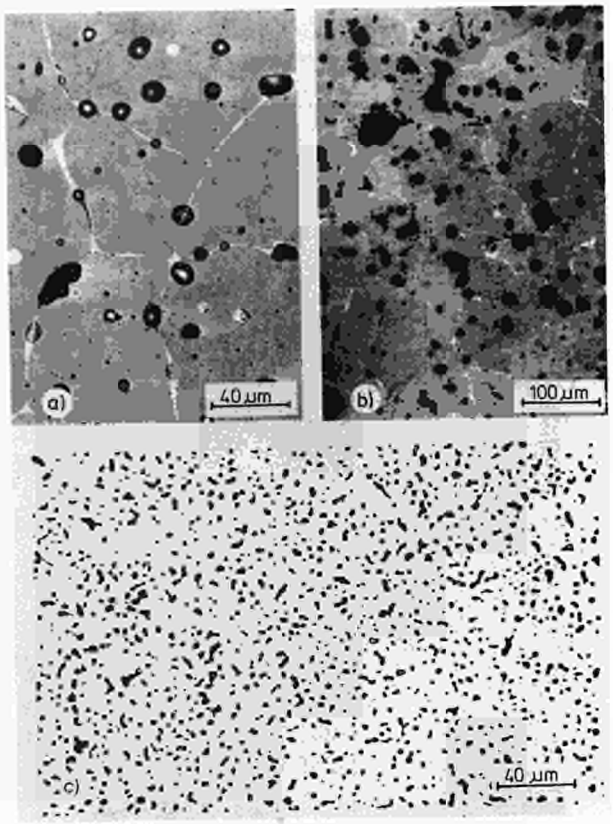


*Fig. 2.3* *Micrographs of mixed nitrides heated in helium (a and b) and in nitrogen (c); a) and b) show a metallic phase (white) in specimens C1 and C4 heated at 2250 and 2300 K, respectively; c) represents a specimen type P heated above 2470 K in nitrogen*

gradient, even after heating times of about two weeks. Large differences between the various types of fuel were not found. The oxide type inclusions, Fig.2.1, were stable even in a flowing helium atmosphere and did not influence the behaviour of the nitrides. However, important densification and grain growth was observed at temperatures above 2000 K.

The analysis of the pellet structures of all fuel types investigated allowed the identifaction of certain structural details to be made. The grain and pore size and geometry changed. The reduction in the diameter of the channel type pores caused the initial porosity network to break up into isolated pores during the densification process. This contributed to the decrease of the amount of open porosity. The data in Tab. 2.2 and the micrographs of Figs. 2.3a and 2.3b, show that a metallic phase, represented by uranium-plutonium alloys, segregated into the grain boundaries of the nitride fuels heated in a flowing helium atmosphere. This was caused by nitride dissociation at temperature above 2000 K according to the reaction MN → M+N (where M=U+Pu). Alexander et al. [4] found that the plutonium-gas pressure over $U_{0.8}$ $Pu_{0.2}$ N is much higher than that of uranium gas, see Tab. 2.3, so that not only the M/N ratio but also the Pu/U ratio changes during the nitride dissociation. Strong plutonium depletion (30-50%) was indeed found by EMPA of both the metallic phase and the matrix of a nitride specimen heated above 2200 K. The liquid metallic phase migrated towards the low temperature region and therefore at the periphery of the pellets the amount of this phase was greater thanin the centre. The pellets heated in helium at temperatures around 2500 K collapsd, see Tab. 2.2 and Fig. 2.4a. This was caused by a catastrophic dissociation of nitrides which led to the formation of a large amount of a

*Tab. 2.2* *Uranium-plutonium nitrides heated in a temperature gradient. Operating conditions and typical results of ceramographic analysis.*

| Fuel type | Oxygen content (ppm) | Temperature (K) | | Atm. | Time (min.) | Porosity decrease (%) | | Grain size increase (%) | Inclusions | |
|---|---|---|---|---|---|---|---|---|---|---|
| | | Surface | Centre | | | Total | Open | | Metal | Oxide |
| C1 | ≈ 500 | 1826 | 1970 | He | 4200 | 0 | 0 | 0 | no | no |
| | | 2073 | 2250 | He | 90 | 40 | 30 | nm | yes | no |
| | | 2053 | 2170 | N2 | 300 | 6 | nm | 2 | no | no |
| P | ≈ 500 | 1850 | 2000 | He | 900 | 0 | 0 | 0 | no | no |
| | | 2073 | 2213 | He | 90 | 40 | 50 | 140 | yes | no |
| | | 2173 | 2323 | N2 | 135 | 25 | nm | 30 | no | no |
| C2 | ≈ 1 500 | 1543 | 1650 | He | 5400 | 0 | 0 | 0 | no | no |
| | | 2073 | 2190 | He | 90 | 45 | 80 | 200 | yes | no |
| | | 2473 | 2624 | N2 | 5 | 50 | nm | 50 | no | no |
| | | 2473 | 2700 | He | 5 | pellets | | collapsed | | |
| | | 2500 | 2720 | N2 | 90 | 80 | nm | nm | no | no |
| C3 | ≈ 3 700 | 2073 | 2180 | He | 15 | 7 | nm | 20 | traces | no |
| | | 2153 | 2278 | He | 75 | 60 | 70 | 130 | yes | no |
| C4 | ≈ 7 600 | 1813 | 1960 | He | 1070 | 0 | 0 | 0 | no | yes |
| | | 2073 | 2190 | He | 90 | 37 | 36 | 30 | no | yes |
| | | 2163 | 2303 | He | 75 | 45 | 64 | 120 | yes | no |
| | | 2198 | 2315 | N2 | 50 | 30 | nm | 1 | no | yes |
| | | 2473 | 2700 | N2 | 5 | pellets | | collapsed | | |

*Tab. 2.3* *Vapour pressure of uranium, plutonium and nitrogen above $U_{0.8}Pu_{0.2}N$ [14].*

| Temperature (K) | Vapour pressure (Pa) | | |
|---|---|---|---|
| | (Pu) | (U) | (N2) |
| 1800 | $5.16 \times 10^{-2}$ | $6.38 \times 10^{-5}$ | $8.91 \times 10^{-3}$ |
| 2000 | $6.78 \times 10^{-1}$ | $4.05 \times 10^{-3}$ | $1.31 \times 10^{-1}$ |
| 2200 | 5.87 | $7.09 \times 10^{-2}$ | 1.01 |
| 2400 | 31,4 | $8.2 \times 10^{-1}$ | 5.57 |

liquid metallic phase, Fig. 2.4b, in a very short time. Moreover, the values of the lattice parameters in Tab. 2.4 indicated that the nitride matrix also lost some plutonium by an evaporation process.The formation of a metallic liquid phase, even in very small quantities and only detectable at a magnification above 1000 x, favoured rapid re-sintering (porosity decrease up to 90% of the initial value) and exaggerated grain growth, Fig. 2.5. During the early stage of the heat treatment of specimens with high oxygen content (type C3 and C4) under helium, the metal formed by nitride dissociation first caused the elimination of the oxinitride inclusions and then precipitated as a second phase, Fig. 2.3c. The behaviour of nitrides type C and P is very similar, as also shown by the porosity change curves plotted in Fig. 2.6 as a function of the reciprocal radius of the pellets.

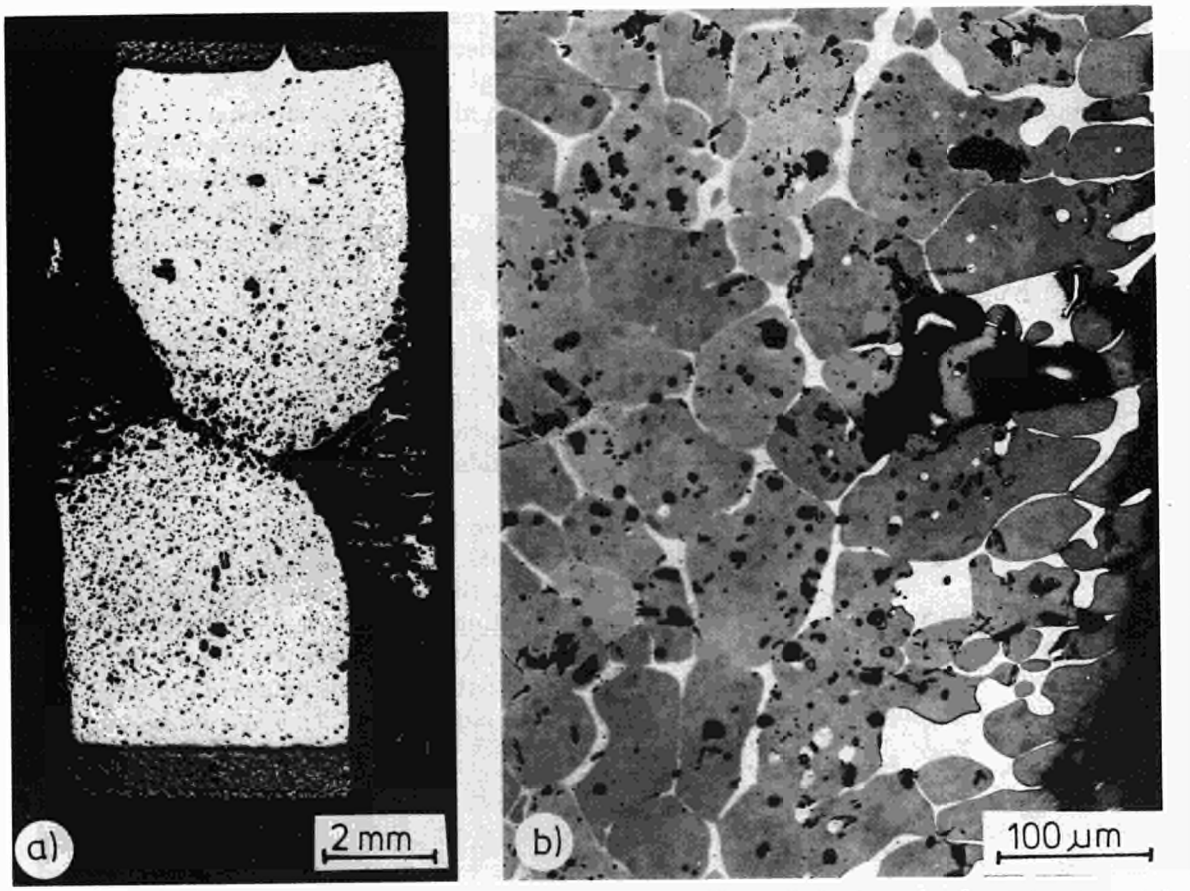


*Fig. 2.4* *Typical example of nitride pellets which collapsed during the heat treatment in helium. a) axial section and b) micrograph of a collapsed region (the white phase is an uranium-plutonium metallic alloy)*

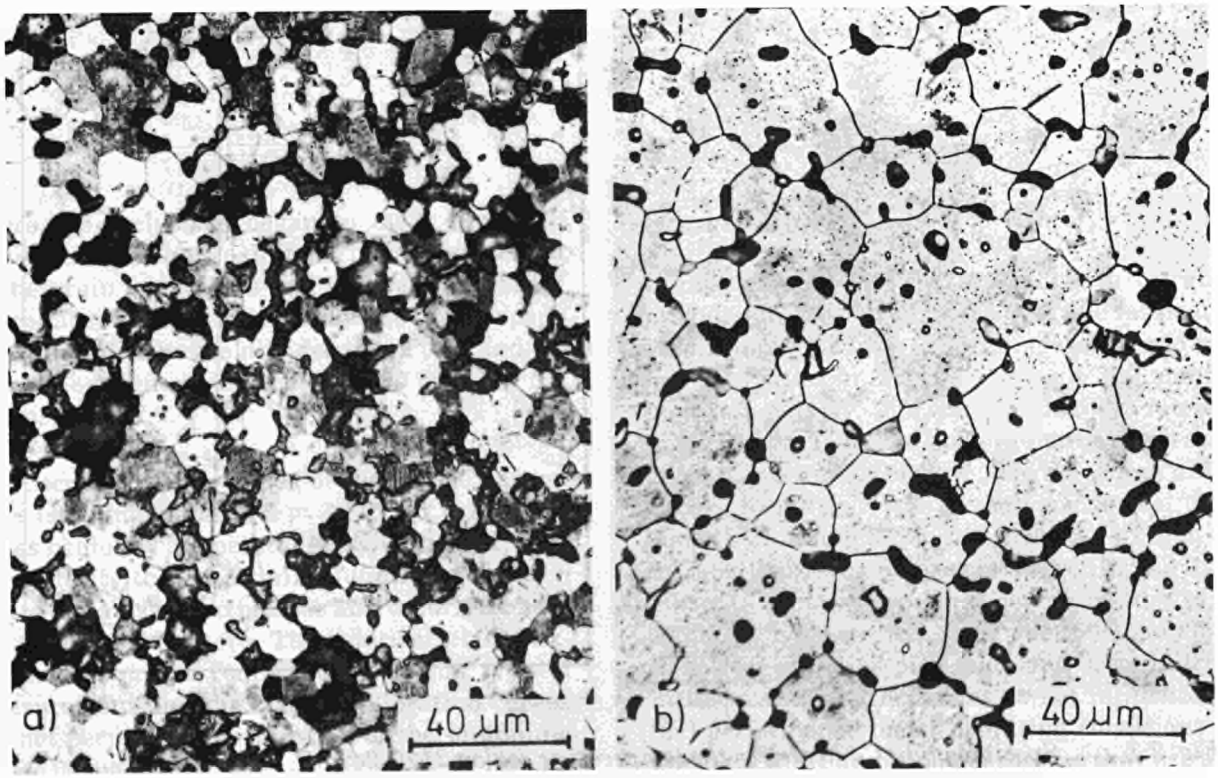


*Fig. 2.5* *Specimen type C2. Typical grain growth in presence of a metallic phase. Grain pattern of: a) starting material and b) after heating in helium during 90 minutes at 2100 K*

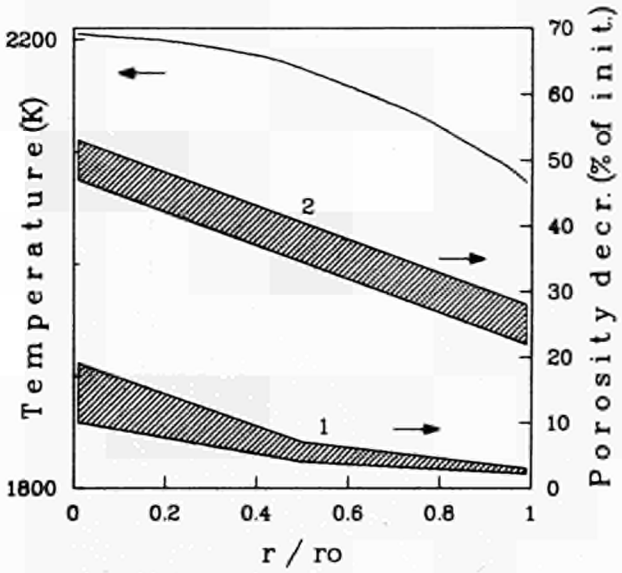


*Fig. 2.6* *Radial porosity changes (% of the initial porosity) of specimens heated under helium (curve 2) and nitrogen (curve 1) atmosphere*

The results represented in Tab. 2.2 also show that the decomposition of the nitrides can be prevented, at least below 2700 K, by replacing helium with nitrogen at atmospheric pressure, Fig. 2.3d. Under this experimental condition and, therefore, in the absence of a liquid metallic phase densification and grain growth occurred at a rate lower than that observed for specimens heated in helium, Fig. 2.6. Moreover, X-ray diffraction and optical analysis showed that large amounts of a needle shaped sesquinitride phase precipitated into the oxide type inclusions of specimens C3 and C4 after heat treatment in nitrogen in the temperature range 2173-2473 K followed by cooling to room temperature, Fig. 2.7.

Above 2473 K the pellets type C3 and C4 collapsed. Optical analysis of an axial section, Fig. 2.8a, showed that high swelling of the pellets and melting of the oxinitride inclusions occurred, Fig. 2.8b. A melting temperature of 2570 ±50 K was estimated from the values of the calculated radial temperature profiles and from the radial position

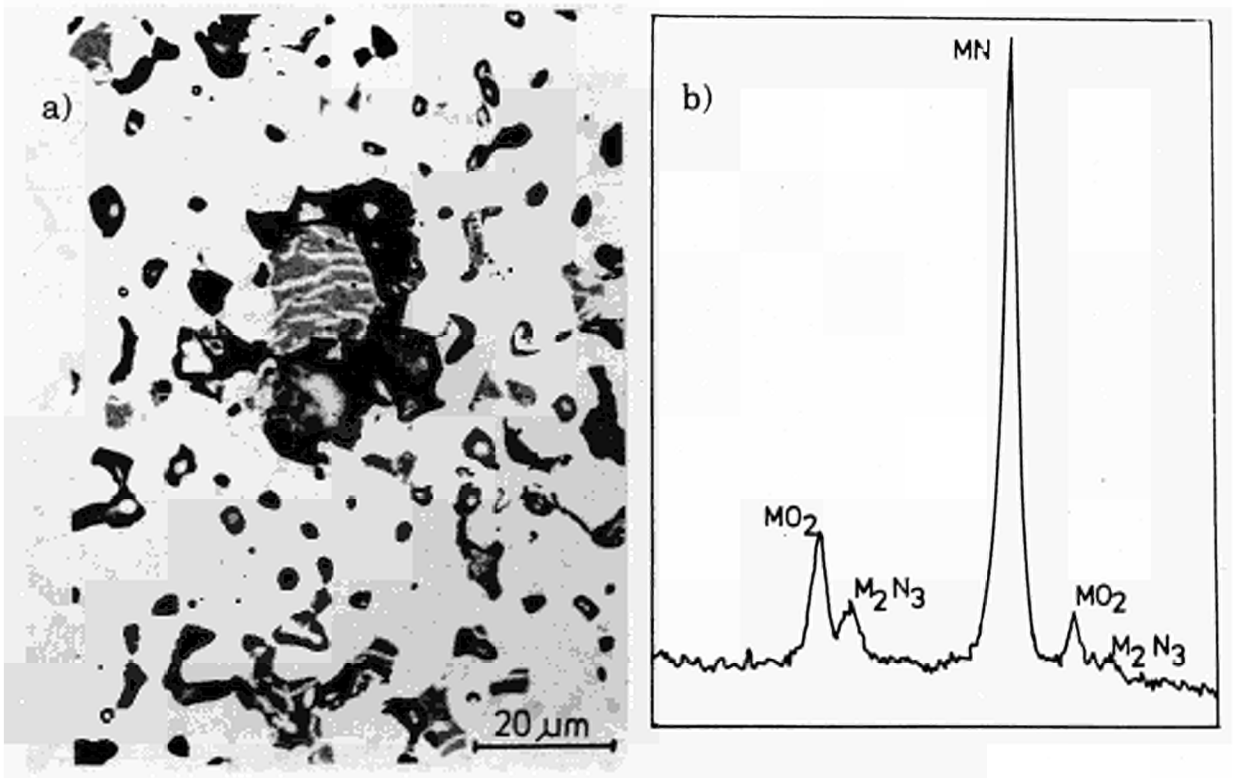


*Fig. 2.7* *Specimen type C4 heated in the temperature region 2170-2470 K. a) needle shaped sesquinitride precipitates in oxide type inclusions and b) X-ray diffraction spectrum*

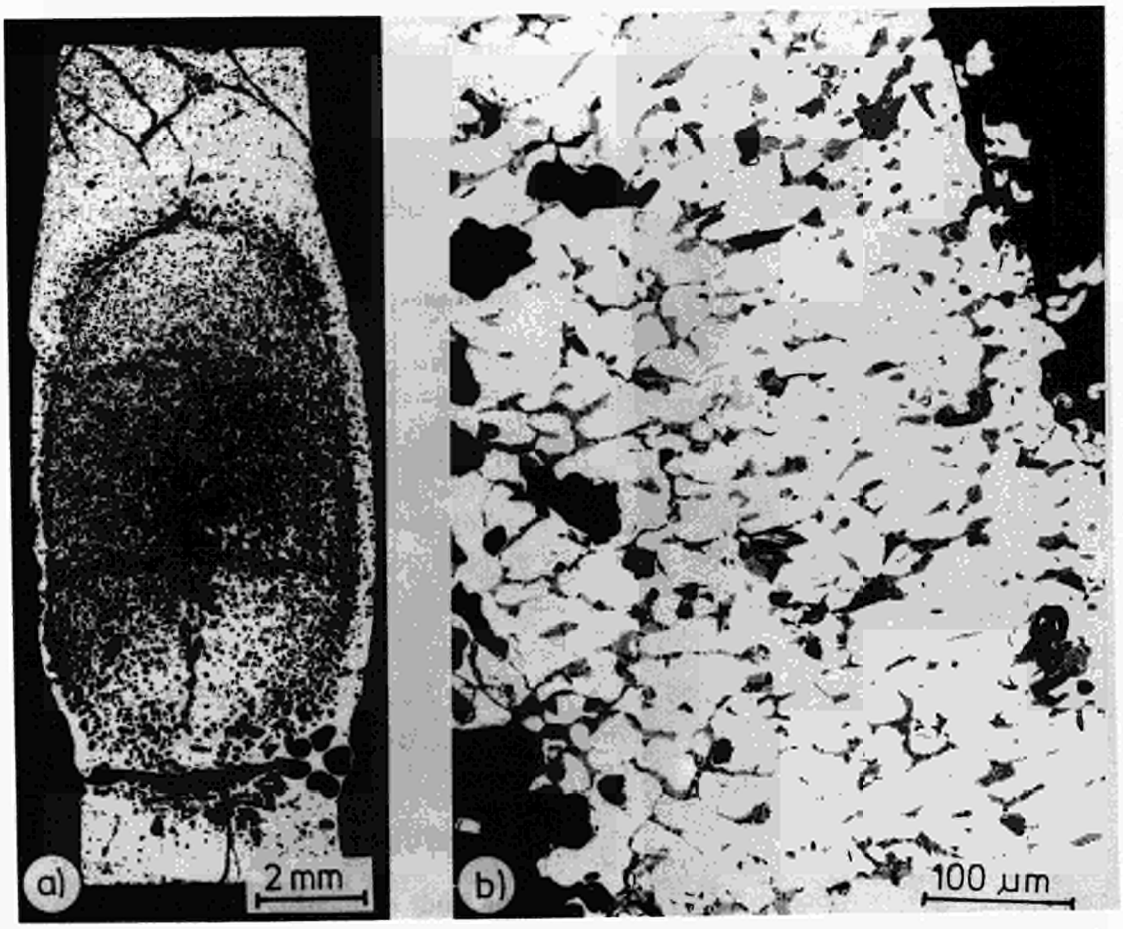


*Fig. 2.8* *Specimen type C4 which collapsed at temperatures above 2470 K in nitrogen. a) axial section and b) oxinitride inclusions (grey phase) in the grain boundaries of the nitride matrix*

where the inclusions began to melt. Fig. 2.8b shows that the liquid oxinitride phase was located at the grain boundaries and was responsible for the collapse of the pellets. Under the same experimental conditions the nitrides type P, C1 and C2 with an oxygen content below 1500 ppm did not collapse, Fig. 2.9.

The decrease of the values of the lattice parameters (starting material a = 4.8921 ± 6 Å) of nitrides heated at temperatures above 2200 K, Tab. 2.4, indicate that a certain plutonium depletion due to an evaporation process also occurred under a nitrogen atmosphere. The relatively large experimental errors connected with this type of measurement and the lack of calibration curves did not permit a quantification of the plutonium loss to be made.

## Conclusion

Carbothermic reduction coupled with nitration provides an economical process for the fabrication of mixed nitride fuels containing carbon and oxygen impurities in amounts of about 300 and 500 ppm respectively. The stability of these nitrides, heated in a temperature gradient, was rather good at least up to 2000 K, and no strong differences in the behaviour of the various fuel types tested containing different amount of oxygen (up to 7600 ppm) was observed. Oxygen impurity in amounts greater than that corresponding to its solubility limit in nitrides (about 1500 ppm) form oxinitride (solution of dioxide and sesquinitride) inclusions. These inclusions do not influence the fuel performance under operating conditions below 2000 K. At higher temperatures they are able to dissolve nitrogen and, within certain limits, even some metal.

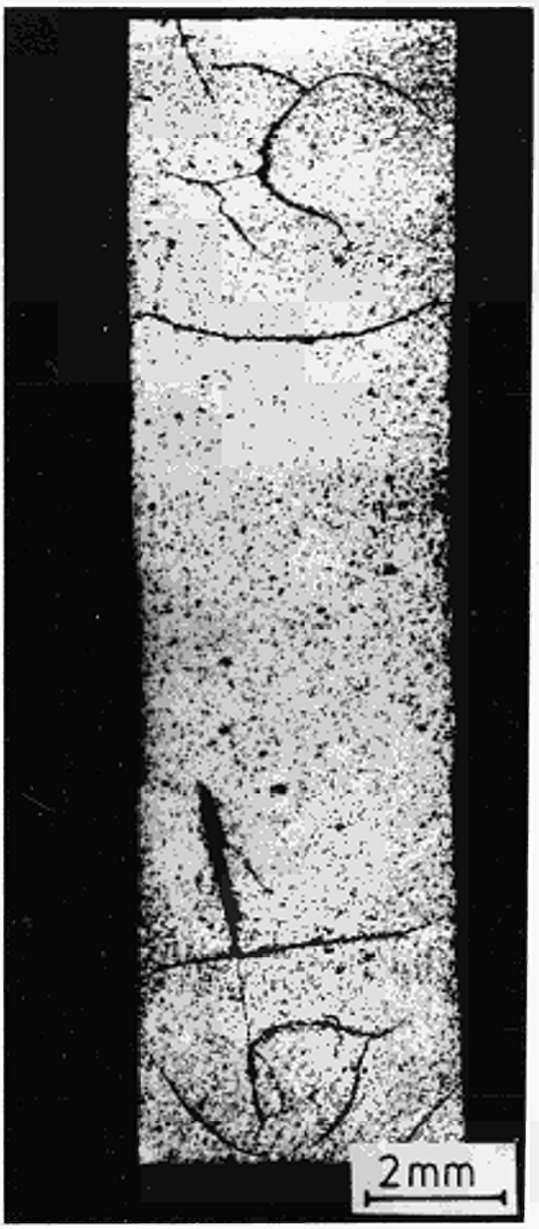


*Fig. 2.9* *Typical axial section of a specimen containing less than 1500 ppm oxygen heated in nitrogen in a temperature region above 2470 K*

A major concern is the stability of the mixed nitrides at temperatures above 2000 K. In fact the decomposition of nitrides is very deleterious for the mechanical and microstructural stability of the pellets and for the homogeneity of the plutonium distribution. The formation of a metallic phase and the evaporation of plutonium causes a rapid restructuring, a densification (which destroys the open porosity network), a transport of plutonium towards the pellet periphery and even to the surface of the cladding material, and in some cases can also cause the collapsing of the fuel.

The use of uranium-plutonium nitrides has there fore limitations with respect to the central fuel temperature. At temperatures above 2000 K restructuring and decomposition of the nitrides accompanied with the appearance of a metallic phase will lead to an important change of the structure, composition and fuel pin behaviour.

**References**

[1] A. Moreno and C. Sari, EUR 6111 EN (1978).
[2] F. Quik and C. Sari, J. Nucl. Mater. 47 (1973) p. 219.
[3] C. Sari, EUR 5812 EN (1978).
[4] C. A. Alexander, J. S. Ogden and W. M. Pardue, 4 Int. Conf. on Plutonium and Other Actinides, Santa Fe, NM., 5 October 1970, Nucl. Met., Met. Soc. AIME vol. 17 (1970) p. 95.

# Fire Experiments under Realistic Laboratory Conditions

## Introduction

The study of the heavy metal transport from contaminated specimens of various materials burned in or exposed to the flames of a standard 0.5 MW polymethylmethacrylate (PMMA)-fire was nearly completed during the reporting period. These materials are those widely used for the construction and equipment of glove boxes. As surface contamination processes, either spreading of cerium-europium-oxide particulates or evaporation of droplets from aqueous Ce-Eu-nitrate solutions, were applied.

The measurements of the particle size distribution of the contaminated combustion aerosols by means of the High Volume Cascade Impactor (HV-CI) were completed, technical problems of calibration of this instrument having been solved.

## Transport rate of contamination into the ventilation exit channel

The previously reported series of experiments with the "dry" contamination process applied to various glove box materials (with the exception of PVC - see below) was completed with a fire involving plywood and with additional fires involving polycarbonate and neoprene (with simultaneous particle size measurements). The data are summarized in Tab. 2.5. They either complete or

*Tab. 2.4* *Lattice parameters of uranium-plutonium mixed nitride fuels type C2 and C4 after heat treatment.*

| Fuel type | Temperature (K) | Time (min.) | Atmosphere | Lattice parameter Å |
|---|---|---|---|---|
| C2 | 2310 | 76 | N2 | 4.8921±7 |
| | 2620 | 5 | N2 | 4.8921±1 |
| | 2720 | 90 | N2 | 4.8908±2 |
| | 2310 | 8 | He | 4.8907±4 |
| | 2680 | 5 | He | 4.8914±5 |
| C4 | 2310 | 50 | N2 | 4.8910±2 |
| | 2470 | 5 | N2 | 4.8911±8 |
| | 2570 | 5 | N2 | 4.8916±7 |
| | 2700 | 5 | N2 | 4.8908±7 |
| | 2700 | 10 | He | 4.8888±3 |

*Tab. 2.5* *Transport of heavy metal from fires involving plates of different materials contaminated with cerium-europium-oxide powder (Completing Tab. 6.1 TUAR-88)*

| Type of contaminated material | Surface contamination level (mg x cm-2) | Percent of original cerium contaminant transported into ventilation exit channel |
|---|---|---|
| Polycarbonate (0.9 kg) | 1 | 0.2 |
| Polycarbonate (0.9 kg) | 1 | < Detection limit |
| Neoprene (40 g) | 0.5 | 3.4 |
| Neoprene (35 g) | 0.5 | 2.0 |
| Plywood (0.8 kg) | 1 | 0.8 |

are in good agreement with those of Tab.6.1 of TUAR-88. This confirms the important result for safety applications that, in general and with the spectacular exception of neoprene, the percentage of heavy metal transported into the ventilation outlet is not higher than with PMMA.

As far as PVC is concerned, its highly corrosive combustion products could cause severe damages to the ventilation system and the analytical equipment. Therefore, fire experiments involving this material will be delayed till the end of the study.

Concerning the "wet" contamination process (deposition from solution, see the description of the method in TUAR-88, p.117), a series of 6 PMMA-fires using the standardized five-plate fuel assembly previously described [1] were carried out, as well as a series of fires involving other contaminated materials according to the same plan as for the "dry" contamination. The available data (some results are still expected) are summarized in Tab.2.6.

*Tab. 2.6* *Transport of heavy metal from fires involving plates of different materials contaminated by evaporation of a cerium-europium-nitrate solution.*

| Type of contaminated material | Surface contamination level (mg x cm-2) | Percent of original cerium contaminant transported into ventilation exit channel |
|---|---|---|
| PMMA | 0.1 | <Detection limit* |
| PMMA | 0.1 | 0.5 |
| PMMA | 0.2 | 0.3 |
| PMMA | 0.2 | 0.25 |
| PMMA | 0.2 | 0.5 |
| PMMA | 0.2 | 0.7 |
| Polycarbonate | 2.0 | < D.L. |
| Polycarbonate | 2.0 | < D.L. |
| Stainless Steel | 2.0 | < D.L. |

(*)The detection limit amounts to 0.1 %

## Difference in transport rate with mechanism of contamination

The data of Tab. 2.6 confirm that the percentage of heavy metal carried away into the ventilation outlet is significantly lower than in the case of "dry" contamination. These results confirm that, as already suggested in TUAR-88, the degrees of

attachment of the contaminant are different for the "dry" and for the "wet" contamination cases. Thus turbulences accompanying the strong combustion seem to act as the essential resuspension mechanism.

## Aerodynamic size measurements

Analyses of the particle size distribution of the contaminated smoke using the Andersen's HV-CI equipment (method described in TUAR-89, p.28) were continued. The HV-CI was recalibrated by means of suspended aluminium-oxide particulates in an air flow rate of 60 m3/h: the cut-off diameters are determinated by weighing the collection substrates of the 4 impaction stages. The ground aluminium oxide was previously analysed for size distribution with the recently acquired TSI aerodynamic particle sizer (APS 3300). Tab.2.7 reproduces Table 1.2 of TUAR-89 with the corrected values of the cut-off sizes. The conclusions which were drawn from these data are not affected by this correction.

*Tab. 2.7* *Particle size analysis of heavy metal particles spread from contaminated PMMA-fires*

| Experiment Number | Cumulative mass percent of Cerium smaller than cut-off size | | | | | |
|---|---|---|---|---|---|---|
| Cut-off size Dp50 (µm) | Contamination from Eu-Ce-nitrate solution | | | Contamination from Eu-Ce-oxide powder | | |
| | 1 | 2 | 3 | 4 | 5 | 6 |
| 13.5 | 80 | 78 | 84 | 66 | 58 | 63 |
| 8.0 | 68 | 53 | 76 | 40 | 30 | 41 |
| 6.1 | 58 | 39 | 68 | 23 | 17 | 22 |
| 5.0 | 46 | 28 | 61 | 12 | 9 | 12 |

This particle size measurement method was also applied to fires involving contaminated polycarbonate and neoprene as above. No suitable sampling times could be reached with neoprene, the very dense smoke from which rapidly clogs the back-up filter of the HV-CI. The results for the polycarbonate, summarized in Tab.2.8, show a relatively good homogeneity and no significant difference between contamination from powder and from solution deposition. This is in contrast to the results for contaminated PMMA where the airborne fraction from "dry" contamination contains a relatively higher percentage of big particles. The difference might be due to the different burning characteristics of the two materials. In

*Tab. 2.8* *Particle size analysis of heavy metal particles spread from contaminated Polycarbonate burned in a 0.5 Mw PMMA-fire.*

| Experiment Number | Cumulative mass percent of Cerium smaller than cut-off size | | | | |
|---|---|---|---|---|---|
| Cut-off size Dp50 (µm) | Contamination from Eu-Ce-nitrate solution | | Contamination from Eu-Ce-oxide powder | | |
| | 1 | 2 | 1 | 2 | 3 |
| 13.5 | 74 | 72 | 74 | 82 | 70 |
| 8.0 | 50 | 46 | 56 | 69 | 49 |
| 6.1 | 35 | 31 | 41 | 56 | 34 |
| 5.0 | 28 | 21 | 30 | 43 | 25 |

the case of PMMA, the extensive formation, just below the burning surface, of bubbles filled with pyrolysis products and then migrating up the temperature gradient to the surface where they burst is regarded as a primary mechanism for particle ejection [2]. No comparable mechanism could be observed in the case of the polycarbonate which chars to a rigid surface crust.

In the case of polycarbonate, it was possible to measure the amount of cerium on the various stages of the HV-CI, in contrast to the previous measurements of total cerium, because the detection limit of cerium on the impaction stages is lower than that on the single collection filter. Unfortunately it is not possible to calculate the total amount of airborne cerium from the HV-CI results, because the particle size measurements were made only for a short time when the rate of burning was more or less near its maximum.

**Reference**

[1] K.Buijs and B.Chavane de Dalmassy, EUR 11089 EN (1988)

[2] K.Buijs, B. Chavane de Dalmassy and S. Pickering, J.Nucl.Mat. 166 (1989) 199-207

# Duct Transport of Big Particles (TRABI)

In September 1986, failed HEPA-filters in the ventilation exhaust system at the BWR of Mühleberg (Switzerland) caused a contamination of the exhaust stack and of the ground in the vicinity of the stack. Nevertheless the aerosol monitors in the exhaust system did not indicate abnormal radioactivity.

Subsequent inspection and measurements showed that this contamination consisted of radioactive resin particles (released from a centrifugal hydroextractor) with diameters ranging from 50μm upwards.

The Mühleberg event has shown that these large particles could not be detected by the sampling and monitoring lines designed on the basis of the usual standards for nuclear power plants (such as DIN 25423 or ISO 2889) and covering preferentially that fraction of aerosols which is retained in the respiratory tract (0.3 to 10μm).

This fact is confirmed by the recently developed American code ASTEC (Sandia National Laboratories, 1989) which provides a quantitative estimate of the airborne particle transport efficiency in pipes and ducts taking into account gravitational settling and turbulent inertial deposition. This code states that, in the actual highly turbulent flow conditions, the transport efficiency of such large particles through the sampling lines (where $Re > 100{,}000$) and even more through the main exhaust duct (where $Re > 1{,}000{,}000$) is very low. Thus airborne particulates with an aerodynamic diameter of 50μm and more are not expected to be transported away by the stack effluents.

Therefore the Mühleberg event suggests the existence of another transport mechanism such as, for instance, "creeping" of the big particles along the duct walls by successive deposition and reentrainement or bouncing.

An experimental study has been started with the aim to investigate the behaviour of big, heavy particles in connection with the problems of emissions from nuclear installations, such as fuel fabrication facilities or research institutes, and to improve the monitoring systems. The information obtained could be used to improve the ASTEC-code (a collaboration with the Sandia Lab. is considered).

This work will consist of two complementary activities:

(1) Installation in a glove box of a wind channel of rectangular cross section being about 1/10 the size of a typical ventilation exhaust duct but with the same air velocity of 8.5 m/s. This channel will be provided with various removable aerosol sampling and analysis systems and the necessary anemometric and air filtering equipment. During the reporting period the project was designed and the equipment was ordered.

(2) Generation and standardization of monodisperse aerosols, ranging from 10 to 100 μm, of depleted uranium oxide, which is obviously a good substitute for nuclear fuel materials.

# 1.3 Actinide Determination and Recycling

## Introduction

The transmutation of minor actinides, the recycling of self-generated plutonium in high burn-up cycles, and the study of methods of actinide extraction from high active waste were the principal objects of concern under this heading in 1990. These studies should be seen in the general context of world-wide efforts to mitigate the consequences of the existence of long-lived radio isotopes in nuclear waste, to which also some of our contractual work contributes.

In these efforts the Institute has a key function in Europe. It coordinates the activities of international working groups which study various aspects of minor actinide partitioning and transmutation, as a follow up of a workshop on the subject which was held in Karlsruhe in October 1989.

## Follow up of the Workshop on Partitioning and Transmutation of Minor Actinides (16-18 October, 1989)

The partitioning of minor actinides from spent fuel and their transmutation into short-lived fission products was the topic of two dedicated meetings organised jointly by the European Commission and the OECD [1,2]. The conclusion of the last meeting in 1980 was that the transmutation appeared technically feasible, but that the incentives of such an alternative waste disposable scheme were not high enough to warrant continuing.

With rising interest in the possibilities of these techniques being shown in recent years, especially in Japan, it was decided to organise and hold a workshop in Karlsruhe. Some 30 participants from Europe, USA and Japan, took part in the workshop which covered four main topics: transmutation processes, target or fuel development, partitioning of minor actinides and transmutation strategies.

As well as organising the meeting, members of the Institute prepared an initial study on each of the topics. References were collected and tabulated in an attempt to show the present day status and more importantly, the gaps in our knowledge which need to be filled before proper decisions can be taken on a political level on the suitability of these techniques and their place in the concept of nuclear waste disposal.

The proceedings of the workshop have already been published privately and distributed to the participants. The final version is being processed as a EUR report and is expected to be published in 1991.

The meeting closed with a list of recommendations for further work in each of the four subtopics. In particular, task forces or working groups were to be set up to continue and coordinate further work. Because of an OECD workshop meeting held in Japan on 6-8th November 1990, the working group meetings were postponed until 1991, except for the first, which is reported below.

### Working group on transmutation methods

The participants of the Workshop on Partitioning and Transmutation of Minor Actinides [3], Karlsruhe, Oct. 16-18, 1989, decided that Working Groups should be set up on the different aspects of P - T. The first meeting of the Working Group on Transmutation Methods concentrated on the use of Fast Reactors in the Transmutation of Minor Actinides and was hosted by DGXII in Brussels, in June 1990.
The Working Group meeting was attended by scientists from Belgium (Belgonucléaire), Germany (KfK), France (CEA), Great Britain (Harwell, BNFL), Japan (CRIEPI), Netherlands (ECN Petten) and the Commission of the European Community (DGXII, ITU).

A short summary on the state-of-art of Minor Actinides Transmutation in Fast Reactors and the relevant recommendations of the Workshop on Partitioning and Transmutation of Minor Actinides were given. Then on-going activities in this field were presented by some of the participants. The presentations included the status of KNK-II experiments and calculations

(TU/CRIEPI), the CEA-Cadarache activities, the status of the SUPERFACT irradiation (TU/CEA), safety features of Fast Reactors (e.g. EFR) fuelled with Minor Actinides (CEC/Interatom), metallic fuel for commercial FBR (CRIEPI), and mixed oxide fuels with Minor Actinides for the EFR (Belgonucléaire).
The discussion that followed, emphasised the importance for irradiation experiments and the need for benefit and risk assessment studies.

### References


[1] Proceedings of the '1st Technical Meeting on the Transmutation of Actinides', JRC-Ispra, 16-18 March 1977, EUR 5897 (1978)

[2] Proceedings of the '2nd Technical Meeting on the Transmutation of Actinides', JRC-Ispra,21-24 April, 1980 , EUR 6929 (1980)

[3] Proceedings of the Workshop on partitioning and transmutation of minor actinides, JRC Karlsruhe, 16 to 18 October 1989, EUR 13347 (1991) Eds: L. Koch, R. Wellum,


## Status of the Irradiation in KNK II

As reported previously (TUAR 89, 34), the samples irradiated in the KNK II reactor in the MTR fuel bundle have been analysed. The experimental results are complete, in that all nuclides of interest have been measured, some with more than one technique (for example Am which was measured by IDMS, gamma spectrometry and alpha spectrometry where possible).

The parallel calculations are being carried out in cooperation with INR, KfK and CRIEPI, Japan. The position of the samples in the reflector of the reactor meant that the neutron spectrum was difficult to calculate as it was highly perturbed by the reflector. Calculations based both on reactor physics calculations and using SAND 2 on the measured monitor samples will yield results which can be compared with each other and the experimentally measured values. We hope to be able to give a final report on this experiment in the next TUAR.

The samples from the irradiation designated KNK IIa are being cooled and will not be available for analysis this year.

## The Status of the Irradiation Experiment 'SUPERFACT'

The 4 fuel pins containing Np and Am which have been irradiated in the PHENIX reactor were delivered to the Institute at the end of the year.It is planned to start the initial analysis (PIE) in the hot cells in January 1991.The delay in the delivery was due to problems in the licensing procedure and due to the renovation of the hot cell during this year.

The duplicate 4 pins have been retained by the CEA and are now being examined. No apparent physical difference was reported between the standard pins and those containing the minor actinides, Np and Am after a nondestructive examination.

## Calculation of the Results of Recycling Self-generated Plutonium in a PWR at 50GWd/t Burnup per Cycle

Plutonium is in practice frequently recycled in light water reactors, especially in Europe, where the usage of MOX fuel is generally accepted. The buildup and burnup of actinides in reactors is the theme of subproject FACT and the posssibility of recycling actinides in LWR's has been investigated previously in the frame of this subproject. The recycling of the intrinsic or self-generated Pu in LWR's has been reported elsewhere [1], using reactor specifications applicable to the reactor practice of the time, i.e. burnups of 33 GWd/t . It is now common for LWR fuel to be designed for high burnups, and a target burnup to be normal in coming time is 50 GWd/t.

To round off the picture of Pu recycling in PWR's it was decided therefore to calculate the concentrations and isotopic compositions of actinides for the following case:

1. The first cycle consists of normal PWR fuel irradiated in a typical PWR (Biblis) to a burnup of 50 GWd/t.

2. After a cooling time of 3 years, the plutonium is separated out (losses of 0.5% are assumed)

and made up into MOX fuel pins. The rest of the fuel is standard PWR uranium fuel.

3. This core is also assumed to stay in the reactor until 50 GWd/t burnup is achieved and the process is then repeated, whereby the plutonium is separated out and made up into fuel pins for the next irradiation.

4. In each case the amount of plutonium in the MOX fuel is adjusted to keep the amount of fissionable material the same which means slightly increasing the amount of Pu in the pins in subsequent cycles as the fission value of the recycled Pu constantly decreases from cycle to cycle. The MOX pins are made up as necessary with natural uranium. No feedback or recycle of neptunium, americium or other actinides is considered in this study.

5. The cycles: irradiation, cooling and separation were repeated 6 times. Most parameters appeared to be approaching an equilibrium value after 6 cycles.

The calculations were done under contract in the KfK using the program KARBUS and the data library pertinent to Biblis. KARBUS is a cell calculation program [2], which calculates the effective cross-sections for all nuclides: the resulting burnup or buildup of nuclides is then calculated with KORIGEN. KARBUS is a large, complex program and to reduce calculation costs it was not applied at every cycle, but rather the cross-sections were interpolated for intermediate cycles.

The actinide mass inventory, 3 years after cycle end, is given in Tab. 3.1 and similarly the percent isotopic concentrations of plutonium in Tab. 3.2. Cycle 1, 'U(0)' is for the end of the first (pure U) irradiation, MOX(1) indicates the end of the first recycle with Pu and so on. After the first recycle there are two sources of Pu: from the MOX pins

*Tab. 3.1 Actinides mass inventory 3 years after cycle end (g/t heavy metal)*

| cycle | U (0) | MOX (1) | MOX (2) | MOX (3) | MOX (4) | MOX (5) |
|---|---|---|---|---|---|---|
| nuclide | | | | | | |
| $^{237}Np$ | 7.24E+02 | 2.75E+02 | 2.75E+02 | 2.76E+02 | 2.74E+02 | 2.72E+02 |
| $^{238}Pu$ | 3.48E+02 | 1.69E+03 | 2.11E+03 | 2.42E+03 | 2.66E+03 | 2.86E+03 |
| $^{239}Pu$ | 5.67E+03 | 1.48E+04 | 1.58E+04 | 1.67E+04 | 1.73E+04 | 1.77E+04 |
| $^{240}Pu$ | 2.74E+03 | 1.32E+04 | 1.54E+04 | 1.69E+04 | 1.79E+04 | 1.87E+04 |
| $^{241}Pu$ | 1.45E+03 | 6.70E+03 | 7.70E+03 | 8.33E+03 | 8.78E+03 | 9.15E+03 |
| $^{242}Pu$ | 9.00E+02 | 6.46E+03 | 9.12E+03 | 1.15E+04 | 1.37E+04 | 1.57E+04 |
| $^{241}Am$ | 2.77E+02 | 1.62E+03 | 1.91E+03 | 2.09E+03 | 2.22E+03 | 2.33E+03 |
| $^{243}Am$ | 2.14E+02 | 1.75E+03 | 2.20E+03 | 2.55E+03 | 2.84E+03 | 3.11E+03 |
| $^{244}Cm$ | 8.21E+01 | 1.00E+03 | 1.22E+03 | 1.37E+03 | 1.49E+03 | 1.60E+03 |
| Total | 9.48E5 | 9.49E5 | 9.49E5 | 9.49E5 | 9.49E5 | 9.49E5 |

*Tab. 3.2 Percent Pu isotope distribution after internal recycling of Pu from MOX fuel. Decay after discharge = 3 years.*

| | U(0) | MOX(1) | MOX(2) | MOX(3) | MOX(4) | MOX(5) |
|---|---|---|---|---|---|---|
| 238 | 3.1 | 3.9 | 4.2 | 4.3 | 4.4 | 4.4 |
| 239 | 51.1 | 34.5 | 31.6 | 29.9 | 28.6 | 27.7 |
| 240 | 24.7 | 30.8 | 30.7 | 30.2 | 29.7 | 29.1 |
| 241 | 13.0 | 15.6 | 15.4 | 14.9 | 14.6 | 14.3 |
| 242 | 8.1 | 15.1 | 18.2 | 20.7 | 22.7 | 24.5 |

and from the rest of uranium core. The fission value of the total Pu, as represented by the percent of $^{239}Pu$ drops steadily however with increasing recycling despite the constant mixing with high-grade Pu from the uranium until after the third MOX recycle the concentrations of isotopes 239 and 240 are very similar.

The total amount of plutonium in the fuel slowly rises to about 9% (Tab. 3.1) at the last cycle whereby the relative amount of fissionable plutonium decreases from cycle to cycle. Fresh fissionable $^{239}Pu$ is provided from reprocessing the uranium together with the plutonium, but this does not compensate for loss of fissionable Pu by fission and neutron capture processes.

The higher actinides, americium and curium are built up to relatively high levels because of the steady increase in the higher Pu isotopes with recyling (Fig. 3.1). $^{238}Pu$ also builds up (Tab. 3.2), mainly due to decay from $^{242}Cm$. The presence of increased amounts of curium and $^{238}Pu$ means that the neutron emission is increased by a factor 2.46 relative to the starting MOX fuel and by a factor of 21 relative to a uranium fuel.

$^{237}Np$, on the other hand, does not increase relative to a standard uranium fuel because the production paths from uranium are reduced, especially that via $^{235}U$ by neutron capture.

The total increased neutron emission however, implies that the usage of such fuels will necessitate the application of remote handling devices for fuel processing.

**References**


[1] U. Fischer, Mehrfacher Rückführung von Plutonium in Thermischen Reaktoren, Atomwirtschaft 31 (1986) 548

[2] C.H.M. Broeders, Möglichkeiten und Verifikation von KARBUS (KArlsruher Reaktor BUrnup System). KfK Nachrichten 17 (1985) 135-137


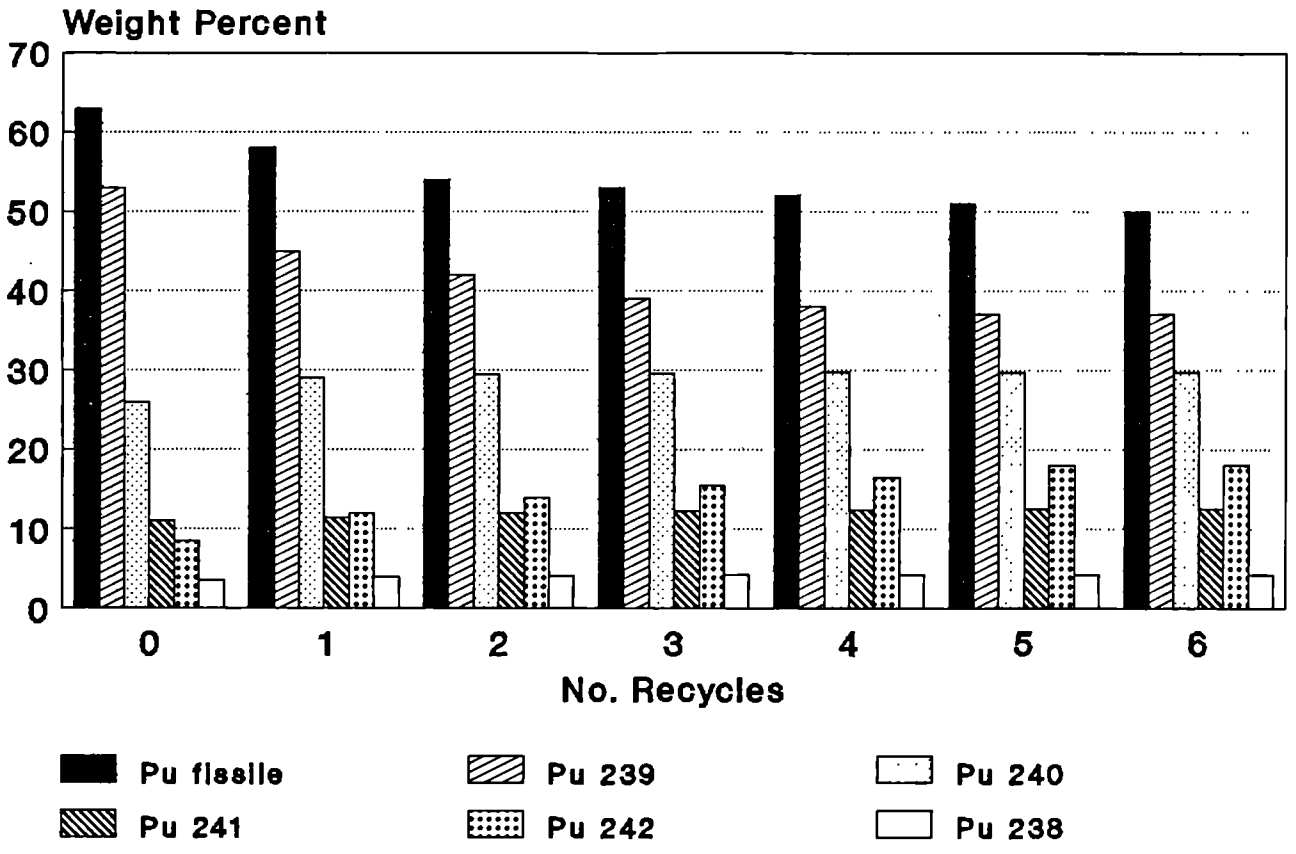


*Fig. 3.1 Plutonium isotope distribution with recycling*

# System-Immanent Long-lived Radioisotope Transmutation

## Introduction

In the Institute, advanced fuels for fast reactors have been developed and tested over the last 25 years. Minor actinide (Np, Am)-containing mixed oxide fuels have been designed and successfully irradiated in fast reactors: KNK II and Phenix [1], (TUAR 88, 81). The composition of the fuel covered the homogeneous as well as the heterogeneous recycle of minor actinides (Tab. 3.3). The advantage of such fuels in a fast breeder reactor is the increased energy generation which at about 4% would compensate for the extra fuel make-up costs, increase the breeding ratio and prolong burn-up reactivity [2, 9]. A recent study showed that the changes in the void and Doppler effect are acceptable from the safety point of view [3].

*Tab. 3.3 Irradiation experiments with different minor actinide fuels*

| Fuel type | Reactor | Status |
|---|---|---|
| $(U_{.73}Pu_{.25}Np_{.02})O_{1.97}$<br>$(U_{.73}Pu_{.25}{}^{241}Am_{.02})O_{1.97}$<br>$NpO_2$<br>$(^{241}Am_{.5}U_{.5})O_{1.92}$ | KNK II | irradiation completed |
| $(U_{.77}Pu_{.21}Np_{.02})O_{1.97}$<br>$(U_{.77}Pu_{.21}{}^{241}Am_{.02})O_{1.97}$<br>$(Np_{.45}U_{.55})O_{2.00}$<br>$(Np_{.2}{}^{241}Am_{.2}U_{.6})O_{1.95}$ | PHENIX | irradiation completed |

When this work was initiated the economic aspect of minor actinides was more important than the recently discussed ecological advantages of partitioning and transmutation schemes. Since then the introduction of fast breeder reactors has been postponed for at least 40 years. Under these changed circumstances we felt it necessary to re-examine all options of the transmutation of long-lived radionuclides. Hence a workshop was organized by the Institute in October 1989 [4] to assess the technical feasibility of the proposed transmutation procedures. A review of this workshop has been given elsewhere[5].

## System-immanent recycling of long-lived radionuclides

For a convincing ecological transmutation scheme other radionuclides as well as the minor actinides have to be considered. Not only the mobile monovalent cation of pentavalent neptunium ($NpO_2^+$) (and hence its parent nuclide, $^{241}Am$) have to be considered but also other monovalent ions of the fission products, the most prominent of which are the anions of $^{129}I$ ($I^-$) and $^{99}Tc$ ($TcO_4^-$). The recycling of plutonium in the so-called self-generated mode has so far been introduced for LWR's [6]. The other nuclides mentioned above show very different behaviour when recycled in the thermal neutron spectrum of a PWR (Tab. 3.4). The transmutation half-lives of $^{237}Np$, 4.0 years, and $^{241}Am$, 0.9 years, are acceptable. However the underlying process is neutron capture leading finally to $^{238}Pu$ and $^{242}Pu$ which when recycled together with the self-generated plutonium would worsen its handling properties due to enhanced neutron radiation by the spontaneous fission of $^{238}Pu$. On the other hand it would denature the plutonium helping to prevent misuse of the fissile material. The table refers to an unloaded spent fuel of a PWR fuel initially enriched with 3.5 % $^{235}U$. If the self-generated Pu is recycled, the amount of $^{243}Am$ will be enhanced by a factor of 25 [6]. The recycling of this nuclide mainly produces $^{244}Cm$. When $^{244}Cm$ is recycled in a thermal neutron spectrum, $^{252}Cf$ builds up significantly, thus making the handling of the spent fuel almost impossible. For this reason $^{244}Cm$ should not be fed back to LWR power stations but rather be burnt in the harder neutron spectra of fast reactors.

*Tab. 3.4 Long-lived radiotoxic nuclides in PWR*

| (33 $GW_{th}$ d/t, initial $^{235}U$ = 3.2 w/o, 3 x $10^{13}$ n $s^{-1}$ $cm^{-2}$) | | | | | | |
|---|---|---|---|---|---|---|
| | $^{99}Tc$ | $^{129}I$ | $^{237}Np$ | $^{241}Am$ | $^{243}Am$ | $^{244}Cm$ |
| Discharge Concentration [g/t] | 780 | 170 | 440 | 67 | 84 | 24 |
| Halflives [y] | | | | | | |
| Total | 12 | 35 | 4.3 | 0.88 | 9.2 | 13.1 |
| Capture | 12 | 35 | 4.3 | 8.7/0.98 | 9.2 | 53 |
| Fission | - | - | $>10^4$ | 230 | $>10^4$ | 610 |
| Decay | $>10^5$ | $>10^7$ | $>10^6$ | 433 | $>10^3$ | 18 |

In order to transmute the two fission products $^{99}Tc$ and $^{129}I$ in a reasonable time period a thermal neutron flux of about $10^{15}$ n/cm$^{-2}$ sec$^{-1}$ would be needed. Reactors of this type have only been developed for research purposes, but they would be the best means of transmuting these nuclides. Fast reactors, although having a higher neutron flux, are not efficient because of the correspondingly lower neutron capture cross-sections of the fission products.

Instead of recycling Np and Am in a LWR they could be recycled together with Cm in fast reactors. This second option of system-immanent minor actinide recycling would be valid for a wide deployment of fast reactors and correspond to our earlier concepts of advanced fast reactor fuels [7].

## Research and development for the system-immanent recycling of minor actinides

There exists some know-how on how to recycle Np in light-water reactors since this nuclide was a source of $^{238}Pu$ used in pacemakers. The recycling of Am in light- water reactors is difficult because of the high resonance shielding of $^{242}Am$. Earlier irradiation tests show that the burn-up in the outer region of the fuel is so strong that the material embrittles [8]. Therefore new concepts must be developed involving, for example, annular fuels. The development of Am- and Np-containing fast reactor fuels in the Institute has been mentioned above. The two fuel compositions cover the extreme cases of self-generated recycling with 2 % minor actinides and the heterogeneous concept with up to 50 % of minor actinides. Concentrations in between have to be tested, since they exhibit additional advantages for reactor operation [3, 9, 10]. Cm-containing fast reactor fuels have not so far been tested. If the concentration of this element is kept in the part per thousand range no major changes in the irradiation behaviour of the fuel is expected. However the handling properties of such a material will require heavier shielding during fuel make-up.

Apart from the need to develop high-thermal-flux reactors the corresponding targets for the transmutation of technetium and iodine have to be designed. Such reactors would transmute Np and Am 10 times faster than LWR's and it is therefore worthwhile considering the recycle of MA's in such reactors. It should be recalled that the concentrations of Np and Am are of the same order as Tc and I (Tab. 3.4). In a high neutron flux the fission of $^{238}Np$ will contribute significantly to the transmutation process.

In order to design the new fuels required for thermal reactors and also improve those for fast reactors, more basic data of the thermal physical behaviour and material properties are needed. So far our studies have concentrated on the phase diagrams of americium oxides [11], neptunium oxides [12] and on a limited sector of the quaternary oxides of Am - Np - U - O relevant to the fuels described above. To assess the compatibility of mixed oxides with sodium the Gibb's free energy was determined [13] and the thermal conductivity over a temperature range from 600 °C to 2000 °C measured [14]. This information, together with known data, was sufficient to predict the irradiation behaviour of minor actinide fuels. For more comprehensive future studies however, a broader data base will be needed. Such studies (Tab. 3.5) are envisaged at present and have to some extent been started.

*Tab. 3.5 MA - related research*

| |
|---|
| Basic Research<br>• Integral neutron cross-sections<br>• Thermodynamic data<br>• Chemophysical data |
| Applied Research<br>• Simulation experiments<br>• Characterisation of targets<br>• Fabrication of targets<br>• Irradiation experiments<br>• Partitioning studies |

There is a common problem for all transmutation options concerning the partitioning of minor actinides from high level waste. The various processes are only capable of separating the lanthanides and actinides as a group together [15]. Recently the extraction properties of a new derivative of phosphine oxide (TRPO) was compared to the chemical of the TRUEX process: CMPO [16]. The synthesis of other compounds however may lead to more specific separations. In the USSR a process based on carbolyles has been developed which achieves the lanthanide / actinide separation in a single extraction process [17]. A comparative "hot" test of the newly proposed partitioning scheme should be made on a lab scale as outlined under [16] for TRPO.

## Conclusion

The recycling of long-lived radionuclides in existing nuclear power stations and the development of high-thermal-flux reactors offers the possibility of transmuting such nuclides into short-lived or stable elements. When compared to more advanced transmutation procedures such as those employing a minor actinide burner [18] or neutron spallation sources [19, 20], one finds that system-immanent recycling would require less research and development effort. The needs for partitioning are unchanged.

### References


[1] R. De Meester, L. Koch, R. Wellum, I. Broeders, L. Schmidt, Proceedings of the International Conference on Nuclear Data for Basic and Applied Science, Santa Fe, USA, May 13 - 17 (1985)

[2] L. Koch, J. Less-Common Metals, 122 (1986) 371

[3] W. Balz, L. Koch, W. Löhr, U.K. Wehmann, International Fast Reactor Safety Meeting, Snowbird, Utah, USA, August 12 - 16 (1990)

[4] Proceedings of the Workshop on Partitioning and Transmutation of Minor Actinides, Institute for Transuranium Elements, Karlsruhe, FRG, 16 to 18 October 1989, EUR 13347 (1991) Eds: L. Koch, R. Wellum

[5] L. Koch, C. Apostolidis, K. Mayer, G. Nicolaou, R. Wellum, Proceedings of the Nuclear and Hazardous Waste Management International Topical Meeting, Knoxville, USA, September 30 - October 4 (1990)

[6] U. Fischer, Jahrestagung Kerntechnik '85 (1985) p. 19

[7] L. Koch, Proceedings of the 5th International Conference on Emerging Nuclear Energy Systems, ICENES, Karlsruhe, FRG, June 3 - 6 (1989)

[8] Institute for Transuranium Elements Program Progress Report 1982, TUSR 34, p. 52, Karlsruhe, FRG (EUR 10251 E)

[9] S. Pilate, R. de Wouters, G. Evrard, H.W. Wiese, U. Wehmann, PHYSOR Conference, Marseille, France, April 23 - 27 (1990)

[10] T. Inoue, 'Transmutation of Transuranium Elements by a Metallic Fuel FBR', ibid.

[11] C. Sari, E. Zamorani, J. Nucl. Mat., 37 (1970) 324

[12] K. Richter, C. Sari, J. Nucl. Mat., 148 (1987) 266

[13] W. Bartscher, C. Sari, J. Nucl. Mat., 118 (1983) 220

[14] H.E. Schmidt et al., J. Less-Common Metals, 121 (1986) 621

[15] C. Apostolidis, Proceedings of the Workshop on Partitioning and Transmutation of Minor Actinides, Institute for Transuranium Elements, Karlsruhe, FRG, 16 to 18 October 1989, EUR 13347 (1991)

[16] C. Apostolidis, R. de Meester, L. Koch, R. Molinet, J. Liang, Y. Zhu, Seminar on New Separations Chemistry Techniques for Radioactive Waste and other Specific Applications, Rome, Italy, May 16 - 18 (1990)

[17] M.A. Afonin, V.V. Korolev, V.N. Romanovski, V.V. Romanovski, V.M. Sedov, Proceedings of the Nuclear and Hazardous Wastes Management Topical Meeting, Knoxville, USA, September 30 - October 4 (1990)

[18] T. Mukaiyama, H. Takano, T. Takizuka, T. Ogawa, Y. Gunigi, S. Okajima, Proceedings of the Workshop on Partitioning and Transmutation of Minor Actinides, Institute for Transuranium Elements, Karlsruhe, FRG, 16 to 18 October 1989, EUR 13347 (1991)

[19] T. Nishida et al., ibid.

[20] R. Rief, ibid.


# Investigation of the (U, Np)-N and (U, Am)-O Systems

Two types of candidate fuels are presently being investigated in the frame of the research on the transmutation of actinides: uranium-neptunium mixed mononitrides and uranium-americium mixed oxides.

## Nitride fuel

$(U_{1-x}Np_x)N$, $0<x<1$, was prepared by carbothermic reduction of the oxide in a flow of nitrogen. In order to achieve low oxygen contamination, an excess of carbon was required, necessitating a subsequent decarburization process in a flow of nitrogen / hydrogen (92% $N_2$, 8% $H_2$). The examination of the final nitrides by X-ray diffraction showed a fcc single phase with high purity and a subsequent low carbon content (ca. 400 ppm).
The kinetics of the two steps of the fabrication were investigated by thermogravimetry. The carbothermic reduction stage obeyed the first order rate equation, except at the very beginning of the reaction. The activation energies varied from 344 to 385 ± 26 kJ/mol. In the incubation period, the reaction followed the interface-controlled equation [1], with an activation energy of 305 to 310 kJ/mol. The decarburization reaction also appeared to obey the interface-controlled equation with an activation energy of 210 ± 16 kJ/mol.
This work was done in collaboration with a visiting scientist from JAERI, Japan.

## Oxide fuel

Three oxides have to be prepared for phase diagram studies: $(U_{0.5}Am_{0.5})O_2$, $(U_{0.8},Am_{0.2})O_2$ and $(U_{0.95},Am_{0.05})O_2$. Preliminary fabrication tests have been started using two different techniques:

arc melting and sintering in a tungsten crucible. For the sintering of $UO_2$ in a tungsten crucible, the best temperature was determined to be 1800 °C.
This work was done in collaboration with a visiting scientist from PCN, Japan.

**Reference**

[1] S.K. Mukerjee, J. V. Dehadraya, V. N. Vaidya and D. D. Sood, J. Nucl. Mater. 172 (1990) 37

# Actinide Separation by High Pressure Cation Exchange - The Neptunium Case.

Chromatographic columns have been utilised in the Institute for several years as a means of separation in the continual efforts to recover actinides from various types of irradiated nuclear fuels and/or waste solutions.

A previously described separation scheme for the actinides, utilising chromatographic columns loaded with TBP and cation exchange resin under pressure (HPLC) as means of separation, [1, 2, 3, 4] has been further investigated.

More than 99 % of the neptunium can be washed out in pure form from the first of the two cation exchangers as the monovalent ion $NpO_2^+$, which is scarcely retained by the resin from weak nitric acid. The strong influence of the strength of the nitric acid on this separation step has been demonstrated.

Subsequently, americium, curium and the lanthanides are eluted individually from the second HPLC column by alpha- hydroxyisobutyric acid.

In the reporting period emphasis has been placed on the behaviour of neptunium, [5]. The separation scheme has also been tested with genuine highly active waste (HAW). As raffinate from the first extraction cycle of the Purex process, such solutions often contain high amounts of neptunium.

In the first pair of columns, TBP impregnated on polystyrene beads is used to extract uranium, plutonium and nitric acid, thus separating the two elements from the rest of the actinides, notably neptunium, americium and curium, and from the fission products.

At low acidities, i.e up to about 2 M $HNO_3$, Np(V) is the most stable oxidation state of neptunium. At higher acidities a disproportionation to Np(IV) and Np(VI) takes place, i.e.:

$$2\,NpO_2 + 4\,H^+ = NpO_2^{2+} + Np^{4+} + 2\,H_2O$$

The tetravalent Np is being stabilized by the formation of the octahedral $Np(NO_3)_6^{2-}$ complex and furthermore the hexavalent Np is stabilized by the oxidizing action of the strong nitric acid.

The absorption spectrum of Np(V) taken with a Cary-17D spectrophotometer is shown in Fig. 3.2 as a function of the nitric acid molarity (between 0.2 M and 8 M). The absorption maximum at 980 nm clearly decreases at the stronger acidities; smaller peaks, assignable to Np(IV), increase in height under the influence of strong acid, according to the above equation, see curve 6, Fig. 3.2.

In up to 2 M nitric acid all of the Np is present as Np(V) (curve 1 of Fig. 3.2) without any addition of redox chemicals. At the higher acidities stabilizing agents such as Fe(II) or Ce(IV) must be added to keep neptunium in the pentavalent state.

Prior to the separation, the neptunium is adjusted to the non-extractable pentavalent oxidation state and is thus washed through the TBP columns and into the cation exchange columns at the low acidity prevailing at the outlet of the second TBP column.The two ions $NpO_2^+$ and $Cs^+$ are eluted from the HPLC column very close to each other [4].

The elution pattern of Np(V) as a function of the strength of nitric acid was studied in more detail. The first HPLC-column, (HPLC-I) might be used not only for pre-concentration, but also for separation. The range 0.1 to 1.2 M $HNO_3$ was investigated with mixtures of Np, Cs and Am; during the collection on HPLC-I the outlet of the column was monitored and a material balance was made.

Fig. 3.3a shows that of the above mentioned nuclides only trivalent Am was retained on the HPLC-I column over the whole acidity range. At low acidities $Cs^+$ also stays on the column; this ion leaks out at about 0.7 M $HNO_3$, so that below a molarity of 0.7 $HNO_3$ only $NpO_2^+$ leaves the HPLC-I column.

In the upper part of Fig. 3.3b the contents of the fractions collected from the HPLC-II column upon

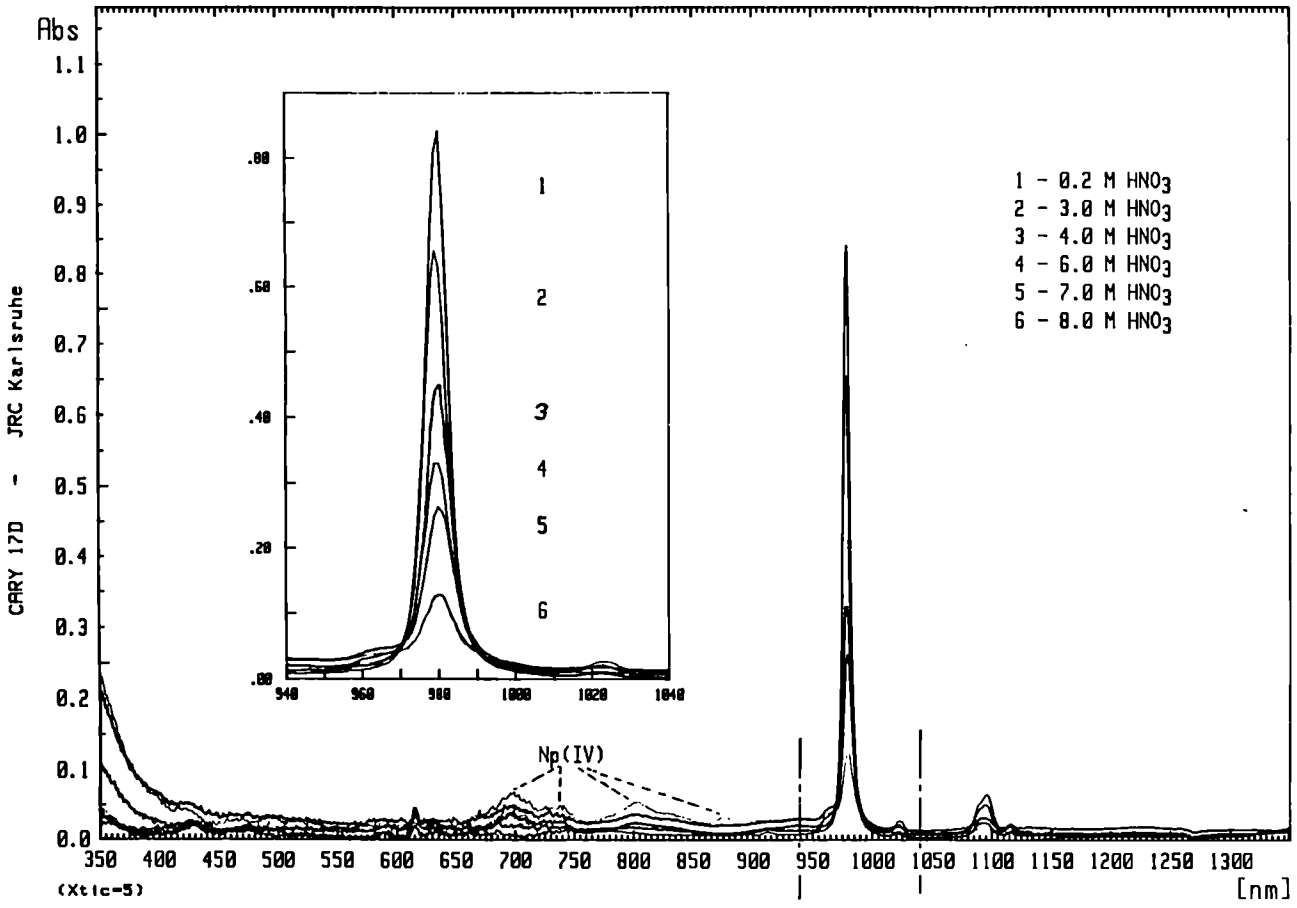


*'ig. 3.2 Absorption spectra of Np(V) in the wavelength range 350-1250 nm as a function of the nitric acid molarity from 0.2M to 8.0M*

the subsequent elution with alpha-hydroxyisobutyric acid are shown. All of the Am (100 %) and only 1 % of the Np(V) are found in the chromatogram. Moreover, the Am is eluted relatively late, whereas the Np(V) is observed at an very early stage of the elution process. The Np fraction contains only about 1 % of the fission product Cs, which follows immediately after the neptunium in the chromatogram.

Up to 99 % of the Np can thus be isolated and collected as the monovalent ion $NpO_2^+$ from the first cation exchange column, provided the acidity of the solution is carefully controlled.

Furthermore, any Np(VI), Np(IV) or Pu(IV) accidentally breaking through the TBP columns would be caught on the cation exchangers, from where these species can be eluted individually.

**References**


[1] J.-P. Glatz, H. Bokelund, S. Valkiers, 'Separation of Fission Products, Nitric Acid and Actinides by Extraction Chromatography with TBP-Polystyrene' ,Inorg. Chim. Acta **94** (1983) 129

[2] J.-P. Glatz, H. Bokelund, M. Ougier, 'Development of a Multipurpose Unit for the Separation of Actinides', J. Less-Common Metals **122** (1986) 419

[3] C. Apostolidis, H. Bokelund, M. Ougier, A. Moens, 'Redox Behaviour of Neptunium in the presence of U, Pu, and Am, Applied in their Separation by TBP and Ion Exchange (HPLC)', Inorg. Chim. Acta **140** (1987) 253

[4] H. Bokelund, C. Apostolidis, J.-P. Glatz, 'Recovery and Chemical Purification of Actinides at JRC, Karlsruhe. J. Nucl. Mat. **166** (1989) 181

[5] C. Apostolidis, H. Bokelund, J.-P. Glatz, Seminar on Separation Chemistry Techniques for Radioactive Waste and Other Specific Applications, Rome, May 1990. Proceedings in Press.

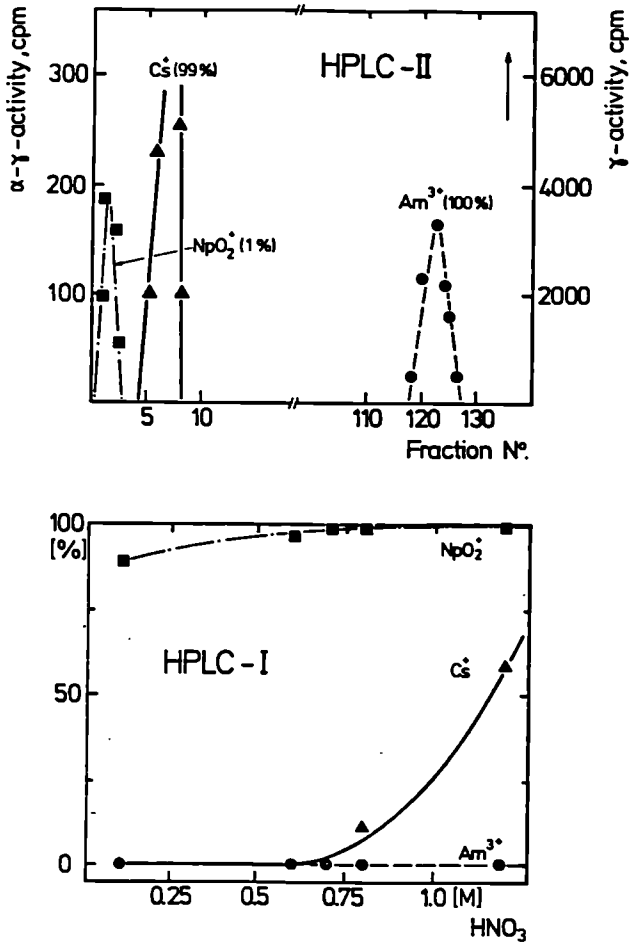


*Fig. 3.3* *a) The breakthrough of $NpO_2^+$ and $Cs^+$ ions from the first cation exchanger as a function of the nitric acid molarity. Americium remains fixed on the column*

*b) Elution pattern from the second exchange column. The various fractions containing the $NpO_2^+$ (1%), $Cs^+$ (99%), and $Am^{3+}$ (100%) are shown*

## Recovery of Minor Actinides from Scrap Materials

Various mixtures of minor actinides (mainly Np and Am) in different degrees of purity are avaiable in the Institute, mainly as solutions in nitric acid. These are the remains of preparations done in the past.

The purification and recovery of these materials was started. About 20 g of Np have been purified by ammonia precipitation followed by redissolution in weak nitric acid and adjustment of the valency state of Np to Np(V) by hydrogen peroxide. The solutions were then passed through a cation exchanger onto which the impurities, mainly iron (at the 3000 ppm level) were absorbed, whereas the Np was collected at the outlet of the column.

For the recovery of actinides from mixtures a set of chromatographic columns has been set up. Uranium and plutonium will be recovered by TBP impregnated on polystyrene beads, the minor actinides, Np, Am, and Cm by cation exchange using alpha- hydroxyisobutyric acid as eluent. The latter columns operate under high pressure (HPLC). This technique, which has been applied previously for the reprocessing of advanced nuclear fuels [1,2], has now been set up for operation in a glovebox behind walls containing water for neutron shielding. The samples in question contain practically no fission products and the amounts of uranium and plutonium are rather low, compared to the case of treating irradiated fuels. The capacity of the elution pump is about 2 l/h. The actinides will be collected individually, precipitated as oxalates and calcined for storage as the oxides.
A further task in this field is the recovery of about 700 mg $^{244}Cm$ from glass. Several glass samples containing percent amounts of $^{244}Cm$ have been prepared for use in accelerated tests on the stability of glasses for the disposal of high level waste. The glass is dissolved in 40 % hydrofluoric acid over one week at room temperature. The Cm is separated from the bulk of the glass constituents by filtration as $CmF_3$, calcined at 400 °C for removal of most of the fluorides, dissolved as $Cm^{3+}$ in nitric acid and passed through the HPLC columns for purification.
Tests were carried out on simulated glasses of types SON 68 and GP 98 , The actual recovery will start when the Cm glasses become available in the beginning of 1991.

**References**

[1] J.-P. Glatz, H. Bokelund, M. Ougier, J. Less Comm. Met. 122 (1986) 419

[2] H. Bokelund, C. Apostolidis, J.-P. Glatz, J. Nucl. Mat. 166 (1989) 181

# Absorption Spectroscopy of Solutions of Curium and Plutonium

For plutonium the tetravalent oxidation state is known to be the most stable under normal conditions. Hexavalent plutonium transforms itself into the tetravalent state by autoreduction; by addition of $H_2O_2$ the transformation is very fast (TUAR **87**, 229).

During a separation of $^{240}Pu$ from the mother nuclide, $^{244}Cm$, some problems arose: not all of the plutonium could be fixed on the ion exchanger used, Dowex 1x4, 50-100, but a part percolated through the column and thus remained with the Cm. The suspicion that the oxidation state was not correct for the separation was confirmed as follows: a small amount of $CmO_2$ (contaminated with about 10% Am) was dissolved in 3M $HNO_3$ and absorption spectra taken. The main part of the plutonium was found to be present as hexavalent Pu (Fig. 3.4). The addition of $H_2O_2$ did not have any effect whereas hydrazine converted the greater part of the plutonium to Pu IV within 3 hours (Fig. 3.5).
After 4 days, hexavalent Pu was again formed in the solution containing the Cm. Probably radiolysis from $^{244}Cm$, $^{240}Pu$, and $^{241}Am$ was responsible for this behaviour.

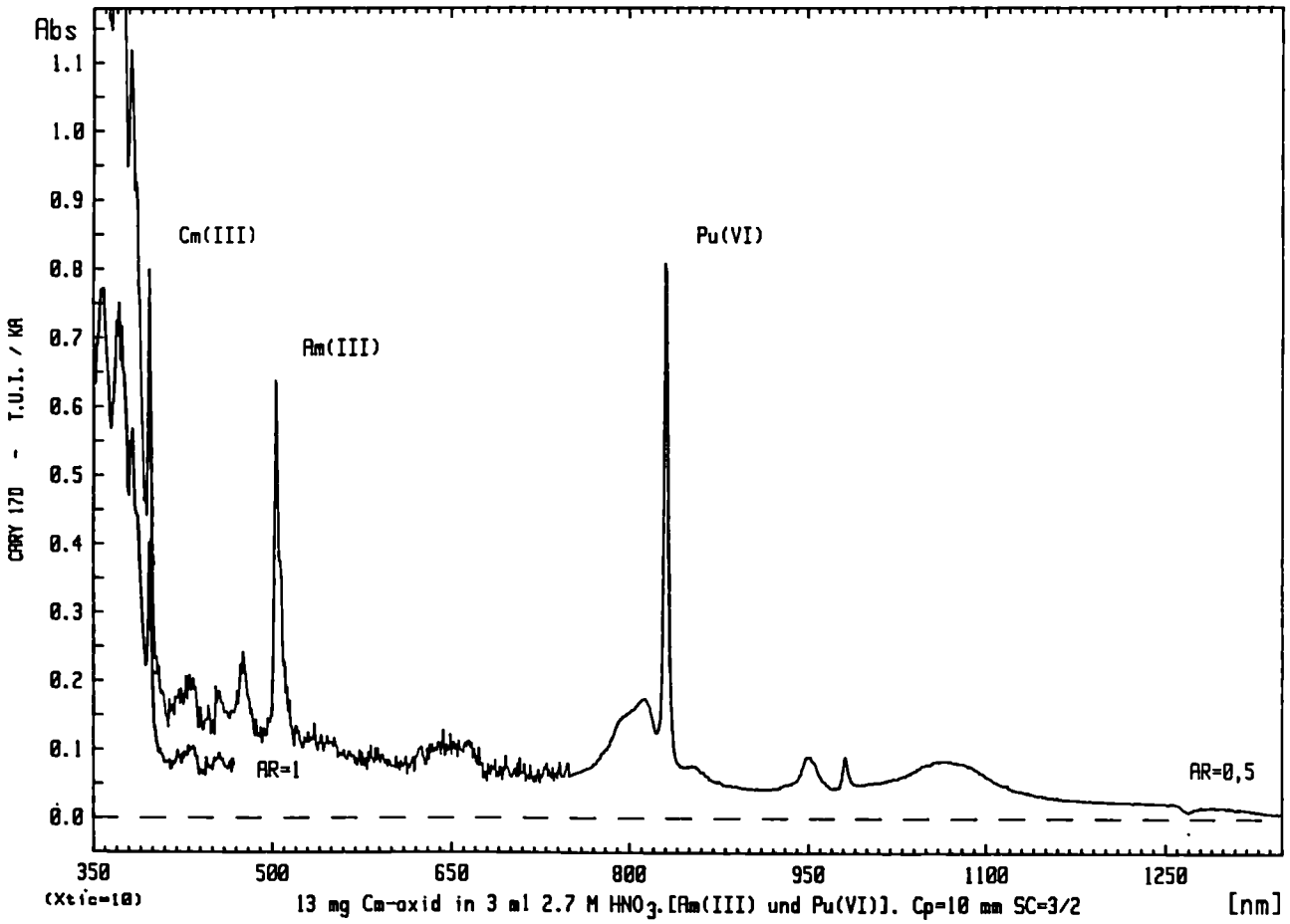


*Fig. 3.4* *Absorption spectrum of $CmO_2$ contaminated with 10 % Am*

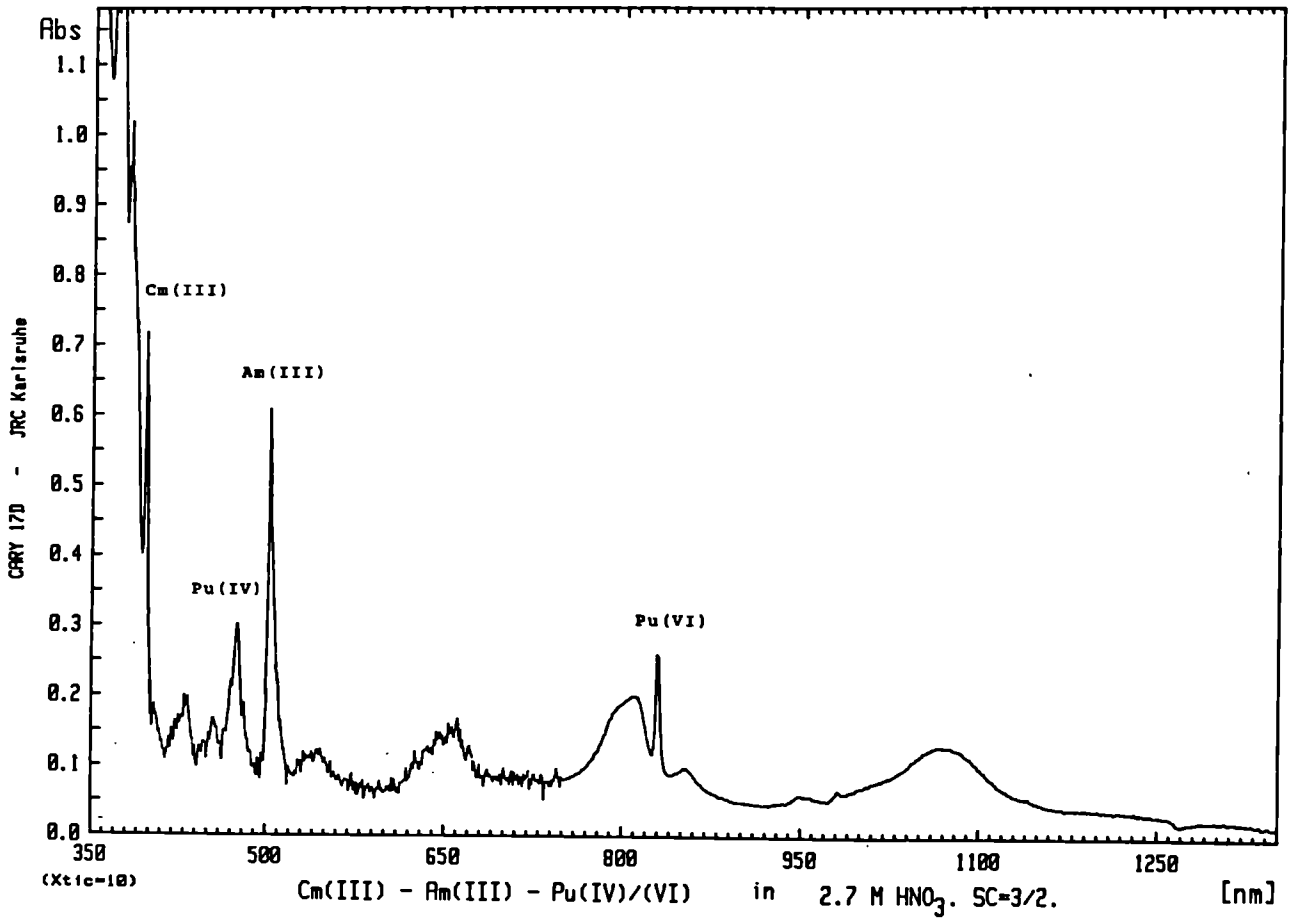


*Fig. 3.5 Absorption spectrum of Cm/Am oxide after treatment with hydrazine*

# The Extraction of Actinides and Other Constituents from HAW by Trialkyl Phosphine Oxide (TRPO)

## Introduction

The removal of actinides, including the major actinides U, Pu and especially the minor actinides Am, Cm and Np from highly radioactive waste (HAW) would reduce the radiological hazard of the HAW. Over the past decade, several organic extractants have been studied for this purpose. In the USA, the application of bifunctional carbamoyl methyl phosphonates and phosphine oxides has received much attention and research efforts have concentrated recently on the development of the TRUEX process [1,2,3] in which octyl(phenyl)-N, N'-diisobutyl carbamoyl methyl phosphine oxide (CMPO) in tributyl phosphate (TBP) and paraffinic diluent is used as extractant. Diisodecyl phosphoric acid (DIDPA) which can extract trivalent actinides at pH = 0.5 has been suggested and tested by Japanese scientists [4, 5].

A mixed trialkyl phosphine oxide (TRPO) has been found to have good extraction behavior for actinides in the People's Republic of China [6, 7]. TRPO, an industrial solvent for uranium extraction, is noticeable for its good solvent behaviour, high radiolytic stability and low cost. Two visiting scientists from Tsinghua University, Beijing, PR China contributed significantly to this study.

The results of trial extractions leading to an extraction of real HAW are reported here.

## The distribution of actinides and fission products from simulated HAW using 30% TRPO in Dodecane and 0.2M CMPO - 1.4M TBP in Conoco.

The extraction of the trivalent actinides Am and Cm varies with acidity (Fig. 3.6). The distribution ratios reach a maximum value of about 10 in ca. 0.5 M $HNO_3$ in the aqueous phase and decrease with increased acidity. For an aqueous phase with a nitric acid concentration of about 4 M, D = 0.1. Thus, low acidity can be used for extraction and high acidity for stripping. For CMPO, the extraction increases with increasing acidity, but the regularity of the experimental data is not good owing to third phase formation even at a high O/A phase ratio.

The extraction of the major actinides U and Pu is very effective (Fig. 3.6). Distribution ratios were obtained by measuring the concentration of U and Pu in the aqueous phase before and after extraction with TRPO. The concentrations in the organic phase were calculated by difference because the stripping of U and Pu from the organic phase for analysis was not successful.

The distribution ratio of Np is also high (Tab. 3.6). Np was at first reduced to the tetravalent state, extracted into the organic solvent and then added to the extraction flask. This was done because the Np stock solution contained a large amount of sulfate ion and could not be added directly into the simulated HAW. The results show that Np(IV) can be extracted effectively and is stable during the extraction if $NH_2OH$ is present in the aqueous phase.

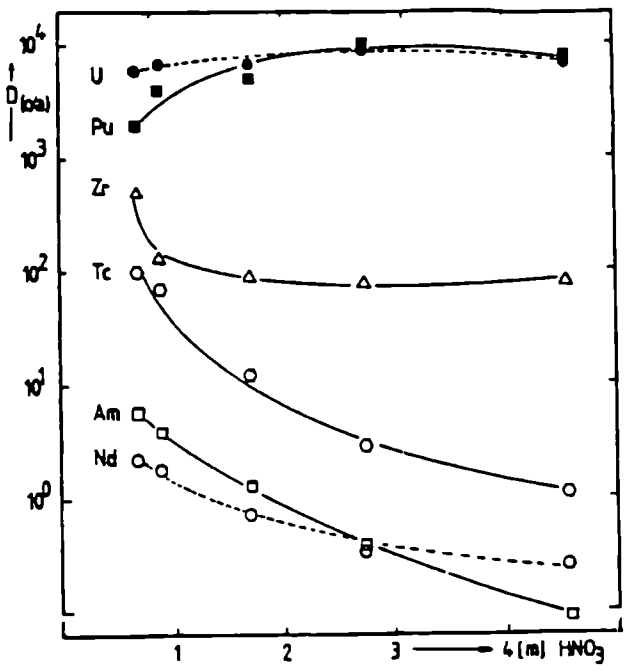


*Fig. 3.6* *Extraction of actinides and fission products by TRPO from simulated HAW*

The behavior of fission products and corrosion products is shown in Tab.3.7. The fission-product rare earths behave similarly to Am and Cm. The extraction of Zr, Tc and Mo is high. In the case of TRPO extraction, the distribution ratio of Zr is on the order of magnitude of $10^2$ and shows a tendency to slowly decrease with increasing acidity (Fig. 3.6). Technetium is strongly extracted in the low acidity region and its distribution ratio decreases quite rapidly with increasing acidity (Fig. 3.6).

*Tab. 3.6* *Extraction of Nd by TRPO and CMPO*

| Sample no. | C aq. µg/ml | C org. µg/ml | phase ratio | D o/a = C org./C aq. | D' (o/a) * |
|---|---|---|---|---|---|
| TRPO 2 | --- | 135.4 | 1:1 | --- | --- |
| TRPO 3 | 1.10 | 187.6 | 1:1 | $1.7 \times 10^2$ | $1.0 \times 10^3$ |
| TRPO 5 | 0.58 | --- | 1:1 | --- | $1.7 \times 10^3$ |
| TRPO 7 | 0.54 | 114.2 | 1:1 | $2.1 \times 10^2$ | $1.9 \times 10^3$ |
| TRPO 9 | 0.30 | 91.1 | 1:1 | $3.0 \times 10^2$ | $3.3 \times 10^3$ |
| CMPO C5 | 0.15 | 34.1 | 4:1 | $2.3 \times 10^2$ | $1.7 \times 10^3$ |

* $D'(o/a) = (C\ aq.\ original - C\ aq.) / (C\ aq.\ phase\ ratio\ (o/a))$
$C\ aq.\ original = 1.0 \times 10^3$ µg/ml

*Tab. 3.7 Distribution of the fission products and corrosion products in the extraction of simulated HAW*

| element | C aq before extraction | TRPO 2 | | TRPO 3 | | TRPO 5 | | TRPO 7 | | TRPO 9 | | CMPO 5 | |
|---|---|---|---|---|---|---|---|---|---|---|---|---|---|
| | | C aq. | C org. | C aq. | C org. | C aq. | C org. | C aq. | C org. | C aq. | C org. | C aq. | C org. |
| Fe | 2000 | 2500 | 113 | 2400 | 140 | 2100 | 160 | 2800 | 202 | 2300 | 394 | 2000 | 72 |
| Cr | 460 | 750 | < 0 1 | 700 | < 0.07 | 640 | 0.4 | 770 | 0.31 | 820 | 0.31 | 900 | < 0.2 |
| Ni | 350 | 300 | < 6 | 370 | < 3.9 | 300 | 24 | 320 | < 3.9 | 380 | < 3 1 | 370 | < 10 |
| Mo | 660 | 40 | 1180 | 40 (16.75) | 1605 | 140 (545) | 1100 | 130 (36.75) | 1260 | 200 (58.75) | 938 | 100 (32.5) | 386 |
| Te | 870 | < 2000 | < 100 | --- | < 62 | < 2000 | < 57 | --- | < 63 | < 2000 | < 60 | < 2000 | < 160 |
| Tc | 1490 | 20 | 2116 | 50 | 3550 | 130 | 1638 | 600 | 1780 | 1000 | 1144 | 30 | 600 |
| Ba | 2900 | 2900 | 67.5 | 2800 (1798) | 38.8 | 3100 (4845) | 30 | 3700 (1790) | 23.6 | 2600 (1178) | 23 | 3700 (1373) | 18 |
| Sr | 1500 | > 1000 | < 1 | > 1000 (1335) | < 0.8 | > 1000 (1387) | 0.7 | > 1000 (1325) | < 0.8 | > 1000 (1253) | < 0.8 | > 1000 (2258) | 2 |
| Zr | 600 | < 2 | 1040 | < 8 (12.75) | 1081 | < 2 (12.5) | 182.3 | 7 (11.5) | 547.5 | 8 (11.25) | 642 | 10 (15.75) | 238 |
| Ru | 3400 | 2700 | 236 | 2200 | 118.6 | 2500 | 125.4 | 2900 | 121.3 | 2900 | 78 | 1500 | 318 |
| Rh | 820 | 1000 | 283 | 800 | 8.5 | 600 | 15 | 900 | 3.9 | 900 | < 2 | 800 | < 4 |
| Pd | 1900 | 1000 | 476 | 900 (647.5) | 252.7 | 1200 (882.5) | 282.8 | 1800 (1150) | 293 | 2500 (1395) | 20.6 | 1360 (377.5) | 8 |
| Ag | 86 | < 10 | 11.3 | < 10 | 10 | 10 | 12.1 | < 10 | 6.3 | < 10 | < 0.8 | < 10 | < 2 |
| Cd | 90 | < 200 | < 3 | < 200 | < 1.6 | < 200 | < 1.5 | < 200 | < 1.6 | < 200 | 6.9 | < 200 | < 4 |
| Y | 710 | 100 | 1156 | 200 | 985 | 250 | 778 | 600 | 581 | 900 | 219 | 200 | 234 |
| La | 2100 | 1200 | 1750 | 1360 (1140) | 1162 | 1600 (1598) | 513 | 2310 (1753) | 131 | 2600 (1798) | 27.5 | 100 (62 5) | 490 |
| Ce | 4600 | 1200 | 3250 | 1700 (1385) | 2970 | 2600 (2565) | 2001 | 5200 (3375) | 1850 | 6100 (3675) | 198 | < 200 (85) | 1180 |
| Pr | 2000 | --- | --- | (460) | --- | (957.5) | --- | (1435) | --- | (1653) | --- | (32.5) | --- |
| Nd | 6200 | 1100 | 2500 | 1200 (1245) | 2217 | 2400 (2705) | 1781 | 4300 (4253) | 1417 | 5500 (5248) | 1373 | 200 (115) | 620 |
| Sm | 1400 | --- | --- | (172.5) | --- | (415) | --- | (742.5) | --- | (1008) | --- | (25) | --- |
| Eu | 300 | 30 | 466 | 38 | 450 | 100 | 356 | 292 | 216.5 | 400 | 58 | < 10 | 92 |
| Gd | 160 | < 10 | 210 | < 10 | 188 | 30 | 177 | 120 | 132.3 | 140 | 32.8 | < 10 | 58 |

Mo shows distribution ratios of around 10. Generally, it seems that the extraction of Zr, Tc and Mo by TRPO is higher than by CMPO. The fission products Pd and Ag are moderately extractable. The corrosion product Fe is extracted to a certain extent. Other HAW constituents are either slightly or very slightly extractable.

## Hot test using HAW

A test was carried out in a hot cell of the extraction with TRPO after denitrification of the HAW with formic acid.

Almost all the U and Cm existed in the HAW solution both before and after denitration. The data on Am were doubtful because of interference in the gamma-spectroscopic determination. A certain amount of Pu (30%) existed in the precipitate and no change could be seen after denitration. The amount of Pu in HAW after denitration decreased appreciably however filtering the denitrated HAW through a Minisart N filter might be the main cause of Pu loss.

According to the material balance between extraction raffinate and strip solutions, in TRPO extraction more than 93% of Am and Cm was extracted in a single stage by extraction with TRPO, even with a feed solution containing 0.02 M $H_2C_2O_4$. The amount of Am and Cm extracted by CMPO in a single stage was about 85%.

In the extraction with TRPO, Pu was selectively stripped out in strip 2 and U was selectively stripped out in strip 3 and no serious cross-interferences occurred. But in CMPO extraction Pu and U were distributed among strips 1, 2 and 3.

The results from the preliminary hot extraction test were only approximate. It was found difficult to separate the two phases clearly in hot-cell operations and a volume change of the test solutions was unavoidable. Nevertheless, the preliminary hot test has proven the feasibility and advantages of the TRPO extraction process. A generic TRPO extraction flowsheet is shown in Fig. 3.7.

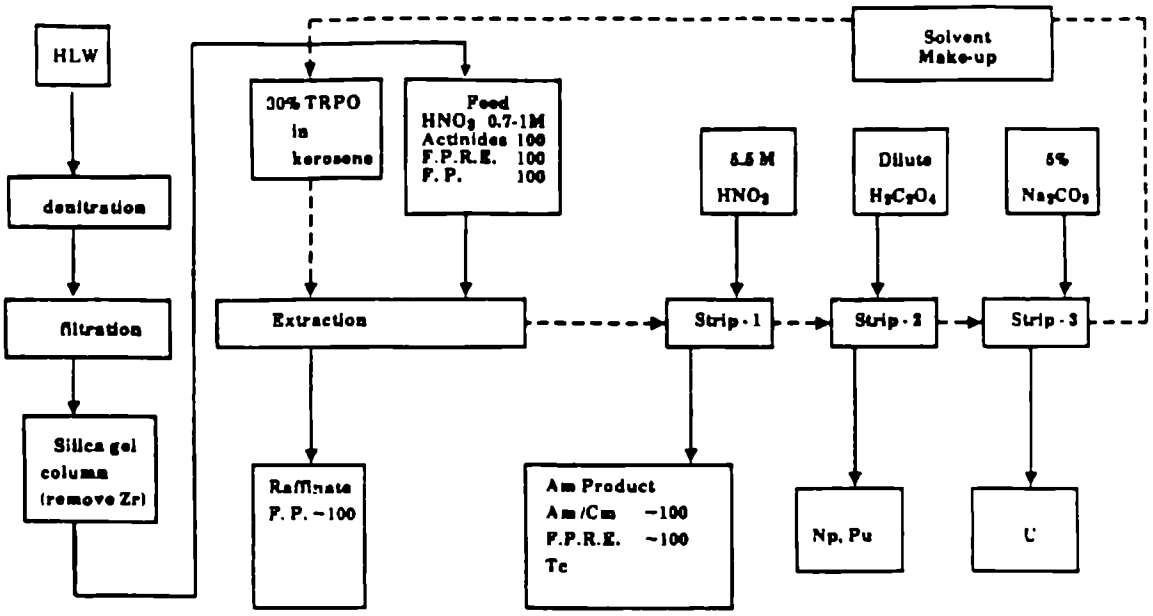


*Fig. 3.7* *Flowsheet of the TRPO extraction process*

## Loading capacity measurement

The capability of the extractants TRPO and CMPO/TBP to extract trivalent ions as a function of $HNO_3$ concentration was investigated using Nd. The maximum Nd(III) loadings, at which no second organic phase is formed, in TRPO and CMPO solvent are shown in Fig. 3.8. The loading capacity of 30 vol% TRPO in dodecane and Conoco are close but show some differences. The loading capacities are high at the low acidity region, with a value of about 0.2 and 0.1 M at aqueous nitric acid concentrations of 0.3 and 2 M respectively. Loading capacities decrease quickly with increasing aqueous phase nitric acid concentration, due to the loading of $HNO_3$ in the organic phase. The measured Nd(III) loading capacity of 0.2 M CMPO-1.4 M TBP-Conoco is in accord with previous measurements [8]. In the low acidity region, the loading capacity of the CMPO solvent is much lower than that of the TRPO solvent. The loading capacity of the CMPO solvent changes only a little over a wide acidity range, because nitric acid is mainly extracted by the TBP.

Under the conditions of extraction ($HNO_3$ concentration after equilibrium = 1 M), the Nd(III) loading capacity of TRPO solvent is considerably higher than that of CMPO.

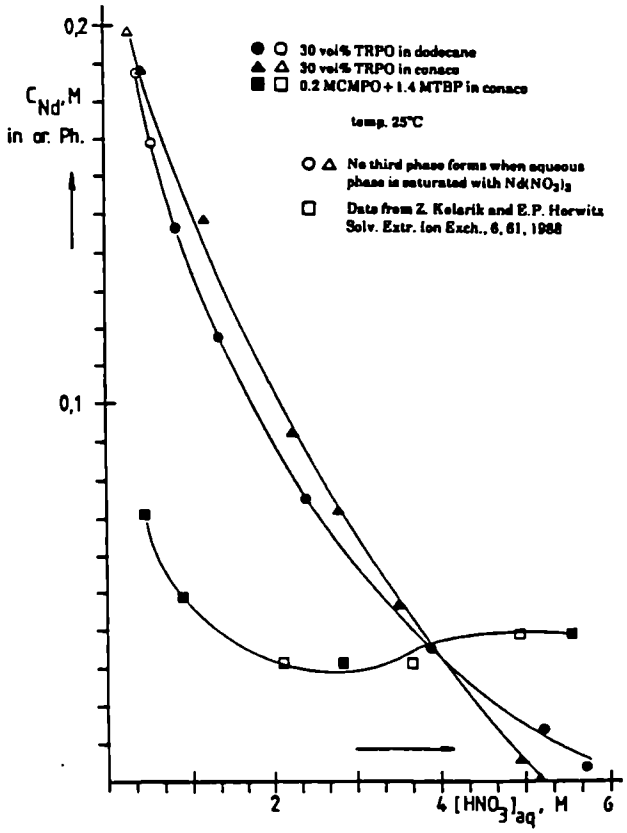


*Fig. 3.8* *Comparison of the loading capacity in the organic phase between TRPO and CMPO/TBP*

## Conclusions

TRPO is effective in the extraction of the major and minor actinides and it lends itself well to an extraction flowsheet as shown by the preliminary hot test. Comparisons with CMPO have demonstrated the suitability of TRPO for the removal of actinides from waste.

### References


[1] G.F. Vandegrift, R.A. Leonard, M.J. Steindler, E.P. Horwitz, L.J. Basile, H. Diamond, D.G. Galina, L. Kaplan, ANL 84-45 (1984)

[2] E.P. Horwitz, D.G. Kalina, H. Diamond, L. Kaplan, G.F. Vandegrift, R.A. Leonard, M.J. Steindler, W.W. Schulz, "Actinide/Lanthanide Separations", G.R. Choppin, J.P. Navratil, W.W. Schulz eds., World Scientific Publication 43 (1985)

[3] E.P. Horwitz, D.G. Kalina, H. Diamond, G.F. Vandegrift, W.W. Schulz, Solvent Extr. Ion Exch. 3 (1985) 75

[4] M. Kubota, H. Nakamura, S. Tachimori, T. Abe, H. Amano, IAEA-SM-246/24 (1981)

[5] M. Kubota, I. Yamaguchi, K. Okada, Y. Morita, K. Nakano, H. Nakamura, Mat. Res. Soc., Symposium Proc. 26 (1984) 551

[6] Y. Zhu, R. Jiao, S. Wang, S. Fan, B. Liu, H. Zheng, S. Zhou, S. Chen, Chinese J. Nucl. Radiochem. 7 (1985) 65

[7] R. Jiao, S. Wang, S. Fan, B. Liu, Y. Zhu, H. Zheng, S. Zhou, S. Chen, Chinese J. Nucl. Radiochem. 1 (1985) 65

[8] Z. Kolarik, P. Horwitz, Solvent Extr. Ion Exch. 6 (1988) 61

# 1.4 Characterization of Waste Forms and High Burn-up Fuel

## Introduction

The studies on radioactive wastes carried out at the Institute for Transuranium Elements are centered on the characterization of the waste forms (mainly non-processed spent fuels and vitrified high level wastes), with respect to properties relevant to their behaviour under conditions of long term storage.

Properties to be investigated include, thermal conductivity, thermal and mechanical stability, redistribution of actinides and fission products within the waste materials, radiation damage, resistance to corrosive agents and investigation of the leaching behaviour with various leachant compositions as well as the radioactive nuclide inventory.

Firstly, a hot cell with techniques for non-destructive examinations, conditioning of LWR fuel rods for reprocessing or storage (He-filling, TiG welding, He-leak test) had to be refurbished. Furthermore, specific results on spent fuels and active glasses were obtained. The state of progress of the different studies and their results are summarized below.

## Spent Fuel Characterization and Related Studies

### Radiation damage effects in waste glasses

The experiments on Cm-doped waste glasses to produce realistic radiation damage were terminated. In this study, waste glasses (the French glass SON 68.18.17 L1C2AZ1, the German glass GP 98/12 and the US glass MCC 76-68) had been doped with 0.5 and 1.5 wt.% of $^{244}Cm$. Volume changes, crack behavior and fracture toughness as well as leach rates were measured. The results were reported at the 3rd EC Conference on Radioactive Waste Management and Disposal, Luxembourg, September 1990 as part of the EC-work in this field [1].

They can be briefly summarized as follows:

- **Fracture behaviour:** the fracture behaviour was tested by applying indentation techniques, (see Proceedings of a workshop, published in the reporting period [2]). Spherical indentors (Hertzian indentation) and sharp indentors (Vickers indentation) were used. Nucleation (crack probability) and the length of cracks emanating from the corners of the Vickers indentations were measured to deduce radiation damage effects on the fracture toughness $K_{Ic}$. Fig. 4.1 shows the variations in mechanical properties as a function of the integrated α-dose for SON 68 waste glass. Similar results were obtained for the other two types of glass. For all of them, a positive feature of radiation damage is that the crack lengths and crack probabilities during Vick-

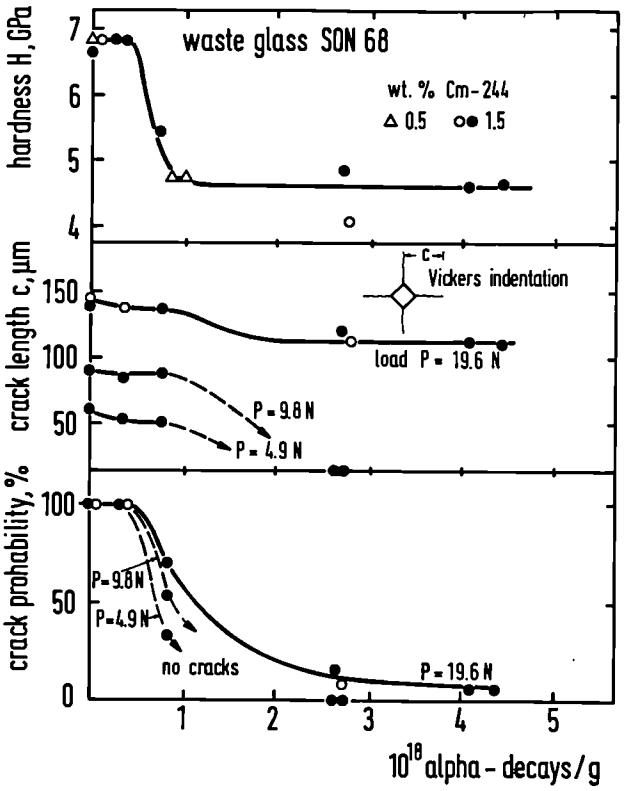


*Fig. 4.1* *Hardness H, crack length c and crack probabilities (in %) of SON 68 waste glass as a function of α-dose*

ers indentations significantly decreased with increasing doses. The fracture toughness, $K_{Ic}$, deduced from the crack lengths, increased by more than 100 %. The hardness dropped by more than 30 % between 5 x $10^{17}$ and 1.5 x $10^{18}$ α-decays/g and then stabilized at higher doses [3]. The net result of these two phenomena is reduced brittleness that enhances the resistance again crack propagation in the glass.

- **Density:** The results of the density measurements for SON 68 glasses are plotted against

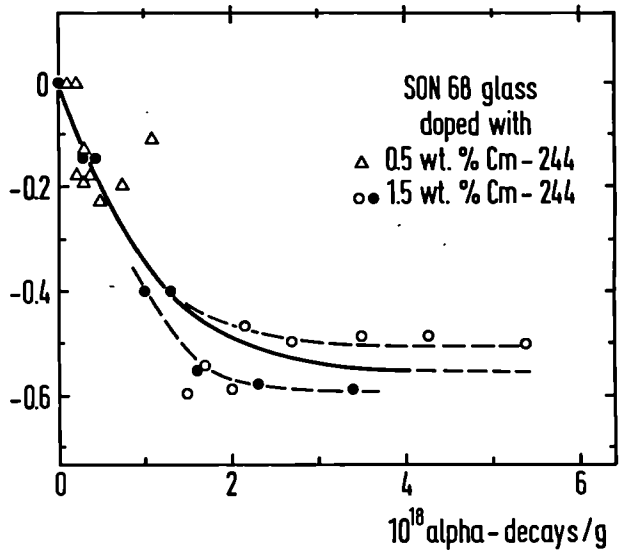


*Fig. 4.2* *Density changes of SON 68 waste glass as a function of α-dose*

α-dose in Fig. 4.2. Such results are usually fitted to an equation of the type

$$\Delta\rho = A(1-\exp\{-BD\})$$

where Δρ is the change in density (%) at dose D (α-decays/g). A is then the change in density at the saturation dose and B is the fraction of the glass totally damaged by each α-decay. The values obtained for SON 68 waste glass were A = 0.55 ± 0.05 % and B = (0.095 ± 0.005) x $10^{-17}$ g. This shows that the density decrease (swelling) of the Cm-doped SON glasses saturates after 0.55 % change at a (simulated) storage time of ~ 100 000 years. Similar small values of A were obtained for the other two glass types. The scatter in the data and the observation that the same SON glass contracted (i.e. the density increased) when during the fabrication step some 2 % porosity remained in the glass, shows that the volume changes can vary for different production campaigns. The important feature is, however, that the density changes are always very small, and much smaller than those occurring in waste ceramics.

- **Leaching:** The leaching results for glass SON 68 are shown in Fig. 4.3. As with the SON glass, the leaching behavior is largely unaffected by α-damage for all three glasses. This is true for the overall leach rate (static leaching, de-ionized water, 150°C, 14 d) and for all analysed elements in solution (ICP analysis). Note that only some of the 30 elements analysed are shown in Fig. 4.3.

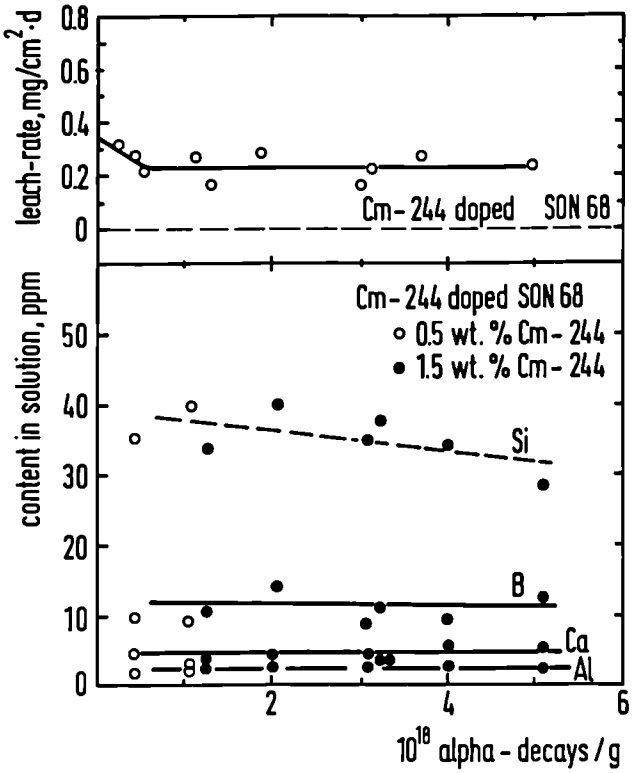


*Fig. 4.3* *Leach rate for SON 68 waste glass (upper part) and concentration of selected elements in the leaching water (lower part) as a function of α-dose*

In conclusion, α-decay damage does not seem to be a problem for long-term storage of the various glasses.

Additional experiments performed with ion implantation to produce damage [4] confirmed the

positive effect of damage on mechanical properties, as shown in Fig. 4.4 for the German waste glass GP 98/12 implanted with $10^{15}$ Kr-ions of 380 keV energy. Ion implantation is very useful for parametric studies, e.g. to investigate the effect of (storage) temperature, by performing hot implantation on glasses annealed to e.g. 175°C, as is the case for Fig. 4.4. It is known that extent and type of damage depend on specimen temperature *during* damage production. For implantation at room temperature, $K_{Ic}$ increased with the ion dose with a maximum at ~ $5 \times 10^{15}$ ion/cm$^2$. Such a dose corresponds to damage levels that will not be surpassed in real waste glasses. The technologically positive feature of damage was largely absent for implantation at T ≥ 250 °C, since the damage induced stresses which increase the fracture toughness are not formed at such high temperatures.

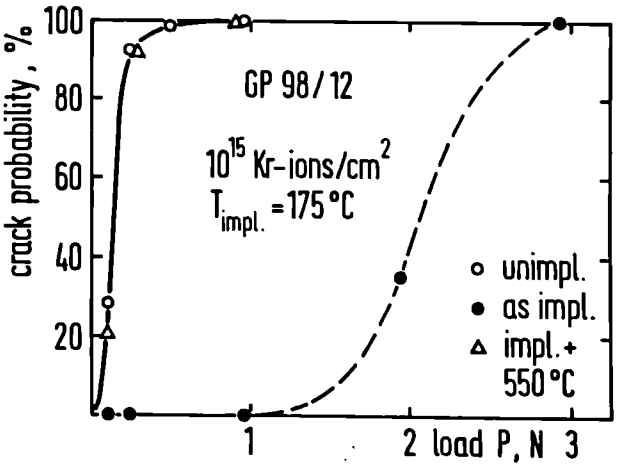


*Fig. 4.4* *Crack probability for an unimplanted waste glass GP 98/12 and a glass implanted with $10^{15}$ Kr-ions of 380 keV at 175 °C*

Finally, a very detailed article for the Handbook on the Physics and Chemistry of the Actinides was written upon invitation by the editors, to appear in Vol. 6. It is entitled "Self-Radiation Effects in the Actinides and Their Compounds: Basic Studies and Practical Implications". The article summarizes also damage effects in waste matrices.

**References**

[1] E. Vernaz, A. Loida, G. Malow, J.A.C. Marples and Hj. Matzke, 3rd EC Conf. on Radioactive Waste Management and Disposal, Luxembourg, Sept. 17-21 (1990), in print

[2] Hj.Matzke and E. Toscano, Indentation Techniques, Special issue Eur. Appl. Res. Reports 7, Nr. 9 (1990)

[3] Hj. Matzke and E. Toscano, in "Indentation Techniques", Eds. Hj. Matzke and E. Toscano, Special Vol. Europ. Appl. Res. Reports 7, Nr. 9 (1990) 1403

[4] Hj Matzke, G. Della Mea, J.C. Dran, G. Linker, and B. Tiveron, Nucl. Instrum. Methods in Phys. Research B46 (1990) 256

## Validation of algorithms for $K_{Ic}$-determination from Vickers indentations: The short rod fractometer, application up to 450 °C

A critical evolution of the published relations and algorithms to calculate $K_{Ic}$ from the crack length c at Vickers indentations shows large deviations in the values obtained [1]. These relations are obtained by fitting the results to $K_{Ic}$-values obtained with more conventional methods, e.g. double torsion, biaxial flexure etc. Since the indentation techniques are particularly useful for small specimens of materials where large numbers of large specimens are not available, a validation method suitable for such small specimens is desirable. Such a method has been used and developed in the Institute [2], i.e. short rod fractometry was applied and further improved for better statistics with a number of materials, in particular with a large series of the German nuclear waste glasses VG 98/12 and GP 98/12 used previously for technological drop tests. These glasses contained different amounts of noble metals and were produced with different cooling rates [3].

The *short rod fractometer* test uses chevron-notched specimens of rod shape (see inset in Fig. 4.5) to determine the plane-strain fracture toughness of small specimens (see also TUAR 1988, p. 169). It is thus a valuable extension of the Vickers test and is also particularly useful for work with radioactive specimens since the samples are small and the rod geometry used (diam. 6.2 mm, length 1.5 x diam.) can rather easily be produced by drilling cylinders from e.g. sintered fuel pellets.

In the inset of Fig. 4.5, the shaded area denotes the crack. The figure shows a measured multicycle test (see below) of the borosilicate glass GP 98/12.2 in a plot of applied load F versus crack mouth opening, x. After producing a thin chevron slot and a groove for a grip system to apply the force and measure the mouth opening, the test is started. The new and improved method consists in using a number of loading/unloading cycles. As explained previously, the thin chevron slot serves

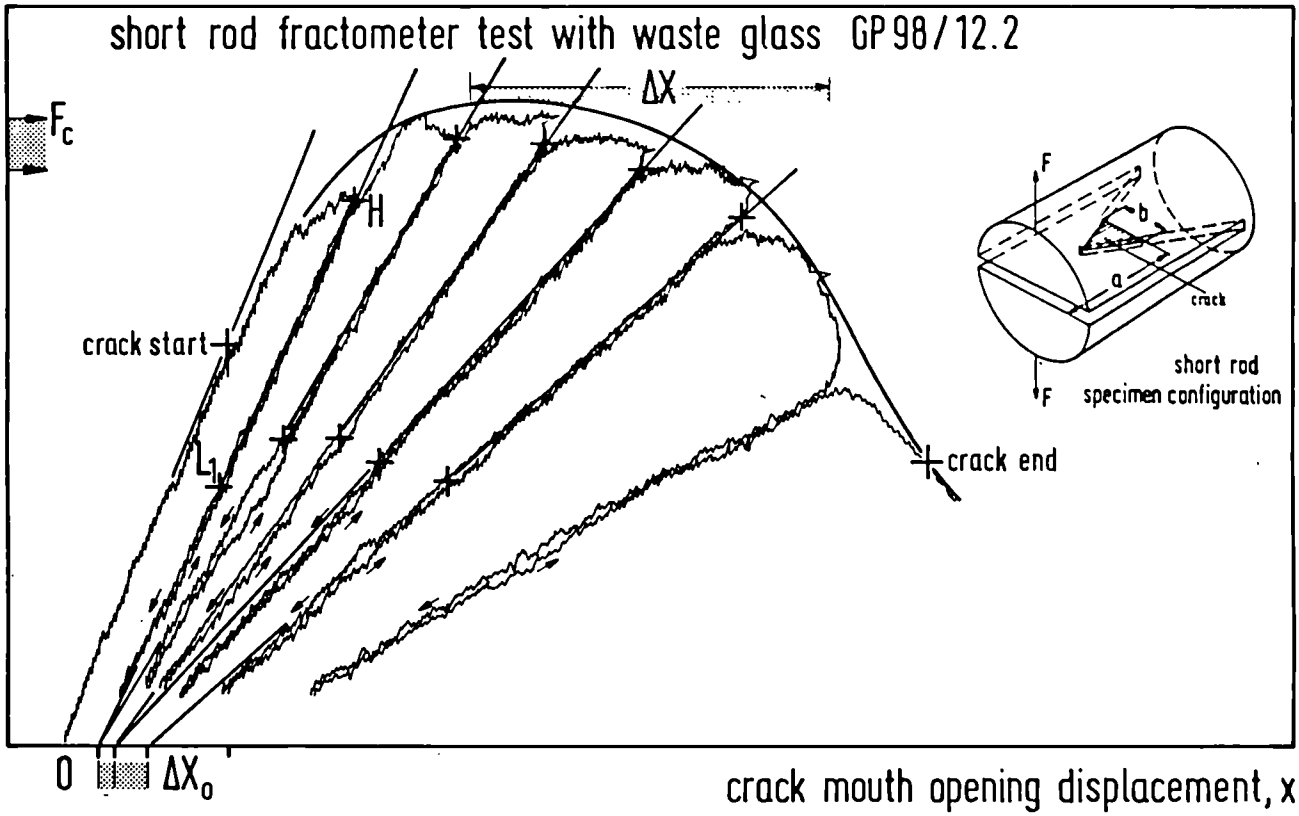


*Fig. 4.5* *Typical short rod fractometer test of the nuclear waste glass GP 98/12.2 with 6 loading / unloading cycles. The short rod geometry is shown in the inset*

several critical functions: it reduces the size of the non-plane-strain zone at the flank ends of the crack, it forces crack initiation at the point of the "V" during crack initiation, it defines the crack plane and the crack propagation direction. Finally, it produces a stable crack growth since the crack front widens as the crack advances. The equipment is described in the literature [4]. In the test, the load is slowly increased (while elastically deforming the specimen) until a crack initiates at the point of the "V". The subsequent crack growth is stable after reaching steady state such that an increase in load is needed to advance a crack until it reaches a critical length, $a_c$, at $F_c$. Thereafter, the load decreases with increasing crack length. The theory developed for the short rod geometry and supporting experimental work [4, 5] have yielded the following relation to obtain $K_{Ic}$:

$$K_{Ic} = \frac{AF_c}{B^{3/2}(1-\nu^2)^{1/2}}\left(\frac{1+p}{1-p}\right)^{1/2} \sim \frac{AF_c}{B^{3/2}}(1+p)$$

here B = specimen diam., v = Poisson ratio, $F_c$ and p are deduced from loading / unloading curves, with $p = \Delta x_0/\Delta x$ (see Fig. 4.5) and the offset $\Delta x_0$ being due to either plastic deformation or residual stresses causing the specimen to be slightly deformed during the test, and A has a recommended value of 22.

As mentioned above, the original method has recently been extended to multiple loading/unloading cycles on the same specimen in ITU [2]. This new *Multi-Cycle Test* constitutes a significant improvement in that several $K_{Ic}$-values can be calculated for the same sample in one test using all pairs of unloading/reloading paths allowing a statistical analysis also on one specimen (see ref. [2] for details).

This modified short-rod fractometry was used to validate the extensive data set for Vickers indentation accumulated previously for nuclear waste glasses and to obtain data at elevated temperatures. Good agreement was achieved whenever the upper limit of the range of values in the empirical constant ($0.016 \pm 0.004$) was used in the relation given by Anstis et al. [6]. Fig. 4.6 shows the type of agreement achieved for different temperatures and the waste glass GP 98/12. Short rod fractometry could successfully be used up to 450 °C. $K_{Ic}$ decreased, as expected by about a factor of 2 between room temperature and 450 °C.

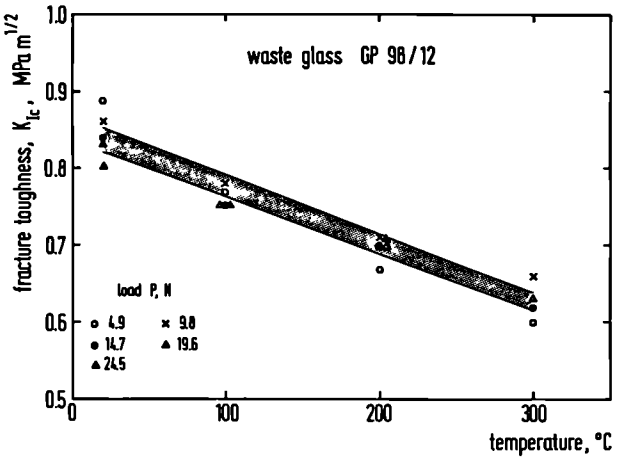


*Fig. 4.6* *Comparison of fracture toughness values as a function of temperature for the nuclear waste glass GP 98/12, as measured with Vickers indentation and with the short rod fractometer*

**References**


[1] Hj. Matzke, Proc. Int. Symp. on Advanced Ceramics, ISAC 90, Bombay, 26. - 30.11.90

[2] A. Bevilacqua and Hj. Matzke, in "Indentation Techniques", Eds. Hj. Matzke and E. Toscano, Special Vol. Europ. Appl. Res. Reports 7, Nr. 9 (1990) 1403

[3] Hj. Matzke, H.G. Scheibel and V. Friehmelt, Mater. Res. Soc. Symp. Proc. Vol. 127 (1989) 173

[4] L.M. Baker, Int. J. Fracture 15 (1979) 515

[5] L.M. Baker, Engin. Fracture Mechanics 9 (1977) 361

[6] G. Anstis, P. Chantikul, B.R. Lawn and D.B. Marshall, J. Amer. Ceram. Soc. 64 (1981) 533


## Ceramic waste forms

A detailed study of the incorporation of transuranic (TRU) elements in titanate nuclear waste ceramics has been performed yielding new partitioning data for three waste forms containing Purex waste simulant in combination with either $NpO_2$, $PuO_2$, or $Am_2O_3$. The TRU elements are often regarded as comparable to rare earth (RE) elements of similar ionic radii and valence for which a good understanding exists in their partitioning in the different phases used in waste ceramics such as the SYNROC formulations. A careful microstructural examination using scanning electron microscopy, powder X-ray diffraction, analytical electron microscopy and selected area electron diffraction showed that the greater portion of TRU elements partition between perovskite and zirconolite while some Am may enter loveringite. Autoradiography, however, revealed clusters of Pu-atoms interpreted as unreacted dioxide or sesquioxide. Details of the results and a review of the relevant literature on TRU and RE element behavior are summarized in ref. [1]. It can be concluded that the solid-state behavior of TRU elements in titanate waste forms needs a better understanding in order to tailor a ceramic for the incorporation of waste from reprocessing of fast breeder reactor fuel, in which TRU elements are more abundant than in Purex waste.

**Reference**


[1] Hj. Matzke, I.L.F. Ray, B.W. Seatonberry, H. Thiele, C. Trisoglio, C.T. Walker and T.J. White, J. Amer. Ceram. Soc. 73 (1990) 370


## Surface analysis of glasses

A number of different techniques using ion beams had been used in the past years to study leaching of simulated waste glasses. In this work, but also elsewhere in glass research and industry, the need for detailed characterisation of glass surfaces with powerful analytical tools has grown in such a way that in 1986 the International Commission on Glass established Technical Committee TC19, Physical Methods for Studying Glass Surfaces. The objective of this committeee, which includes scientists from Europe, USA, and Japan, is to establish a standard protocol for the characterisation of glass surfaces, relying on a wide range of physical tools to determine the optical properties, near-surface elemental composition, thickness of glass coatings, and, in some instances, information on the chemical bonding at the interface between glass and coating. The ITU participated in the first task carried out by TC 19 aiming to obtain a full characterisation of a set of three coated flat glasses. A document was published in the reporting period [12] presenting data obtained by various physical techniques of surface analysis, in order to compare the performance of these methods and to show how they complement each other.

The techniques used were Rutherford backscattering (RBS) of 2 MeV He-ions, elastic recoil detection analysis (ERDA) with 28 MeV Si-ions, nuclear reaction analysis (NRA) with 6.4 MeV N-15 ions, X-ray photoelectron spectroscopy (XPS) and secondary ion mass spectroscopy, (SIMS) with Ar, O and Cs ions. Scientists from 9 different laboratories participated in this round robin test. TU was present with RBS results. The capabilities of

these different surface analytical techniques were described in the report of the Technical Committee [1]. There was good agreement between the different approaches and suitable combinations of the above techniques could be shown to yield good spatial and chemical information on type, composition and thickness of thin layers on glass.

**Reference**

[1] G.W. Arnold, G. Della Mea, J.C. Dran, H. Kawahara, P. Lehuede, Hj. Matzke, P. Mazzoldi, M. Noshiro and C. Pantano, Glass Technology 31 (1990) 58

# Electrochemical Analysis Related to $UO_2$ Corrosion

## Objectives

The objective of the electrochemical testing is to investigate the mechanisms of $UO_2$ corrosion in aqueous solutions, and to pinpoint key species or rate-determining steps in this process, that enable us to understand or control the $UO_2$ leaching that occurs with ground- water flooding of waste repositories.

This year has seen the initial testing of natural $UO_2$ electrodes in various solutions under oxygen-containing and oxygen-deprived atmospheres. Work on electrochemical testing of irradiated $UO_2$ fuel has only reached the stage of equipment adaptation/construction although the first irradiated fuel samples have been mounted and prepared.

An oxygen electrode has been constructed for use in the leach testing of spent fuel with defective cladding to see the influence of oxygen ingress on the fuel's leach rate.

## Natural $UO_2$ testing

### Experimental

Natural $UO_2$ electrodes were constructed by drilling a hole and inserting the electrode wire into position (and maintained in position with adhesive), before mounting in resin and then polishing the surface on SiC papers down to 1000 grit size. Alternatively they were mounted in resin and polished as above, and then a hole was drilled into the back of the $UO_2$ specimen and the electrode wire fixed to the $UO_2$ by means of a screw, before covering over with adhesive to insulate the electrode rear from the solution. The cell arrangement for the runs is given in Figs. 4.7a and 4.7b. The two forms of electrode are shown in Fig 4.8.

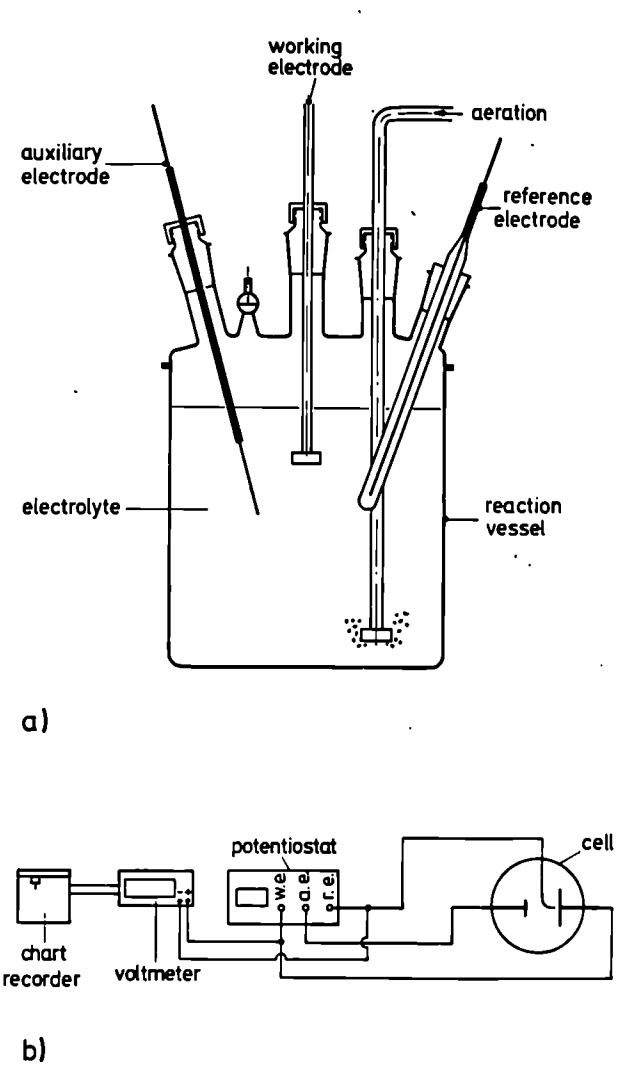


*Fig. 4.7* *a) Reaction Vessel*
*b) Experimental Set-up*

### Preliminary experiments

Initial experiments of shorter duration (about 1 hour) were made in a range of solutions: 3% $Na_2CO_3$, 3% NaCl, 0.1 M $NaClO_4$ in both aerated ($O_2$ purged) and deaerated ($N_2$-8%$H_2$ purged) solutions for a range of pHs.

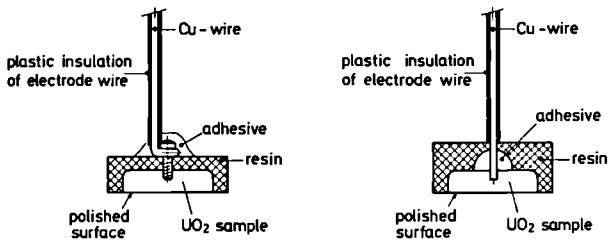


*Fig. 4.8 $UO_2$ electrode construction*

Purging of the solutions in plastic film-covered beakers or vessels with $N_2$-8%$H_2$ was done for at least 2 hours beforehand to reduce the oxygen saturation to 1-2% (~1-3 ppm), while aerated solutions required only shorter bubbling with $O_2$ to ensure equilibrium of the solution. Bubbling was generally discontinued during the measurements in order to have more stable measurements. $O_2$ saturation levels were monitored by an oxygen electrode (WTW OXI 2000).

The specimens were freshly abraded before each experiment using 600 SiC grit (except where otherwise stated). All experiments were carried out at room temperature which was noted as ranging between 21°C and 24°C. Results for demineralised water, 3% NaCl and 3% $Na_2CO_3$ solutions are given in Fig. 4.9. It is seen that the potentials are influenced by solution composition, pH and particularly aeration and surface condition (abrasion). Deaeration results in a more negative (cathodic) potential which is probably the result of reduction of the $UO_{2+x}$ on the specimen surface to a lower value of x (ie. to a less pronounced oxidation of the surface). This is reversible and aeration results in a more positive (anodic) potential as the specimen surface is re-oxidised to $UO_{2+x}$ of higher values of x or $U_2O_5$ (see Fig. 4.9). Reabrading results in a more negative (cathodic) potential that is most probably attributable to removal of surface layers of $UO_{2+x}$.

Some indirect evidence for the capacity for $UO_2$ to take up oxygen readily is the observation of a brown colouration of $UO_3$ particles on the SiC disc after abrading the $UO_2$ sample. The difficulty of maintaining a constant oxygen concentration in solution is seen in the variation of potentials in distilled water purged under various conditions (open but non-agitated solutions, solutions purged before the measurement, and solu-

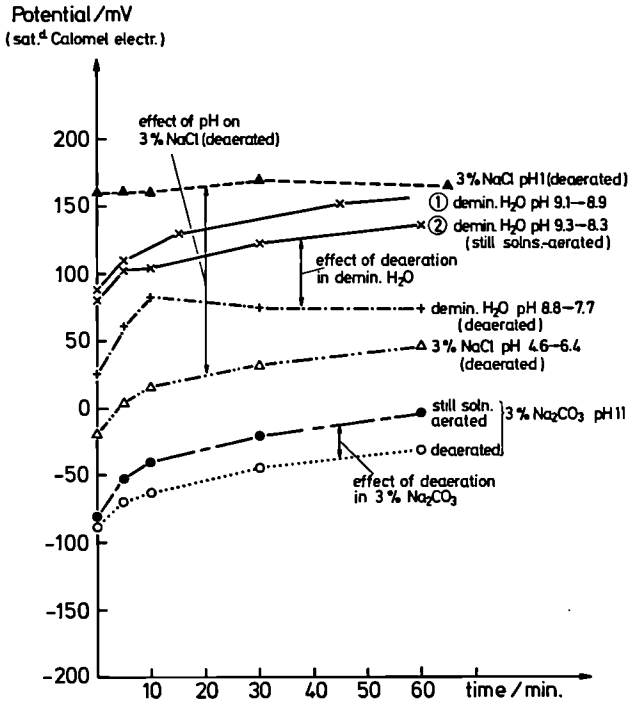


*Fig. 4.9 Natural $UO_2$ electrode potential-time measurements in aqueous solutions*

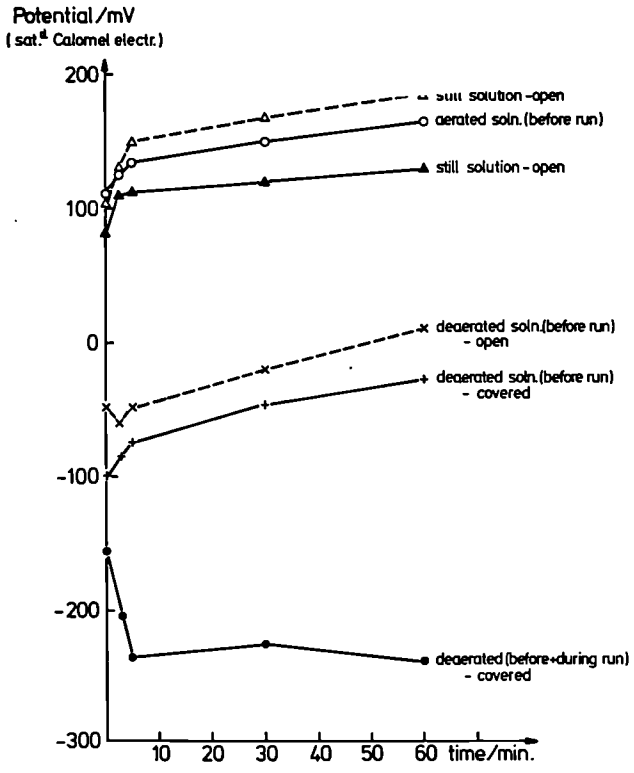


*Fig. 4.10 Effect of aeration conditions on potential-time measurements for a natural $UO_2$ electrode in demineralised water*

tions purged before and after the measurement) (Fig. 4.10). Even during gas purging concentration variations of between 0.4 and 3 ppm $O_2$ were noted. This in turn results in a variable amount of oxygen being taken up by the $UO_2$ surface.
In addition, the gas bubbles accumulating on the electrode surface can also affect its rest potential.

It can be seen that leach tests involving potential or oxygen concentration measurements are preferably carried out with no gas purging.

## Potential-time experiments

The solutions were prepared and purged with gas ($O_2$ for aerated solutions and $N_2$-8%$H_2$ for deaerated solutions). The purging for deaerated solutions required at least 2 hours to reduce the oxygen saturation to approx. 2% (1-2 ppm $O_2$).
The specimen, after freshly abrading the surface, was inserted into the solution and connected to the potentiostat (see Fig. 4.7). The working electrode was then cathodised at -2000 mV for 5 minutes to reduce any higher uranium oxides $UO_{2+x}$ (eg. $U_2O_3$, $U_2O_7$, $U_3O_8$) present on the electrode surface. The potential was then disconnected and then voltmeter readings commenced (Solartron 7050 or 7151). The readings were initially taken every minute and then after 30 minutes at longer intervals. This procedure was carried out for the following solutions:

i) 3 $Na_2CO_3$ aerated with $O_2$
ii) 0.1 M $NaClO_4$ - aerated with $O_2$
iii) 0.1 M $NaClO_4$ - deaerated with $N_2$-8% $H_2$

The results are shown in Fig. 4.11. The potential rises with time, usually rapidly at first, from the initial cathodic potential following precathodisation, and thereafter as a slower drift. This latter drift may result from either longer term oxidation of the electrode directly, or as a result of gradually increasing oxygen concentrations in the deaerated solution after ceasing to purge the solution (gas purging is stopped to allow more accurate potential measurements to be made).

Comparison of these traces with other workers [1] is given in Fig 4.11, and a difference is seen between the potential traces in the 0.1 M $NaClO_4$ solutions from the two sources; the potentials are closest in the case of the two deaerated conditions: Shoesmith et al. [1] for deaerated 0.1 M $NaClO_4$ record a final potential of -140 mV vs. Saturated Calomel Electrode (SCE) while we noted a final potential of -150mV (SCE) for deaerated 3% $Na_2CO_3$ solution. Although this result needs confirming, it implies that oxygen levels in solution are important in determining the potential.

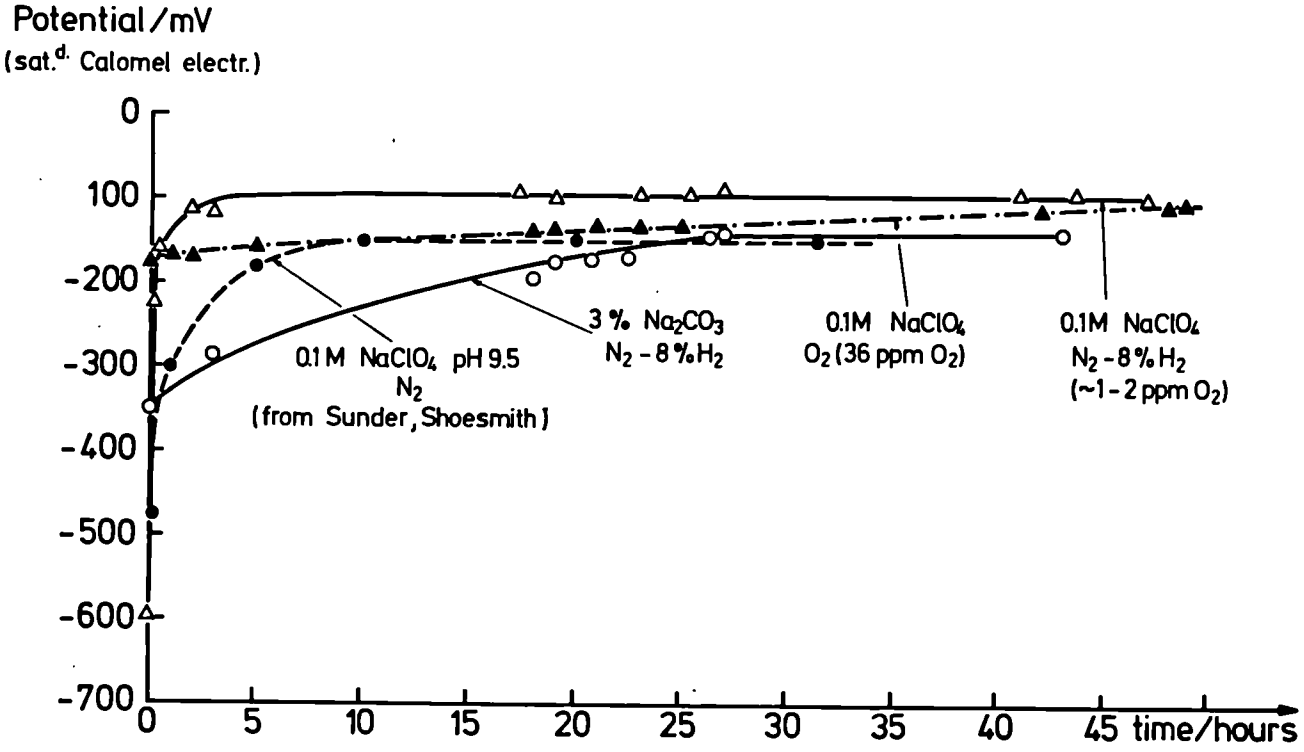


*Fig. 4.11 Corrosion potential of $UO_2$ electrode with time in deaerated and aerated solutions*

## Polarisation curves

In order to obtain a clear surface the $UO_2$ electrodes were abraded with 600 grit and polished with 4 μm diamond paste and then any surface oxidation of the $UO_{2+x}$ was reduced by precathodising at approx. -2.000 V (vs SCE) for 5 minutes before commencing the sweep at 0 V and stepping down 100 mV in the cathodic direction and awaiting the current to stabilise before noting the reading and then making a further cathodic step. The sweep was continued down to -2.000 V (vs SCE). Then an anodic sweep was made from -2.000 V through the rest potential upto +1000 V (SCE) in steps of 100 mV. Thereafter the specimens were allowed to corrode at an open circuit potential which was monitored by means of a voltmeter.

Curves for deaerated and aerated 3% $Na_2CO_3$ are shown in Fig.4.12 and 4.13. The pronounced plateaus at extremely cathodic potentials are likely to be the $H_2$ evolution from water electrolysis. It is noted that the current levels in the aerated solutions are higher for the return sweep in the cathodic (-) domain, than for the initial sweep downward. This may be a result of varying hydrogen or pH levels in the solution, although the causes for this are unknown. The rest potential was approx. - 700 mV vs SCE for the deaerated solution but more anodic (-500 mV vs. SCE) for the aerated solution. The maximum anodic current in both cases was reached at -300 mV (vs SCE) and was higher for the aerated condition ($i_{anodic}$ =30 μA (~40μA.cm$^2$) as opposed to the deaerated condition ($i_{anodic}$= 15μA (~20μA.cm$^{-2}$). The more anodic rest potential and the slightly higher anodic currents would be expected under aerated (higher $O_2$) concentrations.

In the aerated solution a small peak was seen at 0 mV (SCE) which was not seen in the deaerated solution. This could be attributed to a $UO_2/UO_3$ transition peak (Shoesmith et al. [1]).

Compared to metallic specimens the current levels are very low and the internal resistance of the specimen very high (1-3 MΩ). Heppner [2] of FU Berlin also uses electrodes of similar high MΩ resistance with low current (μA) capacities. Shoesmith et al. [1], however, report much higher current levels in the polarisation curves which is presumably due to a reduced electrode resistance (a thinner $UO_2$ disc?).
Further work must be carried out in other solutions and electrode preparations to confirm these results.

Two further observations are that repeated use of a $UO_2$ electrode (re-abrading the surface after each run) is accompanied by a gradual reduction in its activity until it becomes very refractory giving virtually no curve at all (Heppner at FU, Berlin, has also noted this phenomenon). For potential-time curves, there have been the appearance of cracks in the $UO_2$ electrode after repeated abrasion and use. These cracks could then alter the potentials measured during the run.

## Active $UO_2$ specimens

Work is also progressing with the construction of an irradiated $UO_2$ electrode and the construction of a corrosion test cell that can be handled by hot cell manipulators. The first $UO_2$ electrodes have been made and examined on the optical microscope. Modifications to stands for the test cell are being carried out in the workshop.

## Concluding remarks and future work

The influence of electrode preparation method (eg. abrasion) and history as well as conditions of measurement (gas purging /still solutions or aerated/deaerated solutions) on $UO_2$ electrode potentials in aqueous solutions have been examined in these electrochemical studies.The results show that $UO_2$ oxidation state is very sensitive to the $O_2$ content, particularly at low levels (ie. $O_2$ contamination or fluctuation effects).

Future work during 1991 will aim at fixing the experimental method and to repeat potential-time and polarisation curve measurements with solutions of interest for spent fuel leach tests e.g. saturated NaCl and Q-solution (saturated $MgCl_2$ solution) as well as experimental solutions such as 3% NaCl, 0.1 M $NaClO_4$, and distilled water where comparison with other experimental workers is possible.

The second aim of the 1991 future work will be to continue development work with active (irradiated) $UO_2$ specimens. This will involve modification of the test cell and to carry out trial runs using the already constructed electrodes and to make alterations to the electrode design where necessary for such "active" experiments. First trial runs would be potential-time, and polarisation curves in distilled water 3% $Na_2CO_3$ and 3% NaCl, that could be compared with the results from the non-active (natural) $UO_2$ specimens.

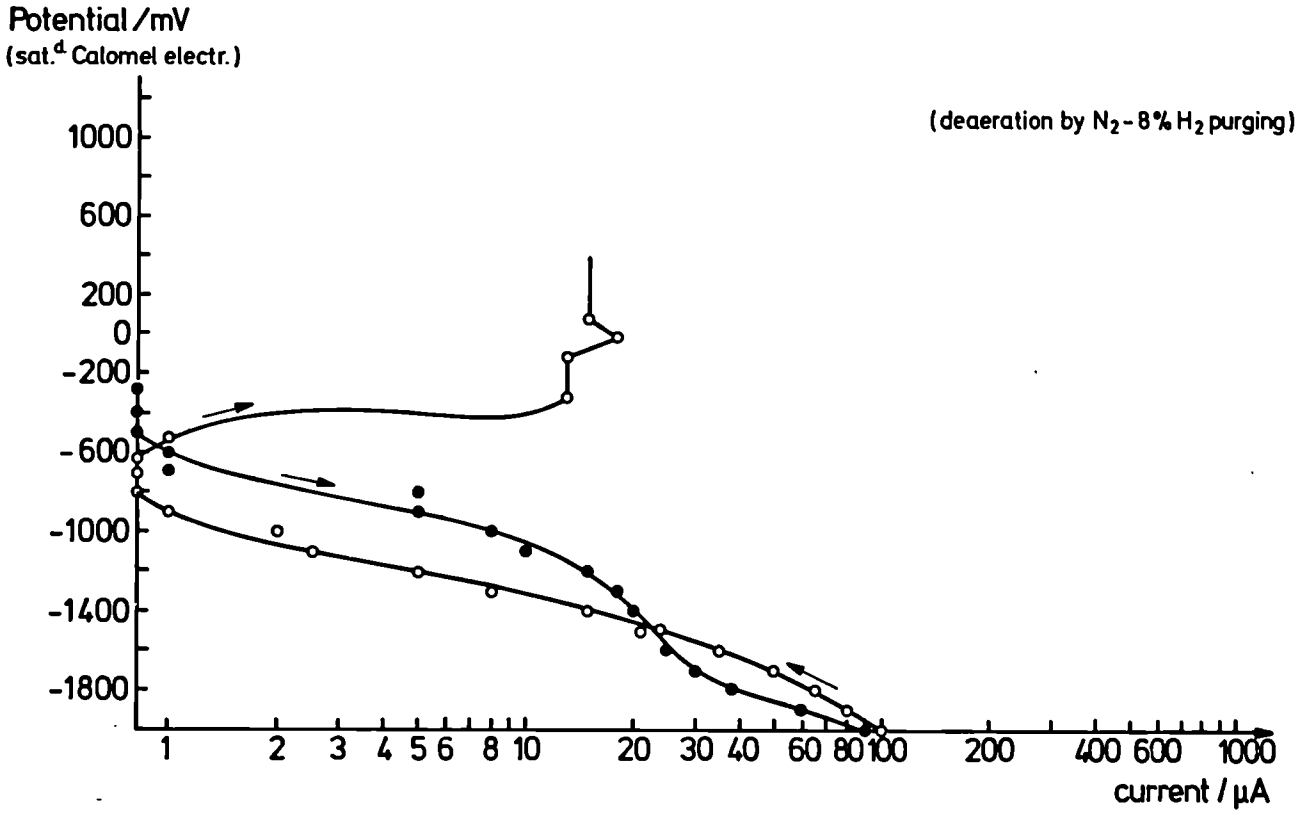


*Fig. 4.12 Polarisation Curve: $UO_2$ electrode in deaerated 3% $Na_2CO_3$ solution*

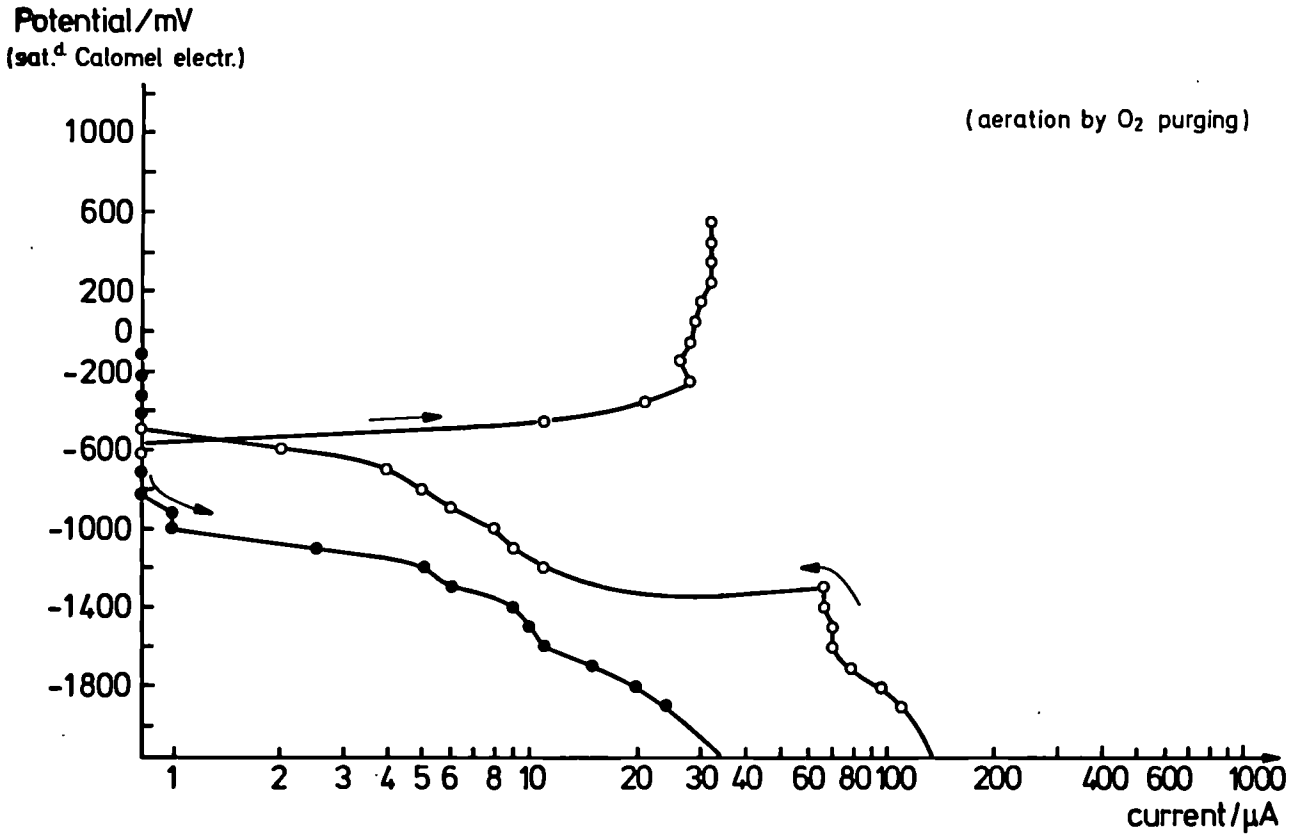


*Fig. 4.13 Polarisation curve: $UO_2$ electrode in aerated 3% $Na_2CO_3$*

A third avenue of research could be the adaptation and use of a glove box provided with a low oxygen content nitrogen atmosphere in which to carry out runs under fixed, low oxygen conditions without gas purging of the solution. These would be carried out using natural $UO_2$ specimens with and without a known radioactive source present to simulate the irradiation, or a simulated fuel sample. The experimental solutions would again be distilled water, 3% $Na_2CO_3$ and 3% NaCl.

**References**


[1] S. Sunder, D. W. Shoesmith, L. H. Johnson, M. G. Bailey & G. J. Wallace. - Proc. 2nd Intl. Conf. on Radioactive Waste Management Sept. 7-11, 1986, Winnipeg, Manitoba.

[2] M. P. Heppner, Jahresbericht für Doktorarbeit, Freie Universität, Berlin, Institut für Radiochemie.


# Characterisation of $UO_2$ and MOX Spent Fuel

As reported in TUAR-89, the study is focussed on fuels relevant to the European technology, i.e., $UO_2$ irradiated at high burn-up and MOX fuels for thermal reactors. Objectives of the study as well as experimental techniques used, microstructural characterization of $UO_2$ fuels and cladding materials were previously reported (TUAR-89, pp.39-40). During 1990 corrosion tests with 30 and 90 days duration were performed on $UO_2$ and MOX-materials. Experimental results concerning the microstructural characterization of MOX-fuel, before and after corrosion, and on the chemical analysis of leachates are reported herewith.

## Characterization of MOX-fuel

### Material

The fuel was fabricated by mechanically blending a "master-mix" of 70/30 $UO_2/PuO_2$ produced by the AUPuC process with natural $UO_2$ powder. The final product contains 3.2 wt% of Pu (fissile) and is a two-phase system consisting of agglomerates of the master-mix irregularly dispersed in a $UO_2$ matrix. The master-mix (MOX) agglomerates were less than 100 µm in size with a content of about 25% of fissile Pu and occupied 15 vol % of the fuel. The irradiation was carried out in the KWO reactor at Obrigheim (FRG). The irradiation and fuel data are given in Tab. 4.1.

*Tab. 4.1 MOX fuel - irradiation and fuel data*

| | |
|---|---|
| Fuel density (% TD) | 94-95 |
| Grain size( µm) | 5-6 |
| Enrichment (% 235U) | 0.72 |
| Fissile Plutonium (wt%) | 3.2 |
| MOX agglomerates (vol%) | 15.0 |
| Stoichiometry (O/M) | 2.00 |
| Pellet diameter (mm) | 9.08 |
| He Fill gas pressure (MPa) | 2.25 |
| Cladding material | Zircaloy 4 |
| Average Linear Power ($KWm^{-1}$) | 25.3 |
| Irradiation Time (EFPD) | 877 |
| Burn-up (GWd/t) | 38.8 |

### Experimental results

Polished cross-sections and freshly fractured specimens of the as received MOX fuel were prepared in order to characterize the material before and after corrosion by scanning electron microscopy and optical microscopy.

#### *Microstructure characterization before corrosion*

Polished cross sections examinations

a) Pu distribution:
The presence of individual Pu-agglomerates all over the cross section was observed by alpha autoradiography and, under the irradiation conditions precised in Tab. 4.1, only a limited Pu interdiffusion in the $UO_2$ matrix was noticed. EPMA measurements on the $UO_2$ matrix reported in Fig. 4.14 revealed the usual Pu build-up at the fuel periphery with a maximum value of 3% Pu and an almost constant value of about 1% within the matrix. Nevertheless a small Pu increase (cf. Fig.4.14) towards the centre of sample was detected, indicating an incipient Pu/U-interdiffusion in the higher temperature zone.

b) Porosity and grain growth:
Two zones with different porosity distribution

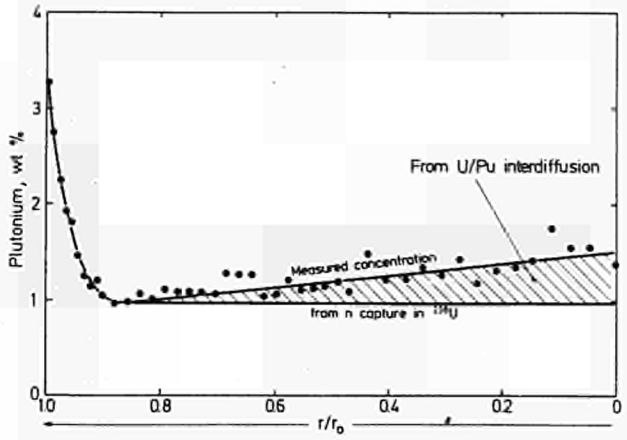


*Fig. 4.14 MOX fuel: Pu radial distribution*

could be determined: In the outer zone (1 < r/ro < 0.5), a rough porosity up to 50% pore concentration could be measured in the Pu-rich agglomerates. In the central zone (0.5 > r/ro > 0), as the fuel temperature increases the atomic mobility increases with the following consequences:

- the Pu-rich particles densified,
- in the central zone, the matrix porosity reaches values between 4 and 5.8% with a predominant contribution of intergranular porosity. The porosity in the Pu-rich particles cannot be differentiated from that in the $UO_2$-matrix, as a result of the interdiffusion. The grain size increased up to 20 μm.

c) Secondary phases:
Metallic fission products (Mo, Tc, Ru, Rh, Pd) (cf. Fig.4.15 ):

At r/ro > 0.5, these precipitates could only be detected in the Pu-agglomerates but not in the matrix. As the fuel temperature increases this clear differentiation disappears and the precipitates can be found in the matrix as well, namely at small inclusions overall and larger ones associated with residual porosity.

Fuel matrix, periphery and cracks examination by SEM

a) Fracture mode:
As can be seen from Fig. 4.16, the fracture mode in the $UO_2$ matrix was mainly transgranular, while in the Pu-rich agglomerates the grain boundaries structure could not be distinguished in the outer rim indicating an intergranular fracture mode. In the central part of the pellet fuel restructuring proceeds mainly by grain growth.

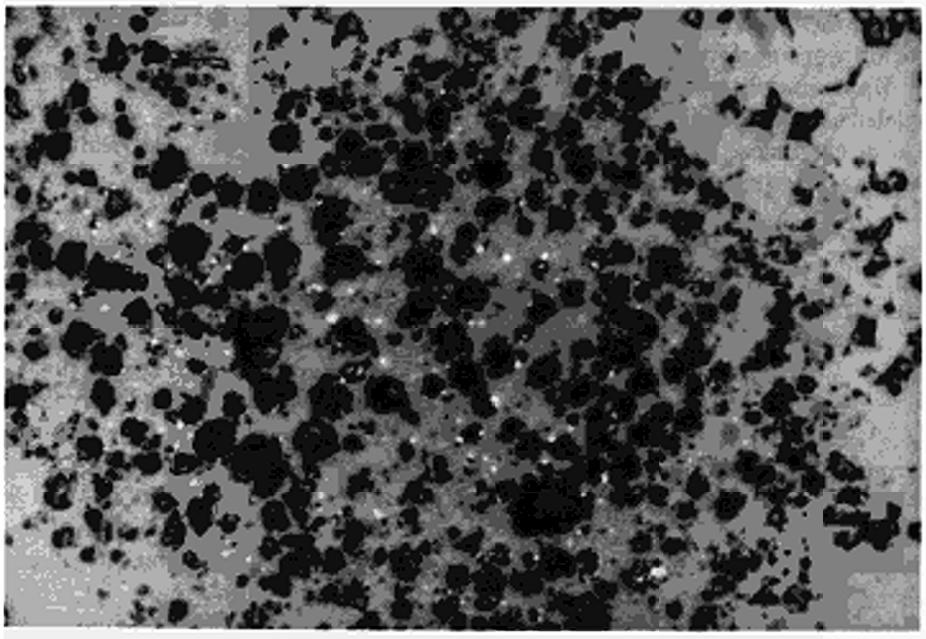

*Fig. 4.15 MOX fuel: Precipitates of metallic fission products within Pu-rich agglomerates ($r/r_o$=0.95, 1033X)*

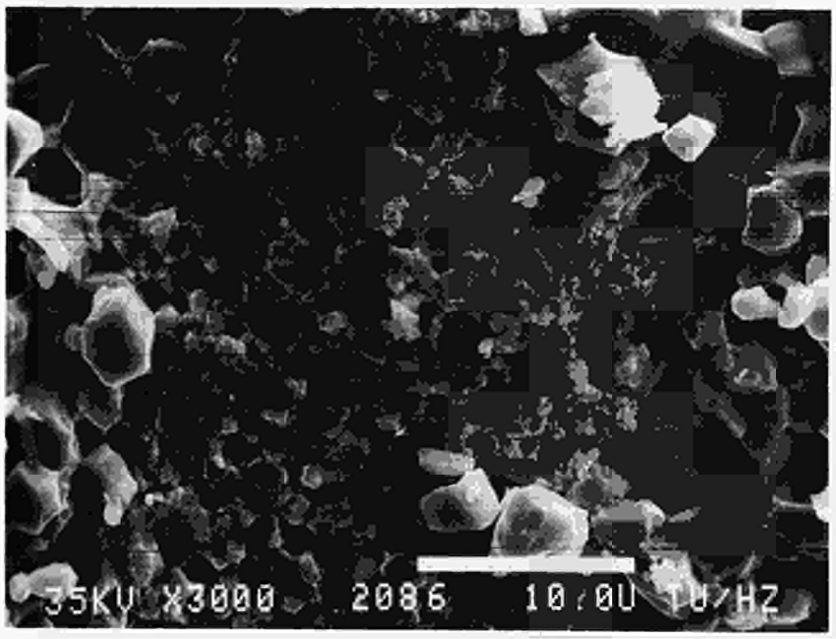


*Fig. 4.16 Fractography of MOX fuel (outer rim)*

b) The main difference in the morphology between fuel matrix and fuel periphery or surfaces representative of cracks produced during irradiation are:

- the porosity observed in the Pu-rich particles on polished cross sections could not be found in the outer surfaces (periphery and radial cracks).

- a nodular microstructure of the Pu-agglomerates, appearing as a two-phase system observed by SEM-EDX, suggests a chemical attack of the metallic inclusions, probably by Cs.

c) Secondary phases:
Two types of oxide phases were detected:

- crystallites with irregular structures (cf. Fig. 4.17) having a composition corresponding to a U,Pu,Cs compound, with Pu/U ratios between 0.15 to 0.20, and Cs-concentration up to about 50 wt %, and

- plate-like crystallites corresponding to a U(Pu,Mo,Ru)-compound (see Fig. 4.18). The Pu/U-ratio was about 0.05 and the Mo concentration of about 5 wt%.

### *Microstructure characterization after corrosion*

Leached fuel pieces coming from the periphery and centre of the pellets were examined by SEM/EDX and priority was put on the determination of the corrosion products. This analysis is completed. Major observations made so far are summarized below.

Fuel periphery:

The morphology of the corrosion products depends on the fuel zone analyzed. Differences were noticed not only between the two types of samples used (pellet periphery and pellet centre) but also in the former case between the outer rim and radial cracks. The morphology of the fuel periphery after corrosion results from the disappearance of fuel debris observed before leaching. The microstructure shows dense material with formation of crevices in the matrix (3 to 5 µm long, 1 to 2 µm depth). Within this eroded zone were noticed small islands corresponding to the Pu-rich agglomerates (10 to 60 µm diameter) but homogenously corroded. The grain structure did not exist anymore; furthermore, a partial dissolution of the dark gray phase in Pu-rich agglomerates was noticed occurred during leaching. (Fig. 4.19)

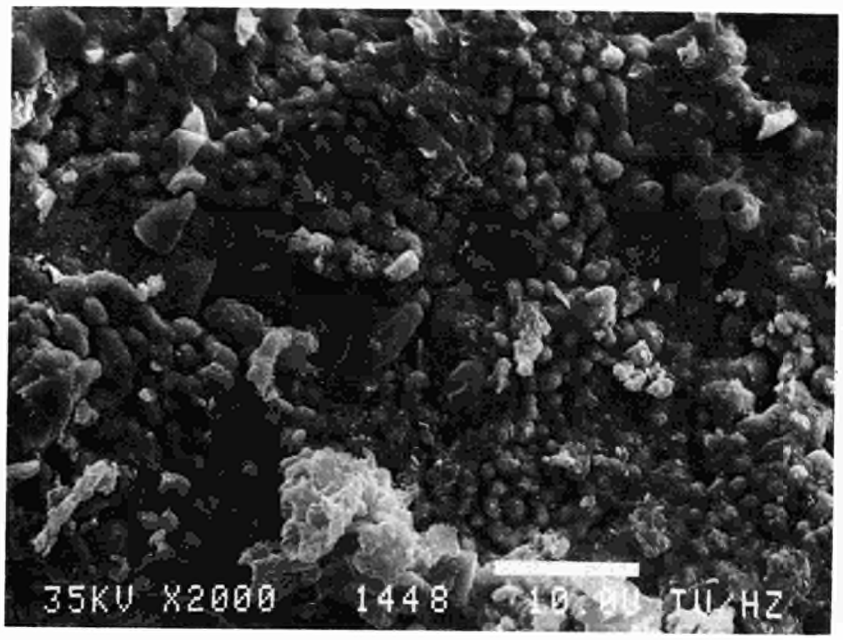


*Fig. 4.17* *U, Pu, Cs compound observed at fuel periphery*

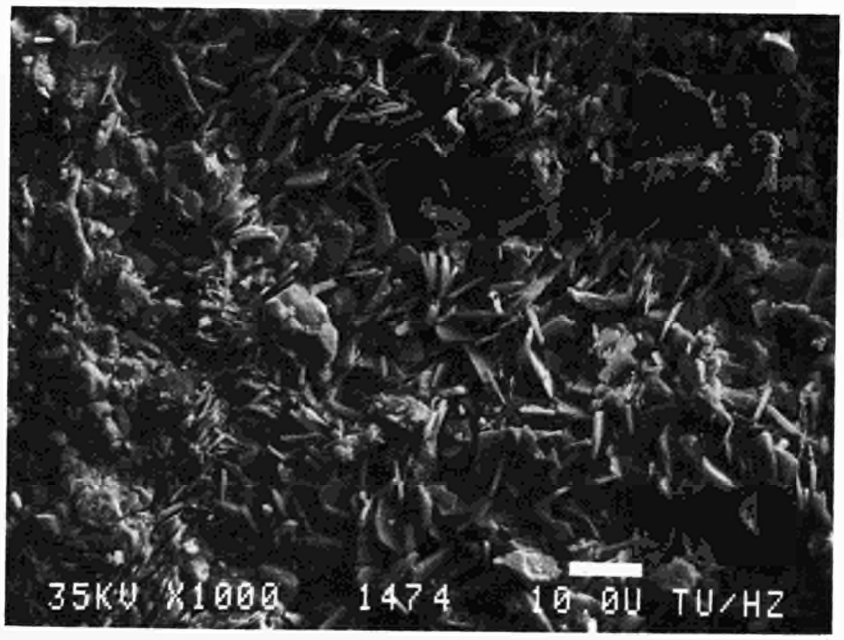


*Fig. 4.18* *U (Pu, Mo, RU) compound observed likely at the interface $UO_2$ matrix - Pu-rich agglomerate*

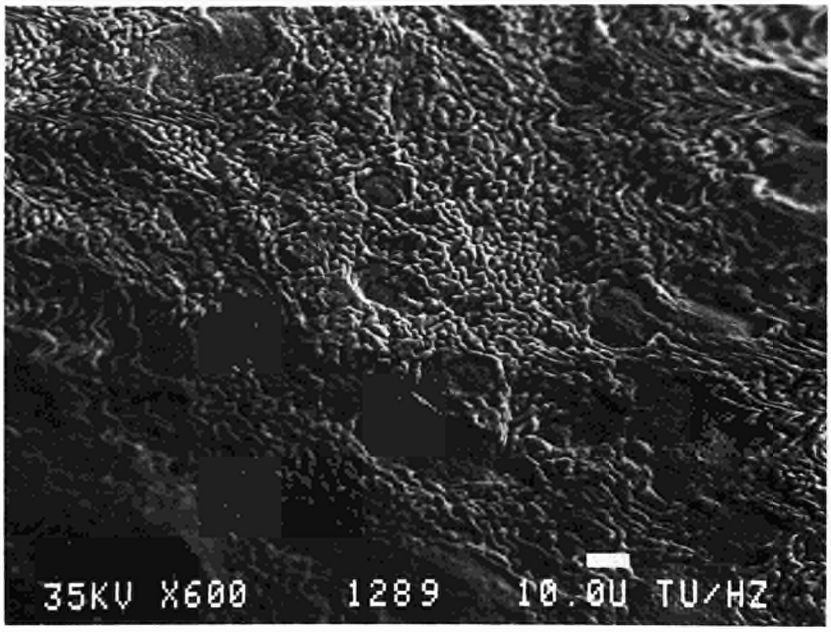


*Fig. 4.19 Fuel periphery surface after leaching*

Fuel Center

A continuous corrosion layer was seen on over all the outer surfaces on which grew isolated crystallites. As a reason of the specimen gamma activity, no X-ray diffraction pattern of the reaction products could be determined but from the morphology the crystallites are assumed to be dehydrated schoepite and the corrosion layer fine-grained $U_3O_8$. (Fig. 4.20)

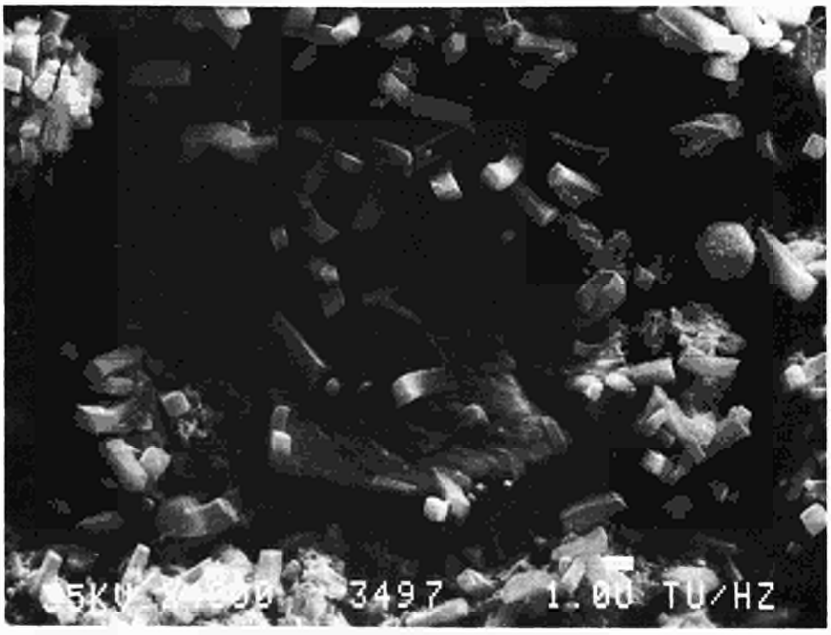


*Fig. 4.20 Fuel center morphology after leaching*

## Corrosion tests and chemical analysis of the leachates

Segments representative either of the central part or of the outer rim of decladded fuels, where corroded in SOXHLET extractors. Four specimens, two from MOX and two from $UO_2$ fuels, were corroded for 30 and 90 days. In the 30 day run, a fifth extractor was used to corrode a piece of cladding ($UO_2$ fuel pin), while the 90 day run provided a blank value.
The boiling flasks were filled with 350 ml water, while the actual leachant volume in the leach container was 12.5 ml. The reflux rate (about 1 ml/min) was adjusted in situ to meet the MCC-5S requirements. Therefore the underpressure of the air atmosphere inside the hot cell had to be kept very stable.

After corrosion, the pH-values of the leachates were measured and the volumes adjusted to 500 ml, prior to chemical analysis by ICP-MS, ICP-OES and alpha- and gamma-spectroscopy. After removal of the samples and leachates, the extractors were filled with 40 ml of a 1M $HNO_3$ solution and heated for 1 day to desorb any activity on the vessel walls. These rinse solutions were also analysed.

In Tab. 4.2 the total amount of different isotopes found in the leachates, is reported as a function of the type of fuel, test duration and position of the samples, while in Tab. 4.3 the leaching rate for selected isotopes is reported together with the apparent removed layer. The latter was calculated, assuming an ideal spherical form of the sample, on the basis of the total amount of U found in the leachates.

*Tab. 4.2 Leachate analysis - total amount measured by ICP-MS*

| ISOTOPE | | | | | | | | | | |
|---|---|---|---|---|---|---|---|---|---|---|
| FUEL | TEST DURATION [days] | POSITION | $^{238}U$ [µg] | $^{239}Pu$ | $^{241}Am$ | $^{244}Cm$ | $^{137}Cs$ | $^{90}Sr$ | $^{99}Tc$ | $^{129}I$ |
| $UO_2$ | 30 | Outer Rim | 129 | 0.94 | 0.07 | 0.002 | 1.3 | <dl | 0.24 | 0.08 |
| | | Center | 389 | 5.26 | 0.45 | 0.009 | 1.99 | 0.36 | 1.28 | <dl |
| $UO_2$ | 90 | *Outer Rim | 7383 | 66.9 | 6.33 | 0.1 | 8.25 | 0.97 | 6.92 | 0.22 |
| | | Center | 1334 | 3.1 | 0.36 | 0.013 | 2.94 | 0.67 | 1.72 | 0.39 |
| MOX | 30 | Outer Rim | 144 | 1.16 | 0.09 | 0.006 | 4.88 | <dl | 0.02 | 1.82 |
| | | Center | 55 | 1.4 | 0.11 | 0.007 | 7.02 | 0.07 | 0.08 | 1.11 |
| MOX | 90 | Outer Rim | 783 | 5.54 | 0.57 | 0.068 | 5.05 | 0.32 | <dl | 1,57 |
| | | Center | 1011 | 6.22 | 0.78 | 0.097 | 6.54 | 0.4 | <dl | 1.14 |
| Cladding | 30 | --- | 30 | 0.6 | 0.044 | 0.01 | 0.32 | 0.03 | 0.32 | nd |

* The results are erratic because a fuel piece fell from the specimen and was dissolved in $HNO_3$ during rinsing

*Tab. 4.3 Leachate analysis - leaching rate estimation*

| FUEL | TEST DURATION [days] | POSITION | LEACHING RATE [g/cm².d] | | | Apparent Removed Layer (µm) | Area (cm²) |
|---|---|---|---|---|---|---|---|
| | | | $^{238}U$ | $^{239}Pu$ | $^{137}Cs$ | | |
| $UO_2$ | 30 | Center | $3.6x10^{-5}$ | $4.9x10^{-7}$ | $1.8x10^{-7}$ | 1 | 0.36 |
| | | Outer Rim | $1x10^{-5}$ | $7.1x10^{-8}$ | $1x10^{-7}$ | 0.3 | 0.44 |
| $UO_2$ | 90 | Center | $4.9x10^{-5}$ | $1.1x10^{-7}$ | $1.1x10^{-7}$ | 4 | 0.3 |
| | | Outer Rim | $4.5x10^{-4}$ | $4x10^{-6}$ | $5x10^{-7}$ | 37 | 0.18 |
| MOX | 30 | Center | $6.5x10^{-6}$ | $1.7x10^{-7}$ | $8.3x10^{-7}$ | 0.2 | 0.28 |
| | | Outer Rim | $1.7x10^{-5}$ | $1.4x10^{-7}$ | $5.9x10^{-7}$ | 0.5 | 0.28 |

## Discussion

From the chemical analyses of the leachates the calculated leach rates of U, Pu, and Am correspond to a low rate oxidation mechanism of the matrix. Bearing in mind the morphology of the leached surfaces, the chemical form of $UO_2$ corroded is very likely an oxidized form of $UO_2$ ($U_3O_8$) associated with $UO_2$ · hydrate.

The mass transfer during the leach tests corresponds to an apparent layer removal of 0.2 to 1 µm and greatest care must be taken by interpretating these results.
Under these conditions no clear differences can be expected between the different pieces of fuel considered whatever their origin. Nevertheless, the leaching of matrix constituents U, Pu proceeds congruently (Tab. 4.4) and presumably a similar mechanism can be predicted for the fission products soluble in the matrix; the transfer of the unsoluble fission products to the leachate can be expected to display a stochastic behaviour depending on their distribution.

*Tab. 4.4 Measured ratios of $^{239}Pu$ / $^{238}U$ and $^{241}Am$ / $^{238}U$ in the leachates*

| Fuel | Leaching duration (day) | Position of fuel segment | $\frac{^{239}Pu}{^{238}U}$ (1) | $\frac{^{241}Am}{^{238}U}$ (2) |
|---|---|---|---|---|
| $UO_2$ | 30 | outer rim | $7.3 \cdot 10^{-3}$ | $5 \cdot 10^{-4}$ |
| | | centre | $1.35 \cdot 10^{-2}$ | $1.2 \cdot 10^{-4}$ |
| | 90 | outer rim | $9 \cdot 10^{-3}$ | $9.1 \cdot 10^{-4}$ |
| | | centre | $2 \cdot 10^{-3}$ | $3.1 \cdot 10^{-4}$ |
| MOX | 30 | outer rim | $8 \cdot 10^{-3}$ | $6 \cdot 10^{-3}$ |
| | | centre | $2.55 \cdot 10^{-2}$ | $1 \cdot 10^{-4}$ |
| | 90 | outer rim | $7 \cdot 10^{-3}$ | $7 \cdot 10^{-4}$ |
| | | centre | $2 \cdot 10^{-2}$ | $8 \cdot 10^{-4}$ |

(1) calculated $\frac{^{239}Pu}{^{238}U}$ ratio by using KORIGEN code

$UO_2$: $4.9 \cdot 10^{-3}$; MOX: $2.3 \cdot 10^{-2}$

(2) calculated $\frac{^{241}Pu}{^{238}U}$ ratio by using KORIGEN code

$UO_2$: $5.8 \cdot 10^{-5}$; MOX: $9.8 \cdot 10^{-4}$

Based on U and Pu leach rates our soxhlet tests showed at least a leach rate of 2 orders of magnitude lower than those previously measured at PNL and Idaho on $UO_2$ irradiated at a burn-up ranging between 20 and 50.000 MWd/t at. [1,2]. The comparison is somewhat difficult because these leaching tests were conducted with different fuels and procedures.

Two leaching procedures (Paige and IAEA) were used to generate the data previously published [1]. In the Paige system, the leach solution was recirculated with an airlift pump and in the IAEA systems, the leachant is static during the leaching interval between sampling periods. Up to one order of magnitude was noted between the Paige procedure and the IAEA procedure. The latter tests were performed in deionized water, WIPP "B" brine, NaCl, $CaCl_2$, $NaHCO_3$ at 25°C. The leaching tests described in references [2] and [3] were conducted in deionized water at ambient hot cell temperatures and used Turkey Point PWR fuel. The leachant is static and solution samples (10 ml) were taken periodically and fresh deionized water added to the test vessel [2] . Similar tests were carried out with J-13 water tests [3]. We suspect that the patchy leach rates arise at least partly from the differences in the procedures used and the difficulty in preparing reproducible specimen surfaces. Nevertheless, the main reason lies in the oxidation mechanism of irradiated $UO_2$.

From our SEM examinations the leaching of $UO_2$ or MOX fuels lead to the formaton of $UO_{2+x}$ and $UO_2$ hydrate; furthermore, the electrochemistry study indicated that the initiation of $UO_2$ oxidation is very sensitive to the $O_2$ content of the aqueous solutions. The understanding of the scattering results is presumably due to various oxidizing states existing in the different leach tests considered. From the literature it is known that in the absence of air or other oxidants $UO_2$ is inert towards water and measurable oxidation by $H_2O$ occurs only above 800°C [4,5] In air saturated water, $UO_2$ powder is oxidized to $UO_3 \cdot 0.8\ H_2O$ at temperatures from 87 to 177°C [6,7]. Campbell et al. [8] have confirmed that moisture can accelerate oxidation of unused fuel near 200°C and $UO_3 \cdot 2H_2O$ has been found in $UO_2$ powder that has been stored in ambient air for 15 years [9]. Recently, the oxidation of unused CANDU $UO_2$ fuel was studied in air-system mixtures, in a closed system at 200 and 225°C [10]. At moisture levels above about 50% of saturation, $UO_3$ hydrates (mainly dehydrated schoepite, $UO_3 \cdot x\ H_2O$, $x = 0.8$) are formed within 20 days at 200°C,

and 5 days at 225°C; $U_3O_8$ also occurred in some cases. Schoepite, $UO_3$, $2H_2O$ were detected in a number of experiments.
Adsorbed moisture has been reported to inhibit the spontaneous oxidation of $UO_2$ powder [11] and in a recent study, Einziger and Buchanan [12] found no effect of moisture on the oxidation of used PWR $UO_2$ for up to 4130 h at temperatures from 110 and 175°C.

As a conclusion, it seems that the extremely low leaching rate measured during one leaching test is coherent with the results provided by Bittel et al [4] and Olander [5] and could be interpreted as consequence of a very low $O_2$ content of the reflux water or by the formation of a protective layer on the surface of the specimen which inhibited the reaction with the system $H_2O$ considered. This assumption must be verified. In the next future our activities will be focussed on attemps to better understand the oxidation of irradiated $UO_2$ and unirradiated $UO_2$ under air-moisture conditions by using thermogravimetry and characterization techniques. Relevant oxidants other than $O_2$ and technologically relevant for the release of radionuclides from a geologic repository to the geosphere will be, as far as possible, envisaged.

**References**


[1] Y. B. Katayama, PNL-2982 (1979), PNL-3713, WA 99352 (1979).
[2] Wilton, C. N.: Handford Co. HEDL-TME 84-30 (1984).
[3] Wilton, C. N. and V. M. Oversby: Lawrence Livermore Natl. Lab., UCLA-91464 (1984).
[4] J. T. Bittel, L. H. Spodahl and J. F. White, J. Am. Ceram. Soc. 52 (1969) 446
[5] D. R. Olander, Nucl. Technol. 74 (1986) 125
[6] S. Aronson, kin: Uranium Dioxide: Properties and Nuclear Applications, Ed. J. Belle, 1961, p. 365.
[7] S. Aronson, WAPD-BT-10 (1958) p. 93
[8] T. K. Campbell, E. R. Gilbert, G. D. White, G. F. Tiebel and B. J. Wrona, Nucl. Technol. 85 (1989) 160
[9] T. Wodsten, J. Nucl. Mater. 64 (1977) 15
[10] P. Taylor, D. D. Wood, A. M. Dudoo and D. G. Dowen, J. Nucl. Mater. 168 (1989) 70-75
[11] M. J. Bannister, J. Nucl. Mater. 26 (1968) 174
[12] R. E. Einziger and H. C. Buchanan, WHC-EP-0070 (1988)


# Modelling of the Underground Water Contamination in a Spent Fuel Deposit

## Objectives

The aim of the study is to model the underground water contamination in a fuel deposit, should such a water accidentaly leach the fuel. In most cases, contact of fuel with water will occur through small defects in the cladding. In some cases the cladding may break and expose the fuel pellets directly to water.
The fuel is supposed to be freshly stored, so that the temperature lies in the range 200-500°C. The water in contact is then in the vapor phase, and the analyzed contamination depends on the fuel corrosion under steam leaching.

The study can be seen as divided in two parts, with the following questions to be answered:

1. What is the fuel state and what is the fission product inventory? Which fission products have migrated onto the grain faces?

2. How does fuel corrosion proceed? How does steam progress towards the center of the fuel, corroding the fuel, forming chemical compounds with the matrix constituants, with the fission products migrated on the grain faces, then with the fission products still dissolved in the grains ?

The first part of the problems can be solved in a rather short time. The calculations will give the expected population of fission products in the grain and on the grain faces as a result of both the nuclear birth-and-decay process and of the diffusion in a thermal gradient. The calculations will not take into account the build-up of chemical species among the several fission products prior to the leaching of the fuel by the steam. The resulting water (steam) contamination will then be approximated by using known solubilities and reaction capabilities of these fission products and of actinides with steam, and a stoechiometry (O/M as a function of temperature history and burn-up) which is estimated as good as possible.

The second part of the approach should provide a more accurate estimation of water contamination. Indeed, due to the relatively low temperatures at which the process occurs and the in-pile temperature history of the fuel, most of the fission

products are to be found in the $UO_2$ matrix. Taking into account only the fission products attached to the grain boundaries would lead to an underestimation of the water contamination. Furthermore, the local fuel stoechiometry (at positions where the reaction proceeds) not only depends on fuel temperature and irradiation history but to a major part on the chemical reactions which, prior to the intrusion of the steam, have already occured among the different nuclides, and on the presence of oxidizing impurities in the water as well. If, at appropriate time spacings, the calculation of such chemical reactions is performed, a more reliable contamination level could be calculated.

## Means

There is no software presently available, which could directly solve all the above problems. But using softwares available at the Institute (FUTURE, MITRA, SOLGASMIX-AUT, KORIGEN) the first set of problems mentioned above can be treated with only minor adaptations to be performed. To solve the above mentioned second set of problems, we propose the development of a specific software (COCAIN), comprising the existing ITU programs, which calculates the progression of steam into the fuel pellet and the evolution of the fuel chemical state according to the radial distribution of the fission products, to the stoechiometry, and to the location of the steam.

The following work has been done in 1990 :

1. Knowledge and adaptation of the ITU software to be used.

   FUTURE [3] : this programme calculates the mechanical integrity of the fuel. For our purpose it will be used on the basis of a normal power history of the fuel. Work made on this software: Programming of missing modules (delay factor, stoechiometry per zone, chart output ), lowering of the computing time (by a factor 2 to 3), correction of several errors, writing of a user's manual [1], completion of an interface with the MITRA software.

   MITRA [4] : this software calculates the list of fission products and actinides for each radial section of the fuel.

   SOLGASMIX-AUT [5,6] : this software calculates the build-up of chemical species. Work made on this software: Search of experimental results for the SOLGASMIX-AUT qualification (The available data base is not sufficient for waste management needs).

2. Definition of a new software: COCAIN, the aim of which is to provide an analytical treatment of the problem considered. COCAIN [2] integrates the ITU programs mentioned above, and adds a calculation of the steam progression in and around the grains. At appropriate time spacing a calculation of the several chemical reactions is foreseen, so that the evolution of the stoechiometry is better accounted for. The specifications and the time planning for this software are given below.

3. Search in the related literature on: the problem of the diffusion coefficients in non-stoechiometric irradiated fuel (lack of reliable information), the problem of stoechiometry evolution due to burn-up (lack of reliable information), the radial distribution of fission products and actinides in an irradiated fuel (satisfactory approximation possible).

## Results

- FUTURE and MITRA are ready to be used for our purposes.
- SOLGASMIX-AUT should be tested with measurements from the literature or with ITU experiments.
- A proposal is made for the construction of a specific software, the architecture and time planning of which are given, and related unresolved difficulties of which are highlighted.

## Prospectives

The present study will focus on the following items:

- Calculations for the above mentioned first set of problems, with the restrictions concerning the validity of the results mentioned.
- Beginning of the construction of COCAIN to treat the second set of problems (progression of steam in and around the grains, interfacing of the several softwares to be used).
- Compilation of a list of measurements to be made, the results of which could provide the missing data.

**References**

[1] C. Messainguiral: The fuel performance code FUTURE. User's manual. Commission of the European Communities (EUR report to be issued).

[2] C. Messainguiral: Proposition de travail - spécifications du logiciel du calcul de la contamination de l'eau au contact d'un combustible stocké comme déchet. JRC Karlsruhe. Technical Note (in press)

[3] C.Ronchi, J. van de Laar : The fuel performance code FUTURE. Commission of the European Communities. EUR 11387 EN.

[4] C. Ronchi, M.Gardani : MITRA, an advanced code to calculate radionuclide release from nuclear fuels under general irradiation conditions. Commission of the European Communities. EUR 12375 EN.

[5] G. Eriksson, E. Rosen : Thermodynamic studies of high temperature equilibria. Chemica Scripta 4 (1973) 193-194.

[6] F. Turrini : Calculation of the thermochemical equilibrium in the irradiated fuel. JRC Karlsruhe, Technical note K0290135.

# Characterization of Highly Active Glasses

This activity was initiated in 1987 and in the framework of a collaboration with ENEA COMB-SUITE and JRC Ispra. In this programme, the chemical and radiochemical composition of ESTER borosilicate glasses after leaching test by means of soxhlets was investigated as well as their microstructure before and after leaching test [1,2].
Recently, CEA-Marcoule provided active glasses produced at the R7 and T7 industrial vitrification units in La Hague which are analysed in our laboratory, with emphasis being placed on studies of the morphology and of the distribution and the composition of the matrix and precipitated phases.
Leach tests by means of soxhlets are being carried out and the interest is focussed on the transfer of $^{239}Pu$, $^{241}Am$ and $^{244}Cm$ to the leachate as well as on the microstructure of the glass after leaching. Glass data are given in Tab.4.5.
The following report describes the experimental results of the characterization of the glass before leaching and of the first leaching test. Results of quantitative microscopy and EMPA as well as of further leaching tests will be published later.

*Tab. 4.5 Average composition of geometrical inclusions*

| Element | Cr | Zn | Ni | Fe | Zr | Mo | Co |
|---|---|---|---|---|---|---|---|
| Atomic % | 58 | 15 | 11 | 5 | 5 | 2 | 1 |

## R7T7 - glass

### Microstructural characterization

Metallographic samples from different axial and radial positions were examined by optical and scanning electron microscopy (SEM). The examinations revealed the presence of inclusions in a homogeneous glass matrix. From the morphology and reflectivity, two different types of inclusions could be distinguished:

- Inclusions with well defined geometry, having sizes in the range 1 to 10 µm, sometimes appearing in the form of clusters up to 100 µm in size.

- Small (about 1 µm) spherical inclusions showing metallic reflectivity. Sometimes these inclusions appear associated with the previous ones.

Both types of inclusions are distributed at random in the matrix and no relevant differences were found between the radial and/or axial locations in the original blocks.

### Chemical composition of matrix and inclusions

The chemical composition was determined by EDX. Based on the average of several measurements, the following chemical compositions of matrix and inclusions were determined:

a) Matrix: in addition to the base-elements, Si, B, Al, Li, Na and Ca, the following elements appear to be, at least partially, dissolved in the matrix network:
Fe, Ni, Cr, Zr, Mu, Mo, Nd and Cs
with some traces of Zr and Ba.

b) Geometrical inclusions: an average compositionis given in Table 4.5.

From the reflectivity and appearance it is supposed that these elements are present as oxides. Probably phases like spinel (nominally $NiFe_2O_4$) are formed during processing.

c) Metallic inclusions: due to the small size (about 1 µm), the quantitative analysis of this type of inclusions was difficult. Nevertheless, the measurements performed revealed the presence of Te together with small amounts of U and Cr.

The inclusions have a spherical form, indicating local melting during processing.

## Leaching of R7T7 HAW glass

The aim of the present study was to compare commercial waste glass as it is produced at the R7 and T7 industrial vitrification units in La Hague to a waste glass produced on a laboratory scale by ENEA at Ispra. The experiments carried out on this so-called ESTER-glass has been presented in the previous report (TUAR-89, pp.42-44). The R7T7 glass delivered by CEA-Marcoule has been characterised and leached using the same procedure, i.e. leaching composition of these glasses compared to the german GP 98/12 glass is given in Tab.4.6. Whereas for the ESTER glass the main loading component was $Fe_2O_3$, the fission product content is higher for the R7T7 glass.

The analytical results obtained by different techniques (Tab. 4.7) are very similar to those obtained for the ESTER glass. After leaching the containers were rinsed with 1 M nitric acid and in these solutions quite high amounts of actinides were found. U cold not be measured neither in the leachate nor in the rinsing solution, and for many elements the results are very close to the detection limit. Thus an increase of the sample surface, the reflux rate or the test duration is planned for further comparison test.

*Tab. 4.7 Leaching results of fully active ESTER glass*

| Sample | Weight (g) | Surface area ($cm^2$) | Normalised mass loss Ri ($g/m^2$) | | | | | |
|---|---|---|---|---|---|---|---|---|
| | | | B | Li | Mo | Cs | Sr | Al |
| c-1 | 0.540 | 1.70 | 17.9 | 16.3 | 12.5 | 17.9 | 20.9 | 2.8 |
| c-2 | 0.650 | 1.83 | 13.3 | 13.4 | 14.3 | 20.1 | 30.9 | 3.9 |
| c-3 | 0.512 | 1.67 | 11.3 | 11.1 | 11.4 | 12.5 | 19.7 | 14.4 |
| e-1 | 0.412 | 1.54 | 26.6 | 31.1 | 29.4 | 35.5 | 35.1 | 2.8 |
| e-2 | 0.509 | 1.66 | 32.7 | 29.2 | 30.0 | 34.6 | 35.4 | 3.4 |
| e-3 | 0.498 | 1.61 | 20.0 | 18.5 | 13.8 | 20.1 | 30.7 | 3.5 |

*Tab. 4.6 Glass composition - waste elements/matrix elements*

Glass composition - waste elements

| element oxide | GP 98/12 (german) | Ester (italian) | R7/T7 (french) |
|---|---|---|---|
| BaO | 0.31 | 0.15 | 0.61 |
| $CeO_2$ | 0.45 | 0.64 | 0.93 |
| $Cr_2O_3$ | 0.05 | 0.11 | 0.51 |
| $Cs_2O$ | 0.23 | 0.19 | 1.32 |
| $Eu_2O_3$ | 0.09 | - | - |
| $Fe_2O_3$ | 0.10 | 2.50 | 2.91 |
| $Cd_2O_3$ | 0.01 | - | - |
| $La_2O_3$ | 0.11 | - | 0.29 |
| $Nd_2O_3$ | 0.37 | - | 1.60 |
| NiO | 0.10 | 0.28 | 0.41 |
| $MnO_2$ | 0.22 | 0.16 | 0.72 |
| $MoO_2$ | 0.91 | 0.76 | 1.70 |
| $P_2O_5$ | - | - | 0.28 |
| $Pr_2O_3$ | - | - | 0.44 |
| $Rb_2O$ | 0.05 | - | 0.13 |
| $Sm_2O_3$ | 0.07 | - | - |
| SrO | 0.24 | 0.12 | 0.33 |
| $TeO_2$ | 0.11 | 0.04 | 0.23 |
| $ThO_2$ | - | - | 0.32 |
| $Y_2O_3$ | 0.06 | - | 0.20 |
| ZnO | - | - | 2.50 |
| $ZrO_2$ | 1.03 | 0.56 | 1.65 |
| $UO_2$ | 0.29 | 0.31 | 0.50 |

Glass composition - matrix elements

| element oxide | GP 98/12 (german) | Ester (italian) | R7/T7 (french) |
|---|---|---|---|
| $SiO_2$ | 55.7 | 50.9 | 45.5 |
| $B_2O_3$ | 10.5 | 11.2 | 14.0 |
| $Al_2O_3$ | 1.5 | 2.1 | 4.9 |
| $Li_2O$ | - | 6.7 | 2.0 |
| $Na_2O$ | 16.6 | 13.0 | 9.9 |
| MgO | 3.2 | - | - |
| CaO | 4.3 | - | 4.0 |
| $TiO_2$ | 3.5 | 0.3 | - |
| total | 95.3 | 84.2 | 80.3 |

References

[1] C. Cantale, J. P. Glatz, E. H. Toscano, A. Donato, M. Coquerelle and J. Fuger, Mat. Res. Soc. Symp. Proc. Vol. 176 (1990) 403

[2] P. Van Iseghem, C. Cantale, M. Coquerelle, J. L. Dussossoy, G. Marlow and H. Roggendorf, 3rd EC Conf. on Radioactive Waste Management and Disposal, Luxembourg, Sept. 17-27 (1990) in print.

# Non-Destructive Assay of Spent Nuclear Fuel

The objective of this study is to characterize spent fuel in terms of its inventory in minor actinides and fission products, and consequently its radiotoxicity, cooling time, burnup and fissile material content. Neutrons and photons will be measured non-destructively. Then Isotopic Correlation Techniques will be used to extrapolate from these measurements the sought information to characterise the fuel [1].

A neutron counting unit (Fig. 4.21) has been developed for passive neutron interrogation of individual fuel rods. The unit will be installed above a

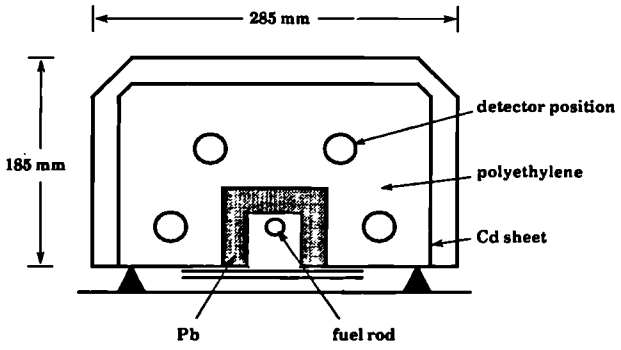


*Fig. 4.21 A schematic representation of the front end of the neutron counting unit*

metrology bench [2], halfway along the bench, inside a β-γ hot cell to measure the spontaneous fission neutrons emitted by the fuel. The unit is a semi-cylindrical array of three B-10 lined proportional neutron counters [25 mm Ø, 100 mm active length, 1cps/nv sensitivity]. In addition, a Geiger-Müller photon detector [17 mm Ø, 100 mm active length, 1.3 x $10^3$ c.s$^{-1}$ per Gy-h$^{-1}$] is included for monitoring the photon dose on the neutron detectors. The detectors are embedded, parallel to the fuel rod axis, in a polyethylene moderator with 25 mm thick moderator towards the fuel, and with the active length in the middle of the unit. To reduce the photon dose from the fuel on the neutron detectors there is a 20 mm thick lead shield around the inside of the moderator. The further 60 mm thick polyethylene moderator beyond the detectors towards the outside of the unit and the 1 mm thick Cd sheet, shield the neutron detectors against background neutrons originating from any other fuel rods present in the hot cell during counting.

The nuclear electronic modules, i.e. EHT, preamp./amp., SCA, associated with the neutron and photon detectors are situated outside the cell. The detectors are connected to the electronics through coaxial cables suitable for operating in a high neutron/photon background. A counter/timer card is incorporated in a PC-AT for registering the neutron and photon count rates.

The fuel can be moved on the metrology bench and passing through the unit is scanned allowing the required information to be obtained as a function of position along the fuel rod.

The unit will be calibrated for counting efficiency and field of view using the fission neutron spectrum of a 10 MBq $^{252}$Cf source. The $^{10}$B and GM detectors are being calibrated to determine their operating characteristics. Furthermore, the effect of different photon fields on the neutron response of the $^{10}$B detectors is being examined and appropriate calibrations will be performed.

Gamma-spectrometry and γ-scanning is performed using an existing facility consisting of a HPGe detector situated outside the cell and 'looking' at the fuel through a collimator mounted in the cell wall [2].

References

[1] TUAR 89, p. 41 (1989)

[2] M. Coquerelle, IAEA Technical Committee Meeting on PIE Techniques on Water Reactor Fuel, Workington, GB, September (1990)

# 1.5 Actinide Research

## Objectives

The central objective of actinide research in ITU as well as in its numerous collaborations is the elucidation of the electronic structure of actinide metals and actinide compounds, in particular of the behaviour of the 5f electrons. The dualism between localised and itinerant characteristics as it is particularly clearly demonstrated in the actinide series, is a key problem in these studies.

These goals are approached by experiment and theory. Experimental study is either selective investigation on the basis of theoretical or other experimental information that indicates the particular material and method are promising, or can also be systematic study of a whole class of compounds. Theoretical calculations can indicate to the experimentalist where he may expect to find important results. On the other hand theory can try to combine experimental evidence from different sources into a general picture. An important basis for the experimental study is the preparation of polycrystalline and single crystal samples of actinides of high specific activity, and their careful characterisation by x-ray diffraction, chemical, and electron microprobe analysis.

## Preparation and Characterisation of Actinide Metals and Compounds

### Introduction

This activity aims at establishing the required expertise for supplying European scientists with the actinide-containing materials necessary for progress in actinide research.

The samples are produced either in the context of collaborative work or in the frame of contract work with universities, national laboratories or industrial companies. During the reporting period, 92 samples were prepared, characterised, encapsulated and sent to different European laboratories for investigations (Tab. 5.1).

A special effort was started to improve the equipment for the preparation and refining of actinide metals. The construction of new equipment to grow single crystals of intermetallic compounds is also in progress. The installation of 10 new glove boxes is under way.

### Preparation and refining of actinide metals

A chain of 3 glove boxes is being set up in order to prepare and refine $^{242}Pu$. Tantalothermic reduction of plutonium carbide, followed by distillation in ultra high vacuum, was selected as preparation method.

A resistance furnace for the preparation of neptunium metal is being installed in a glove box. The neptunium metal is prepared by calciothermic reduction of the oxide in molten $CaCl_2$.

For the large scale preparation and refining of americium and curium metal, a furnace is being installed in a shielded glove box equipped with manipulators. Americium and curium metals are prepared by the metallothermic reduction of the oxide followed by selective evaporation.

A horizontal zone melting facility using a cold boat was set up to refine actinide metals. The equipment was successfully tested with uranium. Analysis of the refined uranium metal by spark source mass spectroscopy is in progress.

### Preparation of alloys

Actinide alloys are prepared by arc melting or by levitation melting. In both cases the alloys can be cast in a water cooled copper mold.

In the systems Am-Pu, Am-Np, Np-Pu, U-Np, Zr-U-Pu, Zr-U-Pu-Np-Am, and Zr-U-Np , alloys of different concentrations were prepared as small spheres or as cylinders and disks of 3 to 8 mm diameter. The alloys are used for physical property measurements or phase diagram studies.

*Tab. 5.1 Samples prepared, characterised and encapsulated in 1990 for the measurements indicated*

| | | | |
|---|---|---|---|
| Magnetization | ETH Zurich | $NpAs_{1-x}Se_x$ (x = 0.1, 0.15)<br>$NpCo_2$, $PuPt_2$<br>$NpPd_2Si_2$<br>NpS, NpP, NpBi | M-SC<br>Cz-SC<br>AcM-SC<br>M-SC |
| Optical | ETH Zurich | PuS, PuSe, PuTe | M-SC |
| Neutron Scattering | ILL Grenoble | $U(C_5H_5)_3Cl$<br>$USb_{0.8}Te_{0.2}$ | Powder<br>M-SC |
| | CEN Saclay | $U(C_5H_5)_3X$ (X = Cl, Br, I) | Powder + GSC-SC |
| | CEN Grenoble | NpS, NpP, NpBi<br>$NpAs_{1-x}Se_x$ (x = 0.05, 0.1)<br>$PuSb_{0.98}Te_{0.02}$ $^{125}Te$<br>$NpM_2Si_2$ (M = Pd, Pt)<br>$NpMn_2Ge_2$ | M-SC<br>M-SC<br>M-SC<br>AcM-Powder<br>AcM-Powder |
| Moessbauer Spectroscopy | CEN Grenoble | $NpSb_{1-x}Te_x$<br>(x = 0.05, 0.1, 0.15, 0.2, 0.25)<br>$NpAs_{1-x}Se_x$ (x = 0.05, 0.1,0.15)<br>NpP, NpS, NpAs, NpBi, NpTe, NpOBi<br>NpMAl (M = Fe, Co, Ni, Rh, Ir, Pt)<br>$NpPd_2T_2$ (T = Si, Ge)<br>$NpM_2Si_2$ (M = Os, Ir, Pt, Au)<br>$NpM_2Ge_2$ (M = Rh, Pd)<br>$PuIr_2Si_2$<br>$Np_4Ru_7Ge_6$<br>$Np_2Mo_3Si_4$<br>$NpAl_2$, $NpAl_3$, $NpSn_3$, $NpPt_3$<br>$Np(Ru_xRh_{1-x})_2Si_2$ (x = 0.25, 0.5, 0.8)<br>$(U_{0.5}Np_{0.5})Pt_3$<br>$^{241}Am$, $^{243}Am$ | GSC-Powder<br>GSC-Powder<br>GSC-Powder<br>AcM-Powder<br>AcM-Powder<br>AcM-Powder<br>AcM-Powder<br>AcM-Powder<br>AcM-Powder<br>AcM-Powder<br>AcM-Powder<br>AcM-Powder<br>AcM-Powder<br>Metal |
| Resistivity | CEN Grenoble | $PuSb_xTe_{1-x}$ (x = 0.2, 0.4, 0.6, 0.7)<br>NpS, NpBi<br>Np<br>$NpPt_3$ | M-SC<br>M-SC<br>Metal<br>AcM-Poly |
| Susceptibility and Resistivity | CEN Grenoble | $NpM_2Ge_2$ (M = Os, Pd, Ir, Pt)<br>$NpM_2Ge_2$ (M = Mn, Rh, Pd)<br>$PuM_2Ge_2$ (M = Rh, Pd, Ir) | AcM-Powder<br>AcM-Powder<br>AcM-Powder |
| Susceptibility | KfK Karlsruhe | $PuM_2Si_2$ (M = Cr, Mn, Fe, Co, Ni)<br>$PuM_2Ge_2$ (M = Ru, Os, Pt) | AcM-Powder<br>AcM-Powder |

M = Mineralization
Cz = Czochralski
GSC = Ground Single Crystals
SC = Single Crystals
AcM = Arc Melting
Poly= Polycrystalline Material

## The crystal chemistry of the AnMX and $AnM_2X_2$ compounds

In AnMX and $AnM_2X_2$, An stands for actinide, M for transition element and X for Si, Ge, Al, Ga and Sn. The actinide and lanthanide elements form large families of ternary isostructural compounds. Worldwide investigations of the lanthanide, uranium and thorium compounds of 1:1:1 and 1:2:2 composition with the transition elements and Al, Ga, Si, Ge and Sn led to the discovery of a large number of new materials with remarkable behaviour. The object of the programme started in the laboratory is to investigate the crystal chemistry of 1:1:1 and 1:2:2 compounds with Np, Pu and Am and to develop preparation techniques for samples, appropriate for physical property measurements.

The compounds are prepared by arc melting. They are characterised by metallography, electron microprobe analysis, X-ray diffraction on powder and single crystals, dilatometry and Mössbauer spectroscopy. The new compounds prepared and characterised in the reporting period are listed in Tab. 5.2 for the 1:1:1 compounds. The crystallographic data of the new actinide ternary intermetallics prepared are given in Tab. 5.3. Electron microprobe analysis, dilatometry and Mössbauer spectroscopy are in progress. As shown in Tab. 5.1, the compounds were encapsulated for resistivity and susceptibility measurements. These measurements are in progress.

## The actinide pnictides of the $Th_3P_4$ structure type

The light actinide elements form pnictides $An_3X_4$ (An = actinide and X = pnictogen) up to $Np_3As_4$. These are isostructural compounds of body centered cubic symmetry. With increasing atomic

*Tab. 5.2 Crystallographic data of new AnMX intermetallic compounds*

| Compounds | Space group | Structure type | Lattice parameters (pm) | | | c/a | Volume/Z ($nm^3$) |
|---|---|---|---|---|---|---|---|
| | | | a | b | c | | |
| UPdGa | Imma | $CeCu_2$ | 446.4(1) | 680.6(3) | 773.2(2) | | 0.05880 |
| NpFeAl | $P6_3mmc$ | $MgZn_2$ | 525.3(2) | - | 848.0(4) | 1.6143 | 0.05066 |
| NpPdAl | $P6_3mmc$ | $MgZn_2$ | 543.8(1) | - | 879.1(6) | 1.6170 | 0.05628 |
| NpCoAl | P-62m | $Fe_2P$ | 672.2(1) | - | 391.9(1) | 0.5830 | 0.05112 |
| NpNiAl | P-62m | $Fe_2P$ | 680.0(1) | - | 398.8(1) | 0.5865 | 0.05323 |
| NpRhAl | P-62m | $Fe_2P$ | 697.55(6) | - | 402.27(7) | 0.5767 | 0.05650 |
| NpIrAl | P-62m | $Fe_2P$ | 697.40(7) | - | 403.40(6) | 0.5784 | 0.05648 |
| NpPtAl | P-62m | $Fe_2P$ | 705.2(1) | - | 409.4(1) | 0.5805 | 0.05877 |
| PuNiAl | P-62m | $Fe_2P$ | 686.7(1) | - | 397.5(1) | 0.5789 | 0.05411 |
| PuNiGa | P-62m | $Fe_2P$ | 684.7(1) | - | 394.5(1) | 0.5762 | 0.05339 |
| PuPtAl | Pnma | $Co_2Si$ | 695.4(2) | 434.7(1) | 771.6(2) | | 0.05829 |
| PuPtGe | Pnma | $Co_2Si$ | 711.5(1) | 439.21(6) | 758.3(1) | | 0.05841 |
| NpRuAl | P-62m | $Fe_2P$ | 677.8(2) | - | 394.5(1) | 0.5820 | 0.05232 |
| NpNiGa | $P6_3mmc$ | $MgZn_2$ | 538.8(1) | - | 840.6(2) | 1.5601 | 0.05284 |

*Tab. 5.3 Crystallographic data of new actinide-based ternary compounds*

| Compounds | Space group | Structure type | Lattice parameters (pm) | Z | Volume ($nm^3$) |
|---|---|---|---|---|---|
| $NpPd_2Ge_2$ | I4/mmm | $ThCr_2Si_2$ | a = 425.23(6)<br>c = 1011.0(3) | 2 | 0.18281 |
| $NpOs_2Si_2$ | I4/mmm | $ThCr_2Si_2$ | a = 411.7(3)<br>c = 969.9(8) | 2 | 0.16439 |
| $PuCu_2Si_2$ | I4/mmm | $ThCr_2Si_2$ | a = 400.30(5)<br>c = 994.0(3) | 2 | 0.15928 |
| $Np_2Tc_3Ge_4$ | $P2_{1/c}$ | $Np_2Tc_3Si_4$ | a = 677.8(1)<br>b = 810.2(1)<br>c = 560.5(1)<br>$\beta$ = 104.09(2)° | 2 | 0.29854 |
| $Pu_2Mo_3Si_4$ | $P2_{1/c}$ | $Ln_2Mo_3Si_4$ | a = 690.3(4)<br>b = 688.3(5)<br>c = 677.2(3)<br>$\beta$ = 109.88(2)° | 2 | 0.30258 |
| $Np_2Re_3Si_5$ | P4/mnc | $U_2Mn_3Si_5$ | a = 1089.0(9)<br>c = 550.9(8) | 4 | 0.65322 |

number, and starting with $Pu_4Sb_3$, they are replaced by the pnictides of composition $An_4X_3$, common in the lanthanide series. This indicates a valence change in going through the actinide series.

Objective of this work is to establish the phase diagram in the An-X composition range and to develop techniques for producing single crystals of the actinide pnictides with the $Th_3P_4$ type structure.

Attempts to prepare $Np_3Bi_4$, $Pu_3As_4$, $Pu_4As_3$ and $Pu_4Bi_3$ at different temperatures failed. In each case, the corresponding monopnictide was obtained. We found that $Pu_4Sb_3$ undergoes a peritectic transformation above 1500 °C. By annealing at 1440 °C small single crystals of $Pu_4Sb_3$ were obtained. $Np_3As_4$ single crystals were obtained by chemical vapour transport with iodine as transporting agent. Attempts to prepare larger single crystals of $Np_3As_4$ by the same technique are in progress.

## Preparation of single crystals of large families of isostructural compounds

### The monopnictides and monochalcogenides of actinides

Single crystals of monopnictides and monochalcogenides are obtained by mineralisation. For the first time, single crystals of NpP and NpBi were prepared, completing the neptunium monopnictide series. NpBi single crystals as large as 200 $mm^3$ were obtained. Attempts to prepare larger NpP single crystals are in progress. The effort to produce single crystals of neptunium pseudobi-

nary compounds was continued. Single crystals of $NpAs_{1-x}Se_x$ (x = 0.1, 0.15, 0.2) and $NpSb_{1-x}Te_x$ (x = 0.05) were prepared.

## Laves phases and compounds with the $AuCu_3$ structure type

The actinide elements form with the transition elements two large families of isostructural compounds of cubic symmetry: the Laves phase compounds ($AnX_2$) and the $AnX_3$ compounds are of great interest for solid state physics investigations.

The mineralisation and Bridgman techniques were tested to prepare single crystals. Small single crystals (a few $mm^3$) of $UPt_3$, $PuNi_2$, $PuPt_2$, $NpSn_3$, $NpPt_3$ were obtained. Attempts to prepare larger single crystals by both methods are in progress.

## Structure of organometallic compounds

The crystal structures of four new organometallic compounds have been determined (Tab. 5.4) in order to establish their molecular structure. This

*Tab. 5.4 Summary of crystal and molecular parameters of organometallics and nitrate complexes studied*

| Compounds | Space group | Z | Lattice parameters (pm) | Coordination Number | Me-X distances (pm) |
|---|---|---|---|---|---|
| $\beta$-$U(C_5H_5)_3Br$ | P $2_12_12_1$ | 4 | a = 826.7(2)<br>b = 1225.9(3)<br>c = 1440.6(4) | 4<br>tetrahedron | U-Br = 280.0 |
| $Tc(C_5H_5)_2Cl_2$ | A m a 2 | 4 | a = 913.4(1)<br>b = 1327.9(2)<br>c = 740.4(1) | 3<br>trigonal | Tc-Cl = 245.0 |
| $Re(C_5H_5)_2Cl$ | P $2_{1/c}$ | 4 | a = 582.8(1)<br>b = 1251.2(2)<br>c = 1306.6(4)<br>$\beta$ = 107.24(2)° | 3<br>trigonal | Re-Cl= 243.8 |
| $Tc(C_5H_5)_3$ | P n a $2_1$ | 4 | a = 1147.7(6)<br>b = 904.2(2)<br>c = 1147.2(2) | 3<br>trigonal | Tc-$C_\sigma$ = 230.0 |
| $Th(NO_3)_6(NH_4)_2$ | P 1 | 2 | a = 832.1(3)<br>b = 689.0(3)<br>c = 1309.7(4)<br>$\alpha$ = 89.87(2)°<br>$\beta$ = 91.55(3)°<br>$\gamma$ = 90.05(3)° | 12<br>icosahedron | Th-O = 244.0 to 268.0 |
| $Pu(NO_3)_6(NH_4)_2$ | P 1 | 2 | a = 816.2(3)<br>b = 689.9(2)<br>c = 1308.9(4)<br>$\alpha$ = 90.02(3)°<br>$\beta$ = 91.34(3)°<br>$\gamma$ = 89.98(3)° | 12<br>icosahedron | Pu-O = 237.0 to 263.2 |

work is performed in collaboration with the Institut für Heisse Chemie, KfK, which supplies the crystals.

To continue the systematic investigation of the organometallic $UCp_3X$ compounds (Cp = $C_5H_5$) (TUSR **37** and TUAR **86**), the structure of $UCp_3Br$ obtained by n-pentane extraction at 36 °C has been determined. This compound shows a new polymeric arrangement of the $UCp_3Br$ tetrahedron in the orthorhombic unit cell compared to the structure reported in TUSR **37** (benzene extraction at 80 °C). Thus, $UCp_3Br$ can be obtained under two different polymorphic varieties depending on the mode of preparation used.

The investigation of the crystal structure of a new series of compounds of the type $MCp_2X$ has started by the determination of the structures of $MCp_2Cl$ (M = Tc, Re) and $TcCp_3$. The two homologous $MCp_2Cl$ compounds were not isostructural and crystallise, respectively, in the orthorhombic space group Ama2 for $TcCp_2Cl$ (isostructural with $VCp_2Cl$) and in the monoclinic space group $P2_1/c$ for $ReCp_2Cl$. The molecular geometry of the two compounds shows that the centroid of the Cp ring, the Tc and Cl atoms form a trigonal plane arrangement with nearly $C_{2v}$ symmetry (Fig. 5.1).

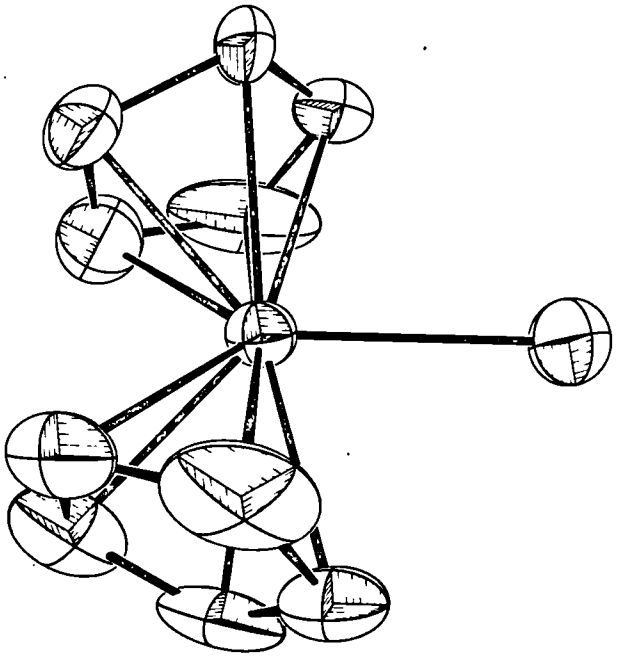

*Fig. 5.1 Molecular structure of $Tc(C_5H_5)_2Cl$*

The distance M-Cp (centroid) of 187.6 pm is identical for the two compounds. The only difference between the two compounds arises from the angle Cp-M-Cl of 143.8° for $TcCp_2Cl$ and of 147.6° for $ReCp_2Cl$. The M-Cl bond lengths reported in Tab. 5.4 were comparable.

In $TcCp_3$, the molecular structure exhibits both $\eta^5$- and bridging $\eta^1$-cyclopentadienyl rings (Fig. 5.2). The two $\eta^5$-Cp (centroid), the $\eta^1$-C of the third Cp and the Tc atom are in a plane within 2.8 pm. The angle from the centers of the $\eta^5$-Cp about the Tc atom is 169.4°. The two angles $\eta^1$-Cp-Tc-Cp (centroid) are 84.1° and 106.3°, respectively.

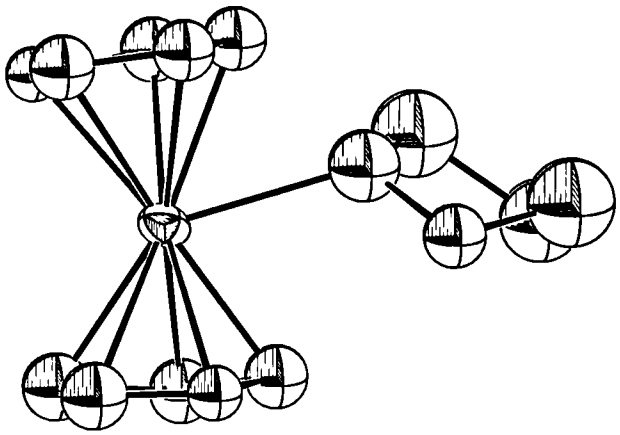

*Fig. 5.2 Molecular structure of $Tc(C_5H_5)_3$*

## Structure of actinide (IV) nitrato complexes

In an effort to understand and to improve the existing separation processes, the systematic investigation of actinide nitrato complexes (TUAR **88**) is continued by the determination of the crystal structure of $[An(NO_3)_6]\ [NH_4]_2$ (An = Th, Pu). This work is performed in collaboration with the Institut für Heisse Chemie, KfK, which supplies the crystals. The crystal and molecular parameters of the two complexes are given in Tab. 5.4. They are isostructural, with two symmetrically independent formula units in the cell. The actinide atom is twelve-coordinated by oxygen atoms which belong to six bidentate nitrate ions. The coordination polyhedron is an irregular icosahedron with An-O distances ranging from 237 to 263 pm and 244 to 268 pm, respectively, for Pu and Th. The connection between the $[An(NO_3)_6]^{2-}$ anions

and the $[NH_4]^+$ cations is established through a threedimensional network of hydrogen bonds. The crystal packing of $[Pu(NO_3)_6]$ $[NH_4]_2$ is represented in Fig. 5.3.

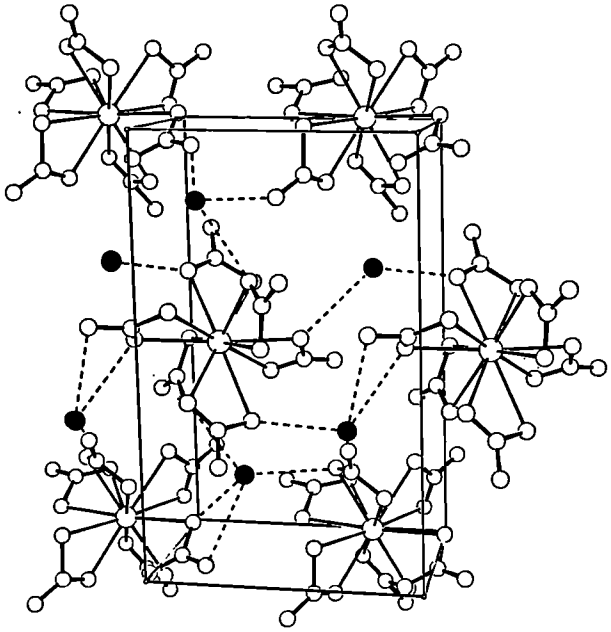

*Fig. 5.3* *View of two unit cells of $[Pu(NO_3)_6]$ $[NH_4]_2$, as a projection along the a axis; b is horizontal from left to right (N of $NH_4^+$ ion represented as dashed circles)*

# Solid State Physics Studies on Actinide Systems

## Theoretical studies

### Fermi surface of UC

UC has proved to be a useful material for nuclear reactor technology because of its unusual properties such as high melting point, hardness, brittleness, metallic conduction, etc. [1]. Recently the Fermi surface (FS) of UC has been measured using the de Haas-van Alphen (dHvA) effect [2]. Since UC crystallises in the NaCl structure and has a non-magnetic ground state, it is relatively easy to do calculations of its electronic structure and Fermi surface. The band structure of UC has already been calculated at ITU using the self-consistent scalar relativistic linear muffin tin orbital (LMTO) method [3]. We have used this band structure to calculate the FS topology of UC. Our calculations indicate that the FS consists of two hole ellipsoids centered at X and an electron sheet centered at W (see Fig. 5.4). We have calculated the extremal areas and masses of some FS orbits on the three sheets of the FS for various directions of the magnetic field. Our calculations are in reasonable agreement with the available experimental data. There is a need for doing more dHvA experiments on UC and other similar compounds to ascertain if the LMTO method gives the correct FS topologies for the actinide compounds.

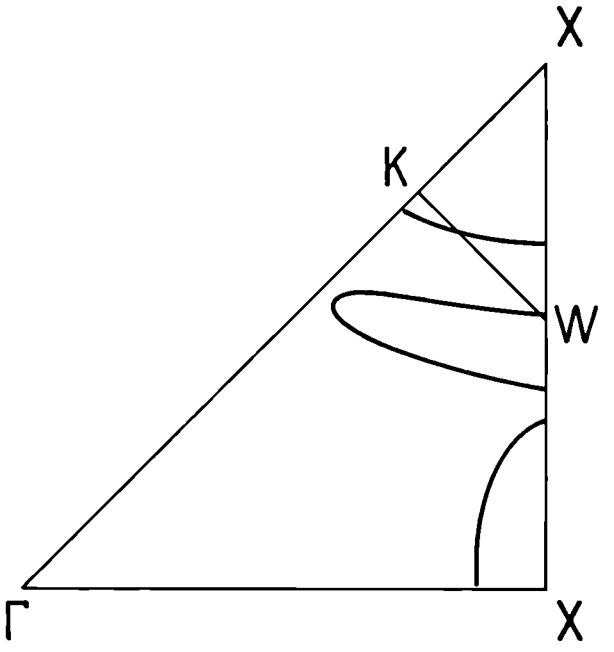


*Fig. 5.4* *Calculated Fermi surface of UC in the (001) plane*

### References

[1] H. Holleck and H. Kleykamp, Gmelin Handbook of Inorganic Chemistry (Springer, Berlin 1987) Supplement C12

[2] Y. Onuki, I. Umehara, Y. Kurosawa, K. Satoh, H. Matsui, A. Masegawa and H. Yamagami, Physica 163B (1990) 273-274

[3] M.S.S. Brooks, J. Phys. F14 (1984) 639-652

## Orbital magnetism in actinides

Most atoms lose their magnetic moments in the solid state but there are three classes of elements - the 3d transition elements, the lanthanides and the actinides - where magnetism is retained in the condensed phase. It is from the former two groups that much of our understanding of solid state magnetism is drawn, and this is primarily due to the success of the standard models of localised and itinerant moments.

The standard model of rare earth magnetism is based upon the approximation that 4f states are essentially the same in the solid as in the free atoms. Hund's first and second rules then assure that both the spin and orbital angular momenta are maximized. Since the states are spatially deeply buried within the rare earth atoms, interaction with the environment is weak and is usually represented quite well by local exchange interactions between 4f and conduction electrons - the so-called RKKY interaction. In contrast, in the standard model of 3d magnetism, the 3d states are part of the conduction electron band structure and, although Hund's first rule again favours as large a spin as possible, this involves an increase in kinetic energy. The values of spin attained are therefore a result of the competition between Hund's first rule and the kinetic energy increase, and are not saturated. Hund's second rule plays no part in the standard model of 3d magnetism because, to a very good approximation, the magnetic moments are pure spin, the orbital moments being quenched. Physically, quenching occurs because itinerant electrons do not spend enough time on a given atom to complete full orbits about the nucleus and the resulting orbital angular momentum is much reduced. Techniques have now been developed to calculate this orbital momentum in the solid [1,2].

A very important property of a magnet is the anisotropy, or dependence of the energy upon the direction of magnetic moment. It is the magnetic anisotropy that is responsible for permanent magnetism for if it were vanishing the magnetic moment would adjust its direction in stray magnetic fields continually with cost in energy and the magnetic moment would not produce a constant direction of magnetic field.The magnetic anisotropy energy is very small compared with the total magnetic energy and, in the limiting approximations (or models) described above, is zero. In the rare earth case the complete rotational symmetry of the free atom is preserved whereas in the 3d case there is no interaction between the orbital and spin degrees of freedom and the energy is independent of spin direction. The theory is rectified in both cases by the introduction of spin-orbit coupling, a relativistic effect arising from the fact that a moving electron feels a magnetic field from the charge of the nucleus. This magnetic field depends upon the direction of the orbit of the electron and acts upon its spin, thus coupling the direction of the spin to the direction of the orbit - if only weakly in most circumstances. Since the total energy of a crystal depends upon the direction of the orbits of the electrons, it also depends upon the direction of the electron spin if spin-orbit coupling is present. In transition metals the spin-orbit interaction also mixes a small amount of orbital moment into the ground state as it couples the spin direction to the crystal lattice. For this reason the presence of an orbital moment tends to be associated, in transition metals, with magnetic anisotropy.In the rare earths, in contrast, the large ambient spin and orbital momenta are coupled together by spin-orbit interaction to form a total angular momentum $J = L + S$. Since orbital and spin degrees of freedom are now coupled, any crystalline electric fields (or non-spherical potentials) are sufficient to reduce the rotational symmetry and are responsible for magnetic anisotropy. In this case, however, the crystalline electric fields *reduce* - or quench - the total and orbital moments. Thus, in rare earths the magnetic anisotropy accompanies a decrease in the orbital moment, whereas in transition metals it accompanies an increase.

In order to understand what happens in actinides we first study the magnitude of spin-orbit coupling itself. The importance of spin-orbit coupling across the periodic table is illustrated in Fig. 5.5,

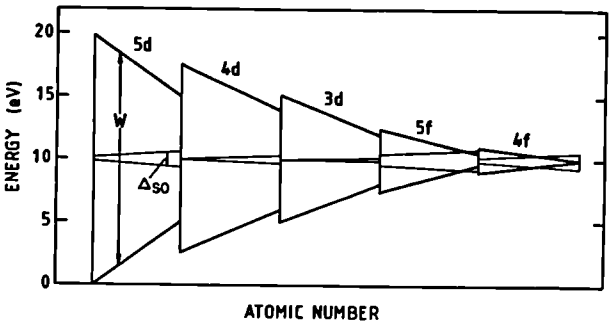


*Fig. 5.5* *Bandwidth and spin-orbit splitting for the d and f series elements. In each transition metal series, atomic numbers increase from left to right*

where we have plotted the energy bandwidths of all the transition metals, rare earths and the actinides and the corresponding magnitude of spin-orbit splitting. The 5f-bandwidths of the actinides are less than those of the 3d transition metals, whereas the spin-orbit interaction for the heavy elements is relatively very large. Now the bandwidth (which is the range of energies over which electron states of a particular type exist) is approximately inversely proportional to the amount of time an electron spends on any given atom before hopping to the next. When the bandwidth is small the electrons spend more time on a given atom and have a better chance of completing orbits inside the atom. Then the quenching of orbital moments in itinerant magnets (such as transition metals or actinides) is least effective when the bandwidths are narrow and the spin-orbit splitting is large - and this is the case in the actinides as may be seen from Fig.5.5.

A series of somewhat complex calculations in the past few years have indicated that orbital magnetism is an important property of actinides - differentiating them from ordinary transition metals. Surprisingly large orbital moments - larger than the spin contributions - have been computed for U, Np and Pu systems using techniques which yield relatively small orbital moments for 3d systems [1,4]. The orbital contributions to magnetic form factors have been measured and theory and measurement are in good agreement. In addition the magnetic anisotropy of US [2] has been computed to be greater by two orders of magnitude than the anisotropy of the rare earths. Recent measurements have confirmed the calculations.

**References**


[1] M. Singh, J. Callaway and C.S. Wang, Phys. Rev. B14 (1976) 1214

[2] M.M.S. Brooks and P. J. Kelly, Phys. Rev. Lett. 51 (1983) 1708

[3] M.M.S. Brooks, Physica B 130 (1985) 6

[4] O. Eriksson, M.S.S. Brooks, B. Johansson et al., Phys. Rev. B41 (1990) 9087-9094

[5] O. Eriksson, B. Johansson, R.C. Albers, A.M. Boring, M.S.S. Brooks et al., Phys. Rev. B 42 (1990) 2707-2710


# Neutron studies

## Spin and orbital components in 5f intermetallic magnets

When actinides are brought together with other elements of the periodic table to produce compounds, there is inevitably an interaction between the spatially extended 5f electrons of the actinide and the other electron states. As explained in the preceding paragraph, one of the characteristics of 5f electrons is that they have a large orbital magnetic moment $\mu_L$ and we may ask what happens to this moment as the 5f electrons become more itinerant.

By analysing the scattering of thermal neutrons from single crystals (made at ITU) we have been able to separate the individual orbital $\mu_L$ and spin $\mu_S$ contributions to the total magnetisation at the actinide site. We can then examine the ratio $\mu_L/\mu_S$ which is plotted for a number of actinide materials in Fig. 5.6. Whereas conventional single-ion type theory (crosses and dashed line) gives a good fit for many compounds, it fails noticeably for the intermetallics $UNi_2$ , $UFe_2$, $NpCo_2$, $PuFe_2$, and $AmFe_2$. These materials except $AmFe_2$ have $\mu_L/\mu_S$ closer to unity than anticipated. In the uranium compounds the ratio is almost unity and since $\mu_L$ and $\mu_S$ are opposed to one another this means that the total moment $\mu \approx \mu_L + \mu_S = 0$. This is observed within experimental precision in $UFe_2$.

Band structure calculations have shown the need to treat the 5f electrons as itinerant but with a term introduced to take account of orbital polarisation effects. Calculated $\mu_L/\mu_S$ ratios are shown as solid points in Fig. 5.6 and are in good agreement with experiment.

## Progress in characterising the charge-density wave in alpha-uranium

Substantial progress in understanding the distortions involved in the charge-density wave (CDW) modulation in alpha-uranium below 43K has come from a theoretical treatment of the free energy. In particular, we have shown the importance of the higher-order terms in the Landau expansion model for the phase transition and the tendency of both components $q_y$ and $q_z$ of the modulation wavevector to take values of 1/6. This would correspond to a completely square wave for the displacements of the atoms off their equilibri-

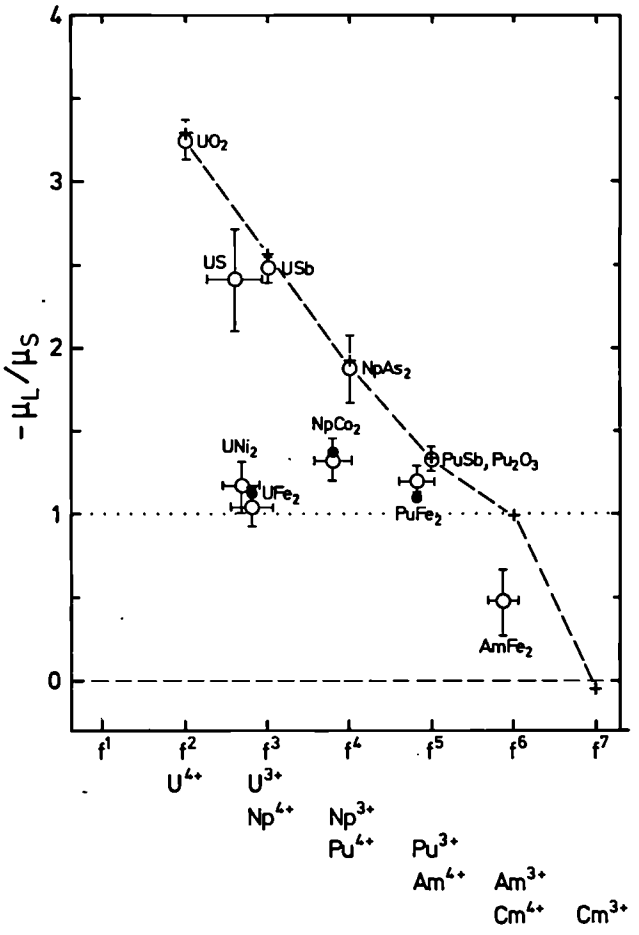


*Fig. 5.6* *Ratio of the orbital $\mu_L$ to spin $\mu_S$ moments in a number of actinide compounds plotted as a function of the f-occupation number. The crosses, which are connected with a dashed line, are the values derived from a single-ion theory including intermediate coupling. Experimental results for many materials agree with the single-ion predictions, but the intermetallic compounds deviate significantly. The solid circles are the predictions of band-structure calculations for the intermetallics and they agree with experiment*

um (high temperature) positions and minimise the strain energy. However, $q_z$ fails to reach this value, reaching instead commensurate values of 5/27 in the bulk, as seen by neutrons, and 2/11 near the surface as seen by synchrotron X-rays.

To account for these unusual values a 'phase-slip' model has been introduced in which discommensurations (or fault regions) relieve the elastic strain caused by $q_z$ being different from 1/6. A test of this model is given by the intensities of the satellites up to 9th-order that have been measured by neutron diffraction at the ILL, Grenoble, France. The product nF, where n is the order and F the structure factor is shown in the top half of Fig.5.7. A square-wave modulation, which would be formed if $q_z = 1/6$, would give a horizontal line. The phase-slip model is clearly a better fit to the data. However, an unexpected feature of the satellites is their linear increase in width with increasing n (lower part of Fig.5.7). This is as yet not explained, although similar effects are found in diffraction from artificial multilayers, and indicates that the higher-order components are progressively less spatially homogeneous. Simple theoretical models presently predict the width proportional to $n^2$.

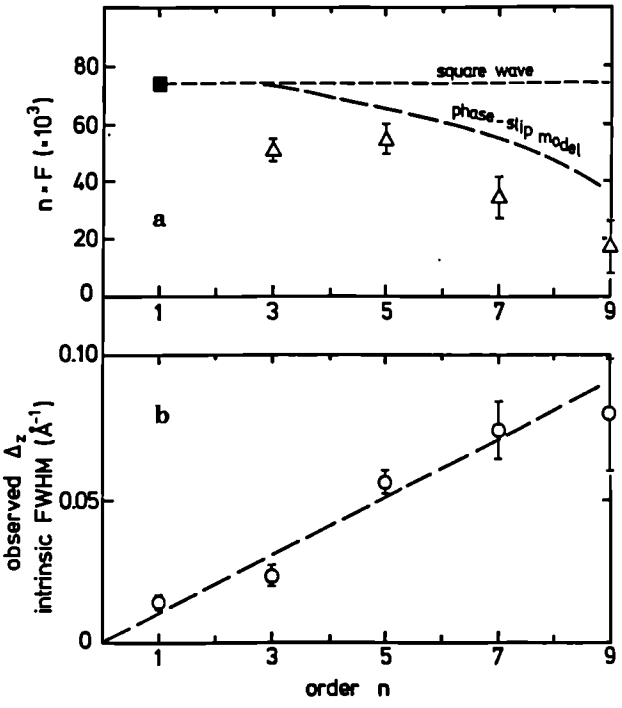


*Fig. 5.7* *(a) Structure factors multiplied by the order n for the CDW phase of a-uranium plotted as a function of n. A square wave modulation would result in nF independent of n. The 'phase-slip' or discommensuration model gives a qualitative fit to the data.*

*(b) Width of the satellites as a function of n. Simple theories give a linear dependence on $n^2$ rather than n*

## Magnetic phase diagram of NpAs

Earlier investigations of the material NpAs (with the fcc NaCl structure) identified it as one of the most interesting actinide compounds. The production of suitable high-quality single crystals at ITU has now allowed a series of complex experiments to be performed on this material, leading to a further increase in our knowledge. In Fig. 5.8 is shown the magnetic phase diagram as a function of temperature as determined by neutron experiments. NpAs becomes antiferro-magnetic at

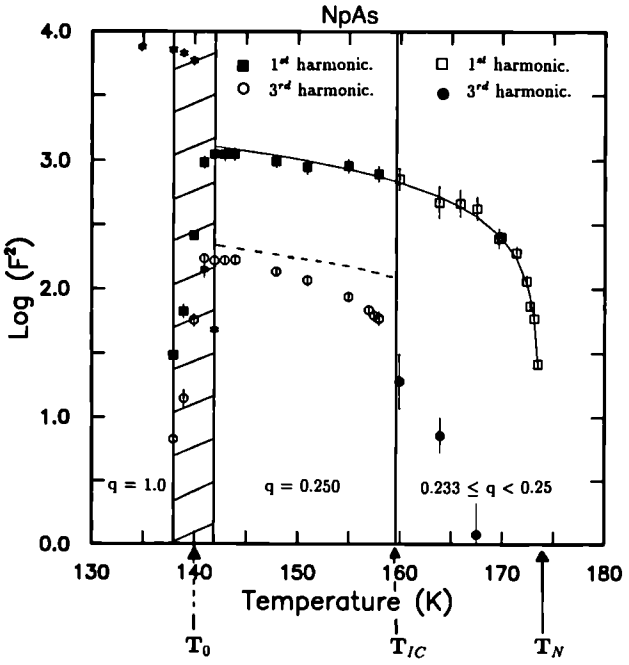


*Fig. 5.8* *Details of the magnetic phase diagram as found in NpAs. The material orders at $T_N$ with an incommensurate wavevector. As it cools the 3rd harmonic develops and leads to a gradual squaring of the modulation. At $T_{IC}$ the material becomes commensurate $q=1/4$. At $T_O$ the material suddenly develops the type I ($q=1$) structure*

174K with an incommensurate magnetic wavevector. This means that the repeat of the magnetic unit cell is not an exact multiple of the chemical unit cell, in this case 4.3 units. This sinusoidal modulation of the moments starts to square up with the appearance of the 3rd-order harmonics and this process is accomplished by 160K. Between 160K and 140K the waveform is almost an ideal square wave with a modulation of the spins given by the sequence 4+, 4- etc. However, at 140K an electronic transition occurs, as shown by the resistivity data, and the magnetic structure reverts to a simple +- configuration of spins, which has a repeat unit identical to the chemical unit cell.

The study of NpAs has also included that of the magnetic short-range correlations that appear just above $T_N$, the temperature at which the material orders antiferromagnetically. The extent and anisotropy of these fluctuations are compared to those measured in similar uranium compounds, as well as to the predictions of existing theories.

## Measurement of magnetic anisotropy with polarized neutrons

One of the key parameters in magnet device technology is the intrinsic magnetic anisotropy $K_1$. This parameter is related to the tendency for the magnetic moments to stay aligned along the easy axis of magnetisation when a magnetic field is applied in a different direction. Many devices require high $K_1$ values, such as supplied by $SmCo_5$ and $Nd_2Fe_{14}B$ magnets. When $K_1$ is large the moments are difficult to deviate from their axis and it then becomes difficult to measure $K_1$ with conventional methods.

The interaction of neutrons with the magnetic moments in a solid is vectoral in nature, and this allows a measurement independently of both the size of the moment and its direction in the solid. In principle, the determination of both these quantities allows a better definition of the anisotropy constant $K_1$.

To test this method we have performed experiments to determine $K_1$ in the actinide ferromagnet US, which is known to be highly anisotropic. $K_1$ could not be determined with any precision by magnetisation techniques. Near the ordering temperature (178K) we are able to turn the moments significantly away from the easy <111> axis and thus determine $K_1$. The latter is shown as a function of the reduced moment ($\mu/\mu_0$), which is an implicit function of temperature, in Fig. 5.9. The highest measured value of $K_1$ is $1.3\times10^8$ ergs/cm$^3$ at a ($\mu/\mu_0$) value of 0.7. Theoretical considerations based on symmetry arguments allow us to extrapolate to $(\mu/\mu_0)=1$, i.e. at T=0K, and we find $K_1\sim10^{10}$ ergs/cm$^3$. This is some 20 times greater than in $TbFe_2$, which has the highest known $K_1$ of any cubic material.

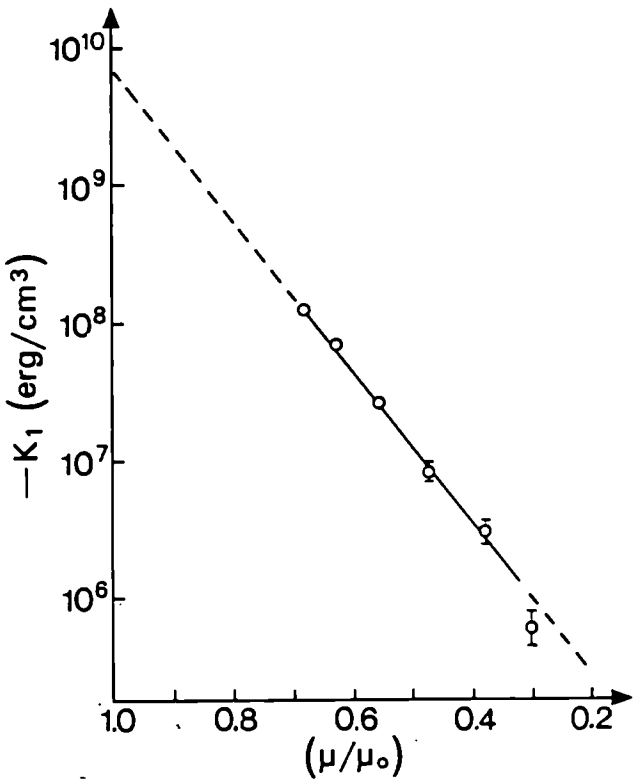


*Fig. 5.9* *Variation of the anisotropy constant $K_1$ with the reduced moment $\mu(T)/\mu(T=0)$ in US. Both quantities are determined simultaneously in the neutron experiment. The semi-log dependence of $K_1$ on $\mu/\mu_o$ is dictated by symmetry arguments and gives confidence in the extrapolation to $K_1 \sim 10^{10}$ ergs/cm at $T=0K$, the highest anisotropy yet determined for a cubic material*

These experiments have developed a new method for measuring $K_1$ and have also indicated the potential importance in using uranium based alloys, presumably alloyed with iron or cobalt to raise the ordering temperature, in device applications.

## Neutron studies of actinide oxides

The high-energy spectroscopy of the actinide dioxides was extended to $PuO_2$ in experiments at the Argonne National Laboratory's neutron spallation source and the value of the overall crystal-field potential was found similar to that identified in $UO_2$ and $NpO_2$. The value in $PuO_2$ is considerably smaller than suggested by susceptibility measurements, and the interpretation of these latter measurements remains a problem.

Considerable progress was made on the long-standing difficulty of identifying the exact nature of the phase transition at 25 K in $NpO_2$, which was first detected in specific heat experiments 25 years ago. Neutron experiments at the Rutherford Spallation Source identified an inelastic feature at ~ 7 meV at low temperature in $NpO_2$, and it is thought that this arises because of the splitting of the ground-state $\Gamma_8$ quartet into two doublets with an energy gap between them. Because of the difficulty of separating magnetic and phonon effects (arising from lattice vibrations) an experiment was then performed in collaboration with the Universities of Ancona and Parma and Rutherford Laboratory (UK) with polarised neutrons at the Institut Laue Langevin. The results are shown in Fig. 5.10.

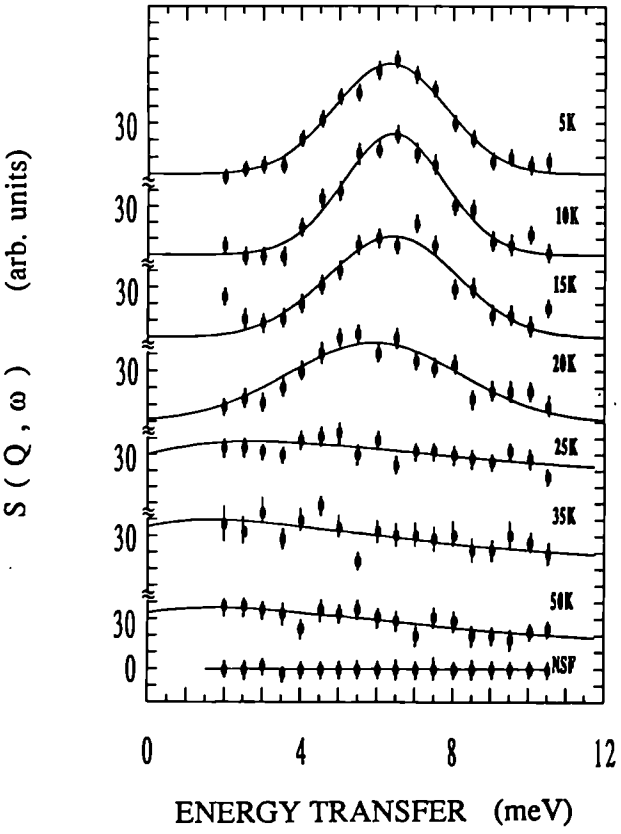


*Fig. 5.10* *Magnetic scattering as a function of temperature from $NpO_2$ showing the development below 25K of an inelastic peak at 6.5 meV due to the lifting of the degeneracy of the $\Gamma_8$ ground-state quartet below 25K*

With polarised neutrons and polarisation analysis only the magnetic scattering is observed. The splitting of the $\Gamma_8$ quartet occurs abruptly between 20 and 25 K, as shown by the sudden appearance of the peak at this temperature. Because we know from the Mössbauer results that there is no magnetic order in $NpO_2$, the lifting of the $\Gamma_8$ degeneracy at 25 K must be due to a structural transition, which is driven by the ordering of the quadruple moments.

Neutron work (at Argonne) has also been performed on a small (50 mg) sample of $^{248}CmO_2$. No ordered vacancies were found on the oxygen sublattice, indicating true $Cm^{4+}$ composition.

## X-ray resonant magnetic scattering

Recent experiments at synchrotron sources, particularly at the NSLS, Brookhaven National Laboratory, USA, have shown that X-ray scattering from ordered magnetic systems may give complementary information to that usually acquired by neutron scattering. In particular, experiments at the $M_{IV}$ and $M_V$ edges of uranium have discovered large enhancements of the magnetic signal, which is a consequence of a resonance between the excited state and the occupied unpaired 5f electrons.

The intensity from a single crystal of $UO_2$ is shown in Fig. 5.11.

We have also performed experiments on USb and $(U_{0.85}Th_{0.15})Sb$ and compared the ratios of the $M_{IV}$ and $M_V$ peaks and the intrinsic widths of the resonance lines. This is an attempt to determine whether the resonance scattering can also provide information on the electronic structure of the materials. Interestingly we find the $M_{IV}/M_V$ ratio similar for all the semimetallic uranium monopnictides, but about a factor of two higher in $UO_2$ with a ratio of ~ 16. Recent calculations by P. Carra at the ESRF have shown that these ratios can be obtained by atomic-physics type calculations, and there is good agreement assuming two 5f electrons in $UO_2$ and three in the monopnictides. These measurements provide a new form of spectroscopy [1].

The large magnetic intensities that are obtained at the M edges make X-ray resonant scattering of particular interest to investigations of actinide systems and we have already used this technique to investigate the magnetic structure of $(U_{0.85}Th_{0.15})Sb$ and we are now planning for measurements at Brookhaven on transuranium materials. Because X-ray diffraction can be done on much smaller samples than needed for neutrons, this technique offers the possibility of extending magnetic diffraction studies up to at least Bk.

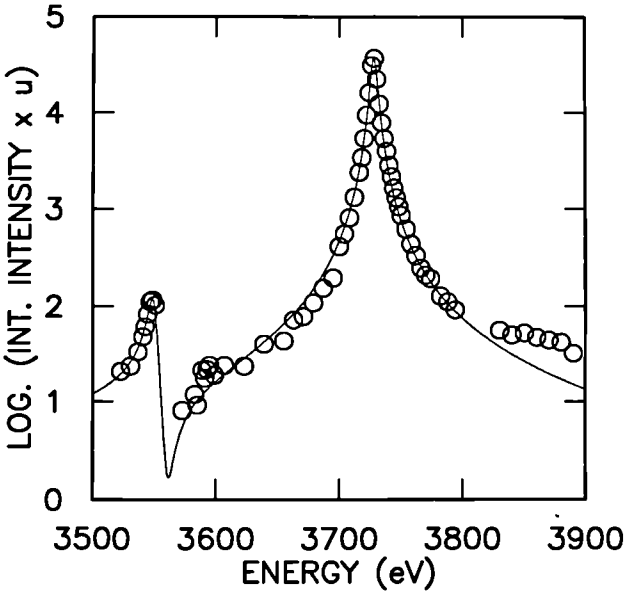


*Fig. 5.11* *Intensity (on a logarithmic scale) versus energy for the (102) magnetic reflection as measured on a single crystal of $UO_2$ at 10K. The very strong resonance effects are at the $M_{IV}$ and $M_V$ absorption edges. The solid line is a fit using resonance theory*

## Photoemission study of the electronic structure of UNiAl

5f electronic states in actinide compounds containing transition metals are strongly influenced by the hybridisation with particular d-states. The strength of the hybridisation can be affected by varying degeneration of 5f- and d-states and, generally, the localisation of 5f-states increases with d-occupation. Thus the highest localisation and increasing significance of electron-electron correlations can be expected for late transition metals.

One of the interesting compounds, UNiAl, is magnetically ordered below $T_N = 19K$. A high value of the linear coefficient of low temperature specific heat, $\gamma$, approaching the heavy-fermion range, (164 mJ/mol $K^2$) and low ordered magnetic moments indicate a rather itinerant character of the 5f electrons.[1].

High-resolution UPS experiments on UNiAl unambiguously show the presence of 5f electronic states at the Fermi energy. Valence-band spectra shown in Fig. 5.12, which were recorded for

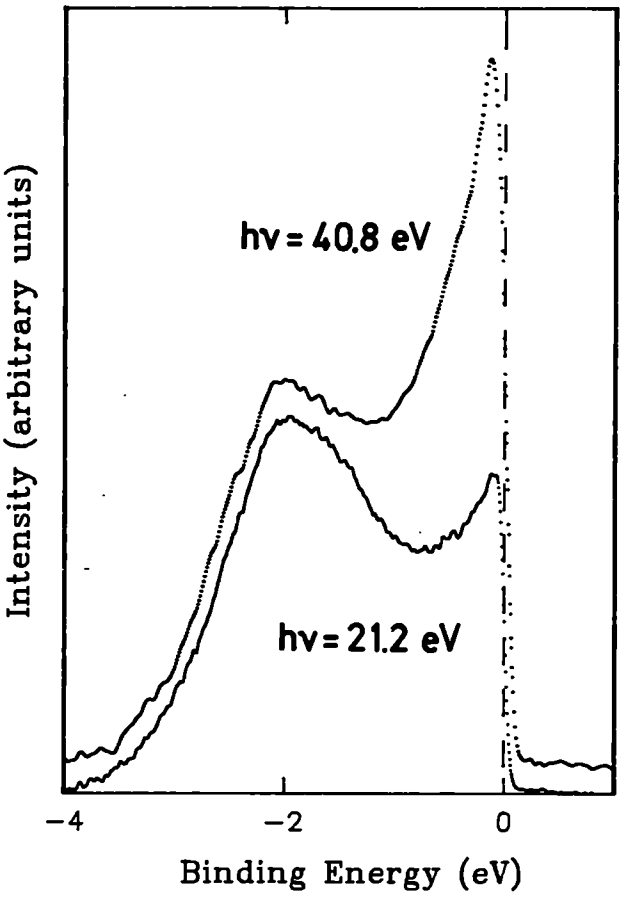


*Fig. 5.12* *UPS conduction band spectra of UNiAl for 21.2 eV and 40.8 eV excitation energies*

hv = 21.2 eV and 40.8 eV (U 5f emission is enhanced relatively to Ni 3d emission for the latter excitation energy) show the emission of 5f origin spread from $E_F$, where it reaches a maximum, down to at least -1 eV. A broad maximum found at ≃ -2 eV mainly consists of the Ni-3d spectral response. This confirms the general picture of d-states located at higher binding energies and separated from 5f states close to the Fermi energy.

The U 5f derived emission found in the vicinity of $E_F$ clearly confirms a highly itinerant 5f character what similarly is found for other uranium intermetallics with high γ-values of the low temperature specific heat. A weak additional 5f spectral intensity found for scraped, i.e. stoichiometric surfaces (with respect to Ar-ion sputtered, i.e. U rich surfaces) around 1.5 eV may be considered as a weak unresolved final state multiplet satellite which would represent correlation effects due to the beginning 5f electron localisation.

However, XPS U4f core level spectra do just display main asymmetric lines corresponding to strong screening of the U4f photo hole by itinerant 5f electrons as found in pure U metal. This contradiction is tentatively explained by the higher surface sensitivity of UPS: atoms in the topmost surface layer are arranged in lower symmetry than atoms in the bulk as probed by XPS; lower symmetry results in a weaker hybridization of the electrons, i.e. more pronounced localisation.

**Reference**

[1] L. Havela et al., Physica 163B (1990) 313

# High Pressure Studies on Actinide Systems

## B1 type compounds

The stable room temperature, ambient pressure phase of the 1:1 actinide compounds AnX is of the NaCl (B1) type. The only known exceptions are ThTe and ThBi, which are of the CsCl (B2) type, and a few truly intermetallic compounds.

This large family of isostructural compounds lends itself particularly well to a systematic study of physical properties as a function of the nature of the anion, the nature of the cation, the pressure and the temperature. A central question in such studies is whether some of the changes in properties observed are linked to the 5f electrons of the actinide element.

Following previous studies of the corresponding thorium and uranium compounds, the monoarsenides, monoantimonides, monoselenides and monotellurides of neptunium and plutonium were investigated by high-pressure X-ray diffraction.

### High-pressure phases and volume compression

NpAs and PuAs transform to the B2 (CsCl) type structure around 35 GPa, as was already ob-

served for ThAs and UAs. B2 remains the stable structure type up to the highest pressures reached, i.e. 42 GPa for ThAs, 54 GPa for UAs, 52 GPa for NpAs, and 45 GPa for PuAs.

The volume decrease between ambient pressure and the phase transition, and the volume difference between the two phases near the transition pressure, for the monoarsenides of actinides Th to Pu, had already been shown in TUAR-89, Fig. 1.8 (except for PaAs which has not been studied up to now). The volume decrease at the phase transition is of the order of 10% for all of these compounds. The cusp in the curve of the ambient pressure volumes around Pa does no longer seem to exist at pressures around the phase transition. Different high-pressure phases are formed in the monoantimonides. Fig. 5.13 shows the pressure-volume curve for NpSb. The B2 type structure was not observed in NpSb. A tetragonal high-pressure phase forms instead which can well be described in space group P4/mmm, as confirmed by calculation of theoretical intensities with the ENDIX program. This phase remains stable to 52 GPa, the highest pressure reached in this experiment. The volume decreases by about 11 % at the phase transition.

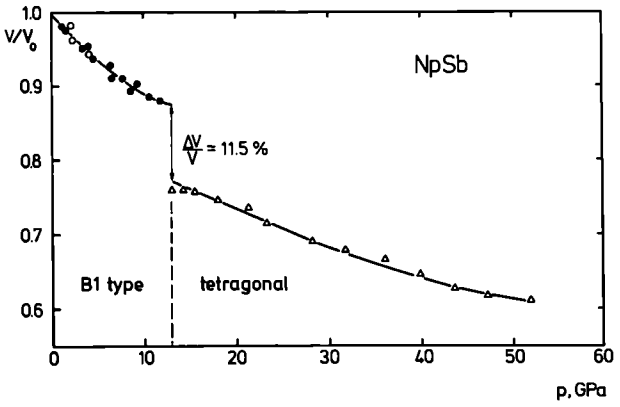


*Fig. 5.13* *Relative volume versus pressure for NpSb*
*increasing pressure:* • *B1 type*
Δ *tetragonal, P4/mm m*
*decreasing pressure:* ∘ *B1 type*

PuSb also forms a similar tetragonal high-pressure phase in the pressure range 38 to 55 GPa, but exhibits an intermediate phase of the B2 type in the pressure range 18 to 38 GPa. Here, the **total** volume decrease over **both** phase transitions is about 9 % (see Fig. 8.18 of TUAR-89).

Preliminary results are available for NpSe. These indicate that NpSe behaves very similar to PuSe. The results for PuSe were reported in TUAR-89. The monotellurides of neptunium and plutonium both have the B2 type as their high-pressure structure, as seen in Fig. 5.14. The transforma-

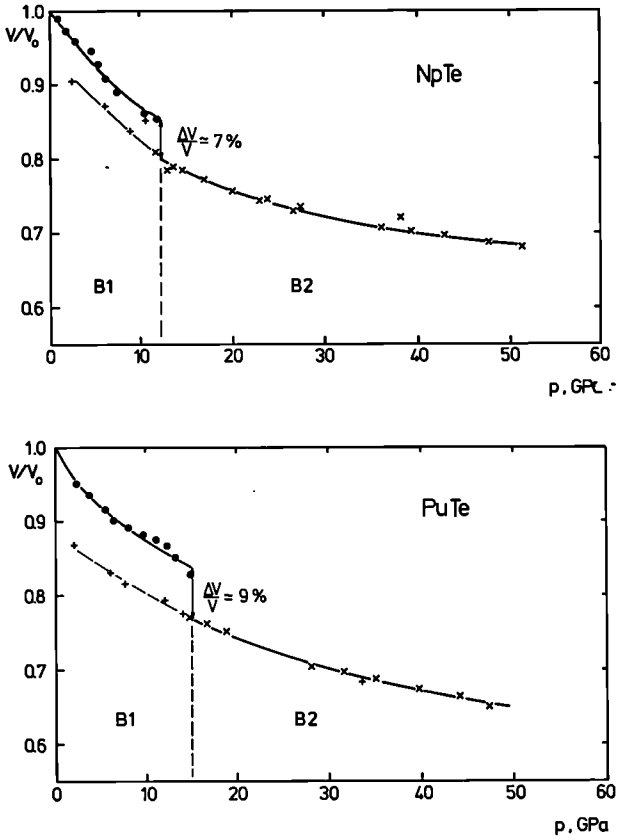


*Fig. 5.14* *Relative volume versus pressure for NpTe (a) and PuTe (b)*
*increasing pressure:* • *B1 type*
x *B2 type*
*decreasing pressure:* + *B2 type*

tions are accompanied by volume decreases of about 7 % in NpTe, and about 9 % in PuTe. The high-pressure phase did not transform further in the pressure range studied, i.e. up to about 50 GPa.

Fig. 5.15 shows comparative bar diagrams of the stability ranges of the different phases for all of the compounds studied. The indicated transition pressures refer to pressure increase. Two general trends are visible in these diagrams:

1) The transition pressures increase with increasing atomic number of the actinide

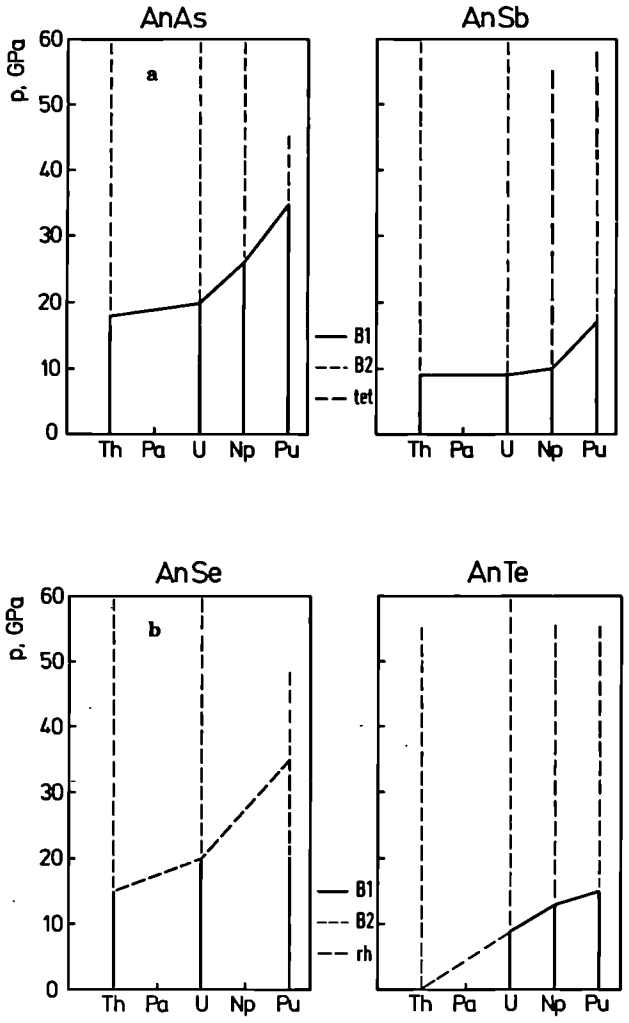


*Fig. 5.15* *Stability ranges for the different phases of AnX compounds*
*a: monoarsenides and monoantimonides*
*b: monoselenides and monotellurides,*

2) The transition pressures decrease with increasing atomic number of the anion in a given column of the Periodic Table.

## Hysteresis to re-transformation

There is in general a large difference between the transition pressure on pressure increase and the transition pressure on pressure decrease (Fig. 5.16). This hysteresis is probably due to delayed establishment of thermodynamic equilibrium. It has been shown in some lanthanide metals that a slight temperature increase reduces the width of this "hysteresis zone". It is likely that also in the case of the AnX compounds, the equilibrium transition pressure has some intermediate value. Note that for UTe and USb re-transformation to the B1 type phase does not occur at room temperature. The B2 type high-pressure phase is maintained in a metastable condition at ambient pressure. This is another example of pressure-induced preparation of a new variety of material, the most famous being high-pressure, high-temperature synthesis of diamond. It will be recalled, too, that ThTe has a stable B2 type phase at ambient pressure, or otherwise expressed, its B1-B2 transformation occurs at negative pressures. The AnTe part of Fig. 5.16 nicely shows that this behaviour fits well into the general trend of phase transitions and hysteresis.

## The bulk moduli

The variation of the bulk modulus (inverse of compressibility) and of its pressure derivative for the monoarsenides, monoantimonides and monotellurides is depicted in Fig. 5.17. There is a tendency to decrease of the bulk moduli with increasing atomic number of the actinide.

## Discussion

The results obtained on the B1 type neptunium and plutonium compounds, together with the previous results on thorium and uranium compounds, allow clear trends to be recognised for the nature of high-pressure phases, the transition pressures, the hysteresis zone, and the compressibility.

The B1-B2 phase transition is the dominating mechanism in the high-pressure structural behaviour of these compounds. This mechanism does not seem to have any link to the 5f electrons because it is also the typical pressure-induced structural transition for the alkali halides. In the actinide compounds, the B1->B2 transition is accompanied by a volume decrease of the order of 10 %. Antimony as an anion favours tetragonal high-pressure structures. Monocarbides, -nitrides, -phosphides, and -sulfides of thorium and uranium either did not transform in the pressure range studied (ThC, ThN) or transformed to structures of relatively low symmetry (UC, UN, UP, US, ThS). In this group of Th and U compounds with light anions, only ThP exhibits the B1-B2 structural transition.

The B1-B2 transition pressures generally increase with the atomic number of the actinide,

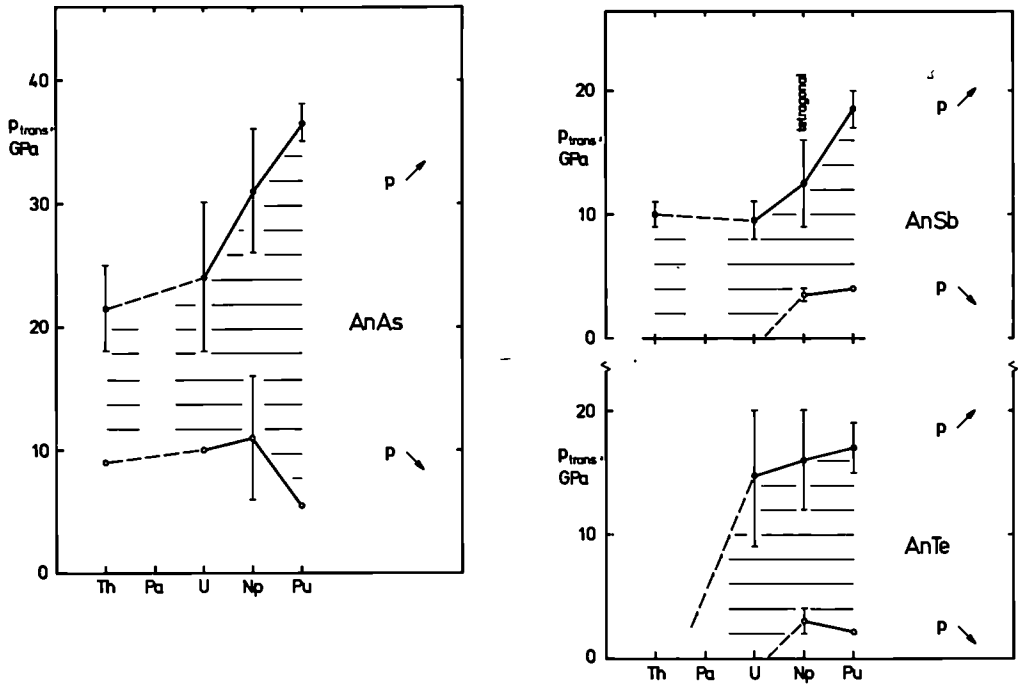


*Fig. 5.16* *Zones of hysteresis for actinide monoarsenides (left), monoantimonides and monotellurides (right). The figure shows the observed transition pressures on pressure increase and decrease. Vertical bars indicate transition ranges.*
*An: actinide*

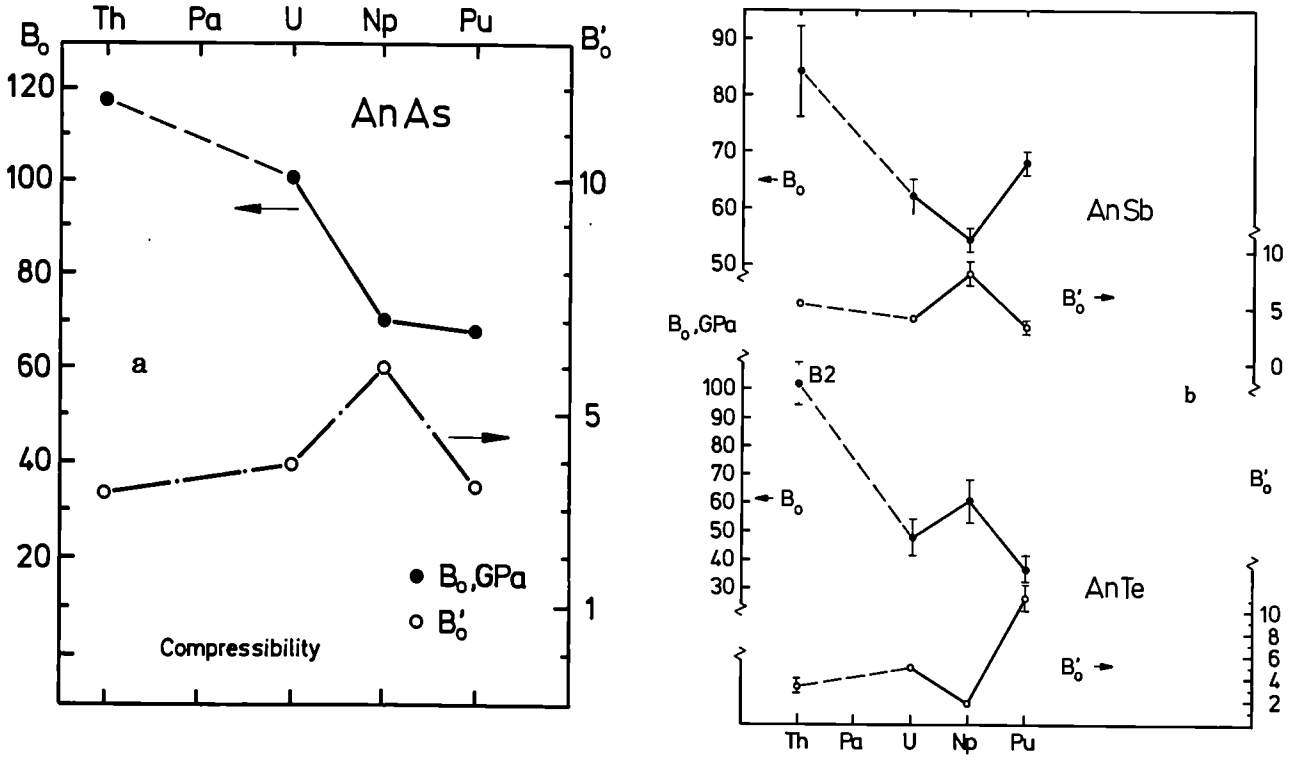


*Fig. 5.17* *Bulk moduli $B_0$(GPa) and pressure derivatives $B_0'$*
*a: actinide monoarsenides AnAs*
*b: actinide monoantimonides (AnSb) and monotellurides (AnTe)*

but decrease with the atomic number of the anion, in a given column of the Periodic Table. The hysteresis zones, i.e. the pressure ranges between transitions at increasing and decreasing pressure, have a tendency to widen with increasing atomic number of the actinide. PuAs has the largest hysteresis zone of these compounds, of the order of 30 GPa. In two uranium compounds, USb and UTe, hysteresis to re-transformation enables us to obtain metastable B2 type phases at ambient pressure.

Generally, there is a trend to increasing compressibility with increasing atomic number of the actinide element. This tendency is most clearly marked for the monoarsenides. There is also a tendency for monoantimonides to be more compressible than monoarsenides of the same actinide.

## Study of dioxides

Pressure induced phase transitions were previously reported for $ThO_2$ [1, 2], $UO_2$ [3, 4], and $NpO_2$ [5]. Recent work on $PuO_2$ showed its high-pressure phase is similar to the high-pressure phases observed for the other actinide dioxides [6].

The fluorite type structure of $PuO_2$ remains stable up to 39 GPa and then transforms to the $PbCl_2$ type structure which is stable at least to 49 GPa, highest pressure attained. On releasing pressure, a marked hysteresis is observed down to 11 GPa. The sample re-transforms to the cubic structure at ambient pressure with the initial lattice parameter. Fig. 5.18a shows the lattice parameters of $PuO_2$ vs. pressure. From the relative volume variations vs. pressure (Fig. 5.18b), we have calculated a bulk modulus of 379 GPa and a pressure derivative of 2.4, using 21 experimental values. This bulk modulus is considerably higher than those of the other actinide dioxides investigated. The volume decrease at the transition is ~ 12 %.

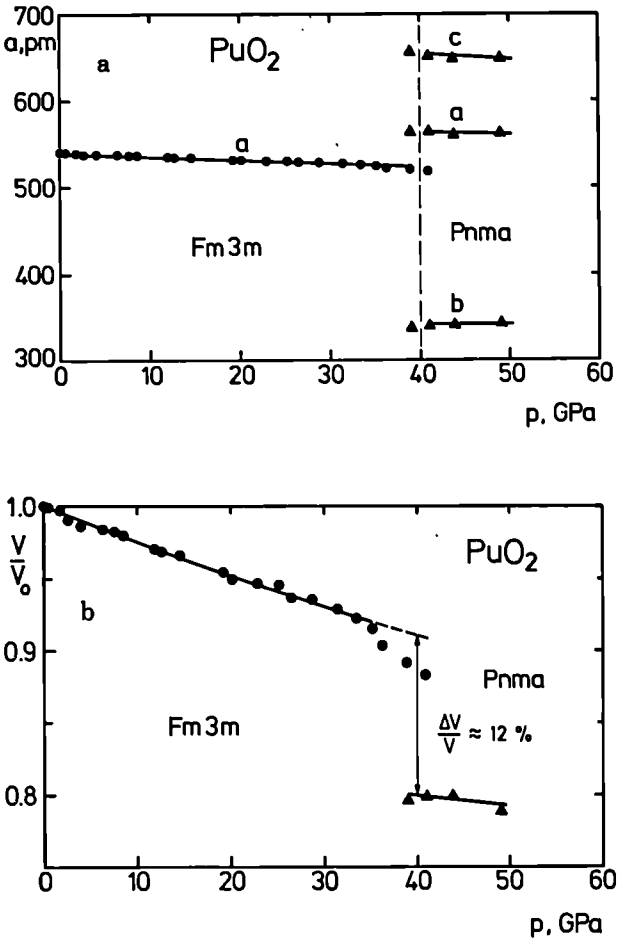


*Fig. 5.18* *Lattice parameters (a) and relative volume (b) of $PuO_2$ vs. pressure (determined on pressure increase)*
- *fluorite type*
- Δ *orthorhombic phase*

### References


[1] U. Benedict, C. Dufour, J.C. Spirlet, J. Staun Olsen, L. Gerward, Communication, 13th Journée des Actinides, 1983, Elat, Israel

[2] A. Jayaraman, G.A. Kourouklis, L.V. van Uitert, Pramana 30 (1988) 225

[3] U. Benedict, G.D. Andreetti, J.M. Fournier, A. Waintal, J. Phys. Lett. 43 (1982) L-171

[4] T.M. Benjamin, G. Zou, H.K. Mao, P.M. Bell, Carnegie Institution of Washington, Yearbook 80 (1981) 280

[5] U. Benedict, S. Dabos, C. Dufour, J.C. Spirlet, M. Pagès, J. Less Common Met. 121 (1986) 461

[6] J.P. Dancausse, E. Gering, S. Heathman, U. Benedict, High Pressure Research 2 (1990) 381


## Crystal structures of $UP_2$, $UAs_2$, UAsS and UAsSe in the pressure range up to 60 GPa

A large majority of binary and ternary compounds of actinides (An) and non-metallic elements (X, Y) with the composition $AnX_2$ or AnXY crystallises under normal conditions in the $Fe_2As$ or PbFCl type structures [1]. Very little was known about the high-pressure behaviour of these compounds. The uranium pnictides $UP_2$

and $UAs_2$ as well as the combined pnictide-chalcogenides UAsS and UAsSe were studied by X-ray powder diffraction in the pressure range up to about 60 GPa. X-ray powder diffraction spectra were recorded at HASYLAB-DESY, Hamburg, FRG, using synchrotron radiation.

A phase transformation is observed in $UAs_2$ around 15 GPa. Use of the trial-and-error indexing program TREOR [2] indicated that the Bravais lattice of the high-pressure phase is orthorhombic. Tentatively, we have assumed the $PbCl_2$ type structure with space group Pbnm (no. 62). Several actinide compounds have this structure already at normal pressure: α-$ThAs_2$, $ThS_2$, $ThSe_2$, UTeS and others [1].

There are some indications that give preference to the $PbCl_2$ type structure as the high-pressure form of $UAs_2$. Firstly, this structure has a high space filling that favours its formation at high pressure. Secondly, it is the high-pressure form of the fluorite type $UO_2$ and $NpO_2$ [3, 4] which are closely related to the $Fe_2As$ type structure of low-pressure $UAs_2$. Thirdly, the very strong peak corresponding to the lattice plane spacing 2.3 Å can be fitted to the 121 line, which according to our simulated spectra is the strongest line from $UAs_2$ with the $PbCl_2$ type structure.

The phase transformation is of the first order with a discontinuity in volume. At the transition pressure there is a volume contraction of 4% when going from the low-pressure to the high-pressure form of $UAs_2$.

A phase transformation to the same orthorhombic high-pressure phase as in $UAs_2$ takes place in $UP_2$ at about 22 GPa. At the phase transformation the volume changes discontinuously by about 7%.

In UAsS, a tetragonal to orthorhombic phase transformation takes place at about 46 GPa. When releasing the pressure the high-pressure phase is present down to about 30 GPa. The phase transition is associated with a volume change of about 7%.

The tetragonal phase of UAsSe is found to be retained in the whole pressure range investigated.

Compressibility data, transition pressures and volume decreases on transition for these four compounds are given in Tab. 5.5.

*Tab. 5.5 Compressibility data, transition pressure, and volume decrease on transition for uranium compounds of the $Fe_2As$ structure type*

| Compound | $B_0$/GPa | $B'_0$ | $P_t$/GPa | $\frac{\Delta V}{V}$ % |
|---|---|---|---|---|
| $UP_2$ | 124(15) | 9(2) | 22 | 4 |
| $UAs_2$ | 101(8) | 4.7(7) | 15 | 7 |
| UAsS | 105(7) | 3.7(5) | 46 | 7 |
| UAsSe | 99(6) | 3.8(5) | - | - |

**References**


[1] U. Benedict, J. Less-Common Metals 128 (1987) 7-45

[2] P.E. Werner, M. Westdahl, J. Appl. Cryst. 18 (1985) 367-370

[3] U. Benedict, G.D. Andreetti, J.M. Fournier, A. Waintal, J. Physique Lettres 43 (1982) L171-L177

[4] U. Benedict, S. Dabos, C. Dufour, J.C. Spirlet, M. Pagès, J. Less-Common Met. 121 (1986) 461-468


## A high-pressure study of $Th_3P_4$ and some $U_3X_4$ compounds

The group V A elements P, As, Sb and Bi form cubic $Th_3P_4$-type compounds with the actinides. The space group of the crystal structure is I-43d (No. 220) with Z = 4. Each actinide atom is surrounded by eight nearest neighbours of the non-actinide element. $Th_3P_4$ and the uranium pnictides $U_3X_4$, where X = P, As and Sb, were studied in the pressure range up to 50 GPa. By X-ray powder diffraction at HASYLAB-DESY using synchrotron radiation. No structural phase transformation occurs within this pressure range. Compressibility data are summarised in Tab. 5.6.

*Tab. 5.6 $An_3X_4$, bulk modulus and its pressure derivative for ambient pressure. The uncertainties in parentheses are given in units of the last decimal place*

| Compound | $B_0$/GPa | $B_0'$ |
|---|---|---|
| $Th_3P_4$ | 126(5) | 4.0(4) |
| $U_3P_4$ | 160(15) | 4.1(9) |
| $U_3As_4$ | 121(10) | 4.3(8) |
| $U_3Sb_4$ | 93(4) | 4.2(9) |

## HPXRD study of oxychalcogenides

ThOS and UOSe have the PbFCl-type structure (tetragonal) at room temperature and atmospheric pressure. They belong to the space group P4/nmm with two molecules per unit cell. High pressure studies were performed at room temperature with a diamond anvil cell of Syassen-Holzapfel type using synchrotron radiation at HASYLAB-DESY. Hydrostatic conditions were approached by adding silicone oil as pressure transmitting medium.

ThOS was studied up to 43.3 GPa in 18 increasing pressure steps. UOSe was studied up to 47.5 GPa in 20 increasing pressure steps. No structural phase transition was observed in the whole pressure range.

Tab. 5.7 shows the bulk modulus and pressure derivative of ThOS and UOSe, These values were calculated by fitting the pressure-volume data to the Murnaghan and Birch equations.

*Tab. 5.7 Isothermal bulk moduli and pressure derivatives of ThOS and UOSe*

| | Birch $B_0$, GPa / $B'_0$ | Murnaghan $B_0$, GPa / $B'_0$ | Average $B_0$ ,GPa/ $B'_0$ |
|---|---|---|---|
| ThOS | 201 / 3.1 | 202 / 2.9 | 201.5 / 3.0 |
| UOSe | 153 / 2.1 | 155 / 1.5 | 154 / 1.8 |

## X-ray diffraction studies on samarium up to one Megabar pressure

Samarium at ambient pressure has the space group R-3m. The Sm-type structure is also found in other trivalent rare-earth metals. Jayaraman and Sherwood [1] have proposed that the sequence of pressure-induced phases is hcp-Sm-dhcp-fcc for increasing pressure. It is assumed that the 4f electrons are localised and mainly the s, p and d electrons are responsible for the metallic state and the structural sequence, which represents various stackings of hexagonal layers. Balster et al. [2], Mao et al. [3] and Grosshans et al. [4] have found that distortion of the fcc structure occurs when pressurising beyond the fcc phase. In the light rare-earth Ce there is a volume collapse (fcc-fcc) before the distorted fcc phases are observed [5]. It is believed that the collapse and the appearance of low-symmetry structures can be explained by a delocalisation of the f electrons. The present work is a structural study of Sm in the extended pressure range up to 100 GPa (= 1 Mbar).

A diamond anvil cell of the Holzapfel type was used up to 52 GPa. A small ruby chip was added to the sample for pressure determination and a methanol-ethanol mixture was used as the pressure-transmitting medium. The Megabar experiments were performed using a Mao and Bell type cell and only a fine ruby powder was placed into the cell together with the sample. Energy-dispersive diffraction spectra were recorded using synchrotron radiation at HASYLAB-DESY. Preferred orientation was partly eliminated by rotating the sample around the incident beam direction. The spectra were deconvoluted using the maximum entropy principle.

Our results confirm the structural sequence Sm-dhcp-fcc-distorted fcc for increasing pressure. The transformation pressures are roughly 6 GPa, 13-15 GPa and 19 GPa. There are no sharp boundaries and weak lines of the previous phase are normally observed. Various crystal structures have been proposed for the distorted fcc phase [6].

However, because of the rather poor resolution of the diffraction method, these structures should merely be considered as indexing schemes at present. The Sm-spectra can be satisfactorily indexed assuming a trigonal six-layered structure (space group $P3_121$) between 19 and 32 GPa and a monoclinic structure (space group C2/m) above 32 GPa. The pressure-volume data shown has been fitted to the Birch and Murnaghan equations of state with the isothermal bulk modulus $B_0$ and its pressure derivative $B_0'$ as parameters. The result is shown in Tab. 5.8 and compared with literature data. A collapsed fcc structure is not observed and there are no volume changes at the phase transitions in the observed pressure range.

*Tab. 5.8. Bulk modulus and its pressure derivative for Sm*

| $B_0$/GPa | $B_0'$ | Reference |
|---|---|---|
| 30.7(19) | 2.5(1) | This work |
| 27.2(6) | 2.8(1) | Grosshans et al. (1987) [6] |
| 37.3 | | Gust & Royce (1973) [7] |
| 27(1) | 6(1) | Bridgman (1964) [8] |

**References**

[1] A. Jayaraman and R.C. Sherwood, Phys. Rev. 134 (1964) A691
[2] A. Balster and J. Wittig J. Low Temp. Phys. 21 (1978) 377
[3] H.K. Mao, R.M. Hazen, P.M. Bell and J. Wittig J. Appl. Phys. 52 (1981) 4572
[4] W.A. Grosshans, Y.K. Vohra, W.B. Holzapfel Phys. Rev. Lett. 49 (1982) 1572
[5] J. Staun Olsen, L. Gerward, U. Benedict and J.-P. Itié Physica 133B (1985) 129
[6] S.K. Sikka and V. Vijayakumar, Physica 144B (1986) 23
[7] W.A. Gust, E.B. Royce, Phys. Rev. B 8 (1973) 3595
[8] P.W. Bridgman (1964) Collected Experimental Papers, Harvard University Press, Cambridge

# Actinide Information Centre

## The data base system THERSYST for the Storage and Handling of Thermophysical Property Data of Actinides and Actinide Compounds

### Introduction

It is one of the tasks of the Institute for Transuranium Elements to collect systematically and keep readily available bibliographical references and physical, chemical, and radiological data related to actinides and transuranium elements. Of particular importance for technical applications are thermophysical property data of actinide compounds, especially of those which are or may be used in the context of nuclear energy production.

The Institute has been involved in experimental and theoretical studies of thermophysical properties (thermal conductivity, thermal diffusivity, heat capacity, thermal expansion, thermal radiative properties) of nuclear fuel materials over many years and thus contributed to a world-wide effort.

During the reporting period we have started to store thermophysical data on actinides produced in our laboratory or collected from the literature in a data basesystem (THERSYST) which has been developed especially for the storage and handling of thermophysical parameters at the Institut für Kernenergetik und Energiesysteme of the University of Stuttgart, Germany [1,2].

### Description of principal features of THERSYST

THERSYST does not only store bibliographical references or abstracts from publications, but also the relevant contents of these publications in numerical form or in the form of codes. These contents may then be further manipulated, for example with an option to establish relations between thermophysical data and materials parameters on which they depend. So, the sample material is characterised by a series of descriptors which enables the user to study in detail the effect e.g. of chemical composition or structure, on a given materials property. THERSYST offers thus the possibility to analyse a multitude of even widely differing experimental data in view of their validity for a well defined practical application.

This implies that not only the measured data but also descriptors for materials specification and the experimental environment must be stored. A complete THERSYST data set may contain up to 200 numerical descriptors and codes to describe information which can not be quantified.

### Application of THERSYST capabilities to the treatment of published thermal conductivity data of uranium dioxide (Example).

Experimental data for the thermal conductivity of uranium dioxide samples of various stoichiometries and densities as a function of temperature from 91 sources are compiled in Fig.5.19.

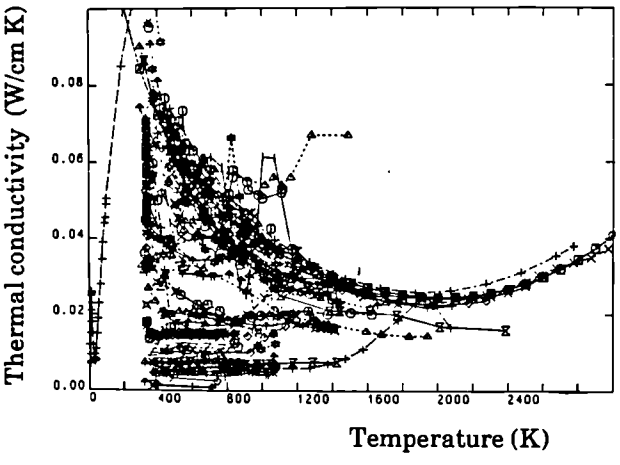


*Fig. 5.19 Thermal conductivity of $UO_2$; available data*

THERSYST is capable, from this input, to establish a relationship between conductivity and porosity (Fig.5.20).

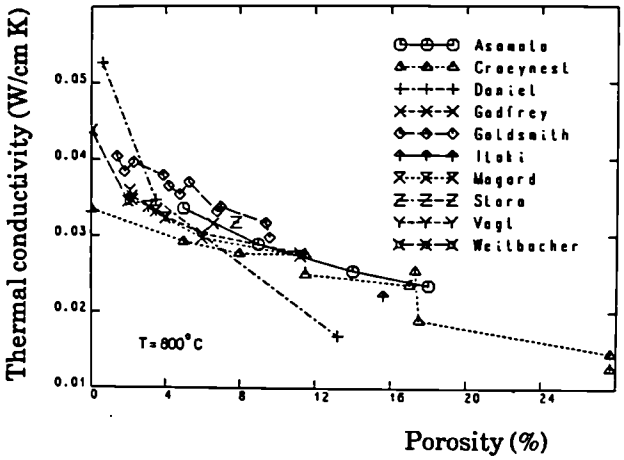


*Fig. 5.20 Porosity dependence of the thermal conductivity of $UO_2$ from the data set in Fig.5.19*

A "recommendation" for the temperature dependence of the thermal conductivity of non-irradiated stoichiometric $UO_2$ from selected experimental data established with the help of THERSYST on the basis of the data set in Fig.5.19 is given in Fig.5.21.

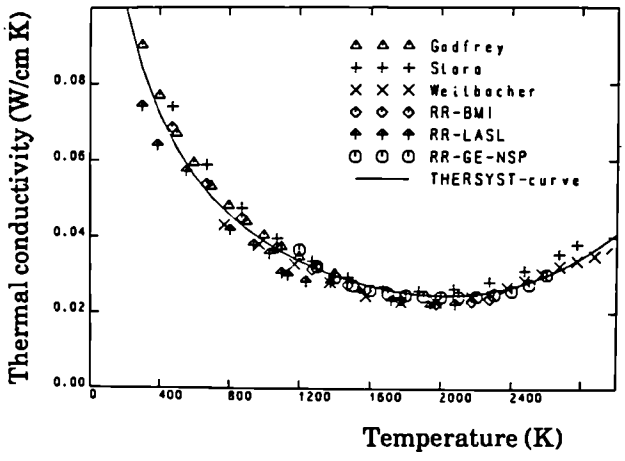


*Fig. 5.21 Thermal conductivity of stoichiometric $UO_2$ from the data in Fig.5.19*

The corresponding analytical expression for the recommended curve as produced by THERSYST is

$$\lambda = \frac{1}{A + B \cdot T} + C \cdot T \exp(D/kT)$$

with A = 5.90, B = 0.01986, C = 3.35 $10^{-4}$ and D = - 0.9499, where $\lambda$ is given in W/mK and T in K (k: Boltzmann constant).

## Status of THERSYST-ACT, the thermophysical properties data base for actinides and actinide compounds

During the reporting period, 179 publications on thermophysical properties of actinides and actinide compounds have been selected from the INIS bibliographical data bases (> 1970) and from Ref.[3] (< 1970) and evaluated. Of these, the contents of 147 articles concerning 72 compounds have been stored in THERSYST-ACT in 1029 data sets.

The status is summarized in Tab. 5.9 .

**References**

[1] R. Brandt, K. Löffer, G. Jaroma-Weiland, G. Neuer, G. Pflugfelder, THERSIST, Eine Datenbank für thermophysikalische Eigenschaften, Report IKE 5-229, Institut für Kernenergetik und Energiesysteme, Universität Stuttgart, 1987.

[2] THERSYST - Thermophysical Properties databank for solid materials. User's'Handbook. Report IKE-5TB-899-87, Institut für Kernenergetik und Energiesysteme, Universität Stuttgart, 1987

[3] J. Richter, H.E. Schmidt, H.A. Tasman, Bibliography on Heat Transport in Nuclear Fuels and related Phenomena, Report EUR 5119, 1974.

*Tab. 5.9* *List of thermophysical properties (number of data sets) of actinide compounds stored in THERSYST-ACT*

| | λ | a | $c_p$ | H | ρ | α | d | ε |
|---|---|---|---|---|---|---|---|---|
| aluminium oxide | - | - | 1 | 1 | - | - | - | 2 |
| americium dioxide | - | - | - | - | - | 5 | - | - |
| berkelium dioxide | - | - | - | - | - | 1 | - | - |
| magnesium oxide | - | - | - | - | - | - | - | 2 |
| neodymium oxide | - | - | - | - | - | - | - | 1 |
| neptunium dioxide | - | - | - | - | - | 1 | - | - |
| plutonium dioxide | 13 | 8 | 3 | 3 | - | 8 | - | - |
| thorium dioxide | 3 | 3 | 2 | 2 | - | 4 | - | 2 |
| uranium oxide $U_3O_8$ | - | - | 3 | - | - | - | - | - |
| uranium oxide $U_4O_9$ | 1 | 1 | - | - | - | - | - | - |
| uranium dioxide | 68 | 23 | 10 | 7 | 1 | 12 | 1 | 3 |
| americium-uranium dioxide | 4 | 2 | - | - | - | - | - | - |
| chromium-uranium oxide | - | - | - | - | 3 | - | - | - |
| europium-uranium dioxide | 6 | 6 | - | - | - | - | - | - |
| gadolinium-uranium oxide | 6 | 6 | - | - | 3 | - | - | - |
| lanthanum-uranium oxide | - | - | - | - | 1 | - | - | - |
| niobium-uranium oxide | - | - | - | - | 6 | - | - | - |
| neodymium-plutonium dioxide | 8 | 8 | - | - | - | - | - | - |
| neodymium-uranium dioxide | 6 | 6 | - | - | - | - | - | - |
| neptunium-uranium dioxide | 4 | 3 | - | - | - | - | - | - |
| plutonium-thorium dioxide | 1 | - | - | - | - | | - | - |
| uranium-plutonium dioxide | 97 | 47 | 26 | 9 | 10 | 14 | 1 | - |
| plutonium-yttrium dioxide | 8 | 8 | - | - | - | - | - | - |
| samarium-uranium dioxide | 6 | 6 | - | - | - | - | - | - |
| thorium-uranium dioxide | 7 | 6 | 7 | 7 | - | 2 | - | - |
| titanium-uranium dioxide | - | - | - | - | 1 | - | - | - |
| uranium-yttrium dioxide | 6 | 6 | - | - | - | - | - | - |
| americium-uranium-neptunium dioxide | 2 | 1 | - | - | - | - | - | - |
| plutonium-uranium-neodymium oxide | 4 | 4 | - | - | - | - | - | - |
| plutonium-uranium-europium oxide | 4 | 4 | - | - | - | - | - | - |
| uranium-plutonium-titanium dioxide | 1 | - | - | - | - | - | - | - |
| plutonium-uranium-zirconium dioxide | - | - | - | - | - | 3 | - | - |
| uranium oxycarbide | 8 | - | - | - | - | - | - | - |
| uranium arsenide | - | - | 1 | - | - | - | - | - |
| uranium-cerium carbide | 4 | 4 | - | - | 1 | - | - | - |
| uranium-molybdenum dicarbide | 2 | 2 | - | - | - | - | - | - |
| plutonium monocarbide | 1 | 1 | 8 | 4 | 1 | 3 | - | - |
| plutonium sesquicarbide | - | - | 4 | 2 | - | 3 | - | - |
| plutonium dicarbide | - | - | - | - | - | 1 | - | - |
| plutonium-uranium carbide | 12 | 3 | 1 | 2 | 2 | 4 | - | - |
| uranium-plutonium-cerium carbide | 2 | 2 | - | - | 1 | - | - | - |
| uranium-plutonium-zirconium carbide | 3 | 3 | - | - | 3 | - | - | - |
| uranium-rhodium dicarbide | 1 | 1 | - | - | - | - | - | - |
| uranium-ruthenium dicarbide | 1 | 1 | - | - | - | - | - | - |
| tantalum carbide | - | - | - | - | - | - | - | 1 |

## Tab.5.9 cont'd

| | λ | a | $c_p$ | H | ρ | α | d | ε |
|---|---|---|---|---|---|---|---|---|
| thorium dicarbide | 1 | - | - | - | 1 | - | - | 2 |
| uranium monocarbide | 41 | 11 | 7 | 4 | 28 | 13 | - | 3 |
| uranium sesquicarbide | 1 | 1 | 2 | 2 | - | 2 | - | - |
| uranium dicarbide | 4 | 3 | 4 | 4 | 2 | - | - | 8 |
| uranium-zirconium carbide | - | - | - | - | 1 | - | - | 1 |
| plutonium-trifluoride | - | - | 1 | 1 | - | - | - | - |
| plutonium tetrafluoride | - | - | 1 | 1 | - | - | - | - |
| plutonium mononitride | 5 | 5 | 4 | 3 | 1 | 2 | - | - |
| plutonium-uranium nitride | 2 | 3 | 1 | 1 | 1 | 3 | - | - |
| trithorium-tetranitride | - | - | - | - | 1 | - | - | - |
| uranium mononitride | 14 | 7 | 11 | 8 | 17 | 2 | - | - |
| uranium sesquinitride | - | - | 3 | 3 | - | - | - | - |
| plutonium monophosphide | - | - | | - | 1 | - | - | - |
| uranium monophosphide | 3 | 2 | 5 | 3 | 2 | - | - | - |
| triuranium tetraphosphide | - | - | 1 | 1 | - | - | - | - |
| uranium monoselenide | - | - | 2 | 1 | - | - | - | - |
| plutonium monosulfide | - | - | - | - | 1 | - | - | - |
| thorium monosulfide | - | - | 2 | - | 1 | - | - | - |
| thorium-uranium monosulfide | - | - | 6 | - | 3 | - | - | - |
| uranium monosulfide | 3 | 2 | 5 | 2 | 7 | - | - | - |
| uranium silicide | - | - | 1 | 1 | - | - | - | - |
| uranium monotelluride | - | - | 1 | - | - | - | - | - |
| uranium antimonide | - | - | 2 | - | - | - | - | - |
| uranium carbonitride | 16 | 16 | - | - | 22 | 1 | - | - |
| uranium cerium carbonitride | - | - | - | - | - | 1 | - | - |
| uranium carbide - uranium* | 1 | - | - | - | - | 1 | - | - |
| plutonium dioxide - 304 SS* | - | - | - | - | - | 2 | - | - |
| * binary systems | | | | | | | | |
| total: 1029 data sets | 380 | 215 | 125 | 72 | 122 | 88 | 2 | 25 |

λ : thermal conductivity
a : thermal diffusivity
$c_p$ : specific heat
H : enthalpy
ρ : electrical resistivity
α : thermal expansion
d : density
ε : emissivity

# 2 Exploratory Research

## Acoustic Aerosol Scavenging

### Introduction

The aim of this project is to investigate the feasibility of using high intensity sound to remove particulate material from the air. The basic idea is to agglomerate the fine particles (aerosol) by the use of a sound field, to a size large enough that they precipitate out either due to sedimentation in the gravitational field or by the action of some externally applied field (e.g. by an electric field in an electrostatic filter). These agglomeration and precipitation steps form the basis of the scavenging process. Potential applications range from routine treatment of industrial off-gases (to improve the efficiency of current separation technology) to large scale 'open-air' applications (e.g. tunnel fires, chemical explosions, fog clearance in restricted ares, pest control in agriculture, smouldering fires in underground rubbish dumps etc.).

During this reporting period as an Exploratory Research project, the effectiveness of acoustic agglomeration has been clearly demonstrated on solid, liquid, and mixtures of solid and liquid aerosols under *static* conditions on small(0.6m$^3$), medium(15m$^3$), and large scale(170m$^3$). These results confirm earlier expectations and provide a scientific platform for launching the more industrially relevent *dynamic* experiments. A brief description is given of what we hope to achieve with this system. Finally, we have identified key areas which will require further investigation in order to exploit fully the potential of acoustic aerosol scavenging.

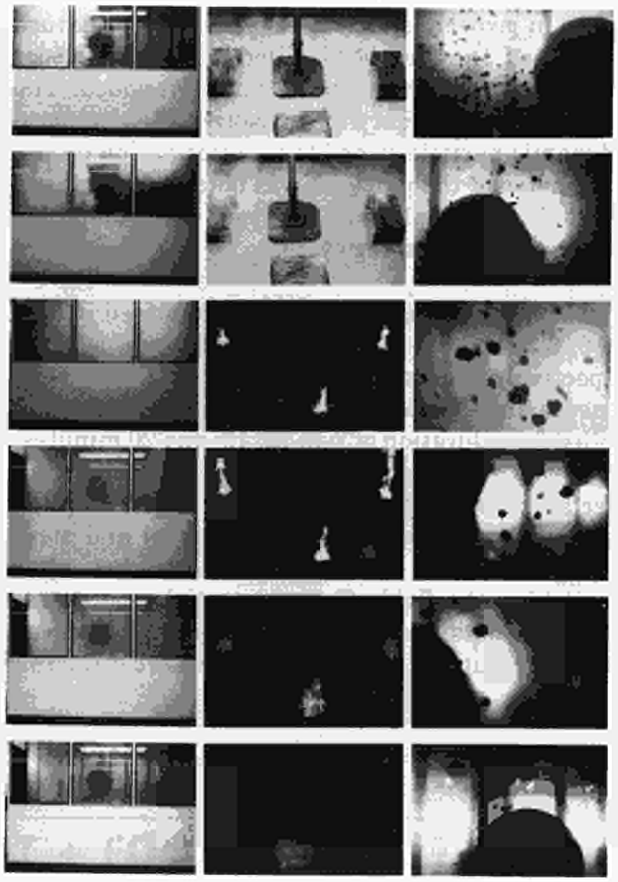

*Fig. 6.1* *Series of photographs showing acoustic agglomeration and precipitation of fog and soot in a 15 m$^3$ chamber*

### Static Experiments

#### 15 m$^3$ chamber

The experiments were carried out in a 15 m$^3$ chamber shown in Fig. 6.1. The acoustic power was provided by three 400 W piëzo-electric transducers operating at a frequency of 21 kHz, and with a conversion efficiency of approximately 70% (electric to acoustic power). The resulting sound pressure level ranged from 160 dB along the axis of the transducer, to 140 dB far from the sound sources. Aerosols of smoke (solid) and artificial fog (liquid) were used. Burning 200g of porous foam resulted in a dense black soot aerosol from the condensation of the hot gases. After a few minutes, the fire self-extinguishes leaving behind an aerosol with mass loading $M_L$ = 1 gm$^{-3}$, concentration N = $10^6$ cm$^{-3}$, and particle diameters of a few microns. The artificial fog was produced by a commercially available device. A liquid mixture containing glycerine is heated rapidly to produce a very hot (> 300 °C) vapour. Rapid expansion through a nozzle, followed by turbulent

mixing with "cold" air, results in immediate condensation of the vapour to produce a fine, low vapour pressure liquid aerosol. After fifteen seconds of operation, the fog device produces a dense white aerosol with $M_L$ = 1 g $m^{-3}$, concentration N = $10^6$ $cm^{-3}$, and particle diameters around 0.8 µm. In experiments where an aerosol mixture was used, the chamber is filled initially with soot particles to which the liquid aerosol is added. The aerosol distribution was measured using an aerodynamic particle sizer (APS). Information on the geometry of the particles was obtained by taking glass slide samples and analysed by a computerised image processing system.

The experimental results are summarised in Figs 6.2, 6.3, and 6.4 for fog, soot, and fog + soot respectively. In each figure, data from five experiments are shown in which the sound field is applied for a duration of 2, 5, 10, 15, and 20 minutes. To separate clearly acoustic and non-acoustic effects, the sound field is switched on ten minutes after filling the chamber with aerosol and measurements are continued ten minutes after switching the field off. Total particle concentrations are obtained from the APS by summing over the distributions, examples of which are shown on the right-hand side of each figure. Information on the particle geometry is obtained by taking samples on glass slides (results of which are shown on the left-hand side of each figure). The main conclusions are as follows [1].

## Fog

The concentration of liquid droplets decreases by three orders of magnitude from $10^6$ to $10^3$ $cm^{-3}$ during twenty minutes of acoustic treatment. The variation of log(N) vs t shows a distinct change of slope after approximately five minutes. acoustic treatment. During this time, log (N) decreases linearly over two orders of magnitude - consistent with the orthokinetic mechanism of agglomeration and a rate equation of the form dN/dt = - KN. Further evidence for this mechanism is provided by the emergence of a second peak in the distribution function. In the following 15 minutes acoustic treatment a different mechanism dominates the agglomeration process which now occurs on a much longer timescale and is presumably responsible for the giant droplets (≃ 40 µm) observed on glass slide samples. This mechanism is most likely driven by the observed acoustic streaming inside the chamber.

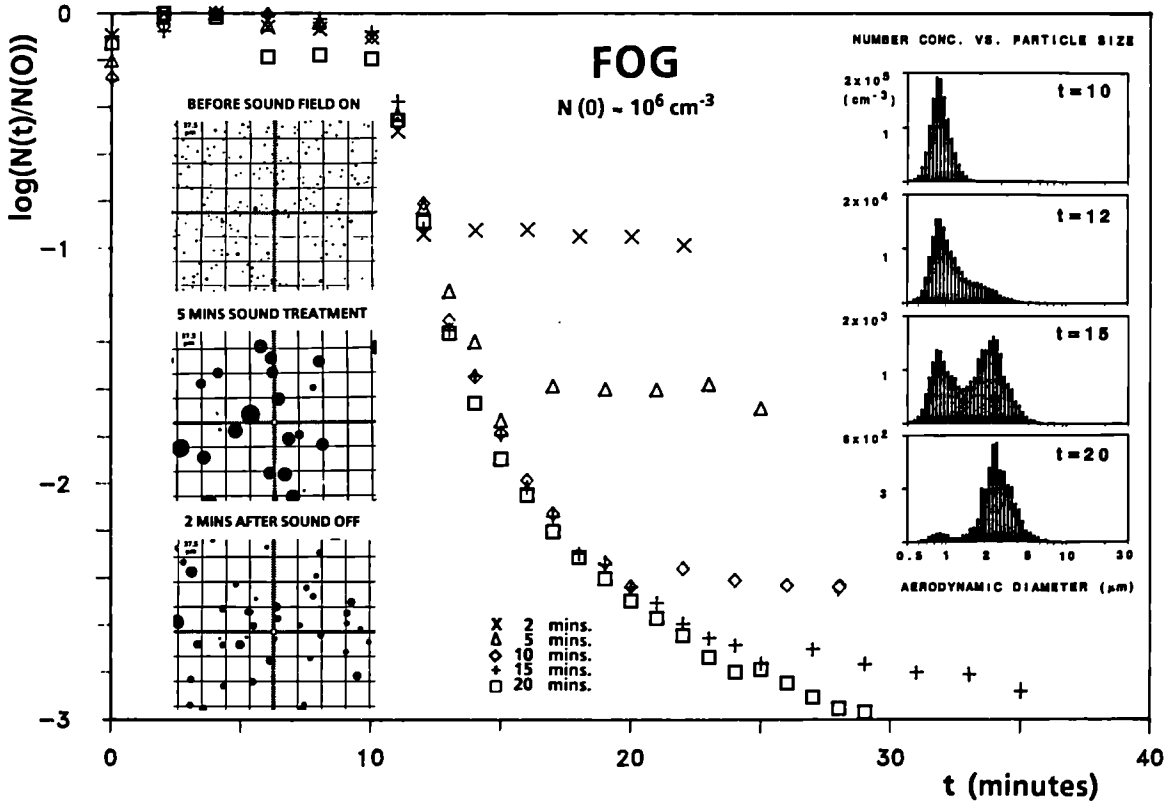


*Fig. 6.2 Acoustic agglomeration of artificial fog aerosol - summary of results*

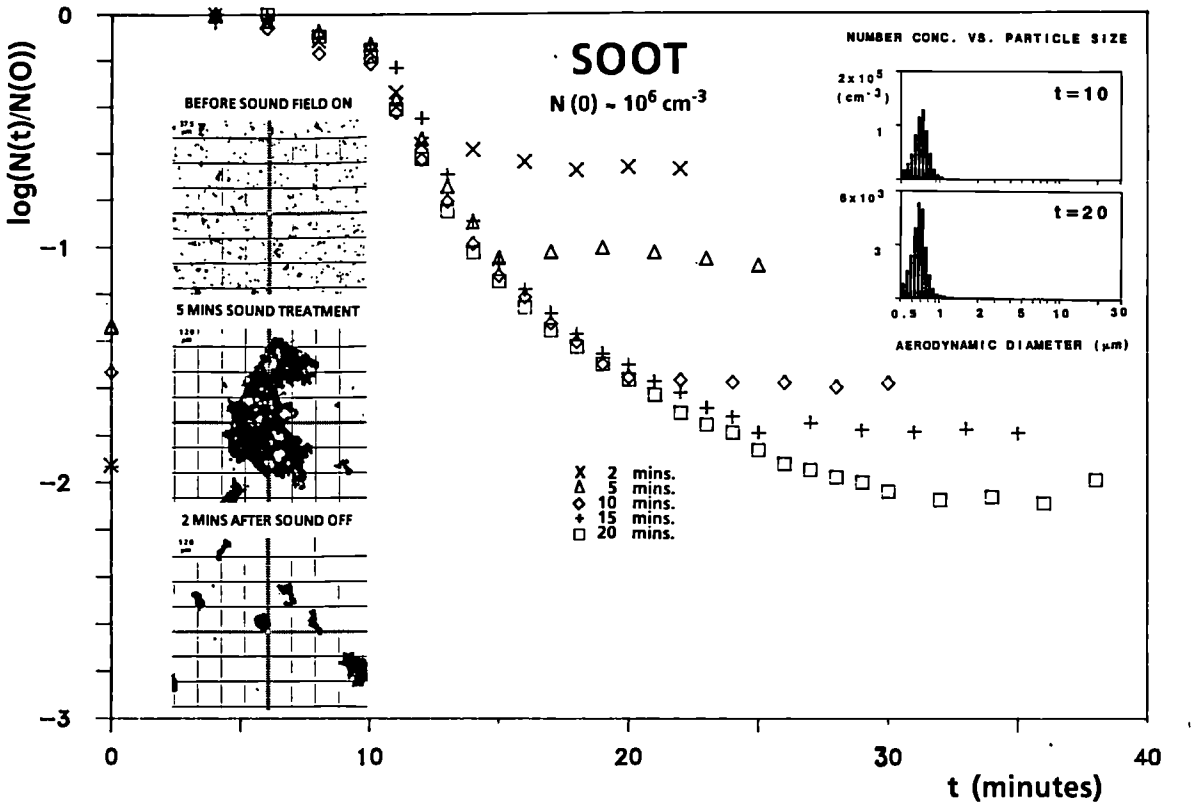


*Fig. 6.3* *Acoustic agglomeration of soot aerosol - summary of results*

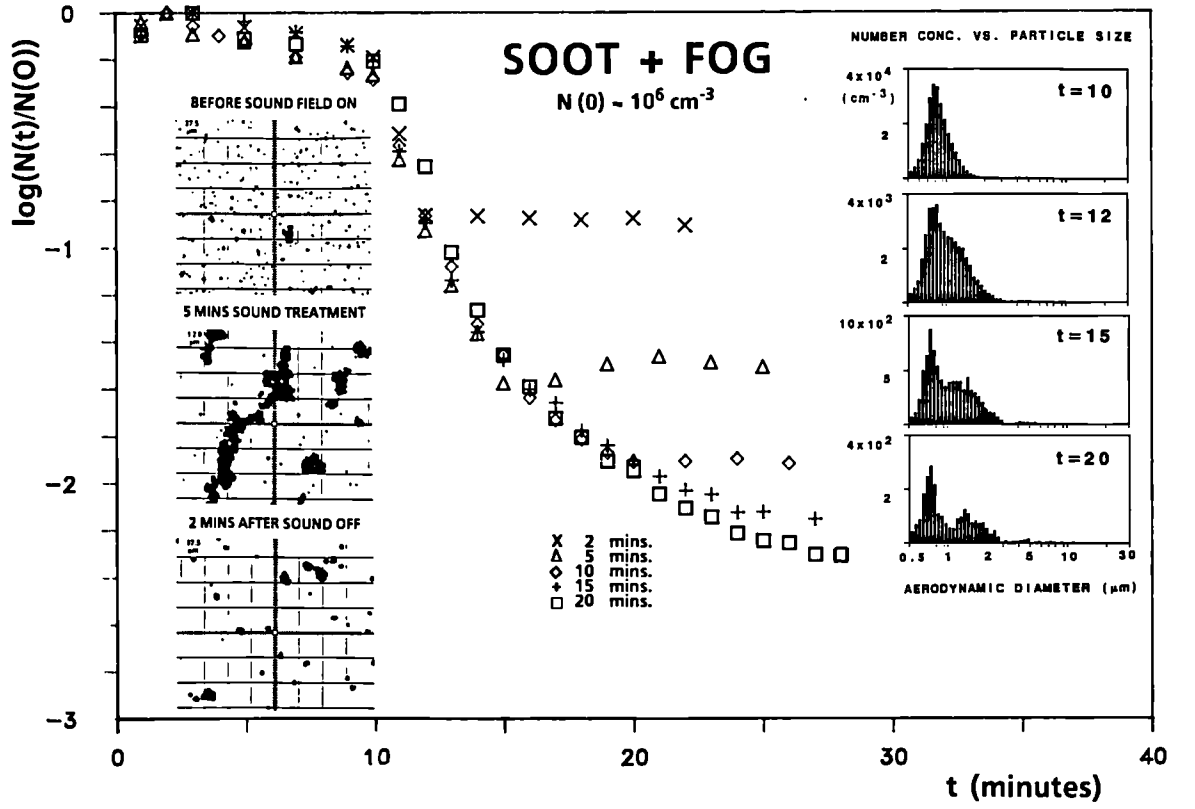


*Fig. 6.4* *Acoustic agglomeration of a mixture of soot and fog - summary of results*

## Soot

In comparison with fog, the concentration of soot particles decreases less rapidly. For the same conditions of acoustic field and starting concentrations, the soot concentration decreases by two orders of magnitude during twenty minutes acoustic treatment. The variation of log (N) vs t indicated the same two agglomeration mechanisms identified for fog. The effective (mass) density of soot agglomerates can, however, be orders of magnitude less than that of the primary particles resulting from condensation of the hot vapours. A direct consequence of this is the observed discrepancy between the geometric diameter obtained from the glass slide samples and the aerodynamic diameter measured by the APS. This discrepancy is resolved by accounting for the fractal structure of these aggregates which have a fractal dimension of = 1.7 [2]. Such calculations show that soot particles with diameters <100 μm are fully entrained in the field. Agglomeration centres for orthokinetic agglomeration are provided by particles beyond 200 μm which, however, cannot be "seen" by the present instrumentation.

## Fog and Soot

Addition of liquid aerosol particles to the soot aerosol does not result in an increase in concentration. This implies that the liquid and solid particles attach rapidly. The resulting particles have basically the same structure as soot particles but are heavier due to the presence of the liquid. The concentration of fog + soot decreases less rapidly than for fog but more rapidly than for soot. The orthokinetic mechanism of agglomeration, which we claim is occurring with soot particles beyond 200 μm, has been made "visible" in the APS distribution function by the addition of heavy liquid droplets.

## 0.6 m$^3$ chamber

In order to obtain further information on the processes important in acoustic agglomeration of aerosols, some of the fog experiments described above were repeated in a smaller (0.6 m$^3$) cylindrical chamber shown in Fig. 6.5. As the measurement equipment could be located in a vertical configuration directly underneath the chamber an improvement in the sampling of larger particles was achieved. Furthermore the particle concentration following agglomeration was sufficiently low to permit measurements without dilution of the aerosol sample, thus another source of error in the measurements was eliminated.

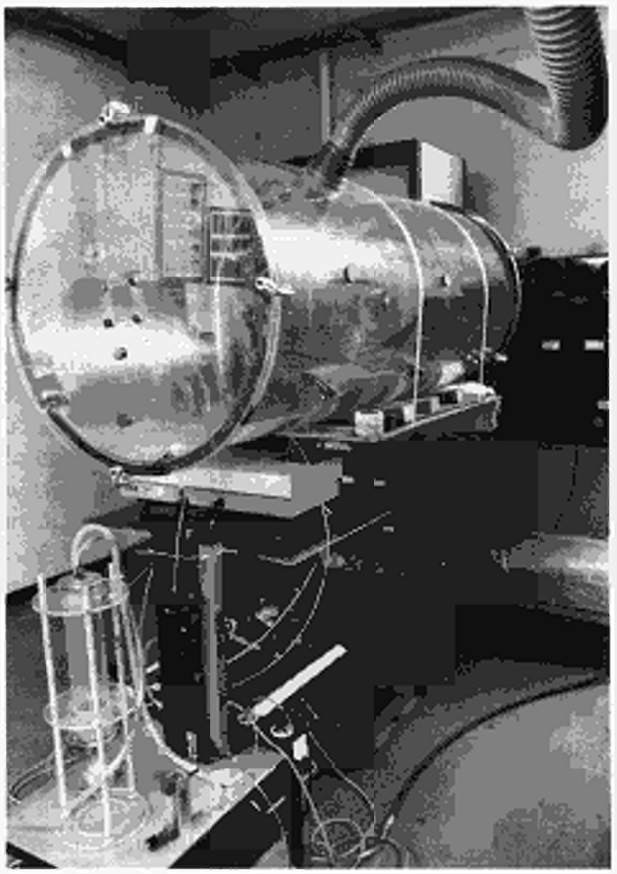

*Fig. 6.5* *The 0.6 m$^3$ agglomeration chamber with aerosol measurement equipment underneath.*

The chamber was filled with fog to give a mass loading of 1 gm$^{-3}$, a particle concentration of $10^6$ cm$^{-3}$ with particle diameters around 0.8 microns. The sound field (21kHz at a sound pressure level of 160dB) was then applied for two minutes, in which time the dense white aerosol appeared to clear completely. The results are summarised in Fig. 6.6.

The concentration of droplets decreases by three orders of magnitude from $10^6$ to $10^3$ cm$^{-3}$ within two minutes acoustic treatment. The increased rate of particle agglomeration as compared to the experiments in the 15 m$^3$ chamber is due to the higher sound pressure level attainable in the smaller chamber. Further comparison with the results for the 15 m$^3$ chamber show that after acoustic treatment the maximum in the size distribution lies at 4.5 μm (Fig. 6.6, middle panel) rather than 3 μm (see Fig. 6.2). Furthermore, a

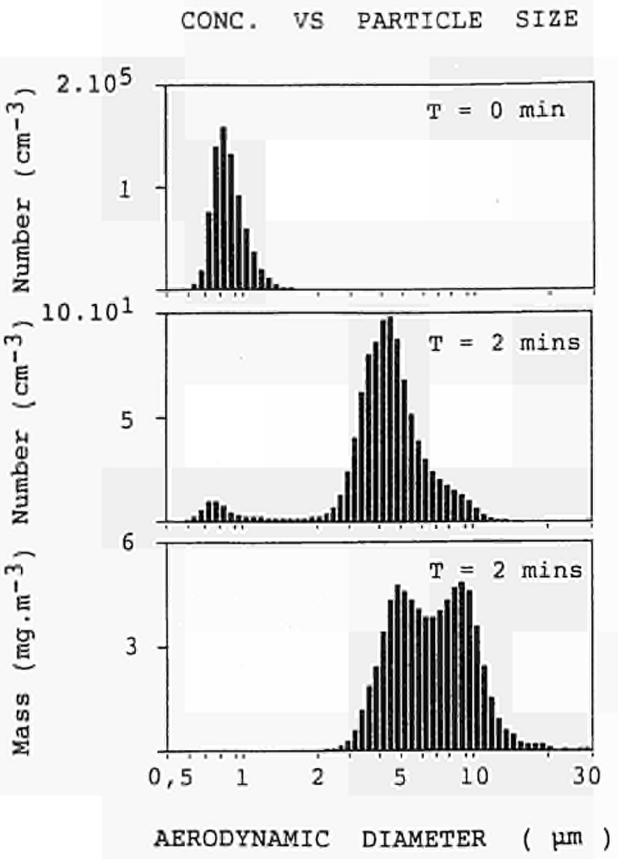


*Fig. 6.6* *Distribution functions of fog aerosol before and after sound treatment (using a 400W transducer operating at 21kHz in the 0.6 m³ chamber).*
*a) Number distribution before application of acoustic field*
*b) Number distribution of fog following 2 minutes acoustic treatment*
*c) Mass distribution after acoustic treatment.*

shoulder in the distribution curve at 8 µm is clearly recognised in the measurements made in the smaller chamber. Its presence is demonstrated more dramatically when the mass of aerosol as a function of size is plotted as is shown in the bottom panel of Fig. 6.6. These small discrepancies between the data sets are due to the improved sampling conditions used in the experiments performed in the 0.6 m³ chamber.

The peak at 4.5 µm is believed to be due to agglomeration via the orthokinetic mechanism, while that at 8 µm is most likely due to acoustic streaming within the chamber. The improved accuracy of the measurements due to the vertical sampling geometry and the removal of as many dilution stages as possible is necessary if a detailed understanding of the acoustic agglomeration mechanisms is to be achieved.

## 170 m³ chamber

Application of acoustic agglomeration on a large scale, either enclosed or in open air, will require high power sound sources operating at low frequencies. The agglomeration of fog has been investigated using a pulse jet as sound source. The pulse jet is a simple device, which converts chemical energy into thermal and acoustic energy. It consists of a tube in which propane gas is ignited (see photograph in Fig. 6.7). The expanding combustion gases set up a resonant shock wave by reflection at the ends of the tube. The fundamental frequency of the jet used in these experiments was 200 Hz. A maximum sound pressure level of 140 dB could be attained. A major disadvantage of this device is the large amount of heat produced. During a typical experiment the temperature in the chamber rose to 50 C.

*Fig. 6.7* *Pulse jet in operation being used to agglomerate a fog aerosol*

The 170 m³ chamber was filled with fog so as to give a particle concentration of $7 \times 10^5$ particles $cm^{-3}$, with a particle diameter of 0.8 µm. Following operation of the pulse jet, a decrease in the particle concentration by a factor of 10 was observed. This decrease in particle concentration is partially due to evaporation as a consequence of the temperature rise in the chamber, but analysis of the particle distribution curves prior to and following operation of the pulse jet (see Fig. 6.8) indicates that the concentration decrease is also

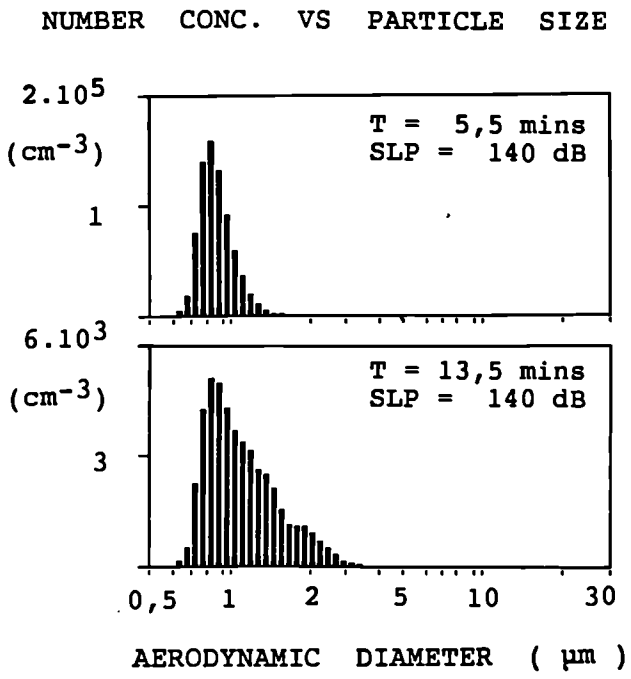


*Fig. 6.8* *Distribution function of fog aerosol size*
*a) before application of acoustic field*
*b) following 8 mins acoustic treatment (using a pulse jet at 200 Hz)*

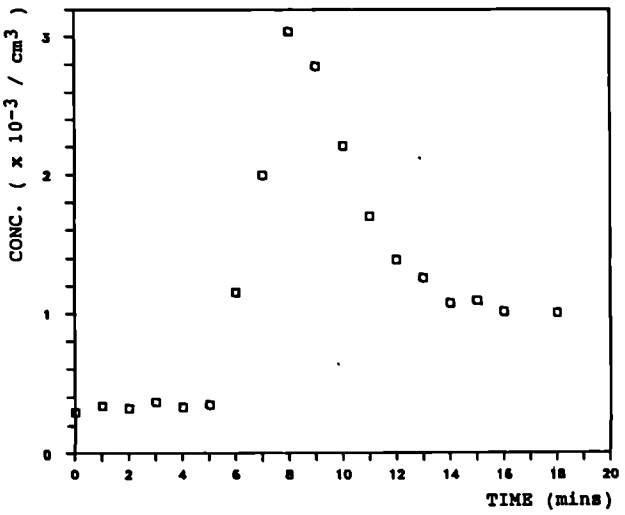


*Fig. 6.9* *Time evolution of 1.98 µm diameter fog particles during exposure to the pulse jet (200Hz, 140dB). The pulse jet is switched on at t=5.5 minutes and off at t=13.5 minutes*

partially due to agglomeration of the droplets. More pronounced evidence for agglomeration is found by plotting the concentration of 1.98 µm particles as a function of time during a typical experiment. Such a plot is shown in Fig. 6.9. During the first five minutes of the experiment the pulse jet is not running. After 5.5 minutes the pulse jet operates under normal resonant conditions, whereupon a sharp increase in the number of 1.98 µm particles is observed. This increase is due to agglomeration of smaller particles. Eventually the concentration of 1.98 µm particles begins to decrease due to further agglomeration to produce yet larger particles.

Consideration of the possible mechanisms giving rise to agglomeration shows that the orthokinetic mechanism cannot play a significant role for this combination of frequency and particle size. The observed agglomeration could be due to streaming induced by the combustion gases. Control experiments in which compressed air was passed through the pulse jet in the presence of fog tend not to support this mechanism. As yet, the exact mechanism remains unidentified but further experiments using a combination of seed aerosols and a more efficient sound source, which does not generate so much heat, will certainly assist in the solution of this problem. Nevertheless, the observed agglomeration of the fog aerosol indicates that the pulse jet could be used as a sound source in the mitigation of larger scale hazards in an enclosed environment.

# Future Research Directions

In the course of the research project we have identified four key areas which require further investigation and could form the basis of a new research project. A brief description of these key areas follows:

## Collection efficiency of scavenging centres

To agglomerate aerosols by a sound wave, energy is dissipated. For large scale applications the energy requirements may become prohibitive. The power dissipated through viscous absorption is shown in Fig. 6.10 as a function of sound wave frequency and particle diameter. As can be seen of the diagram, for a mass loading of 1 g $m^{-3}$ and a particle diameter of 1 µm, the power dissipated at 20 kHz is about 9 W · $m^{-3}$.

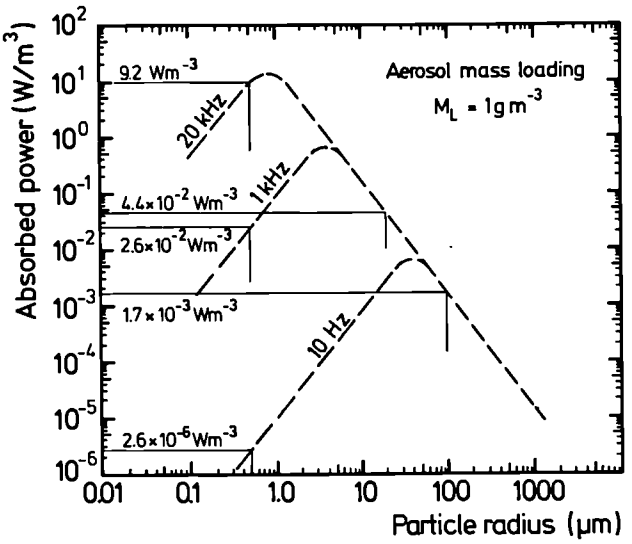


*Fig. 6.10* *Power dissipated through viscous sound absorption by aerosol of unit density in air as a function of particle diameter and sound frequency*

This absorbed power can be considerably reduced by working at lower frequencies. The problem here, however, is, that the fine aerosol particles are now fully entrained in the sound field, i.e. they are all moving backwards and forwards in phase with each other, and no agglomeration can take place. This difficulty can be overcome by the use of scavenging centres or "seed" aerosols.

These "seed" particles are much less entrained in the field and can act as scavenging centres. Consider a seed aerosol with a particle diameter of 33 μm at a mass loading of 1 $gm^{-3}$. The power dissipated by the 1 and 33 μm particles together through viscous absoprtion at a frequency of 1 kHz and a sound pressure level of 140 dB is, from Fig. 6.10, now only 0.09 W $m^{-3}$ (c.f the value of 9 W · $m^{-3}$ for 1 μm diameter particles at 20 kHz).

The power requirements can be further reduced by the use of infrasound. In this case one is forced to use seed particles around 200 μm to ensure differential entrainment. The difficulty here, however, is that during the time it takes for a small particle to complete one cycle of motion, the heavy seed particle has fallen a distance much greater than its diameter and "misses" the particle to be scavenged. In principle this problem can be solved by suitably designing the seed particles. They must be heavy enough not to be entrained in the sound field but have enough resistance to motion in the vertical direction to ensure sufficient collisions with the small particles during one cycle of the wave.

Another difficulty arising here, however, is due to the tendency for small particles to follow the streamlines and thereby flow around the large particle, thus reducing the collection efficiency. This type of problem is well known in cloud physics where considerable effort has been made to determine the collection rate of aerosol particles by water droplet scavenging.

In particular, Greenfield [3] identified a "gap" in the collection efficiency of atmospheric particles by rain drops. He showed that the collection efficiency of particles with radius in the range 0.1 - 1 μm is very low, whereas for larger and smaller particles it is much higher due to Brownian motion and inertial impaction, respectively. Since this early work, the calculations have been considerably refined to include the effects of phoretic forces and electric charge on the particles [4, 5, 6]. It is sufficient to state here that the most recent calculations [7] indicate that the collection efficiency is very sensitive to the radius of the particles to be collected. Based on inertial impaction calculations, the collection efficiency of particles in the range 1 - 5 μm varies by many orders of magnitude.

These calculations were made for water droplets based on the terminal velocity of such droplets in air. In the case of acoustic scavenging, it is the horizontal velocity of the fine particles, induced through viscous coupling to the sound wave, which leads to collision and collection by the scavenging centre (approximately 70 cm $s^{-1}$ for a sound pressure level of 140 dB). An additional complication arises due to the fact that as the seed particle grows, a rough surface will develop which will tend to increase the collection efficiency. Detailed investigations on these points are required.

## Fractal nature of solid agglomerates

The fractal dimension of a solid aggregate is of crucial importance in determining the aerodynamic behaviour of the particle. This is seen clearly in Fig.6.11 where the particle velocities are compared for (a) spherical liquid particles and (b) fractal solid aggregates. The fractal aggregates have such a low effective density that the sedimentation velocities can be orders of magnitude lower than for spherical particles of the same diameter. In addition, an aerosol distribu-

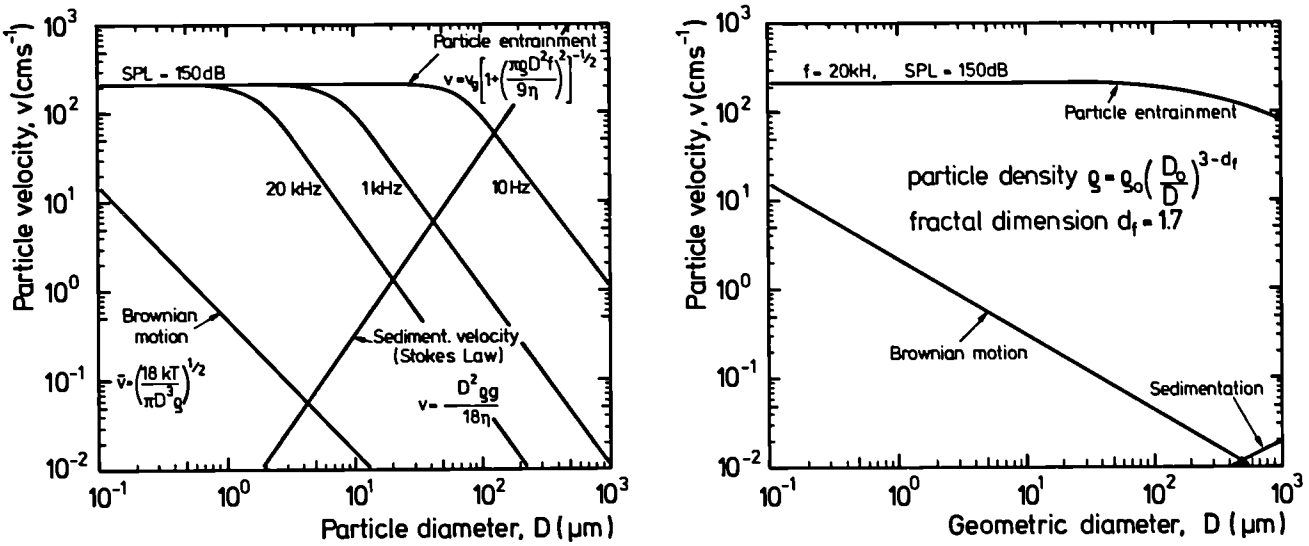


*Fig. 6.11* *Particle velocities due to Brownian motion, sedimentation and enhancement in a sound wave*
*a) for spherical particles with unit density and*
*b) for solid aggregates with fractal dimension 1.7*

tion function which may be strongly polydisperse with regard to the "geometric" diameter is monodisperse with regard to the aerodynamic diameter. These effects are also very important for industrial applications.

## Gas scavenging/acoustically enhanced gas scrubbing

The basic idea here is to extend the application of particle scavenging to gases. In the "wet gas washing" process used at some power stations the $SO_2$ present in the flue gases is removed by making the gas rise against a downpour of water drops (acting as scavenging centres) containing dissolved lime ($CaCO_3$). When NOx has to be removed the "seed" aerosol is water droplets containing ammonium hydroxide for the downpour. The byproducts in these processes are $CaSO_4$ and $NH_4NO_3$. The efficiency of this process can be increased by the application of high intensity sound. In principle any gas can be scavenged either through the chemical reactions in the above processes or through absorption by using activated carbon or zeolites as scavenging centres. The action of the sound field is to increase the effective volume of gas swept out by the falling scavenging centre. Our own preliminary investigations on the use of activated carbon aerosol to remove $NO_x$ in a sound field gave positive results.

## Acoustic power sources

To date, most of our experimental work has been carried out with piezo-electrically driven transducers operating at a frequency of 21 kHz. For industrial and large scale applications it is necessary to use lower frequencies to increase the total volume treated and the residence time of the aerosol. At present, high efficiency, highly directive transducers are being constructed for operation at 10 kHz. In the longer term, transducers operating at 5 kHz and 1 kHz will be constructed on the same principles. For open air applications other power sources are being investigated. Pulse jets running on propane gas are of interest here because of their very high chemical power rating (hundreds of kilowatts). Conversion of chemical to acoustical energy is, however, very inefficient (< 1%). Infrasound sources capable of delivering 1 kW of acoustic power are commercially available. They are, however, bulky, and have a very poor directionality. Ideally for such applications one would like to have a source working at low frequencies with high directionality.

## Discussions and Conclusions

In the area of gas cleaning technology there is, at present, a renewed interest in the problem of fine particle collection. Future bylaws of the European Community relating to particle emission will almost certainly be more specific with regard to the number concentration of fine particles in addition to limiting the maximum mass concentration. The acoustic preconditioning system [7] offers a potential solution to this important problem. Nevertheless several questions have to be solved for successful application on a large scale.

For efficient industrial application it is necessary to decrease the strong linear and non-linear attenuation produced at ultrasonic frequencies. To overcome this limitation we are using new emitters at lower frequencies (10 kHz) and with more extensive radiator area (670 mm in diameter). In this way the aerosol volume and power capacity of the system are increased. The immediate target is to develop transducers operating at 10 kHz with a power capacity of 1 kW.

With respect to large scale open air applications (tunnel fires, chemical explosions, fog clearance in restricted areas), the prospects are to work in the frequency range of 1 to 5 kHz or even lower, in order to reach high intensity levels over long distances. Large low frequency transducers with the corresponding electronic equipment should be developed in the future. In practical for open air applications an array of high power transducers of 5 kHz should be used to work in emergency situations. The main problem which arises here, i.e. the increased attenuation of the acoustic field and the dispersion of the toxic cloud by wind can be overcome by increasing the acoustic power. The "acoustic pollution" produced by working with sound sources operating in the audible range can be minimized due to the directivity of the transmitters and by restricting their application to non-routine hazard mitigation.

Last but not least, a deeper knowledge of the complex mechanism involved in acoustic agglomeration of aerosols is absolutely necessary for a succesful scaling of this process towards large scale applications.

**References**


[1] J. Magill, K. Richter, S. Fourcaudot, P. Barraux, J.A. Gallego-Juarez, E. Riera-Franco De Sarabia, G. Rodriguez-Corral, 'Agglomeration of Aerosol and Aerosol Mixtures in a Sound Field', Frontiers of Nonlinear Acoustics: Proceedings of 12th International Symposium on Non-Linear Acoustics, pp. 615 - 620, Edited by M. F. Hamilton and D. T. Blackstock, Elsevier Science Publishers Ltd; London, 1990.

[2] Forrest, T.A. Witten, J. Phys. A, **B12** (1979) L 109, Long-range correlations in smoke-particle aggregates

[3] S. Greenfield, J. Meteor. 14 (1957) 114, Rain scavenging of radioactive particulate matter from the atmosphere

[4] J. Latham, Rep. Prog. Phys. 32 (1969) 69

[5] J.M. Hales, in Wiley Series in "Advances in Environment Science and Technology", John Wiley & Sons, New York 1986, p.211, Precipitation Chemistry, Its Behaviour and its Calculations

[6] P.K. Wang, S.N. Grover, H.R. Pruppacher, J. Atmos. Sci. 35 (1978) 1735, On the Effect of Electric Charges on the Scavenging of Aerosol Particles by Clouds and Small raindrops

[7] J.A. Gallego-Juarez, E. Riera-Franco De Sarabia, G. Rodriguez-Corral, J. Magill, K. Richter, S. Fourcaudot, P. Barraux, 'An Acoustic System for Particulate Precipitation', to be presented at the 1st International Conference on Environmental Pollution, Lisboa, Portugal.

# 3 Scientific-Technical Support to Community Policies

## Introduction

In 1990, about 15% of the Institute's research potential was devoted to activities in support of the policies of the European Commission. The major part of it dealt with the execution of analyses for the EURATOM Safeguards Directorate and with the development and refinement of analytical methods in this context.

Work was started to develope and test automated equipment and to train staff in anticipation of a project to install laboratories for safeguards analyses on-site at reprocessing plants in Sellafield and La Hague.

To a lesser extent, Institute staff were involved in activities to develope laboratory equipment for industrial use on behalf of the Commission's Directorate on Innovation and Technology Transfer.

# Support to DG XVII

## Laser Ablation

In order to extend the ICP-MS method to the chemical analysis of solids, the samples have to be transformed into an aerosol before they are carried on to the ICP-torch for ionization. The technique reported here is that of laser ablation, by which a short pulse of infra-red laser light is focused onto the solid sample to be analyzed; the ablated particles are collected and transported by a flow of argon. The laser is operated at a high repetition rate, to produce a continuous flow of aerosols to the ICP-MS. This is necessary to achieve a stable signal.

The laser ablation technique is not yet completely understood, and the settings of the laser pulse and of the argon flow have to be empirically determined to produce an optimum signal on the mass spectrometer for a given mass range. For the study of the laser ablation process itself and its efficiency as a function of the experimental parameters, a special cell has been constructed and mounted in a caisson. A system of mirrors allows the light beam to be transported from the laser room (constant temperature, non-contaminated zone) to the caisson, where radioactive material can be handled. The laser used for this study is a frequency doubled Nd:YAG, generating a visible light beam at 0.532 µm wavelength. The pulse length is 25 ns, and the pulse energy 45 mJ. A dye unit can be added to the system to study the influence of the wavelength of the laser. The pressure in the argon filled cell can be varied from 0.125 to 1 bar. The laser beam enters the cell through a window; three other windows are used for visual observations and optical diagnosis of the ablated aerosol. The cell is also equipped with a metal disk collector, held at a potential of 2 to 4 kV and positioned above the sample. From the crater of a sintered $UO_2$ sample after 1 shot at 130 mbar, (Fig. 7.1), it is evident that no melting of the surface occurred during ablation. The crater diameter is 0.2 mm. Fig.7.2 shows a collected particle of 4 µm diameter, which was ablated from the surface (pressure in the cell : 250 mbar).

The model 320 Laser Sampler (Perkin Elmer) has been acquired for use with the ICP-MS. The laser is a Nd:YAG, operating at 1064 nm, delivering 320 mJ in 2.5 to 8 ns, with a maximum frequency of 15 Hz. In order to obtain a continuous flux of aerosol, one must either scan the laser light over the surface or stay on the same spot, and shoot hundreds of times on it, or a combination of both. For the characterisation of highly active materials, the sampling cell has to be placed within a hot cell : this implied some modifications of the original device. A periscope will be installed on the hot cell, and protected against contamination by a "booting" : the laser can be fixed on the wall, outside the hot cell, and the light sent to the sample through the periscope. The focusing lens is mounted at the end of the periscope, just above the sampling cell. A parallel viewing optical path allows observation of the sample through the periscope, permitting adjustment of the laser spot with a video-camera. The aerosol is carried up to the ICP-MS by means of a 10 m teflon tube. Most of the instruments are therefore outside the hot cell, which facilitates maintenance operations.

Before definitive installation of the laser sampler

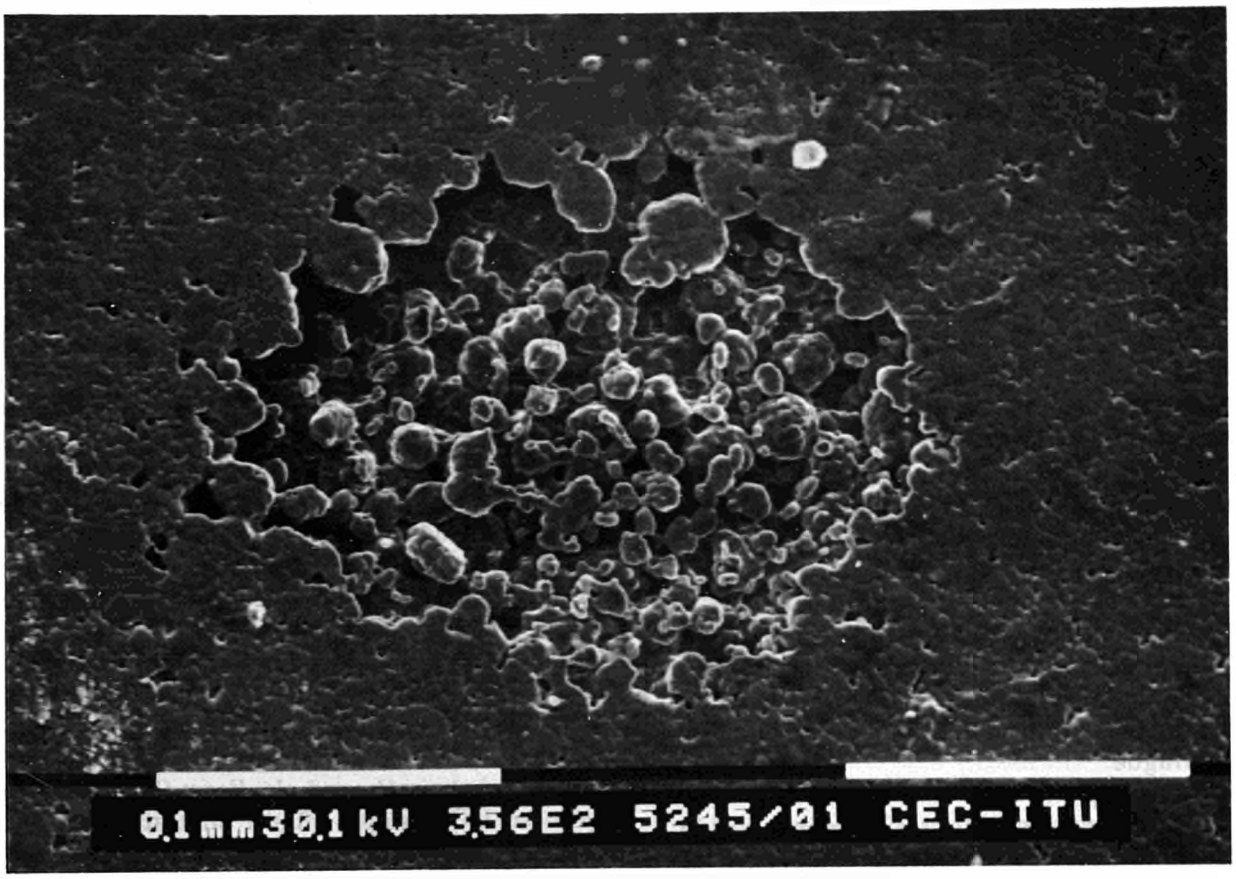


*Fig. 7.1* *Surface of sintered $UO_2$ pellet after 1 laser shot (532 nm, 25 ns, 45 mJ)*


*Fig. 7.2* *Particle ablated from $UO_2$ pellet*

in the hot cell, some tests were done with a simulated HAW glass, and with a certified reference powder (lake sediment, NBS SL-1) containing traces of uranium utilising various laser powers and shooting times. The reference material was analysed both as powder and as a pressed pellet. When ablation is started, the ion intensity for a given mass number increases sharply and reaches a plateau after about 1 minute of sampling. The precision of the steady signal for 4 ppm uranium was 3.8%. The other elements present in the reference material in the 1 to 0.1 ppm range were clearly detected. Semi-quantitative analysis, using internal standards, resulted in concentrations within one order of magnitude of the certified values for most of the elements. The mass spectrum obtained with the simulated HAW glass is shown in Fig.7.3 ; the major elements are clearly identified, and traces of rare earths, thorium and uranium were detected.

## Analysis of Fines coming from the Dissolution of an LWR Fuel

The fines (0.1-15 µm) from a fuel solution were analysed for their chemical composition by ICP-MS and for their isotopic composition by thermal ionisation mass-spectrometry (TIMS). The original fuel was a LWR fuel with an original uranium enrichment of 3.28% and a burn-up of 34,274 MWd/t U. The fuel was dissolved in the WAK reprocessing plant in a continous process. After separation of the main residue, samples of 3ml were taken and filtered. One of these filters with 204 mg of fines was transferred to the Institute for analysis.

Using a dissolution procedure used for simulated residues [1], i.e. dissolution in an autoclave at

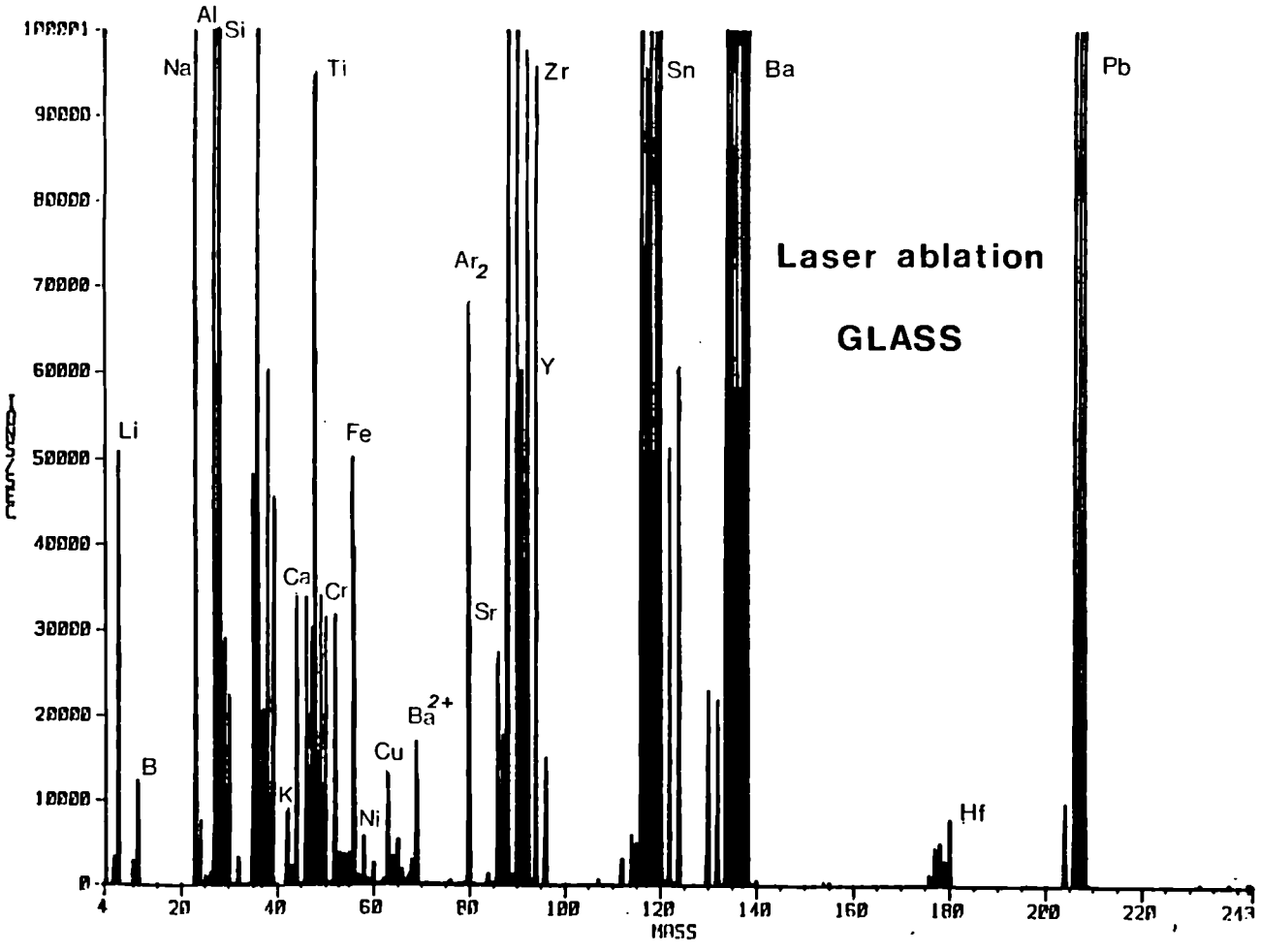


*Fig. 7.3 Qualitative analysis of a simulated HAW glass obtained by ICP-MS and laser ablation*

180 °C in a mixture of HCl and $HNO_3$ (9:1) for 24 hours a complete dissolution of 23 mg of the residue was achieved, obtaining a final volume of 100 ml. This solution was been analysed by α- and γ-spectrometry and after a dilution of 200 times were analysed by ICP-MS and IDMS. An attempt to determine the crystallographic structure was not successful because of the high radiation dose-rate coming from the sample.

At present a semi-quantitative mass spectrum has been obtained by ICP-MS (Fig. 7.4.). A quantitative evaluation has not yet been completed. The results by IDMS are shown in Tab. 7.1. A total of 639 µg of U (2.78%) and 1090 µg of Pu (4.74%) was found in the residue. The Pu value corresponds to 613 µg of $^{239}Pu$ (2.67%) confirmed by an α-spectrometric analysis of the same solution, where 690 µg of $^{239}Pu$ (3%) were found. Furthermore 50 µg of $^{241}Am$ (0.22%) and 28.3 pg of $^{244}Cm$ (1.2ppm) were measured. Gamma analysis showed the presence of 1.4 µg of $^{154}Eu$, 2.4 µg of $^{125}Sb$ and 3.6 µg of $^{106}Rh$.

*Tab. 7.1 Isotopic composition of U and Pu*

| | At% | Wt% | Stand. devn. |
|---|---|---|---|
| U-234 | 0.052 | 0.051 | 73.599 |
| U-235 | 0.871 | 0.861 | 1.896 |
| U-236 | 0.394 | 0.391 | 4.444 |
| U-238 | 98.683 | 98.698 | - |
| Pu-238 | 1.733 | 1.722 | 0.250 |
| Pu-239 | 56.220 | 56.070 | - |
| Pu-240 | 25.122 | 25.160 | 0.011 |
| Pu-241 | 10.691 | 10.752 | 0.145 |
| Pu-242 | 6.234 | 6.296 | 0.107 |

**Reference**

[1] T. Adachi, T. Mutomura, H. Takeishi and T. Yamamoto, J. Nucl. Mater. 160 (1988) 81-87

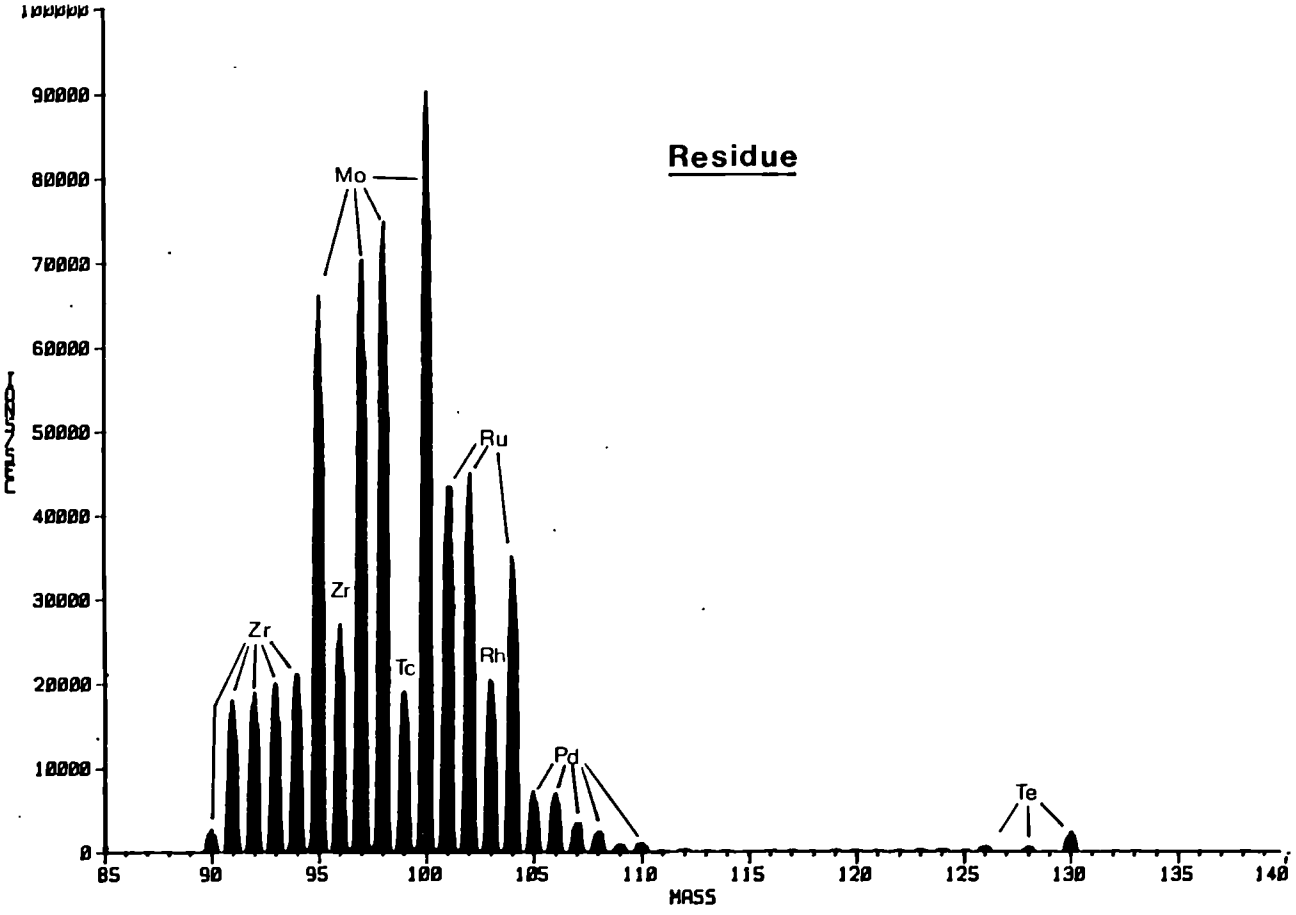


*Fig. 7.4 ICP-MS spectrum of the residue*

# Determination of Neptunium by ICP/MS

## Introduction

Since the first publication describing the principles of the coupling of an Inductively Coupled Plasma to a Mass Spectrometer (ICP-MS) in 1980 [1] based on previous studies by Gray [2,3] many developments to this powerful analytical technique have been described [4,5]. The use of an ICP as ion source for mass-spectrometry provides extremely low detection limits (ng/l levels) and requires minimum sample preparation. Simple spectral features, wide dynamic ranges and the possibility of obtaining the isotopic composition of the sample are some of the outstanding advantages of this new emerging technique. For the analysis of nuclear samples ICP-MS can provide information both on stable and unstable isotopes at very low concentrations which allows us to work with samples of low activity. However, in spite of all these potential advantages very few reports have been published on the application of ICP-MS to nuclear samples and they refer mainly to the determination of impurities in non-irradiated uranium oxides and zirconium alloys.

Current methods for the analysis of nuclear samples include mainly ICP-AES, AAS, XRF, α- and γ-spectrometry, liquid scintillation and TIMS with isotopic dilution. However, ICP-AES, AAS and XRF do not give isotopic information and lack enough sensitivity for the analysis of low ng/ml levels. Additionally, ICP-AES suffers from severe spectral interferences in the presence of lanthanides and actinides. α- and γ-spectroscopy and liquid scintillation are very sensitive and selective methods but are not suited for the analysis of stable isotopes and long-lived nuclides like neptunium. The application of ICP-MS to the analysis of neptunium impurities in uranium or plutonium solutions obtained after reprocessing of the spent fuel is one of the clearer examples in which ICP/MS can compete favourably with ICP-AES, TIMS and various radiochemical methods.

## Experimental

The ICP/MS instrument used was an Elan 250 from Sciex (Canada) and has been modified in order to work with radioactive samples in a glove box as described previously [6]. The operating conditions used for the determination of neptunium are listed in Tab. 7.2. The plasma conditions used were those recommended by the manufacturer; the ion lenses were optimised for the lanthanides in order to be able to measure fission products as well as actinides under the same conditions. The distance of the load coil to the sample cone was fixed at 25 mm in our modified instrument when mounting the instrument in the glove box.

*Tab. 7.2 Operating conditions*

| Plasma | Operating conditions |
|---|---|
| Power | 1200 w |
| Reflected power | < 5 w |
| Argon Cooling | 12 l/min |
| Argon Aux. | 1.40 l/min |
| Argon Neb. | 0.86 l/min |
| Uptake sample | 1 ml/min |
| Nebulizer type | Meinhard |
| Spray chamber | Scott type/double pass |
| Distance load coil / sample cone | 25 mm (fixed) |
| **Vacuum** | |
| Interface | 1 Torr |
| Quadrupole | $2.5 \times 10^{-6}$ Torr |
| **Ion lenses** | |
| Bessel Box B | Setting 32 |
| Einzel lens $E_1$ | Setting 74 |
| Bessel Box P | Setting 12 |
| Photon stop S2 | Setting 25 |

## Results and discussions

### Selection of an internal standard

Due to the intrinsic instability of the ICP-MS (5 to 10 % long term precision) an internal standard should be present both in samples and standards in order to correct for instrumental drift during the analysis. The internal standard should be close in mass to the analyte and possess similar ionisation characteristics. For the analysis of neptunium, thorium, uranium and plutonium were tested as suitable internal standards. Fig. 7.5 shows the mass spectrum of a uranium solution containing impurities of both neptunium and plutonium. Thorium was added externally as there was no thorium in the sample. The method applied for the determination was that of standard addition in order to correct for the possible matrix

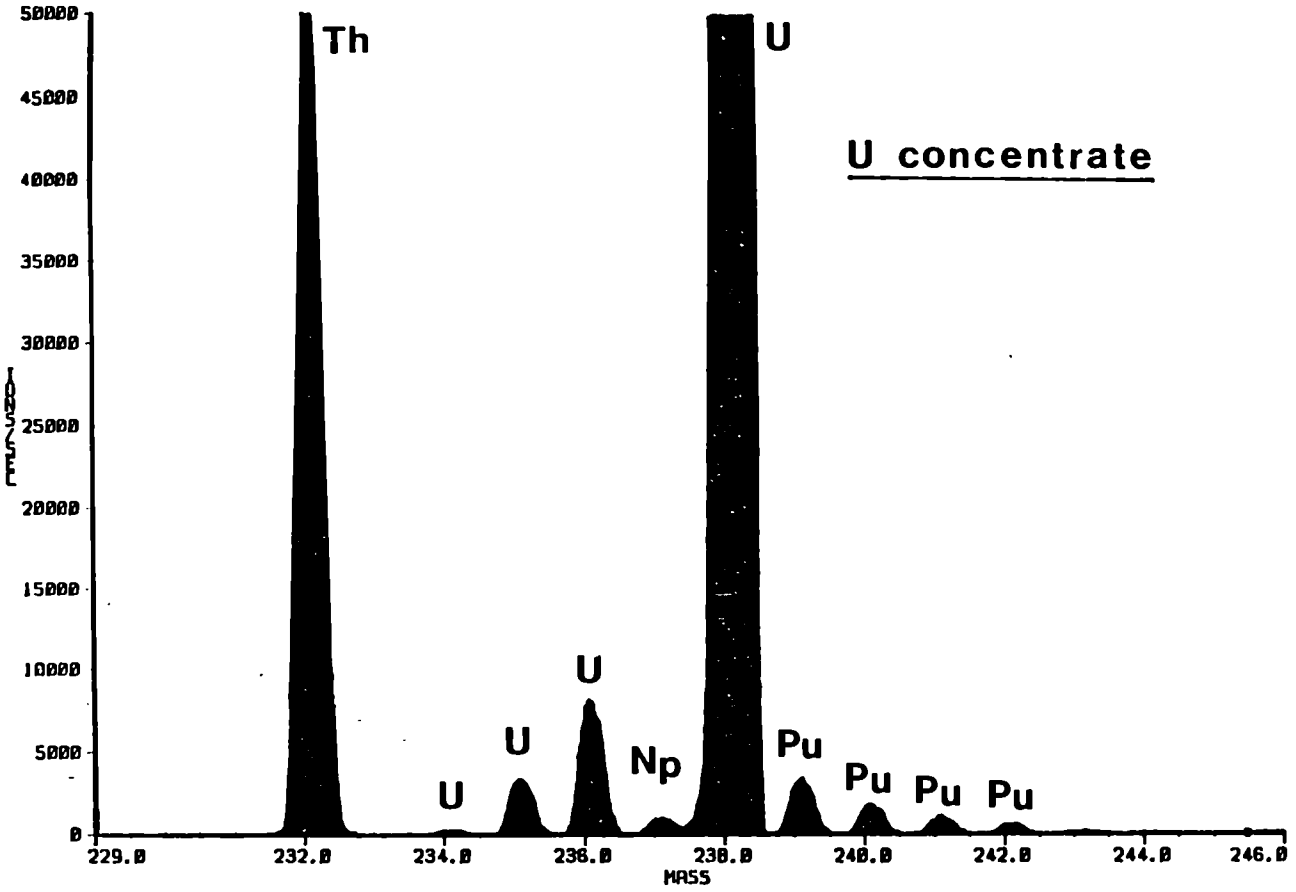


*Fig. 7.5 Mass spectrum of uranium solution*

suppression effects caused by the high uranium concentration in the sample. The results obtained using six different isotopes of the three elements mentioned above are shown in Tab. 7.3. As can be observed the results are identical regardless of the internal standard used. As the samples to be analysed contained either uranium or plutonium or both, those elements were selected as internal standards when using the method of standard additions and spiking the sample with a pure $^{237}Np$ solution. (In that case the concentration of the internal standard is the same in both the sample and in the spiked sample.)

*Tab. 7.3 Determination of Np in U concentrates by standard additions using different internal standards*

| Isotope used as IS | Np 237 found (ppm) |
|---|---|
| Th 232 (added) | 0.468 |
| U 235 | 0.469 |
| U 236 | 0.456 |
| U 238 | 0.471 |
| Pu 239 | 0.464 |
| Pu 240 | 0.455 |
| Mean 0.464 | Std. dev. 0.006 |

## Direct calibration versus standard additions

The ICP-MS is prone to severe matrix interferences due to ionisation suppression in the plasma and space-charge effects in the ion lenses [4,5]. The space-charge effects seem to be predominate and this means that any matrix element in sufficiently high concentration will reduce the sensitivity of the trace elements in the sample. In order to ascertain the influence of uranium in the neptunium signal we have prepared an uranium quality control sample containing 0.110 % neptunium as impurity and analysed it both by direct

calibration (using Th as I.S.) and standard additions (using $^{235}U$ as I.S.). The results obtained are shown in Tab. 7.4 and it can be seen that the results are comparable by both methods so that there is no matrix interference of uranium and neptunium at this concentration level.

*Tab. 7.4 Determination of neptunium in a uranium quality control sample*

| Determination method | Np found (% U conc.) |
|---|---|
| Calibration | 0.114 |
| Standard additions | 0.117 |
| Theoretical value | 0.110 |

However, the addition of the internal standard is essential to achieve good precision. In that case the sample preparation will not be simplified by choosing calibration versus standard additions. So, the method of standard additions using the isotopes already present in the sample as internal standard was selected as the routine method for neptunium determination in uranium and plutonium solutions.

## Similarities between standard additions with internal standard (SA-IS) and isotopic dilution (ID) for neptunium analysis

The formulae to apply for the determination of neptunium by SA-IS and by ID when spiking with a pure $^{237}Np$ isotope are given in Tab. 7.5 where the superscript (S) refer to the sample and (Sp) to the spiked sample. $C_{Np}$ is the concentration of neptunium; $I_{Np}$ and $I_{IS}$ are the blank corrected raw intensities obtained for neptunium and for the Internal Standard respectively. In the formula of isotopic dilution $N_{Np}$ is the number of $^{237}Np$ atoms and R is the isotopic ratio obtained before (S) and after (Sp) spiking.

*Tab. 7.5 Similarities between standard additions and isotopic dilution*

| | |
|---|---|
| Standard Additions with Internal Standard | $C_{Np}^{S} = \dfrac{(I_{Np}/I_{IS})^{S} \times C_{Np}^{Sp}}{(I_{Np}/I_{IS})^{Sp} - (I_{Np}/I_{IS})^{S}}$ |
| Isotopic Dilution when Spiking with a pure isotope | $N_{Np}^{S} = \dfrac{R^{S} \times N_{Np}^{Sp}}{R^{Sp} - R^{S}}$ |

As can be seen, the formulae are equivalent; the only difference is that the isotope used as reference is not of the same element in the standard additions method. However, taking into account the results shown in Tab. 7.3 and 7.4 we can conclude that all actinides behave similarly in ICP-MS so this approach of "pseudoisotopic dilution" could be regarded as an isotopic dilution method in this context with all the inherent advantages of precision and accuracy of this method.

## Determination of neptunium in plutonium solutions

Plutonium solutions obtained after the reprocessing of spent nuclear fuel have to be analysed for their Pu contents for Safeguards purposes. The analytical method of choice is titration because of the high levels of precision and accuracy obtained which cannot be obtained by ICP-MS. However, when the Pu solutions contain Np, this is also titrated giving erroneous results for the Pu concentration. We have analysed different Pu solutions for their Np contents by SA-IS and the results obtained appear in Tab. 7.6. Values from 0.07 to 1.49 % were obtained. The mass spectra of sample F is shown in Fig. 7.6 where the $^{237}Np$ peak can be easily observed together with the five Pu isotopes in the sample. The Np content in sample F was also checked by α-spectrometry and a value of 0.60 % was found so confirming the ICP-MS results.

*Tab. 7.6 Neptunium impurities in plutonium solutions*

| Sample | Pu Conc. (mg/g) (Titration) | Np Conc. (mg/g) (ICP/MS) | % Np |
|---|---|---|---|
| A | 10.00 | 0.149 | 1.49 |
| B | 235.37 | 0.169 | 0.07 |
| C | 222.98 | 1.124 | 0.50 |
| D | 220.76 | 0.305 | 0.14 |
| E | 244.74 | 0.356 | 0.15 |
| F | 302.62 | 1.788 | 0.59 |

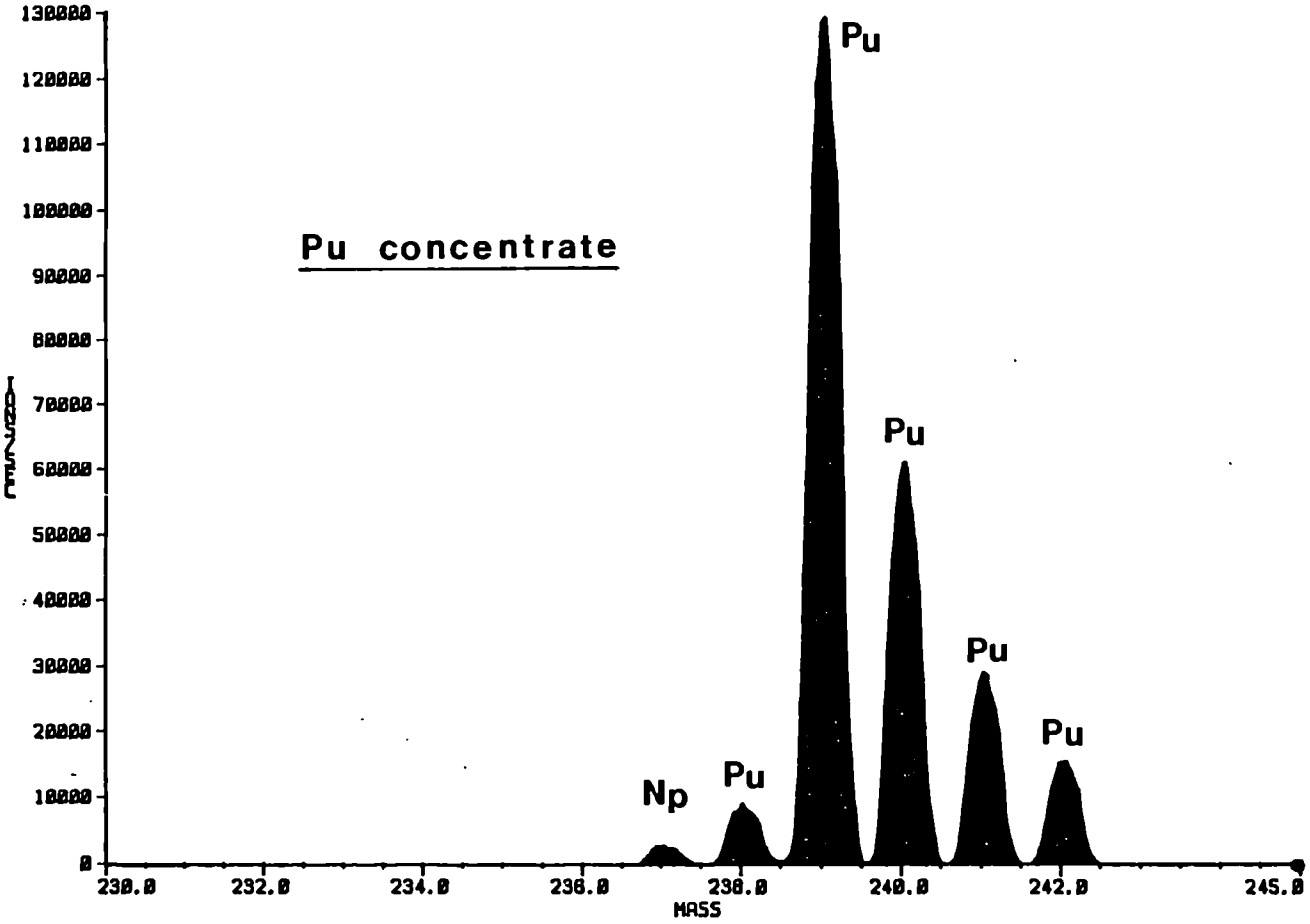


*Fig. 7.6 Mass spectrum of plutonium solution*

## Conclusions

The use of ICP/MS for neptunium determination is the method of choice for uranium or plutonium solutions due to the high sensitivity of the technique and the similar response of all actinides in the ICP which allows us to use the "Pseudo-Isotopic Dilution" method which provides good accuracy. The precision obtained (around 5 %) can be considered as satisfactory for trace analysis.

**References**

[1] R.S. Houk, V.A. Fassel, G.D. Flesch, H.J. Svec, A.L. Gray and C.E. Taylor, Anal. Chem. 52 (1980) 2283-9
[2] A.L. Gray, Anal. Chem. 47 (1975) 600
[3] A.L. Gray, Analyst 100 (1975) 289
[4] R.S. Houk, Anal. Chem. 58 (1986) 97 A
[5] G.M. Hieftje and G.H. Vickers, Anal. Chem. Acta 216 (1989) 1
[6] L. Koch, R. de Meester, S. Franzini and H. Wiesmann, '1st International Conference on Plasma Source Mass Spectrometry', Durham, UK, 12-16 Sept. 1988

## Gamma-spectrometry

Much of the routine work with gamma-spectrometry involves the determination of americium or fission products. Americium is measured using a planar germanium detector with a resolution at 122 keV of about 660 eV. Fission products are measured using a larger pure germanium detector with a resolution of 2.1 keV at 1.33 MeV. An alternative is a pure germanium well detector also with a resolution of 2.1 keV at 1.33 MeV.

Because of the rising demand for gamma-spectrometry analyses, a new counting room has been built in the cellar where the laboratory background is low. This room has just been completed and the detectors installed. The positioning of the detectors was critical because the electrical leads leading to and from the pre-amplifiers have been found to be prone to pick up electrical interference from the multichannel analyser (ND 66) and computer. External interference is also

prominent and this needs to be reduced by a combination of earthing measures and attacking the interference at source.

During the year the first attempts have been made at using the program MGA for the determination of Pu isotopic ratios. This program has been developed over several years by Gunnink and co-workers [1] and promises to be a valuable adjunct method for Pu product or output samples where the amount of Pu is several milligrams. The program however, demands stable counting conditions and normally a detector with a resolution in the lower energy range rather better than that of our present planar detector. Part of the ongoing work is to determine whether the present detector is adequate for this application and how well the isotopic ratios determined by gamma-spectrometry agree with those measured by mass-spectrometry.

The program MGA runs at present on the MicroVAX computer and to analyse the spectra a rather complicated procedure transfer on disk via a PDP 11 is needed. The situation is sufficient to test the program for our needs but is too ungainly for routine work. During the next year it is planned to link the gamma spectrometers via a ETHERLINK network directly to the MicroVAX and also to a VAX 3100 workstation which is to be installed for the K-edge densitometry. These installations will make the program easier to use and will also approach closely the situation as planned for the On-Site Laboratories.

**Reference**

[1] R. Gunnink, Proc 28th Institute of Nuclear Material Management, Newport Beach, California, July 12-15, 1987, Nucl. Mater. Manage. XVI (1987) 352-358

# The Caldex Tracer Experiment

The determination of the quantities of fissile materials present in a tank in a reprocessing plant is normally carried out by measurements of the concentration of uranium and plutonium and of the volume of the liquid in the tank containing the material.

The tank volume is usually calibrated by the "dip tube method", in which the level of the weighed-in liquid is found by measurements of the prevailing hydrostatic pressure by a high precision manometer.

An independent method for checking the tank calibration and thus the volume could be of interest for Safeguards purposes. Tracer techniques have been used for such verification in several experiments over the years. In this method a known amount of an isotope of a selected element is added to the tank and the concentration of that element is determined by isotope dilution mass spectrometry. In the various earlier experiments of this kind elements such as lithium, magnesium or the isotope deuterium have been used [1].

In a recent multi-laboratory experiment natural lutetium ($^{175}$Lu: 97.4 % and $^{176}$Lu: 2.6 %) was used as tracer in the tank and $^{176}$Lu (about 87%) was the spiking isotope used in the laboratory.

In the experiment 5 laboratories took part, including this Institute. According to the agreed scheme more than 100 analyses were carried out, involving spiked as well as unspiked samples. Laboratory dilutions had also to be performed prior to the mass spectrometric measurements.

The exercise organized by DWK, Hannover is presently under evaluation. It will allow the adequacy of this technique for Safeguards verification purposes to be judged and in addition give information on the internal and external measurement variances.

**Reference**

[1] P.R. Trincherini, 'Volume and Mass Measurement in the Input Accountancy Tank of the Reprocessing Plant by the IDMS Tracer Technique', EUR 12623 (1990).

# Components for an On-Site Safeguards Laboratory

## Introduction

The concept of an on-site laboratory was introduced previously [1]. It included automatic analytical instruments which could analyse nuclear fuel samples taken under routine nuclear material safeguards inspections. To reduce the labour costs in such an on-site laboratory, expert systems and computer links to a central laboratory would be employed.

The present status is described here, including:

- the bulk analysis of Pu and MOX samples, which employs robot techniques extensively,

- the components needed for alpha- and mass-spectrometry, again employing robot techniques,

- an expert system which delivers the necessary information to the laboratory robots for the appropriate conditioning procedures for the samples.

Under the present time schedule, the development and construction, followed by field-testing is planned for 1992.

## Bulk analysis of Pu and MOX samples

For the bulk analysis of Pu and U in reprocessing output samples (solutions of nitrate or oxide powders) and from fuel production (mainly MOX pellets), three options are foreseen:

- titration for quantitative element analysis and thermal ionisation mass-spectrometry (TIMS) for isotopic analysis ,

- K-edge densitometry for quantitative elemental analysis, γ-spectrometry for isotope analysis of Pu and TIMS for the isotope distribution of U (for the MOX samples only),

  passive neutron counting for Pu-containing powders plus γ-spectrometry for the isotope ratios.

The layout of a glovebox housing an analytical robot and the necessary instruments for the bulk analyses are given in Fig. 7.7.

## Automation titration of U and Pu in product (output) solutions

For the titration of U and Pu, a commercial titrator (type RADIOMETER) has been adapted for glove-box operation and is now in routine use.The setup has been coupled into the laboratory data system so that the expert system described below designates which samples have to be analysed. Barcode labels are printed which are attached to the flasks and checked at weighing.

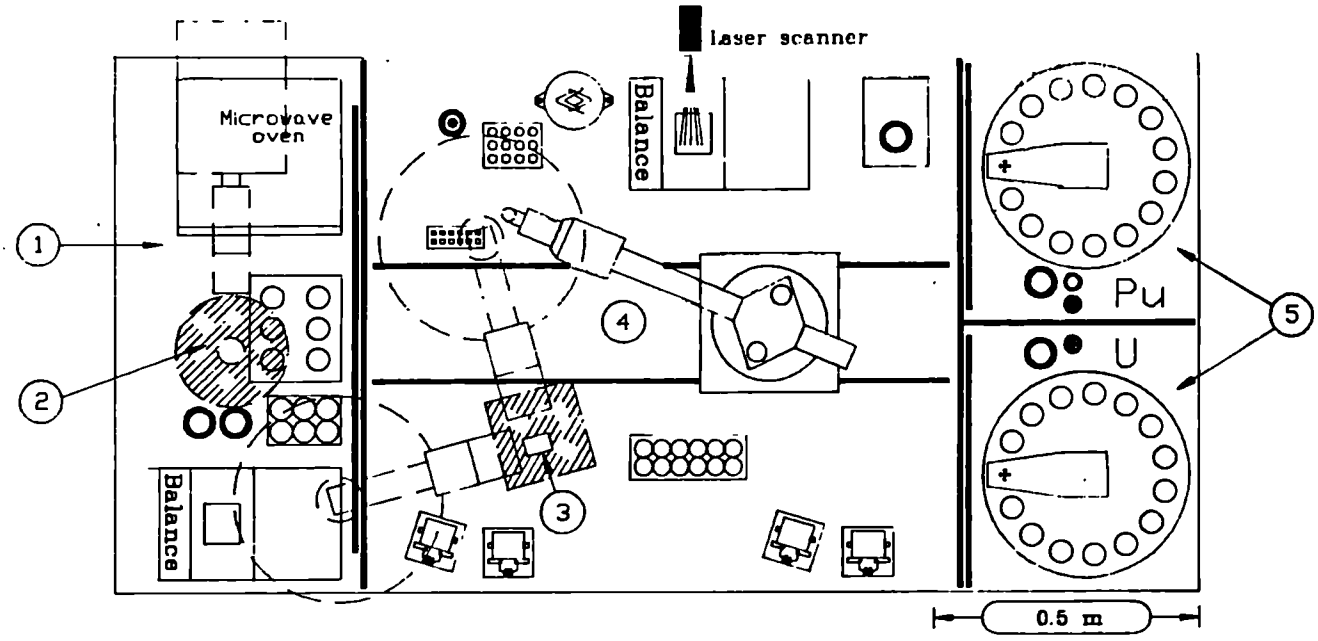


① Area for sample digestion and conditioning for n and gamma measurement
② n and gamma measurement device beneath the box
③ K-edge measurement chamber beneath the box
④ Area for sample conditioning for titration and K-edge densitometry
⑤ Area for sample titration

*Fig. 7.7 Instrument layout for robotised bulk analysis of Pu and MOX samples*

The procedure is given in Fig. 7.8 and the instrumental layout in Fig. 7.9. After dissolution of the samples aliquots are weighed. The titration is then carried out automatically. All necessary data are sent to the main laboratory computer. After the titration is finished the concentration is calculated so that the analyst is in the position to judge if the analysis is acceptable or not.

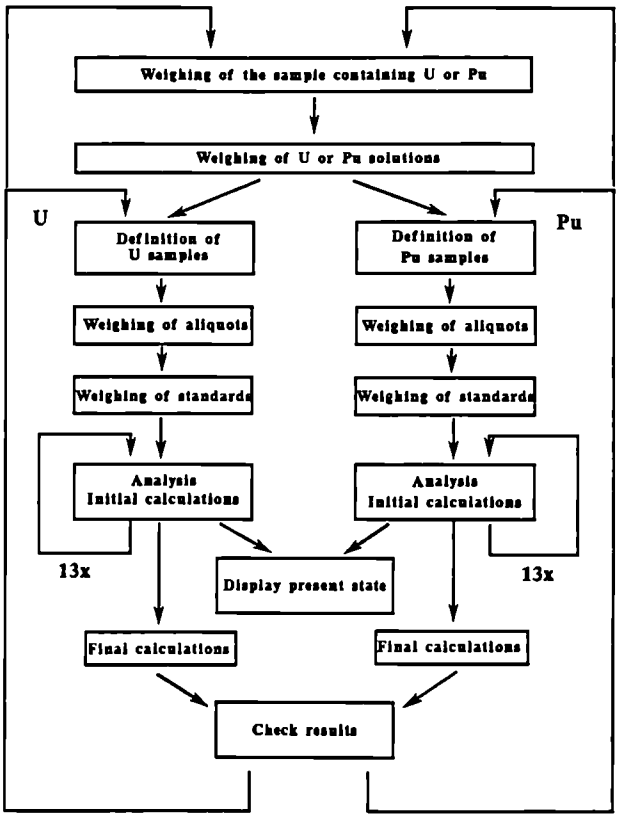


*Fig. 7.8* *Automatic titration procedure*

Blank measurements and standards are routinely measured. The results from these are archived. At the end of each day or on instigation of the operator all measured samples in the period are recalculated using the latest standards and blank values as a basis.

The results can be checked by the operator who is in the position to recall the titration curve onto the computer screen. All measurements are archived for further statistical control and also for internal fissile material control purposes.

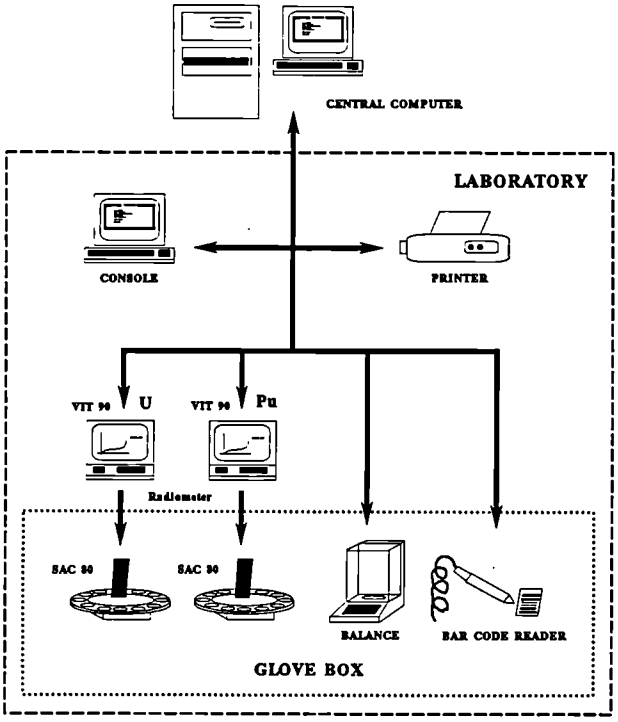


*Fig. 7.9* *Instrument layout for automatic titration*

## An enhanced robotised conditioning of solutions for isotope dilution

A system based on a laboratory robot installed in a glovebox for the spiking, conditioning and separation of reprocessing input samples has been successfully implemented in the Safeguards laboratory of the Institute and has been fully operational since 1987 (TUAR 87, 225). This first version (Fig. 7.10) has been improved and extended with a view to its implementation for the on-site Safeguards laboratories.

Two pieces of apparatus have been developed which extend the function of the robot and are described here. The first is a sample changer for alpha counting to determine the $^{238}Pu$ / $^{(239+240)}Pu$ ratios. The robot, after preparing the samples for alpha spectrometry, loads the sample changer and signalises that the first batch can be counted. It has positions for 18 samples and can measure 6 samples simultaneously. The spectra are sent from the multichannel analyser to a computer which calculates the peak ratios for the subsequent determination of $^{238}Pu$ and also an ap-

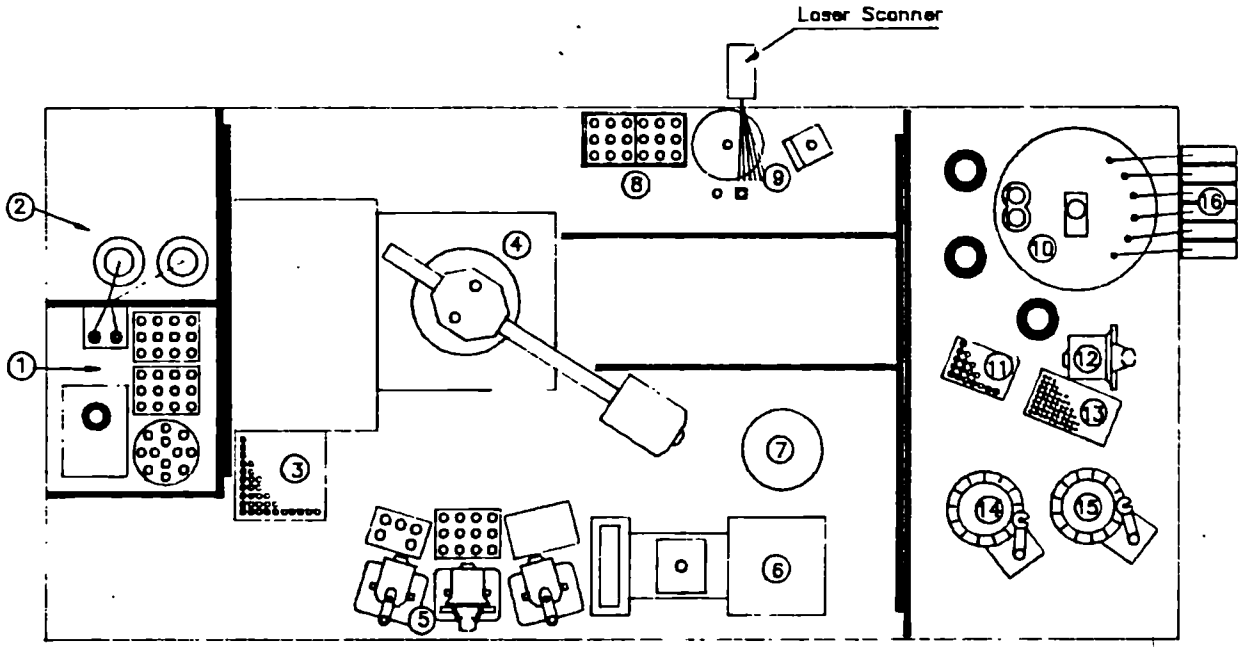


① Hood for sample conditioning
② Hood for collection of liquid waste
③ Pipet Tips
④ Robot
⑤ Robot hands and racks
⑥ Balance
⑦ Waste for used tips
⑧ Rack for fresh samples
⑨ Copper and new caps
⑩ Alpha planchet preparation, sample changer and counting chamber
⑪ Rack for tubes containing extracted U and Pu
⑫ Bifunctional robot hand
⑬ Pipet tips
⑭⑮ System for Mass spectrometry filament preparation
⑯ Alpha counting preamplifier

*Fig. 7.10 Enhanced robot conditioning for isotope dilution analysis*

proximate value of the concentration of the plutonium in the solution as well as that of uranium from the concentration of $^{233}U$. These concentrations are used to calculate the optimal amounts of solution to be loaded on the filaments for mass-spectrometry.

The second apparatus is for the preparation of mass-spectrometer filaments. An Eppindorf pipette is used by the robot to deposit a volume of between 1 and 10 µl of the sample on the filament. The filaments are mounted on a magazine which is rotated under robot control to expose the next filament. After all filaments have been prepared, they are heated by an electrical current to dry the samples and are then ready to be taken out for mass-spectrometry.

## Extension of the expert system for the automatic safeguards laboratory

The expert system as described previously (TUAR 89, 68) has been extended and can now choose between 22 different analytical procedures. All types of Safeguards samples can be dealt with. The program works out the following necessary parameters for the preparation of the sample:

- determination of the analysis code from the sample data with a simultaneous check of the completeness and coherence of the data,
- assignment of internal numbers which are used to check the flow of the sample through the measurement steps,

- calculation of the analytical parameters: dilution factor (should a dilution be necessary), amounts of the redox reagents in the chemical conditioning stage and weights of spikes and sample,
- determination of the number of alpha planchettes and mass-spectrometry filaments to be prepared. Later on the robot (after having identified the sample by its bar-code) will employ this information together with the parameters calculated as above.

The samples are measured and the results evaluated. Measurement repeats where necessary are then reinitialised by the expert system. Different types of repeats are possible:

- a new dilution of the original sample, assuming enough material is available, followed by a complete new measurement process,
- the chemical conditioning only is repeated,
- further measurements are needed: the robot then prepares fresh filaments and/or alpha planchettes.

The expert system at present covers the isotope dilution mass-spectrometry. It is being extended to include the bulk analysis methods for Pu and MOX samples.

## Data aquisition and evaluation for bulk and isotope analysis of U and Pu

A system of automatic data collection, reduction and evaluation has been developed for all the analytical techniques at present being employed. The instruments are presently situated in different laboratories where dedicated processors collect and partially reduce the data before sending them to a PDP 11/73 computer: The full evaluation takes place later in a Micro VAX II computer (Fig. 7.11).

The information from the expert system (see above) for the robot is filed in the PDP 11/73. At the same time data files specific for the sample are opened into which the reduced data are deposited in after each measurement. For the moment some instruments have to be programmed by the operators according to instructions given by the expert system. In the future this step will be eliminated as far as possible.

The status of the analysis of each sample can be followed, to see for instance if the results are already available from mass-spectrometry.

For each of the instruments and robots, individual software has been written. The software is at present either being tested or in routine use. For the future an extension is planned to include an expert system for the quality assurance of the measurements.

## Quality control of safeguards analytical measurements

A concept for an improved quality control (QC) system is under development for the various analytical measurement methods in use in this laboratory for safeguards purposes. The QC system is to be employed in possible future on-site laboratories and will be included in an Expert System also under development.

The ultimate goal is to reach an accuracy of 0.1% for the most important methods used. This implies that the present precision and absolute bias must be characterised and improved.

The analytical methods considered in this study are:

1. Isotopic analysis and isotope dilution analysis (IDMS) for U and Pu
2. Alpha counting (mainly of $^{238}Pu$)
3. Determination of U and Pu by K-edge densitometry, including gamma spectrometry for the isotopic composition of Pu
4. Determination of U and Pu by titration.

The knowledge of the distribution of the errors in the various steps in a complex procedure is of importance for the efforts to decrease the analytical variance in the long term; this is true for the random as well as the systematic error components. Emphasis can then be placed on improving the most relevant steps and distributing the working load properly.

As an example given here, the IDMS analysis procedure, consisting of many steps carried out in different laboratories and by different analysts will be considered. The sequential steps given below were selected for a study of the error sources involved in the procedure. The experiment was designed as a statistical hierarchical classifica-

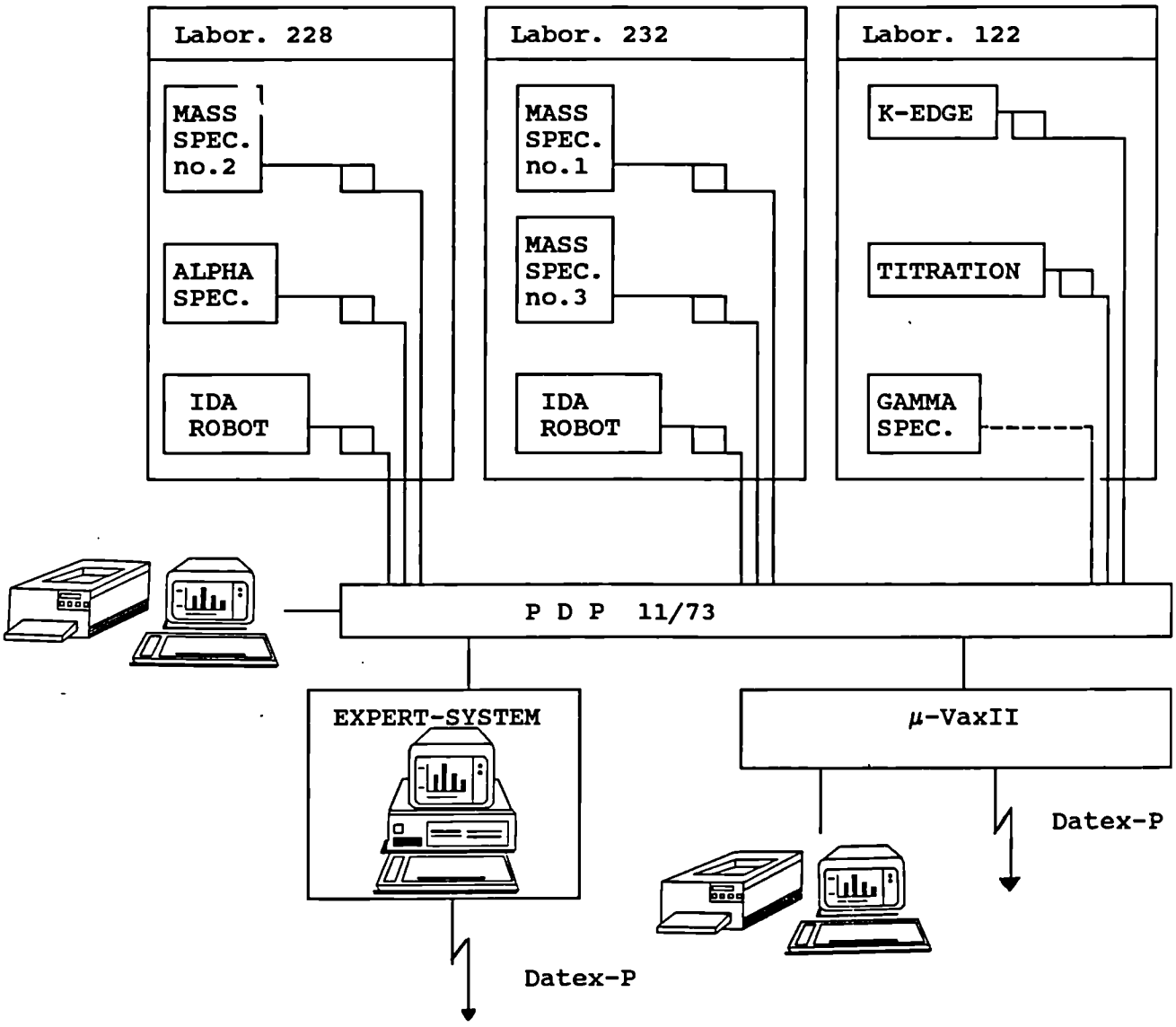


*Fig. 7.11 Data aquisition and evaluation for bulk U and Pu analyses*

tion for treatment by analysis of variance (ANOVA).

The scheme was the following:

1. Dilution of sample
2. Weighing of sample and spikes under robot control
3. Mixing and redox
4. Measurement of isotope ratios using 3 mass-spectrometers.

Of critical importance in this investigation was the variance between samples, comparing U and Pu, and variation between mass-spectrometers.

As the isotopic equilibration of uranium is much easier compared with that of plutonium, any excess variation of Pu compared to U can be assigned to the redox process itself, assuming the same precision in measuring the isotope ratios of the two elements.

An analysis of variance was made on the concentration analyses of this campaign. The analysis was thus made using both U and Pu concentrations (strictly speaking the concentrations of the main isotopes $^{238}U$ and $^{239}Pu$) as dependent parameters and the sample, ie. measurement repeat and the mass-spectrometer as the independent parameters.

The results of the ANOVA are given in Tabs 7.7

*Tab. 7.7* *ANOVA for U concentration: parameters are 'sample' and 'mass-spectrometer'. Total number of measurements = 18*

| Effect | SS | df | MS | F | p |
|---|---|---|---|---|---|
| ms | .01045 | 2 | .00523 | 6.84 | 0.0105 |
| within | .00917 | 12 | .00076 | | |
| sample | .00742 | 5 | .00148 | 1.094 | 0.427 |
| within | .01220 | 9 | .00136 | | |

and 7.8. For both elements it can be seen that the main part of the variance comes from the parameter 'mass-spectrometer', ie. a systematic difference exists between measurements performed with different mass-spectrometers, although in principle the instruments and evaluation software are very similar. The probability of this effect arising through chance is very low: 0.5% for U and 1% for Pu.

*Tab. 7.8* *ANOVA for Pu concentration: parameters are 'sample' and 'mass-spectrometer'. Total number of measurements = 15*

| Effect | SS | df | MS | F | p |
|---|---|---|---|---|---|
| ms | .00015 | 2 | .00007 | 7.69 | 0.005 |
| within | .00014 | 15 | .00001 | | |
| sample | .00003 | 5 | .00001 | .264 | 0.923 |
| within | .00026 | 12 | .00002 | | |

The variance connected with the parameter 'samples' is not significant however which implies that dispensing and aliquotation of the samples and spikes is not a significant source of error. The total error, as observed in the sum of squares (SS) or mean squares (MS) is much greater for Pu than for U, as expected from experience. Whether this is indeed due to chemical effects during spiking and isotope equilibrium or to mass-spectrometric associated error sources has still to be investigated.

The measurement methods are still being refined and improvements are expected in the near future. Repeats of this experiment will be made, and an attempt will be made to determine the source of the extra errors associated with the measurement of Pu. Systematic errors from the spikes and the dispensing/aliquoting procedure would not be seen by this analysis and must be addressed separately.

**Reference**

[1] L. Koch, M. Blumhofer, B. Brandalise, M. de Rossi, R. Wellum, D. Wojnowski, R. Schenkel, H. Wagner, 'Conceptual design of an on-site laboratory for nuclear materials safeguards', Proceedings of the 11th Annual Symposium on Safeguards and Nuclear Material Management, Luxembourg, 30 May 1989, pp 225-229

# Intrinsic Densitometry Techniques for High-burnup Plutonium Solutions

## Introduction

An accurate measurement of the plutonium concentration of a sample is always necessary for nuclear material control and accounting. Two methods have previously been used for determining low burnup plutonium concentrations [1] which depend only on the intrinsic radiation in the sample. In this work the measurements have been extended to high burnup solutions.

## Experimental methods

A set of six high burnup solutions were prepared from one batch of plutonium having concentrations ranging from 50 g/L to 310 g/L. A seventh solution taken from a batch with different plutonium isotope ratios was also measured. The solutions were pipetted into a spectrometric cell mounted on the wall of a glovebox and viewed axially by a low energy photon detector with a resolution of 500 eV at 122 keV. Each solution was assayed 7 to 10 times for 3600 seconds.

The solutions were characterised by titrimetry and K-edge absorption and the isotopics measured by mass-spectrometry. The plutonium concentrations are listed in Tab. 7.9 and the isotopics in Tab. 7.10.

*Tab. 7.9 Plutonium concentration of samples*

| Sample | Concentration (g/L) | Thickness (cm) |
|---|---|---|
| 1 | 50.36 | 1.974 |
| 2 | 101.54 | 1.981 |
| 3 | 151.52 | 1.977 |
| 4 | 208.09 | 1.973 |
| 5 | 253.44 | 1.974 |
| 6 | 308.61 | 1.981 |
| 7 | 145.92 | 1.978 |

*Tab. 7.10 Isotope distributions of the plutonium*

| Sample | $^{238}$Pu (wt %) | $^{239}$Pu (wt %) | $^{240}$Pu (wt %) | $^{241}$Pu (wt %) | $^{242}$Pu (wt %) |
|---|---|---|---|---|---|
| 1-6 | 2.002 | 54.541 | 25.257 | 11.771 | 6.429 |
| 7 | 0.228 | 70.078 | 24.249 | 4.398 | 1.130 |

## Calculational methods

Both methods use the MGA2 program developed by R. Gunnink of the Livermore National Laboratory [2]. The program fits a relative efficiency curve through 10 peaks from 59 to 208 keV, including the discontinuity at the plutonium K-absorption edge at 121.8 keV. For fixed solution sample thickness the magnitude of the discontinuity should be proportional to the plutonium concentration. The results are summarised in Tab. 7.11 where it can be seen that the density measurement is proportional to the concentration determined by titration. Excluding the sample with the lowest concentration, the plutonium can be determined by this method with a precision between 3% and 17% in a 3600 second assay. The error quoted is the standard deviation of repeated measurements.

The second method uses the ratio of a pair of gamma or X-ray peaks - one above the discontiuity and one below. The peaks chosen are the 148 keV peak of $^{241}$Pu and the 111 keV X-ray complex of $^{238}$Pu, $^{239}$Pu and $^{241}$Pu. To test the method the 111 keV and the 148 keV net peak areas were extracted with the MGA2 code. An isotope correction is required which must be calculated from the mass-spectrometry measurements. The peak ratios, corrected for the isotopic factor are fitted to a quadratic function with the plutonium concentration.

The results are given in Tab. 7.12. The error shown on the peak ratio is the standard deviation from repeated counts; the error on the concentrations takes into account also the sensitivity, defined as the fractional change in the plutonium concentration per fractional change in the ratio of 111/148. The relative standard deviation calculated from the ratios of the concentration determinations of the ratio method to titration values is 2.4% over the concentration range 50 to 310 g/L.The error can be improved by increasing the count rate.

*Tab. 7.11 Comparison between titration and densitometry determinations of Pu*

| Chemistry (g/L) | Densitometry (g/L) | Densit./ Chem. | Error (%) |
|---|---|---|---|
| 50.36 | 26.20 | 0.52[a] | 43.00 |
| 101.54 | 80.70 | 0.80 | 17.00 |
| 151.52 | 128.12 | 0.85 | 4.60 |
| 208.09 | 163.80 | 0.79 | 4.70 |
| 253.44 | 205.20 | 0.81 | 2.60 |
| 308.61 | 237.92 | 0.77 | 7.90 |
| 145.92 | 121.43 | 0.83 | 4.80 |

*Tab. 7.12 Plutonium ratios determined from the 111/148 peak ratios*

| Chem. (g/L) | No. of runs | Ratio (111/148) | Error in ratio (%) | Pu Conc. from ratio (g/L) | Error in conc. (%) | Pu Conc. / Chem. |
|---|---|---|---|---|---|---|
| 50.36 | 16 | 0.89614 | 0.53 | 52.04 | 9.3 | 1.04 |
| 101.54 | 16 | 0.93617 | 0.20 | 96.91 | 1.9 | 0.95 |
| 151.52 | 7 | 0.98434 | 0.41 | 154.98 | 2.8 | 1.02 |
| 151.52 | 4 | 0.98236 | 0.53 | 152.50 | 3.6 | 1.01 |
| 208.09 | 7 | 1.02606 | 0.28 | 208.87 | 1.5 | 1.00 |
| 208.09 | 3 | 1.02449 | 0.24 | 206.79 | 1.3 | 0.99 |
| 253.44 | 16 | 1.05791 | 0.24 | 252.27 | 1.2 | 1.00 |
| 308.61 | 7 | 1.09917 | 0.23 | 311.39 | 1.0 | 1.01 |
| 308.61 | 2 | 1.09552 | 0.32 | 306.03 | 1.4 | 0.99 |
| 145.92 | 16 | 0.97349 | 0.70 | 141.51 | 4.8 | 0.97 |
| | | | | | Av | 1.00 |
| | | | | | RSD | 2.4 % |

## Conclusions

The main advantage of the two techniques is that no external radioactive source or X-ray generator is needed. The experimental measurements demonstrate that the method works reasonably well for high burnup plutonium with counting periods of 1 hour. However the solution must be pure: product solutions from a reprocessing plant for example.

**References**

[1] S.-T. Hue and R. Zhu, Proc 30th Institute of Nuclear Material Management Meeting, Orlando, Florida, July 9-12, 1989, Nucl. Mater. Manage. XVIII (1989) 806-813

[2] R. Gunnink, Proc 28th Institute of Nuclear Material Management, Newport Beach, CA, July 12-15, 1987, Nucl. Mater. Manage. XVI (1987) 352-358

# Support to DG I

## Installation and Field Testing of a Robotised System for Sample Preparation and Conditioning for Mass-Spectrometry in Gatchina (USSR)

The field testing of the robotised system is being carried out in cooperation with the IAEA, Vienna and the Radium Khlopin Institute, Leningrad. The intention was to install a robot system in the Institute in Khlopin and analyse samples from a reprocessing plant there. This will serve as a test of the concept under real conditions.

The system was built and tested in the robot construction workshop of the Institute within 4 months. A technician from the Radium Institute stayed at the Institute for a week for introductory training in the apparatus and programs. The system was delivered to the Radium Institute in August 1990.

Previous discussions with technical staff of the Radium Institute had already taken place at the end of 1989 so that the necessary preparations to receive the apparatus could be made. Three workers from the Institute travelled to Leningrad in October 1990 to install and check the system. The installation of the system was carried out smoothly: no major obstacles or problems were encountered.

The first tests with natural uranium were carried out successfully. Following these, the glovebox containing the apparatus was sealed and the system tested with the first active samples which were also sent to Leningrad to be measured by mass-spectrometry.

A comparative test was made in the presence of representatives of the IAEA and our Institute of a reprocessing input sample containing 5 µg Pu and 500 µg U per gram solution. $^{242}Pu$ and $^{233}U$ were used as spikes. Filaments for mass-spectrometry in Vienna and Karlsruhe were prepared by the robot and an aliquot of 10 µl of the solution was taken for subsequent analysis in the Institute.
The field tests are expected to last for a year. Samples will be aliquoted, under the supervision of a video monitor installed by the IAEA, before being sent to Vienna and Karlsruhe for parallel analysis. The first comparitive results are expected to be made in Spring 1991.

# Support to DG XIII

## Construction of a Multichannel Pyrometer for Industry

The construction of a product prototype of a six-color pyrometer is underway. This instrument is characterised by a compact design and a modular assembly. Two types of optics are being tested: With the first one, colour beam splitting is obtained through a glass fiber bundle and six interferometric filters; with the second, a dispersion prisma will be adopted. The chosen technique should provide the best compromise between a high signal-to-noise ratio and a stable and reproducible spectral resolution, in order to widen the detection range towards lower temperatures by preserving an accuracy of better than 1% in the photodiode output.

The software for temperature and emissivity evaluation is being rewritten in C according to the detection mode and display requirements.

# Acoustic Aerosol Scavenging

## Status of the new dynamic test rig

During 1990 the experimental concept and design of the new test rig for aerosol preconditioning under dynamic flow conditions were finalised [1]. Construction and installation in a new laboratory have been completed. The electrostatic filter with high tension transformer and controlling electronics have been delivered and installed by our industrial collaborators in this project. This test rig will provide us with the facility to acoustically precondition the aerosol under dynamic flow conditions similar to those in industry. The rig is shown schematically in Fig.7.12 where the acoustic preconditioner, the electrostatic filter, the aerosol measuring chamber, the bag filter, and the flow regulation system can be seen. A photograph of the test rig in the new laboratory is shown in Fig. 7.13.

First tests will concentrate on the acoustic characterisation of the aerosol preconditioning modules (i.e. measurements of the sound pressure levels throughout the chamber volume). Thereafter, the agglomeration rates of solid and liquid aerosols will be measured and the results compared to those obtained under static conditions. Following these experiments, the precipitation efficiency of the electrostatic filter will be determined for aerosols which have been acoustically agglomerated. In later experiments, the electro-

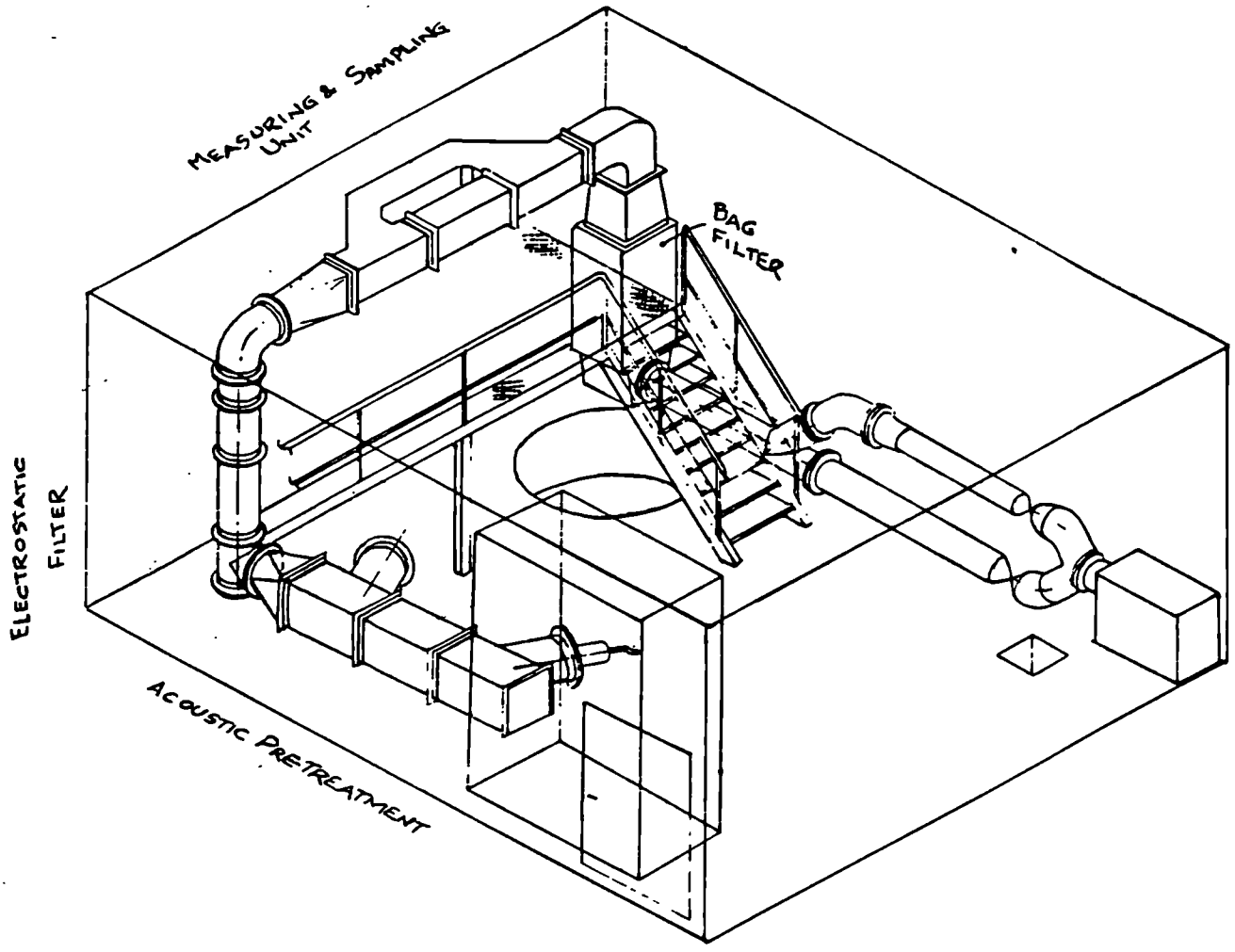


*Fig 7.12 Schematic diagram of the 'dynamic' test rig showing acoustic preconditioner, electrostatic filter, aerosol measuring chamber, bag filter, and flow regulation system*

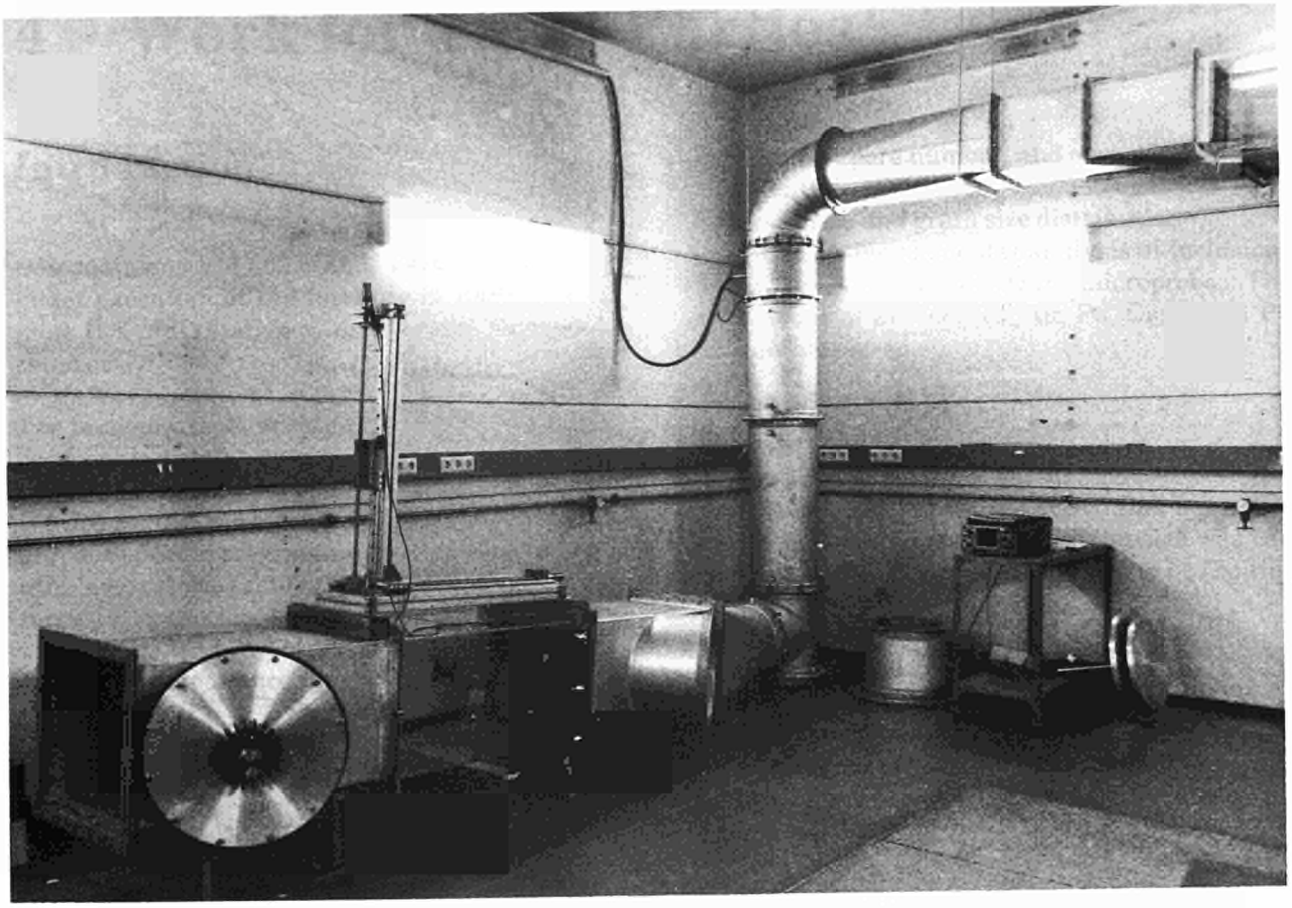

*Fig.7.13* *Photograph of test rig showing the acoustic preconditioner, electrostatic filter, and aerosol measuring chamber*

static filter will be replaced by cyclones, Venturi scrubbers, etc to investigate the enhanced efficiency of such devices with acoustically preconditioned aerosol.

**Reference**

[1] J. Magill, K. Richter, J. McGinley, 'An Acoustic Chamber for Aerosol Preconditioning of Industrial Off-Gases', Patent pending.

# 4 Work for Third Parties

## Introduction

Contracts worth 4,682 MECU were signed and/or under execution at the Institute in 1990 with almost 10% of its staff part- or full-time involved in these activities.

The tendency to do work for third parties against payment is rising.

We are aware, however, of the necessity to maintain our specific programme work at a high scientific level, since this is the pre-requisite for the succesful execution of contract work. A situation which may lead, eventually, to conflicts due to shortage in experienced staff.

## Dissolution Characteristics of High Burnup Fuel

### Objective

The dissolution behavior of high burnup LWR fuel is presently being investigated. Extending the burnup leads to a more efficient use of uranium fuel on the one hand, but on the other hand, the dissolution of such fuel leaves higher amounts of residue. The present study should provide data on the dissolution characteristics for this type of LWR fuel. The amount of residue as well as its composition is being determined for a well characterised high burnup fuel dissolved under PUREX type conditions.

### Experimental

#### Characterisation of the fuel

Prior to dissolution two samples were prepared for a ceramographic analysis of the fuel. This characterisation has yielded important information on the irradiated fuel, including:

- physical appearance; different phases and intra- or intergranular pores were identified
- porosity, pore number, and pore number distribution
- grain size and grain size distribution
- quantitative elemental analysis of inclusions in the fuel by electron microprobe. The amount of Zr, Mo, Ru, Rh, Pd, Cr, U and Pu was measured.

#### Dissolution

Five samples of the characterised fuel have been cut for dissolution tests. The dissolution was carried out under Purex-type conditions i.e. boiling nitric acid at 3-7 moles/l.

The following parameters were studied:

- dissolution kinetics
- influence of nitric acid concentration
- recovery rate, i.e. the amount of material dissolved

To obtain a material balance, the chemical and the isotopic composition of the solution are being determined. Each of the five solutions will be analysed for those fission products which form the main part of the residue.

#### Characterisation of the residue

A part of the residue has been characterised similarly to the fuel using hot ceramography techniques; the rest will be dissolved and analysed for the chemical composition.

##### *Hot ceramography*

After washing and drying, a part of the residue of the five samples was prepared for microscopic and microprobe analysis to yield information on:

- grain size and grain size distribution (optical microscope / TAS)
- the chemical composition (SEM / EDAX and EMPA).

The rest of the residue was dissolved by acid digestion. These solutions will be analysed in the same way as the centrifuged solutions.

The results of the investigations are commercial confidential. However it is agreed in the contract that 2 years after finishing the work will be published jointly showing the outcome of the study.

## Preparation of Minor Actinide Alloys

A summary of the earlier results was given in a joint publication (CRIEPI, ITU) at the OECD Workshop held at Mito, Japan, October 1990.

Alloys containing Np and $^{241}$Am have been investigated. These contain the following amounts of minor actinides (MA) and rare earths (RE):

- 2% MA+RE
- 5% MA+RE
- reference U/Pu/Zr
- 10% MA
- 20% MA

whereby a constant mixture of 40% Am, 60% Np was maintained throughout and a 1:1 ratio of MA to RE was used.

The structures of the alloys have been investigated by optical microscopy, EPMA and autoradiography after annealing and quenching to examine their thermal stability. Of interest was the fact that the pure MA alloys showed no segregation of Am.

The behaviour of the reference material has been examined in a thermal gradient. Both axial and radial thermal gradients were employed. Analysis methods included optical and electron microscopy, EPMA and autoradiography. The behaviour of the material containing 5% MA+RE will be investigated next under a thermal gradient for comparison.

Alloys containing Cm and possibly $^{243}$Am will be manufactured next and investigated. This work is expected to take place in 1991.

## Production of Alpha Emitting Nuclides

The application of alpha emitting nuclides conjugated to monoclonal antibodies for the treatment of cancer is being investigated in a joint project with AKZO-Pharma.

$^{225}$Ac has been selected as the most promising alpha emitter for this purpose for several reasons: it is relatively easily produced from the $^{229}$Th parent, has a favourable halflife of 10 d and is easily detected and measured with its daughter nuclides by alpha and gamma spectrometry. The short-lived daughter nuclide $^{213}$Bi may be applied in the treatment of localised tumours.

The project is expected to consist of several consecutive phases:

- selection and optimisation of the separation methods (setting up a $^{229}$Th 'cow' for $^{225}$Ac and a $^{225}$Ac 'cow' for $^{213}$Bi production);
- conjugation of the particular nuclide onto an antibody using chelates;
- determination of the interaction and killing potential of the antibodies loaded with alpha emitting nuclides with tumour cells (this part of the work carried out in cooperation with IGT, KfK);
- biodistribution and efficacy of the same antibodies in vivo (IGT, KfK) in tumour-bearing mice;
- assuming positive results, clinical studies.

The first two points have been successfully completed and at present the binding of the radioactive material on the antibodies is a major research issue. The results of the study may be released in a joint publication at a later date. Two patents have been applied for in the course of this work [1, 2].

**References**

[1] Radioimmunotherapy using alpha-particles emission.M.W. Geerlings, F.M. Kaspersen (AKZO N.V.)Patent: PCT/EP 90/00990

[2] A method for producing actinium-225 and bismuth-213.J. van Geel, J. Fuger, L. Koch (Commission of the European Commission, JRC Karlsruhe)Patent application: PCT/EP 91/00306; 91 102 260.6

# Fuel Pin Code Development and Application

As in previous years, the TRANSURANUS fuel pin code has been made available and adapted to the use of external organisations also in 1990.

In particular, the ITU Modelling Group offered the following services to Electricité de France, Paris:

- detailed discussions on the TRANSURANUS code,
- demonstration of the TRANSURANUS capabilities by running several test cases,
- training course of the usage of the TRANSURANUS code,
- Transfer of the TRANSURANUS Code to EdF and its successful installation.

With the Paul-Scherrer-Institut, Würenlingen, Switzerland,

- several details of the TRANSURANUS code were discussed,
- the capabilities of TRANSURANUS were demonstrated by running several test cases (ABB Atom fuel rods and 3 selected rods from the Tribulation program)
- the usage of the TRANSURANUS code was explained in detail, and
- the TRANSURANUS code was transferred to PSI and successfully installed.

# ANNEXES

# Annex I

# Publications 1990

## 1. Conferences

**Enlarged Halden Project Meeting on Fuel Performance Experiments and Analysis, 11.2.-16.2.1990, Bolkesjo (Norway)**

*C.T. Walker, C. Bagger, M. Mogensen*
Migration of Fission Product Barium in Transient-tested $UO_2$ Fuel

**Polar Solids Meeting "Ion Transport in Solids" Royal Chem. Soc., 28.3.-30.3.1990, Oxford (UK)**

*Hj. Matzke*
Ion Transport in Ceramics
Proceedings Philos. Mag.

**March 1990 Meeting of the American Physical Society, 12.3.-16.3.1990, Cincinnati (USA)**

*X.L. Wang, D.C. Johnston, C. Stassis, G.H. Lander, A.J. Schultz, C.K. Loong, J. Spalek, J.M. Honig*
Antiferromagnetic Form Factor of $La_2NiO_4$

**Transphase-3, Univ. de Picardie, Amiens, 18.3.-24.3.1990, Djerba (Tunisie)**

*P. Raison, A. Delapalme, G.H. Lander, J.M. Kiat, P. Schweiss, B. Kanellakopulos, A. Apostolidis, J. Rebizant*
Phase Transition in Tricyclopentadienyl-Chloro-Uranium(IV), $U(C_5H_5)_3Cl$
Proceedings: Transition Phase

**INTERMAG '90 International Magnetic Conference, 17.4.-20.4.1990, Brighton (UK)**

*M.S.S. Brooks, L. Nordström, B. Johansson*
Calculated Total and Site-Resolved Magnetic Moments of $RFe_2$ (R = Gd - Yb) Laves Phase Compounds

*G.H. Lander, M.S.S. Brooks, B. Lebech, P.J. Brown, O. Vogt*
Measurement of Giant Magnetic Anisotropy in a Uranium Compound

**10th General Conference of the European Physical Society, 9.4.-12.4.1990, Lisbon (Portugal)**

*O. Eriksson, B. Johansson, M.S.S. Brooks*
The Magnetism of Ferromagnetic $AnFe_2$ Systems

*L. Nordström, B. Johansson, M.S.S. Brooks*
Electronic Structure of $Nd_2Fe_{14}B$

*L. Severin, L. Nordström, M.S.S. Brooks*
Calculated Spin and Orbital Moment in $UNi_2$

**American Chemical Society Meeting, 23.4.-27.4.1990, Boston (USA)**

*R.G. Haire, S. Dabos, U. Benedict, C. Dufour*
The Effect of Pressure on Am-Cm Alloys

**20. Journées des Actinides, 18.4.-21.4.1990, Prague (CSSR)**

*T. Almeida, L. Havela, J. Naegele, J.C. Spirlet*
Surface Chemistry of U-Intermetallics studied by Photoemission

*C. Apostolidis, B. Kanellakopulos, R. Maier, N. Marques, A. Pires de Matos, I. Santos*
Chloro-Neptunium(IV) Complexes Containing Poly(Pyrazol-1-yl) Borate Ligands

*U. Benedict, M. Gensini, E. Gering, L. Gerward, S. Heathman, J. Staun Olsen*
Recent Work on AnX Compounds under Pressure

*S. Bertram, G. Kaindl, J. Rebizant, J.C. Spirlet*
X-Ray Absorption on the L-Edges of Light Actinide Compounds

*S. Bettonville, J. Goffart, J. Fuger*
Organo-f-element Thermochemistry. Uranium-ligand Bond Disruption Enthalpies of the $(C_9H_7)_3U$/ $(C_9H_7)_3UI$/ $(C_9H_7)_3U\text{-}CH_3$ System

*P. Burlet, J.M. Fournier, E. Pleaska, J. Rossat-Mignod, J.-P. Sanchez, J. Rebizant, O. Vogt*
Magnetic Behaviour of NpTe

*P. Burlet, E. Pleska, J. Rossat-Mignod, J.-P. Sanchez, J. Rebizant, J.C. Spirlet, O. Vogt*
Magnetic Structures of $NpSb_{0.90}Te_{0.10}$ and $NpSb_{0.95}Te_{0.05}$

*J.P. Dancausse, S. Heathman, E. Gering, U. Benedict, C. Apostolidis, L. Gerward, J. Staun Olsen*
High Pressure Investigation on Borides, Dioxides and Tetrachlorides of Actinides using X-ray Diffraction

*T. Gasche, M.S.S. Brooks, B. Johansson*
Band Structure Calculations: The Role of Hybridization in 1:1:1 Compounds

*G.H. Lander*
Progress in the Study of the Charge-Density-Waves in Alpha-Uranium in 1989

*K. Mattenberger, O. Vogt, J. Rebizant, J.C. Spirlet*
Magnetic Properties of NpP Single Crystals

*J.R. Naegele, F. Schiavo, J.C. Spirlet*
Is PuSe a High Kondo-temperature Metal? A Photoemission Study

*E. Pleska, J.M. Fournier, J. Chiapusio, J. Rossat-Mignod, J. Rebizant, J.C. Spirlet, O. Vogt*
Electrical Transport Properties on NpAs Single Crystal

*P. Raison, A. Delapalme, G.H. Lander, J.M. Kiat, P. Schweiss, B. Kanellakopulos, C. Apostolidis, J. Rebizant*
Phase Transitions and High Temperature Structures in Tricyclopentadienyl-Chloro-Uranium(IV), $U(C_5H_5)_3Cl$

*J.P. Sanchez, J. Rebizant, J.C. Spirlet*
Mössbauer Study of the Magnetic Properties of $NpCo_2$

*W.G. Stirling, D. Gibbs, G.H. Lander*
X-Ray Magnetic Scattering New Possibilities for Actinide Research

**Frühjahrstreffen des Arbeitskreises Thermophysik, 7.5.-8.5.1990, Stuttgart (FRG)**

*H.A. Tasman*
Differentielle Pyrometrie im Infra-Rot bis hinunter zu 400°C

**Jahrestagung Kerntechnik 1990, 15.5.-17.5.1990, Nürnberg (FRG)**

*C.T. Walker, M. Coquerelle*
Behaviour of MOX Fuel Irradiated under Normal and Transient Conditions Proceedings of the Conference

**Orbital Magnetism in Energy Bands, 21.5.-23.5.1990, Studsvik (Sweden)**

*M.S.S. Brooks, O. Eriksson, B. Johansson, L. Nordström, L. Severin*
Orbital Magnetism in Energy bands

*G.H. Lander*
Spin and Orbital Magnetic Moments in Actinide Compounds

**New Separation Chemistry for Radioactive Waste and Other Specific Applications ENEA-CEC, 16.5.-18.5.1990, Rome (Italy)**

*C. Apostolidis, H. Bokelund, J.-P. Glatz*
Acinide Separations by High Pressure Cation Exchange - The Neptunium Case

*C. Apostolidis, R. de Meester, L. Koch, R. Molinet, J. Liang, Y. Zhu*
The Extraction of Actinides and other Constituents from Highly Active Waste (HAW) by Trialkyl Phosphine Oxide (TRPO)

**OECD-CSNI TMI-2 Sample Examination Specialists Meeting, 21 - 26 May 1990JAERI, Tokyo (Japan)**

*P.D.W. Bottomley and M. Coquerelle*
Final report of the metallurgical examination of samples extracted from the damaged TMI-2 reactor core

**11th Annual Conference of the Canadian Nuclear Society, 3.6.-7.6.1990, Toronto, Ontario (Canada)**

*R.A. Verrall, I.J. Hastings, P.G. Lucuta, Hj. Matzke, B.J.F. Palmer*
Preparation and Applications of Simulated High-Burnup Nuclear Fuel

**Int. Conf. on Fast Reactor Core and Fuel Structural Behaviour, 4.6.-6.6.1990, Inverness (UK)**

*G. Peter, K. Lassmann, H.U. Wider*
Improved Treatment of Molten Fuel Inside LMFBR Pins and its Effect on the Pin Mechanics Calculation
Proceedings of the Conference

*G. Van Goethem, H.U. Wider, G. Peter, K. Lassmann*
Mechanical Fuel Element Loading and Pin Failure Thresholds in EAC-2
Proceedings of the Conference

**7th CIMTEC World Ceramics Congress, 24.6.-30.6.1990, Montecatini-Terme (Italy)**

*Hj. Matzke*
Fabrication and Testing of Non-Oxide Nuclear Fuels for Fast Breeders

**IAEA Technical Committee Meeting on Fuel Performance at High Burn-up for Water Reactors, 5.6.-8.6.1990, Nyköping (Sweden)**

*M. Coquerelle, C.T. Walker*
$UO_2$ Irradiated at Extended Burn-Up: Fission Gas Release and Correlated Structural Features
Proceedings IAEA

**Seminar on Advanced Methods for Nuclear Fuel Characterization and Quality Control, 22.6.1990, Karlsruhe (FRG)**

*O. Cromboom, L. Koch, R. Wellum*
The Determination of Uranium and Plutonium in Fuel Materials by Titration and by K-Edge Absorption
Proceedings

**Gordon Research Conference "Research at High Pressure", 25.6.-29.6.1990, Meriden, N.H. (USA)**

*U. Benedict, J.P. Dancausse, E. Gering, S. Heathman*
High pressure Phases and Compressibility of $PuO_2$ and $ThO_2$

**23. Diskussionstagung der Arbeitsgemeinschaft Massen-spektrometrie, 5.6.-8.6.1990,Konstanz (FRG)**

*L. Koch*
Verfahren zur schnellen, automatischen Isotopenanalyse von Uran und Plutonium

**15th General Assembly and Int. Congress of Crystallography, 19.7.-28.7.1990 ,Bordeaux (France)**

*M.R. Spirlet, J. Rebizant, C. Apostolidis, B. Kanellakopulos, M. Böhm*
Structural Investigations of Nitrato Actinides (IV) Complexes

**28th Annual Meeting of the European High Pressure Research Group, 8.7.-13.7.1990, Bordeaux (France)**

*U. Benedict, S. Dabos-Seignon, R.G. Haire, S. Heathman, J.C. Spirlet*
High Pressure Structural Behaviour and Compressibility of Binary Alloys of Actinides and Lanthanides

**15th General Assembly and Int. Congress of Crystallography, 19.7.-28.7.1990, Bordeaux (France)**

*J.-Cl. Marmeggi, G.H. Lander, T. Brueckel, C.M.E. Heyen, S. van Smaalen*
High-Resolution Neutron Study of the Structural Phase Transition in α-U

*P. Raison, A. Delapalme, G.H. Lander, J.M. Kiat, P. Schweiss, B. Kanellakopulos, C. Apostolidis, J. Rebizant*
Phase Transition in Tricyclopentadienyl-Chloro-Uranium(IV), $U(C_5H_5)_3Cl$

**Electronic Structure in the 1990's, 24.7.-26.7.1990, Bad Honnef (FRG))**

*M.S.S. Brooks, L. Nordström, B. Johansson*
Rare Earth Transition Metal Intermetallics
Proceedings Physica B

*B. Johansson, O. Eriksson, L. Nordström, L. Severin, M.S.S. Brooks*
Orbital Magnetism in Energy Bands
Proceedings Physica B

**Conference on the Complementarity of Neutrons and X-Rays, 30.7.-1.8.1990, Alpe d'Huez (France)**

*J.C. Marmeggi, G. Grübel, G.H. Lander, J.D. Axe, D. Gibbs, T. Brueckel, S. van Smaalen, H.G. Smith, C.M.E. Zeyen*
Studies of the Charge-Density Wave in α-Uranium by both Neutrons and X-Ray Synchroton Radiation

**12. International Congress on Electron Microscopy (ICEM-12), 12.8.-18.8.1990, Seattle, WA (USA)**

*H.L. Müller, E. Drosselmeyer, G. Hotz, A. Seidel, H. Thiele, S. Pickering, I.L.F. Ray*
Electron Microscope Studies of the Take up of Uranium-Plutonium Mixed Oxide Particles by Alveolar Macrophages: In Vivo and in Vitro Experiments

*I.L.F. Ray, H. Thiele, W. Huber*
Electron Microscopy of Radioactive Samples

*I.L.F. Ray, H. Thiele, Hj. Matzke*
Transmission Electron Microscopy of Transiented Tested LWR Nuclear Fuel Samples

**International Symposium Commemorating the 50th Anniversary of the Discovery of Neptunium and Plutonium, 26.8.-31.8.1990, Washington, D.C. (USA)**

*U. Benedict, S. Dabos-Seignon, S. Heathman, J.P. Dancausse, M. Gensini, E. Gering, J.C. Spirlet*
High Pressure Phases and Compressibility of Neptunium and Plutonium Compounds
Proceedings of the Conference

*G.H. Lander*
Metallic Covalency in Actinide Compounds
Proceedings of the Conference

*Z. Liang, A.G. Marshall, A. Pires de Matos, J.C. Spirlet*
Gas Phase Uranium Ion Reactions with 2,4,6-tri-t-buthyl-phenol and 1,3,5-tri-t-butyl benzene by Means of FT/ICR Mass Spectrometry
Proceedings of the Conference

*K. Mattenberger, O. Vogt, J. Rebizant, J.C. Spirlet*
Magnetization Measurements on Single Crystals of Neptunium Monopnictides
Proceedings o the Conference

*J. Rossat-Mignod, P. Burlet, J.M. Fournier, E. Pleska, J.P. Sanchez, J. Rebizant, J.C. Spirlet, O. Vogt*
Impact of Magnetic and Transport Properties on Electronic Structure of Actinide Compounds
Proceedings of the Conference

**International Symposium on Nonlinear Acoustics (INSA-12), 27.8.-31.8.1990, Austin, TX (USA)**

*J. Magill, K. Richter, S. Fourcaudot, J.A. Gallego, E. Riera, G. Rodriguez*
Agglomeration of Aerosol and Aerosol Mixtures in an Acoustic Field

**International Conference on Fast Reactor Safety, 12.8.-16.8.1990, Snowbird, Utah (USA)**

*H.U. Wider, A. Clusaz, J.J. Devos, K. Jirlow, K. Lassmann, Z.H. Li, R.B. Nicholson, H. Nguyen, G. Peter, R.A. Rydin, G. Van Goethem*
The European Accident Code-2: Overview and Status

*W. Balz, L. Koch, W. Löhr, U.K. Wehmann*
Core design and safety aspects of large LMFBRs with minor actinide recycling

**International Conference on f-Elements 4.9.-7.9.1990 Leuven (Belgium)**

*R.G. Haire, S. Heathman, U. Benedict*
The Behavior of Pm Metal Under Pressure and its Significance for the Systematics of f Electron Delocalization in the f Elements

**4th Int. Symposium on Temperature and Thermal Measurement in Industry and Science TEMPMEKO 90, 17.9.-19.9.1990, Helsinki (Finland)**

*J.-F. Babelot, M. Hoch*
Extension of the Integral Six-Color Pyrometer to Lower Temperatures and to the Near Infrared Region

**2nd International Conference on Plasma Source Mass Spectrometry, 24.9.-28.9.1990, Durham (UK)**

*J.I. Garcia Alonso, J.F. Babelot, L. Koch*
The ICP-MS in an EEC Nuclear Research Establishment: Applications and Perspectives

**NATO Advanced Research Workshop Fundamental Aspects of Inert Gases, 16.9.-22.9.1990, Bonas (France)**

*Hj. Matzke*
Fundamental Aspects of Inert Gas Behaviour in Nuclear Fuels: Oxides, Carbides and Nitrides
Proceedings NATO ARW, Kluwer Acad. Publ.

*I.L.F. Ray, Hj. Matzke*
Fission Gas Behaviour During Transients in High Burnup LWR, Nuclear Fuel Samples Studied by Electron Microscopy
Proceedings NATO ARW, Kluwer Acad. Publ.

**3rd European Community Conference on Radioactive Waste Management and Disposal, 17.9.-21.9.1990, Luxembourg**

*E. Vernaz, A. Loida, G. Malow, J.A.C. Marples, Hj. Matzke*
Long-Term Stability of High-Level Waste Forms
Proceedings of the Conference

**12th European Conference on Thermophysical Properties ETPC-12, 24.9.-28.9.1990, Vienna (Austria)**

*J.P. Hiernaut, C. Ronchi*
The Spectral Emissivity Behavior Around the Melting Point in Refractory Metals and Oxides
Proceedings High Temp. - High Pressures

*H. E. Schmidt*
The Thermal Conductivity of Inhomogeneous Bodies - A Historical Account
Proceedings High Temp. - High Pressures

*H.A. Tasman*
Differential Pyrometry in the Infra-Red
Proceedings High Temp. - High Pressures

**Second Workshop on Subsecond Thermophysics, 20.9.-21.9.1990, Torino (Italy)**

*R. Beukers, H. Heinz, J.P. Hiernaut, C. Ronchi, R. Selfslag*
Determination of the Melting Point of Graphite
Proceedings of the Conference

**6th Europ. Conf. on Lattice Defects in Ionic Materials LATDIM-90, 3.9.-7.9.1990, Groningen (NL)**

*Hj. Matzke, F. Dyment*
Diffusion of Actinides in NaCl Single Crystals and in Real Rock Salt
Proceedings Radiation Effects and Defects in Solids

*Hj. Matzke, O. Meyer, A. Turos*
Damage Recovery in the U-Sublattice of Ion-Implanted $UO_2$ between 5 and 2000 K
Proceedings Radiation Effects and Defects in Solids

**Spectrum '90: International Topical Meeting on Nuclear and Hazardous Waste Management, 30.9.-10.10.1990, Knoxville, TN (USA)**

*L. Koch, C. Apostolidis, K. Mayer, G. Nicolaou, R. Wellum*
How Technically Feasible is the Partitioning and Transmutation of Long-Lived Radiotoxic Nuclides in the Waste from Reprocessed Spent Nuclear Fuel?

**XXXIV Welch Foundation Conference on Chemical Research "Fifty Years with Transuranium Elements", 22.10.-23.10.1990, Houston, TX (USA)**

*J. Fuger*
Actinide Research at the European Institute for Transuranium Elements
Proceedings of the Conference

**XVII. Annual Meeting of the Argentinian Nucl. Society, 22.10.-26.10.1990, Buenos Aires (Argentina)**

*A.M. Bevilacqua, Hj. Matzke*
Fenomenos de sorcion del Pu-238 desde un medio acuoso sobre vidrio de $SiO_2$

**Herbstsitzung des Arbeitskreises Thermophysik, 7.11.-8.11.1990, Karlsruhe (FRG)**

*H.A. Tasman*
Wärmeleitfähigkeit von $UO_2$-W Cermets

**International Symposium on Advanced Ceramics ISAC 90, 26.11.-30.11.1990, Bombay (India)**

*Hj. Matzke*
Indentation Techniques for the Evaluation of Mechanical Properties of Ceramics and Glasses
Trans Tech Publ.

**35th Annual Conference on Magnetism and Magnetic Materials, 29.10.-1.11.1990 San Diego, CA (USA)**

*M.S.S. Brooks, L. Nordström, B. Johansson*
Magnetism of $RFe_2$ Compounds
Proceedings J. Appl. Phys.

*O. Eriksson, M.S.S. Brooks, B. Johansson*
Magnetism and Bonding in Actinide and Rare Earth Systems
Proceedings J. Appl. Phys.

*G.H. Lander, M.S.S. Brooks, B. Lebech, P.J. Brown, O. Vogt, K. Mattenberger*
Measurement of Anisotropy Constant in US with Polarized Neutrons
Proceedings J. Appl. Phys.

*G.H. Lander, P.J. Brown, C. Stassis, J. Spalek, G. Honig*
Neutron and Magnetization Study of $La_{1.8}Sr_{0.2}NiO_4$
Proceedings J. Appl. Phys.

*B. Lebech, M. Wulff, G.H. Lander*
Spin and Orbital Moments in Actinide Compounds
Proceedings J. Appl. Phys.

*L. Nordström, B. Johansson, M.S.S. Brooks*
Calculated Magnetic Moments of $Nd_2Fe_{14}B$
Proceedings J. Appl. Phys.

*X.L. Wang, C. Stassis, D.C. Johnston, T.C. Leung, J. Ye, B.N. Harman, G.H. Lander, A.J. Schultz, C.K. Loong, J. Spalek, J.M. Honig*
The Antiferromagnetic Form Factor of $La_2NiO_4$
Proceedings J. Appl. Phys.

**First OECD/NEA Information Exchange Meeting-on Separation and Transmutation of Actinides and Fission Products**
**05.11.-09.11.1990, Mito (Japan)**

*L. Koch*
Systemimmanent Long-lived Radioisotope Transmutation

*T. Inoue, M. Kurata, L. Koch, C. Sari, J.C. Spirlet, C. Walker*
Transmutation of Transuranium Elements by a Metallic Fuel FBR

**Winter Meeting of the American Nuclear Society,**
**11.11. - 16.11.1990, Washington DC (USA)**

*L. Koch*
Research on Actinide Partitioning and Transmutation

**International Conference on Non-Stoichiometric Compounds,**
**3.12.-5.12.1990, Tokyo (Japan)**

*Hj. Matzke, A. Turos*
Mechanisms and Kinetics of Leaching of $UO_2$ in Water
Proceedings in Solid State Ionics

*T.Ogawa, R.A.Verral, Hj.Matzke*
Release of Ion-Implanted Kr from $(Th,U)O_2$ - Effect of Matrix Oxidation
Proceedings in Solid State Ionics

# 2. Books and Periodicals

*C. Apostolidis, B. Kanellakopulos, R. Maier, J. Rebizant, M.L. Ziegler*
Bis (cyclopentadienyl) technetium (III) Chlorid and tris (cyclopentadienyl) Technetium (III), Neue metallorganische Verbindungen des dreiwertigen Technetiums
J. Organomet. Chem. 396 (1990) 315

*G.W. Arnold, G. Della Mea, J.C. Dran, K. Kawahara, P. Lehuede, Hj. Matzke, P. Mazzoldi, M. Noshiro, C. Pantano*
Surface Analysis of Coated Flat Glasses: A Comparison of Various Techniques
Glass Technology 31 (1990) 58-63

*J.-F. Babelot, M. Hoch*
Detailed Analysis of the Integral Six-Color Pyrometer
High Temp. - High Pressures (submitted)

*U. Benedict, S. Dabos-Seignon, C. Dufour, H. Luo, S. Heathman*
Transuranium Materials under extreme pressures (Translation into Russian)
Atomnaya Tekhnika sa rubjeschom, no. 10 (1990), 30-34

*S. Bettonville, J. Goffart, J. Fuger*
Organo-f-Element Thermochemistry. Actinide-Ligand Bond Disruption Enthalpies in Tris(indenyl)Actinide Hydrocarbyls
J. Organomet. Chem. 377 (1990) 59-67

*S. Bettonville, J. Goffart, J. Fuger*
Organo-f-element Thermochemistry. Uranium-ligand Bond disruption Enthalpies in the $(C_9H_7)_3U/(C_9H_7)_3UI/(C_9H_7)_3$ U-$CH_3$ System
J. Organomet. Chem. (submitted)

*P.D.W. Bottomley*
The TMI-2 Reactor Core: an Investigation of Samples taken from Damaged Core,
Seminar on the Commission Contribution to Reactor Safety Research, Nov. 1989, Varese (Italy),
Proc. Elsevier, Ed. W. Krischer (1990), p. 18

*M.S.S. Brooks, L. Nordström, B. Johansson*
Origin and ab Initio Evaluation of Magnetic Interactions in Rare Earth Intermetallics
Phys. Rev. Lett. (submitted)

*M.S.S. Brooks, G.H. Lander, B. Johansson*
Orbital Magnetism from itinerant Electrons
Europhys. News (submitted)

*M.S.S. Brooks, B. Johansson, O. Eriksson*
The Relativistic Equation of State of Actinide Metals and Compounds
High Pressure Research 2 (1990) 265-271

*M.S.S. Brooks, L. Nordstrom, B. Johansson*
3d-5d Band magnetism in rare-earth transition metal intermetallics
J. Phys. Cond. Matter (submitted)

*S. Dabos-Seignon, U. Benedict, S. Heathman, J.C. Spirlet, M. Pagès*
Phase Transformation of AnX Compounds Under High Pressure (An = Np, Pu; X = Sb, Te)
J. Less-Common Met. 160 (1990) 35-52

*S. Dabos-Seignon, E. Gering, U. Benedict, J.C. Spirlet, M. Pagès*
High-Pressure X-Ray Diffraction Study of the δ-Phase in the Uranium-Neptunium Binary System
High Pressure Research 2 (1990) 255-261

*S. Dabos-Seignon and U. Benedict*
High-pressure study of Np and Pu compounds
High-Pressure Research 4 384-6 (1990)

*J.-P. Dancausse, E. Gering, S. Heathman*
Pressure-induced Phase Transition in $ThO_2$ and $PuO_2$
High Pressure Research 2 (1990) 381-389

*O. Eriksson, M.S.S. Brooks, B. Johansson*
Calculated Cohesive Properties of Lanthanide and Lanthanide-Like Actinide Elements
J. Less-Common Met. 158 (1990) 207-220

*O. Eriksson, B. Johansson, R.C. Albers, A.M. Boring, M.S.S. Brooks*
Orbital Magnetism in Fe, Co and Ni
Phys. Rev. B42 (1990) 2707

*O. Eriksson, M.S.S. Brooks, B. Johansson*
Theoretical Aspects of the Magnetism in the Ferro-magnetic $AnFe_2$ Systems (An = U,Np,Pu and Am)
Phys. Rev. B 41 (1990) 9087-9094

*O. Eriksson, B. Johansson, M.S.S. Brooks*
Theory of Orbital Splittings Applied to $NpAl_2$
J. Phys.: Condens. Matter 2 (1990) 1529

*O. Eriksson, B. Johansson, M.S.S. Brooks*
Orbital Magnetism in the Itinerant Ferromagnet $NpOs_2$
Phys. Rev. B 41 (1990) 9095-9100

*O. Eriksson, M.S.S. Brooks, B. Johansson*
Orbital Polarization in Narrow Band Systems: Application to Volume Collapses in Light Lanthanides
Phys. Rev. B 41 (1990) 7311-7314

*R. Feduzi, F. Lanza, J. Fuger*
Effects of Lithium Oxide on the Electrical Properties of CuO at Low Temperatures
J. Mater. Res. 5 (1990) 1739-1744

*J. Fuger, R.G. Haire, W.R. Wilmarth, J.R. Peterson*
Molar Enthalpy of Formation of Californium Tribromide
J. Less-Common Met. 158 (1990) 99-104

*J. Fuger, Hj. Matzke*
Self-Radiation Effects in the Actinides and their Compounds: Basic Studies and Practical Implications
Handbook on the Physics and Chemistry of the Actinides, A.J.Freeman and G.H.Lander Eds, Elsevier Science Publishers B.V.

*M. Gensini, E. Gering, S. Heathman, J.C. Spirlet*
High-pressure Phase of Plutonium Mono-selenide Studied by X-Ray Diffraction
High Pressure Research 2 (1990) 347-359

*M. Gensini, E. Gering, U. Benedict, L. Gerward, J. Staun Olsen, F. Hulliger*
High-Pressure X-Ray Diffraction Study of ThOS and UOSe by Synchrotron Radiation
J. Less-Common Met. (submitted)

*L. Gerward, J. Staun Olsen, U. Benedict, S. Dabos-Seignon, H. Luo*
Crystal Structures of $UP_2$, $UAs_2$, UAsS and UAsSe in the pressure range up to 60 GPa
High Temp. - High Pressures (submitted)

*L. Gerward, J. Staun Olsen, U. Benedict, H. Luo*
Compression of ThC to 50 GPa
J. Less-Common Met. 161 (1990) L11-L14

*L. Gerward, J. Staun Olsen, U. Benedict, H. Luo, and F. Hulliger*
A high-pressure study of $Th_3P_4$ and some $U_3X_4$ compounds
High-Pressure Research 4 357-9 (1990)

*L. Gerward, J. Staun Olsen, U. Benedict, S. Dabos-Seignon*
The transformation B1 to B2 in actinide compounds
J. Appl. Cryst. 1990 (submitted)

*L. Gerward, J. Staun Olsen, U. Benedict, H. Luo*
Compression of ThC to 50 GPa
J. Less-Common Metals 161 L11-L14 (1990)

*M.D. Giardina, R. Feduzzi, A. Manara, J.C. Spirlet, M. Zocchi, S. Mobilio*
An Investigation of the Crystalline and Electronic Structures of a 4:3:3:4 Layered Bi-Ca-Sr-Cu Oxide
J. Mater. Res. (submitted)

*J.-P. Glatz, H. Bokelund, S. Zierfuss*
Analysis of the Off-Gas from Dissolution of Nuclear Oxide - and Carbide Fuels in Nitric Acid
Radiochim. Acta 51 (1990) 17-22

*T. Gouder, C.A. Colmenares, J.R. Naegele, J. Verbist*
Photoemission Study of the $C_2H_4$ absorption on uranium
J. Catalysis (submitted)

*T. Gouder, C. Colmenares, J.R. Naegele, J. Verbist*
Study of the Surface Oxidation of Uranium by UV Photoemission Spectroscopy
Surf. Sci. 235 (1990) 280-286

*J. Goudiakas, X. Jemine, J. Fuger*
Thermodynamics of Lanthanide and Actinide Perovskite-type and Related Oxides. V. Molar Enthalpies of Formation of $M_2NpO_4$ (M = Li, Na, K or Cs) and of $\beta$-$Na_4NpO_5$ Compounds
J. Chem. Thermodyn. (submitted)

*J. Goudiakas, R.G. Haire, J. Fuger*
Thermodynamics of Lanthanide and Actinide Perovskite-Type Oxides. IV. Molar Enthalpies of Formation of $MM'O_3$(M = Ba or Sr,M'= Ce,Tb or Am) Compounds
J. Chem. Thermodyn. 22 (1990) 577-587

*G. Grübel, J.D. Axe, Doon Gibbs, G.H. Lander, H.G. Smith, J.C. Marmeggi, T. Brueckel*
The Incommensurate Charge-Density-Wave-State inα-Uranium. A High Resolution X-Ray and Neutron Study
Phys. Rev. Lett. (submitted)

*R.G. Haire, S. Heathman, U. Benedict*
A structural study of promethium metal under pressure
High-Pressure Research 2 (1990) 273-288

*B. Johansson, O. Eriksson, M.S.S. Brooks*
Pressure Effects on Intermetallic Atinide Compounds
High Pressure Research 2 (1990) 303-313

*D.L. Jones, W.G. Stirling, G.H. Lander, J. Rebizant, J.C. Spirlet, and O. Vogt*
Neutron scattering study of single crystals of NpAs and NpSb
J. Phys. Condensed Matter (submitted)

*G.M. Kalvius, S. Zwirner, U. Potzel, J. Moser, W. Potzel, F.J. Litterst, J. Gal, S. Fredo, I.Yaar, J.C. Spirlet*
Localized Properties of the Itinerant 5f-Electron Antiferromagnet $NpSn_3$
Phys. Rev. Lett. 65 (1990) 2290

*S. Kern, F. Trouw, C.-K. Loong, G.H. Lander*
Dynamic Quadrupolar Excitation in $PrO_2$
J. Appl. Phys. 67 (1990) 4830-4831

*S. Kern, C.-K. Loong, G.L. Goodman, B. Cort, G.H. Lander*
Crystal-field Spectroscopy of $PuO_2$: Further Complications in Actinide Dioxides
J. Phys.: Condens. Matter 2 (1990) 1933-1940

*G.H. Lander, M.S.S. Brooks, B. Johansson*
Orbital Band Magnetism in Actinide Intermetallics
Phys. Rev. Lett. (submitted)

*G.H. Lander, P.J. Brown, C. Stassis, P. Gopalan, J. Spalek, G. Honig*
Magnetic and Structural Study of $La_{1.8}Sr_{0.2}NiO_4$
Phys. Rev. 43 (1990) 448-456

*G.H.Lander*
Sleuthing in Reciprocal Space: the Search for a Charge-Density Wave in α-Uranium
Endeavour 14 (1990) 179-184

*G.H. Lander, M.S.S. Brooks, B. Lebech, P.J. Brown, O. Vogt, K. Mattenberger*
Measurement of Giant Magnetic Anisotropy in a Uranium Compound
Appl. Phys. Lett. 57 (1990) 989-991

*G.H. Lander, W.G. Stirling, J.M. Rossat-Mignod, M. Hagen, O. Vogt*
Magnetic Excitations in Monodomain Ferromagnetic Uranium Telluride
Phys. Rev. B 41 (1990) 6899-6906

*F. Lanza, R. Feduzi and J. Fuger*
Effects of lithium oxide on the electrical properties of CuO at low temperatures
J. Material Research 5, 1739-1744 (1990)

*K. Lassmann, G. Peter*
Calculating the In-Pin Fuel Motion in a Hypothetical FBR Core Disruptive Accident by the Coupled Systems TRANSURANUS-CAMDYN,
Nucl. Eng. Design (submitted)

*P.G. Lucuta, R.A. Verrall, Hj. Matzke*
Microstructural Features of SIMFUEL: Simulated High-Burnup $UO_2$-based Nuclear Fuel,
J. Nucl. Mater. (submitted)

*J.C. Marmeggi, G.H. Lander, S. van Smaalen, T. Brückel, C.M.E. Zeyen*
Neutron Diffraction Study of the Charge-Density Wave in α-Uranium
Phys. Rev. 42 (1990) 9365-9376

*J.C. Marmeggi, G.H. Lander, T. Brückel, C.M.E. Zeyen*
New Development in Modulated Phases of α-U Phase Transition
Phase Transitions (submitted)

*Hj. Matzke*
Mass Transport in Carbides and Nitrides, in "The Physics and Chemistry of Carbides, Nitrides and Borides", Ed. R. Freer, Nato ARW, Manchester, Sept. 1989, Kluwer Acad. Publ., Netherlands, (1990) p. 357

*Hj. Matzke, G. Della Mea, J.C. Dran, G.Linker, and B. Tiveron*
Radiation Damage in Nuclear Waste Glasses Following Ion Implantation at Different Temperatures,
Int. Conf. Radiation Effects in Insulators,
Nucl. Instrum. Methods in Phys. Research B46, 256 (1990)

*Hj. Matzke and A. Turos*
A Channeling Study of Ion Implantation Damage in $UO_2$ and UN
Int. Conf. Radiation Effects in Insulators,
Nucl. Instrum. Methods in Phys. Research B46 117 (1990)

*Hj. Matzke, G. Della Mea, F.Z.L. Freire, jr. and V. Rigato*
Determination of Hydrogen in Leached $UO_2$ and Synroc,
Proc. Int. Conf. Ion Beam Analysis,
Nucl. Instrum. Methods in Phys. Research B45, 194 (1990)

*Hj. Matzke*
Atomic Mechanisms of Mass Transport in Ceramic Nuclear Fuel Materials,
J. Chem. Soc., Faraday Transactions 86, 1243 (1990)

*Hj. Matzke, R.A. Verrall*
Release of Volatile Fission Products from $ThO_2$ with a Simulated Burnup of 4 at.%
J. Nucl. Mater. (submitted)

*Hj. Matzke*
Inert Gases as a Probe for Chemical, Physical or Structural Changes in Solids
Thermochim. Acta (submitted)

*Hj. Matzke*
Diffusion in Carbides and Nitrides: Unsolved Problems in "Diffusion in Solids - Unsolved Problems"
Trans Tech Publ. Switzerland, G.E. Murch,, ed.

*Hj. Matzke, I.L.F. Ray, B.W. Seatonberry, H. Thiele, C. Trisoglio, C.T. Walker, T.J. White*
Incorporation of Transuranic Elements in Titanate Nuclear Waste Ceramics
J. Amer. Ceram. Soc. 73(2) (1990) 370-378

*Hj. Matzke, O. Meyer and A. Turos*
Damage Recovery in the U-Sublattice of Ion Implanted $UO_2$ Between 5 K and 2000 K,
Proc. 6. Latdim Conf., Groningen, Sept. 1990,
Rad. Effects and Defects in Solids, in print

*Hj. Matzke*
Fundamental Aspects of Inert Gas Behaviour in Nuclear Fuels: Oxides, Carbides and Nitrides, Proc. NATO ARW, Bonas, France, Sept. 1990, Kluwer Acad. Publ.

*L.R. Morss, W.T. Carnall, C.W. Williams, J.A. Fahey, J. Fuger, G. Meyer, M. Irmler*
Syntheses and X-Ray Diffraction Studies of $(N(CH_3)_4)_2BkCl_6$ and $(N(CH_3)_4)_2ZrCl_6$; Absorption Spectrum of $Bk^{4+}$ in $(N(CH_3)_4)_2BkCl_6$
J. Less-Common Met. (submitted)

*L. Nordström, O. Eriksson, M.S.S. Brooks, B. Johansson*
Theory of the Ferromagnetism in $CeCo_5$
Phys. Rev. B 41 (1990) 9111-9120

*L. Nordström, B. Johansson, O. Eriksson, M.S.S. Brooks*
Theoretical Study of the Metamagnetism in $ThCo_5$
Phys. Rev. 42 (1990) 8367-8374

*C. O'Carroll*
What can a Physicist do in Europe?
Phys. World (submitted)

*A.J.F. Praxedes and J.R. Naegele*
$O_2$ Absorption on $UNi_5$ studied by ion scattering and UV photoelectron spectroscopy
Surface Science (submitted)

*J. Rebizant, M.R. Spirlet, C. Apostolidis, B. Kanellakopulos*
Structure of Tris(η-cyclopentadienyl) Uranium Iodide
Acta Crystallogr. (submitted)

*J. Rebizant, M.R. Spirlet, C. Apostolidis, G. Van den Bossche, B. Kanellakopulos*
Structure of Di-μ-Chloro-bis {trichlorobis (tetrahydrofuran) uranium (IV) }
Acta Crystallogr. (submitted)

*J. Rebizant, M.R. Spirlet, C. Apostolidis, B. Kanellakopulos*
Structure of (Acetonitrile-d3)-Tris( η-cyclo pentadienyl) samarium
Acta Crystallogr. C46 (1990) 2076-2078

*H. Reddmann, H. Schultze, H.-D. Amberger, C. Apostolidis, B. Kanellakopulos*
Interpretation der optischen und magnetochemischen Eigenschaften von $Cp_3Ce(III)$ .THF auf der Grundlage der Kristallfeldtheorie
Spectrochim. Acta 46A (1990) 1223-1229

*J. P. Sanchez, K. Tomala, J. Rebizant, J.C. Spirlet and O. Vogt*
Mössbauer study of the $NpSb_{1-x}Te_x$ solid solutions
Hyperfine Interactions 54 701-704 (1990)

*M.R. Spirlet, J. Rebizant, C. Apostolidis, B. Kanellakopulos*
Structure of Bis(Ammonium)Hexanitrato-plutonium(IV) and Bis(Ammonium)Hexanitrato-thorium(IV)
Acta Crystallogr. (submitted)

*M.R. Spirlet, J. Rebizant, S. Bettonville, J. Goffart*
Structure of Chlorotris(1-3-η-1-ethylindenyl) thorium(IV)
Acta Crystallogr. C46 (1990) 1234-1236

*M.R. Spirlet, J. Rebizant, C. Apostolidis, G. Van den Bossche, B. Kanellakopulos*
Structure of Tris(η-cyclopentadienyl) phenolatouranium (IV)
Acta Crystallogr. C46 (1990) 2318-2320

*M.R. Spirlet, J. Rebizant and M. Liegeois-Duyckaerts*
The structure of Lithium Copper Pyrophosphate, $Li_2CuP_2O_7$
Acta Cryst. C (submitted)

*J.C. Spirlet, J. Kalbusch, A. Moens, C. Rijkeboer, J. Rebizant*
Advances in the Preparation of Single Crystals of Actinide Compounds
Lanthanide and Actinide Research (submitted)

*J.C. Spirlet, E. Bednarczyk, J. Kalbusch, A. Moens, J. Rebizant, C. Rijkeboer, F. Wastin*
Actinide Samples Available for High-Pressure Studies and Their Preparation
High Pressure Research 2 (1990) 399-400

*J. Staun Olsen, S. Steenstrup, L. Gerward, U. Benedict, J. Akella, and G. Smith*
X-ray diffraction studies on samarium up to 1 Megabar
High-Pressure Research 4 366-8 (1990)

*C. Syros, C. Ronchi, C. Spano*
An Analytical Solution for the Calculation of Burst Release of Volatile Fission Products from Nuclear Fuels
Nucl. Sci. Eng. (submitted)

*H.A. Tasman*
Differential Pyrometry in the Infra-Red, High Temperatures, High Pressures (submitted)

*A. Turos, S. Fritz, Hj. Matzke*
Defects in Ion-Implanted Uranium Nitride
Phys. Rev. B 41 (1990) 3968-3977

*A. Turos, Hj. Matzke, S. Kwiatkowski*
Recovery Stages in $UO_2$ at Low Temperatures
Phys. Rev. Lett. 65 (1990) 1215-1218

*G. van Goethem, H.U. Wider, K. Lassmann, et al.*
Applications of the European Accident Code EAC in LMFBR Whole Core Safety Analysis and Pretest Calculations, Seminar on the Commission Contribution to Reactor Safety Research, Nov. 1989, Varese (Italy),
Proc. Elsevier, Ed. W. Krischer (1990), p. 795

*C.T. Walker, M. Coquerelle, W. Goll, R. Manzel*
Irradiation Behaviour of MOX Fuel: Results of an EPMA Investigation
Nucl. Eng. Des. (submitted)

*C.T. Walker, C. Bagger, M. Mogensen*
Migration of Fission Product Barium in $UO_2$ Fuel Under Transient Conditions
J. Nucl. Mater. 173 (1990) 14-25

*C.T. Walker, K. Lassmann, C. Ronchi, M. Coquerelle, M. Mogensen*
The D-COM Blind Problem in Fission Gas Release: The Predictions of the TRANSURANUS and FUTURE Codes,
Nucl. Eng. Design, 117 (1989) 211-233

*H.U. Wider, J.J. Devos, K. Lassmann, et al.*
The European Accident Code-2: Overview on the Modelling, Seminar on the Commission Contribution to Reactor Safety Research, Nov.1989, Varese (Italy),
Proc. Elsevier, Ed. W. Krischer (1990) p. 787

*M. Wulff, O. Eriksson, B. Johansson,*
*B. Lebech, M.S.S. Brooks, G.H. Lander,*
*J. Rebizant, J.C. Spirlet, P.J. Brown*
Experiment and Theory of Actinide Intermetallic Magnetism: A Test Case of $NpCo_2$
Europhys. Lett. 11 (3) (1990) 269-274

# 3. Reports

Annual Report 1989
EUR 12849 EN (1990)

*A. Bevilacqua and Hj. Matzke*
A Comparison of $K_{IC}$ Values of Nuclear Waste Glasses Obtained by Vickers Indentations and by Short Rod Fractometry, Proc. 2nd International Workshop on Indentation Techniques, Bologna, Italy, in connection with 7th SIMCER
Europ. Appl. Res. Reports 7, nr. 9 1369 (1990)

*H. Blank*
Fabrication of Carbide and Nitride Pellets and the
Nitride Irraddiations NILOC 1 and NILOC 2
Europ. Appl. Res. Report (in press)

*P.D.W. Bottomley, H. Thiele*
Report of a brief metallographic examination of dual-density $ZrO_2$ specimen at ITU
ITU Technical Note K 0290136, 1990

*P.D.W. Bottomley*
ITU Examination of specimens TP29 and TP36 of the Silène experiment
Internal Report, August 1990 (produced for DERS/SEMAR, CEN-Cadarache, France).

*M. Campana, J.F. Gueugnon, K. Richter*
Expériences NILOC 3 et 4
ITU Technical Note K0290133, 1990

*R.Dal Maschio, Hj.Matzke and G.Della Mea*
Fracture Toughness of Nuclear Waste Glasses Following Ion Implantation at Different Temperatures, Proc. Int. Workshop on Indentation Techniques, Bologna, Italy, in connection with the 7th SIMCER
Europ. Appl. Res. Reports 7, nr. 9 (1990) 1389

*L. Dechamp, H.A. Tasman*
Differential pyrometry in the infra-red
Part 2: Detectors and Pre-Amplifiers (Preliminary Results)
ITU Technical Note K0290130, 1990

*I.R. Farthing, C.T. Walker*
Heinrichs Mass Absorption Coefficients (For the K,L and M X-Ray Lines)
ITU Technical Note K0290140, 1990

*R. Forst*
Einsatzmöglichkeiten einer SIMS a DIDA 3000 Macrosonde
ITU Technical Note K0290134, 1990

*I. Grenthe, J. Fuger, R.J. Lemire, A.B. Muller, Chinh Nguyen-Trung, H. Wanner*
Chemical Thermodynamics of Uranium
OECD, NEA Report

*J.F. Gueugnon, K. Richter*
Standard (U,Pu)$O_2$ pour spectromètre à rayons X
ITU Technical Note K0290139, 1990

*R. Jansson, K. Lassmann and A. Massih*
Comparison Between the Fuel-to-Cladding Gap Conductance Models URGAP and GTEMP with Out-of-Pile Experiments EUR Report (in press)

*L. Koch, R. Wellum*
Proceedings of the Workshop on Partitioning and Transmutation of Minor Actinides
Karlsruhe, 16-18 October 1989

*K. Lassmann, G. Peter*
Scoping Analysis of the Lambda Experiment using the TRANSURANUS Code
ITU Technical Note K0290132, 1990

*K. Lassmann, J. van de Laar*
TRANSURANUS Änderungsprotokoll
Version 1 Modifikation 3,Jahr 1989 ('V1M3J89')
ITU Technical Note K0290138, 1990

*P.C. Lucuta, B.J. Palmer, Hj. Matzke, D.S. Hartwig*
Preparation and Characterization of SIMFUEL: Simulated CANDU High-Burnup Nuclear Fuel,
Proc. Int. Conf. on CANDU Fuel, Chalk River, Ed. I.J. Hastings, Can. Nucl. Soc. Toronto,
Report AECL-10117 (1990) 132

*Hj. Matzke and E. Toscano, eds*
Indentation Techniques,
Proc. 2nd International Workshop on Indentation Techniques, Bologna, Italy, in connection with 7th SIMCER,
Europ. Appl. Res. Reports, 7, nr. 9 (1990)

*Hj. Matzke*
Recent Developments in Indentation Techniques, Proc. 2nd International Workshop on Indentation Techniques, Bologna, Italy, in connection with 7th SIMCER,
Europ. Appl. Res. Reports 7, nr. 9 (1990) 1335

*Hj. Matzke*
Vickers Indentation on Radiation Damaged Cm-containing Waste Glasses, Proc. 2nd International Workshop on Indentation Techniques, Bologna, Italy, in connection with 7th SIMCER
Europ. Appl. Res. Reports 7, nr. 9 1403 (1990)

*Hj. Matzke, E.H. Toscano, M. Coquerelle, M. Ougier, R. Schreiber*
Fabrication and Characterization of Waste Glasses and of SYNROC Doped with Curium
ITU Technical Note K0290131, 1990

*C. Ronchi, F. Turrini*
Thermochemical Data for Reactor Materials
EUR 12819 EN (1990)

*G.J. Small*
The Modelling of Fission Gas Release for Thermal Reactor Safety Studies
ITU Technical Note K0290128, 1990

*G.J. Small*
An Improved Fission Gas Release Model for "TRANSURANUS"
ITU Technical Note K0290129, 1990

*H.A. Tasman*
Specific Heat of Simulated Fuel with 6% Burn-up
ITU Technical Note K0290137, 1990

*F. Turrini*
Calculation of the Thermochemical Equilibrium in Irradiated Fuel
ITU Technical Note K0290135, 1990

*R.A. Verrall, Hj. Matzke, I.J. Hastings, I.L.F. Ray and D.H. Rose*
Fission Gas Mobility in $UO_2$ Simulating a Burnup of 30 MWd/kgU,
Proc. Int. Conf. on CANDU Fuel, Chalk River, Ed. I.J. Hastings, Can. Nucl. Soc. Toronto
Report AECL-10116 (1990) 172

# Annex II

# Collaborations with External Organisations

Argentina

CNEA Buenos Aires: Diffusion in solids (F.Dyment)

CNEA Bariloche: Waste glasses, Actinide migration (A.Bevilacqua)

Austria

International Atomic Energy Agency, Vienna: Evaluation and Automation of techniques for safeguards analysis

Belgium

University of Liège: Single crystal growth, X-ray diffraction, and analysis (J. Goffart, L. Martinot, M.R. Spirlet)

Canada

AECL Chalk River: Gas release, SIMfuel production and property studies (I.Hastings, P.Lucuta, R.Verrall)

AECL Whiteshell: Behaviour of Rb and Cs in SIMfuel (W.Hocking)

Czechoslovakia

University of Prague: Photoelectron Spectroscopy, magnetic and electrical measurements (V. Sechovsky, L. Havela)

University of Prague: Gas release measurements (V.Balek)

Denmark

Risø National Laboratory: Neutron scattering (B. Lebech)

Technical University Lingby: High-pressure X-ray diffraction (L. Gerward)

University of Copenhagen: High pressure X-ray diffraction (J. Staun-Olsen)

France

CEN, Grenoble: Neutron diffraction, magnetic studies, transport properties and Mössbauer studies (J. Rossat-Mignod, P. Burlet, J.M. Fournier, A. Blaise, and J. Sanchez)

CEN, Saclay: Neutron diffraction (A. Delapalme)

CEN Cadarache (DRN/DEC): Optimisation of dense fuels

CEN Marcoule: Waste characterisation

CEN Cadarache: Reactor safety studies (F.Schmitz)

CNRS, Grenoble: Crystallography of phase transitions (J.C. Marmeggi)

Electricité de France, Paris: TRANSURANUS fuel pin code development

ILL, Grenoble: Polarized neutron diffraction and neutron inelastic scattering (P.J. Brown, C. Zeyen, T. Brueckel)

Inst. Curie, Paris: Mössbauer and high-pressure studies (M. Pagès, A. Tabuteau, A. Cousson, S. Dabos-Seignon)

Germany

Apparatebau Rothemühle, Wenden: Acoustic aerosol scavenging

Freie Universität Berlin: X-ray absorption spectroscopy (G. Kaindl)

Hahn-Meitner-Institut, Berlin: Ranges of ions in solids, B-profiles in leached glasses (D.Fink, J.Biersack)

Hahn-Meitner-Institut, Berlin: High-energy ion implantation (S.Klaumünzer)

Keller, Pyrowerk, Hannover: Fast multichannel pyrometry

KfA Jülich, Inst. für Festkörperforschung: Electrical resistivity under pressure (J. Wittig)

KfA Jülich, Institut für Chemische Technologie: Sample characterization (A. Solomah)

KfK, Karlsruhe, Inst. für Heisse Chemie: Susceptibility and crystal preparation (B. Kanellakopulos)

KfK, Karlsruhe, Inst. für Nukleare Festkörperphysik: Electron spectroscopies (G. Fink)

KfK, Karlsruhe, Inst. für Technische Physik: Electrical resistivity under pressure (H. Wühl)

KfK, Karlsruhe, EFR: Optimisation of dense fuels (G.Mühling)

KfK, Karlsruhe: TRANSURANUS fuel pin code development

KfK, Karlsruhe, INE: Waste characterisation (L.Kahl)

KfK, Karlsruhe, INFP: Radiation damage studies, RBS analyses, channeling, ion implantation (O.Meyer, G.Linker)

Max Planck Institut für Festkörperphysik Stuttgart: High-pressure reflectivity studies (K. Syassen)

Siemens/KWU, Erlangen: Nuclear fuel analysis

Siemens/KWU: Post-irradiation fuel element examination

Technischer Überwachungsverein Baden, Karlsruhe: TRANSURANUS fuel pin code development

Technischer Überwachungsverein Bayern, München: TRANSURANUS fuel pin code development

Technische Universität München: Mössbauer and μSR studies (M. Kalvius, W. Potzel, L. Asch, F. Litterst); X-ray absorption spectroscopy (G.Schütz)

Universität Erlangen: Photoelectron spectroscopy (A. Grassmann)

Universität Stuttgart, IKE: Source term studies

Universität Stuttgart, IKE: Data bank system THERSYST (G.Neuer, G.Jaroma-Weiland)

Univ. München, Inst.Anorg.Chem.:Single crystal growth and X-ray diffraction (F. Lux, M. Böhme)

Italy

Centro Ceramico Bologna: Leaching studies, Indentation techniques (L.Esposito)

Centro Legnaro/Padova: RBS, Ion implantation, H-analysis on leached waste matrices ((G.Della Mea, V.Rigato)

ENEA, Rome: Waste characterisation

University of Ancona: Neutron studies of oxides (R. Caciuffo)

University of Parma: Theory of actinide insulators (G. Amoretti)

University of Padova: Analysis of glass surfases (P.Mazzoldi)

University of Trento: Indentation techniques (R.DalMaschio)

University of Rome: Development of temperature standards (G.Ruffino)

Japan

Central Research Institute of Electricity Producing Industries (CRIEPI), Tokyo: Preparation and characterisation of minor actinide alloys

Central Research Institute of Electricity Producing Industries (CRIEPI), Tokyo: Dissolution studies on high burn-up fuel

Glass Institute, Osaka: Diffusion in waste glasses (M.Yamashita)

JAERI, Tokai Mura: Basic studies on nitride fuels (T.Ohmichi)

University of Nagoya: Basic properties of nuclear carbides ((H.Matsui)

Netherlands

AKZO n.v., Arnhem: Production of alpha-emitting nuclides

University of Amsterdam: Low temperature magnetization and resistivity (J. Franse)

University of Groningen: Theory (S. van Smaalen)

University of Groningen: Resonant photoelectron spectroscopy (J. Ghijsen)

Poland

Nuclear Institute, Warszawa: Channeling techniques, Radiation damage studies (A.Turos)

Sweden

University of Uppsala: Solid state theory of actinides (B. Johansson)

Switzerland

ETH, Zürich: Single crystal growth, magnetic, optical and transport properties, preparation of U and Th compounds (O. Vogt, J. Schoenes, P. Wachter, F. Hulliger, K. Mattenberger)

Paul-Scherrer-Institut, Würenlingen: TRANSURANUS fuel pin code development

Paul-Scherrer-Institut, Würenlingen: Optimisation of dense fuels

Paul-Scherrer-Institut, Würenlingen: Post-irradiation structural investigations by electron microscopy

Paul-Scherrer-Institut, Würenlingen: MITRA code development, release of radionuclides

Spain

CIEMAT, Madrid: TRANSURANUS fuel pin code development

Instituto di Acustica, Madrid: Acoustic aerosol scavenging

United Kingdom

AERE, Harwell: Low temperature specific heat measurements (R. Hall, M. Mortimer)

AERE, Harwell: High temperature thermophysical property measurements

Birkbeck College: neutron and magnetization studies (K. McEwen)

Royal Institute, London: Calculation of fission products in $UO_2$

Rutherford-Appleton Laboratory: Neutron spectroscopy (R. Osborn, M. Hagen)

University of Birmingham: Prep. of high purity single crystals (D. Fort)

University of Keele: X-ray and neutron scattering (W.G. Stirling, D. Jones, C. Tang)

University of Warwick: X-ray absorption spectroscopy (M.J. Cooper)

University of Warwick: Radiative properties at high temperatures (G.Hyland)

University of Salford: Solid gas precipitates (S.Donnelly)

USA

Argonne National Laboratory: Neutron scattering (C.K. Loong; L. Morss, S. Kern, G. Goodman)

Brookhaven National Laboratory: High-resolution and magnetic X-ray scattering (D. Gibbs, J. Axe, G. Grubel)

Lawrence Livermore National Laboratory: Surface reactions (C. Colmenares); high pressure studies (J. Akella)

Los Alamos National Laboratory: Materials preparation and photoemission (B. Cort, J. Ward, L. Cox)

Oak Ridge National Laboratory: Material preparation, high pressure X-ray and optical studies (R.G. Haire, J.R. Peterson)

University of W. Virginia: Theory (G.J. Hu, B.R. Cooper)

University of Purdue: Magnetisation and sample preparation (G. Honig and J. Spalek)

University of Florida: Low temperature specific heat (G. Stewart)

USSR

Academy of Sciences, IVTAN, Moscow: Studies on high-melting materials (A.E.Sheindlin)

Radium Khlopin Institute, Leningrad: Installation and field testing of a robotized system for safeguards analysis.

## Annex III

# Human Resources

### 1. Institute's Staff

The evolution of the staff situation in 1990 is given for three reference dates on the table below:

| Date | A2-A4 | A5-A8 | B | C | D | total |
|---|---|---|---|---|---|---|
| 01.01. | 18 | 22 | 73 | 72 | 1 | 186 |
| 20.10. | 17 | 22 | 77 | 74 | 1 | 191 |
| 31.12. | 17 | 23 | 82 | 74 | 1 | 197 |

### 2. Visiting Scientists and Scientific Fellows

4 visiting scientists and 12 graduate sectorial grantees from the following countries spent in 1990 prolonged periods of time at the Institute:

| | |
|---|---|
| B (2) | I (1) |
| F (4) | P (1) |
| D (3) | UK (1) |
| GR (2) | non-EC (2) |

### 3. Secondment from other laboratories

4 experts were delegated from other European research establishments to carry out specific tasks at the ITU in 1990, i.e. from CEA-CEN Grenoble (F), CEA-CEN Cadarache (F), EDF (F), and from the University of Liège (B).

## Annex IV

# Organisational Chart

| | |
|---|---|
| Institute Director | Jacques VAN GEEL |
| Adviser, acting as Institute Deputy Director | Jean FUGER |
| Adviser (Programmes) | Hans Eberhard SCHMIDT |
| Personnel and Administration | Paul BLAES |
| S/T Services: | |
| - Technical Physics | Michel COQUERELLE |
| - Applied Physics | Hansjoachim MATZKE |
| - Nuclear Technology | Karl RICHTER |
| - Nuclear Chemistry | Lothar KOCH |
| - Actinide Research | Ulrich BENEDICT |
| S/T-Support: | |
| - Radiation Protection | Klaas BUIJS |
| - Technical Services | Gérard SAMSEL |

## Annex V

# Glossary of Acronyms and Abbreviations

**AAS**: Atomic Absorption Spectroscopy
**ABB**: Asea Brown Bovery
**AERE**: Atomic Energy Research Establishment
**ANOVA**: ANalysis Of VAriance
**APS**: Aerodynamic Particle Sizer
**ASTEC**: Aerosol Sampling and Transport Efficiency Calculation code
**BNFL**: British Nuclear Fuels plc
**BOL**: Beginning of Life (of a fuel pin)
**CABRI**: CEA test reactor in Cadarache, France
**CANDU**: CANadian-Deuterium-Uranium reactor
**CBNM**: Central Bureau for Nuclear Measurements, Geel
**CDW**: Charge Density Wave
**CEA**: Commissariat à l'Energie Atomique
**CEN**: Centre d'Etudes Nucléaires
**CIEMAT**: Centro de Investigaciones Energeticas, Medioambientales y Tecnologicas (Spain)
**CMPO**: Carbonyl-Methyl-Phosphine Oxide
**CNRS**: Centre National de la Recherche Scientifique
**COCAIN**: code to calculate the COrrosion by steam Cloud on An Irradiated Nuclear fuel element
**COMB-SVITE ENEA** laboratory (Ispra)
**CORSOR**: code to calculate gas release in irradiated fuel through experimental correlation
**CRIEPI**: Central Research Institute of Electric Power Industry (Japan)
**DEH**: Direct Electrical Heating
**DESY**: Deutsche Elektronen-Synchroton (Hamburg)
**DG I**: Directorate General "External Relations" of the Commission of the European Communities, Brussels
**DG XII**: Directorate General "Science, Research, and Development" of the Commission of the European Communities, Brussels
**DG XIII**: Directorate General "Telecommunication, Information Industry, and Innovation" of the Commission of the European Communities, Brussels and Luxembourg
**DG XVII**: Directorate General "Energy" of the Commission of the European Communities, Brussels and Luxembourg
**dHvA**: de Haas-van Alphen effect
**DIN**: Deutsches Institut für Normung
**DWK**: Deutsche Gesellschaft für Wiederaufarbeitung von Kernbrennstoffen (Hannover)
**EAC**: European Accident Code
**ECN**: Energie Centrum Nederland
**EDAX**: Energy-Dispersive X-Ray Analysis
**EDF**: Electricité de France
**EDX**: Energy-Dispersive X-ray spectroscopy
**EFR**: European Fast Reactor
**EMPA**: Electron Microprobe Analysis (also EPMA)
**ENEA**: Entente Nazionale dell' Energia Alternativa
**EOL**: End-Of-Life (of a fuel pin)
**EPMA**: Electron Probe Micro-Analysis
**ERDA**: Elastic Recoil Detection Analysis
**ESRF**: European Synchrotron Radiation Facility (Grenoble)

ESTER: Hot vitrification pilot plant (Ispra)
ETH: Eidgenössische Technische Hochschule (Zürich)
FACT: Sub-project "Formation of ACTinides in-pile"
FBR: Fast Breeder Reactor
FIMA: Fissions per Initial Metal Atom
FORTRAN: FORmula TRANslation (programming language)
FS: Fermi Surface
FUTURE: code for fuel transient calculations
HASYLAB: HAmburger SYnchrotronstrahlungs-LABor (DESY)
HAW: Highly Active Waste
HEDL: Hanford Engineering Development Laboratory (Richland, WA)
HEPA filter: High Efficiency Particulate Air filter
HPLC: High Performance Liquid Chromatography
HPXRD: High-Pressure X-Ray Diffraction
HV-CI: High Volume-Cascade Impactor
IAEA: International Atomic Energy Agency (Vienna)
ICP-AES: Inductively-Coupled Plasma Atomic-Emission Spectroscopy
ICP-MS: Inductively Coupled Plasma Mass Spectrometry
ICP-OES: Inductively Coupled Plasma Optical Emission Spectroscopy
ID: Isotopic Dilution
IDMS: Isotope Dilution Mass Spectrometry
ILL: Institut Laue-Langevin (Grenoble)
INFP: Institut für Nukleare FestkörperPhysik (KfK)
ISO: International Standards Organization
ITU: Institute for Transuranium Elements
JAERI: Japan Atomic Energy Research Institute
JANAF: Joint Army-Navy-Air Force thermochemical tables (database)
JRC: Joint Research Centre
KARBUS: KArlsruhe Reactor BUrnup System
KfK: Kernforschungszentrum Karlsruhe
KNK: Kompakte Natrium-gekühlte Kernenergieanlage Karlsruhe
KORIGEN: Depletion code
LAKU: model to calculate fission gas release (KfK)
LMFBR: Liquid Metal (cooled) Fast Breeder Reactor
LMTO: Linear Muffin Tin Orbitals
LURE: Laboratoire d'Utilisation du Rayonnement Electronique (Orsay)
LWR: Light Water Reactor
MA: Minor Actinides (Np, Am, Cm)
MGA: program for the determination of Pu isotopic ratios
MITRA: code to calculate the release of radio-nuclides
MOX: Mixed Oxide fuel
MX: U,Pu-fuel containing a combination of the elements C,N,O
Nd-YAG: Neodymium-Yttrium Aluminium Garnet laser
NEA: Nuclear Energy Agency (OECD)
NISTTHERMO :National Institute of Standards and Technology tables of chemical THERMOdynamic properties
NSLS: National Synchrotron Light Source (Brookhaven)
OECD: Organisation for Economic Cooperation and Development
ORIGEN: code to calculate fission yields (Oak Ridge version)
PCI: Pellet Cladding Interaction
PCMI: Pellet Cladding Mechanical Interaction
PHEBUS: French test reactor, Cadarache
PHEBUS-FP: Programme to study fission product release and their distribution in the primary circuit
PHENIX: French prototype fast reactor
PIE: Post Irradiation Examination
PMMA: Polymethylmethacrylate (Plexiglass)
PSI: Paul Scherrer Institut (Würenlingen, CH)

**PWR**: Pressurized Water Reactor
**QMA**: Quantitative Metallographic Analysis
**RBS**: Rutherford Backscattering Spectroscopy
**RE**: Rare Earths
**REM**: Reflection Electron Microscopy
**SAED**: Selective Area Electron Diffraction
**SA-IS**: Standard Additions with Internal Standard
**SAWG**: Scientific Analytical Working Group
**SCE**: Saturated Calomel Electrode
**SIMFUEL**: Th-based fuel with major non-volatile fission products (simulated)
**SIMS**: Secondary Ion Mass Spectroscopy
**SEM**: Scanning Electron Microscopy
**SNR-300**: German prototype fast reactor
**SOLGASMIX**: code to calculate the build-up of chemical species
**SUPERFACT**: Minor Actinide Irradiation in Phenix
**SUPERPHENIX**: French fast reactor
**SYNROC**: SYNthetic ROCk
**TAS**: Textur AnalyseSystem
**TBP**: TriButyl Phosphate
**TEM**: Transmission Electron Microscopy
**THERSYST**: THERmophysical properties database SYSTem
**TIMS**: Thermal Ionization Mass Spectrometry
**TMI**: Three Mile Island reactor
**TRABI**: project to study TRAnsport of BIg particles
**TRANSURANUS**: Fuel behaviour code
**TREAT**: TRansient REActor Test facility
**TREOR**: Trial-and-ErrOR indexing program
**TRPO**: TRialkyl Phosphine Oxide
**TRU**: TRansUranium elements
**TRUEX**: TRansUranium EXtraction
**TUAR**: TU Annual Report
**TVO**: Industrial Power Company Ltd. (BWR reactors at Olkiluoto, Finland)
**UPS**: Ultraviolet Photoelectron Spectroscopy
**UTS**: Ultimate Tensile Strength
**WAK**: WiederAufarbeitungsanlage Karlsruhe
**XPS**: X-ray Photoelectron Spectroscopy
**XRF**: X-Ray Fluorescence

## Annex VI

# List of Authors

### 1. Specific Programmes

Basic Safety Research on Nuclear Fuels
*Hj.Matzke, D.Bottomley, M.Coquerelle, J.P.Hiernaut, K.Lassmann, I.Ray, C.Ronchi, H.A.Tasman, C.Walker, P.Werner*

Safety Aspects of Fuel Operation and Handling
*K.Richter, K.Buijs, J.F.Gueugnon, B.Chavane, C.Sari*

Actinide Determination and Recycling
*L.Koch, C. Apostolidis, H.Bokelund, R.Wellum*

Characterisation of Waste Forms and of High Burn-Up Fuel
*M.Coquerelle, D.Bottomley, Hj.Matzke, C.Messainguiral, G. Nicolaou*

Actinide Research
*U.Benedict, M.Brooks, G.Lander, J.Naegele, J.Rebizant, J.C.Spirlet, G. Jaroma-Weiland*

### 2. Exploratory Research (Acoustic Aerosol Scavenging)

*J.Magill, K.Richter, J.Somers*

### 3. Support to Community Policies

Support to the EURATOM Safeguards Directorate
*L.Koch, J.F.Babelot, H.Bokelund, J.P.Glatz, J.I.Garcia-Alonzo, R.Wellum*

Support to the Directorate General for External Relations (Evaluation and Automation of Analytical Techniques)
*L.Koch, H.Bokelund, R.Wellum*

Support to the Directorate for Innovation and Technology Transfer
*J.Magill, K.Richter, C.Ronchi*

### 4. Work for Third Parties

*L.Koch, K.Lassmann*

# Annex VII

## Previous Progress Reports of the Institute for Transuranium Elements

| TUSR | Period | COM-Nr | EUR-Nr |
|---|---|---|---|
| 1 | Jan - Jun 1966 | 1580 | |
| 2 | Jul - Dec 1966 | 1522 | |
| 3 | Jan - Jun 1967 | 1745 | |
| 4 | Jul - Dec 1967 | 2007 | |
| 5 | Jan - Jun 1968 | 2172 | |
| 6 | Jul - Dec 1968 | 2300 | |
| 7 | Jan - Jun 1969 | 2434 | |
| 8 | Jul - Dec 1969 | 2576 | |
| 9 | Jan - Jun 1970 | 2664 | |
| 10 | Jul - Dec 1970 | 2750 | |
| 11 | Jan - Jun 1971 | 2833 | |
| 12 | Jul - Dec 1971 | 2874 | |
| 13 | Jan - Jun 1972 | 2939 | |
| 14 | Jul - Dec 1972 | 3014 | |
| 15 | Jan - Jun 1973 | 3050 | |
| 16 | Jul - Dec 1973 | 3115 | |
| 17 | Jan - Jun 1974 | 3161 | |
| 18 | Jul - Dec 1974 | 3204 | |
| 19 | Jan - Jun 1975 | 3241 | |
| 20 | Jul - Dec 1975 | 3289 | |
| 21 | Jan - Jun 1976 | 3358 | |
| 22 | Jul - Dec 1976 | 3384 | |
| 23 | Jan - Jun 1977 | 3438 | 6475 E |
| 24 | Jul - Dec 1977 | 3484 | 7209 E |
| 25 | Jan - Jun 1978 | 3526 | 7459 E |
| 26 | Jul - Dec 1978 | 3582 | 7227 E |
| 27 | Jan - Jun 1979 | 3657 | 7483 E |
| 28 | Jul - Dec 1979 | 3714 | 7509 E |
| 29 | Jan - Jun 1980 | 3822 | 7857 E |
| 30 | Jul - Dec 1980 | 3846 | 8230 E |
| 31 | Jan - Jun 1981 | 3898 | 8447 E |
| 32 | Jul - Dec 1981 | 3927 | 8777 E |
| 33 | Jan - Jun 1982 | 3990 | 9581 E |
| 34 | Jul - Dec 1982 | 4048 | 10251 E |
| 35 | Jan - Jun 1983 | 4094 | 10266 E |
| 36 | Jul - Dec 1983 | 4117 | 10454 E |
| 37 | Jan - Jun 1984 | 4150 | 10470 E |
| 38 | Jul - Dec 1984 | 4165 | 11013 E |
| 39 | Jan - Jun 1985 | 4201 | 11835 E |
| 40 | Jul - Dec 1985 | 4263 | 11836 E |
| TUAR | | | |
| 86 | Jan - Dec 1986 | 4302 | 12233 E |
| 87 | Jan - Dec 1987 | ------ | 11783 E |
| 88 | Jan - Dec 1988 | ------ | 12385 E |
| 89 | Jan - Dec 1989 | | 12849 E |
| 90 | Jan - Dec 1990 | | 13815 E |

Previous Programme Progress Reports were confidential for a period of two years. Since 1977 they are made freely accessible after that period as EUR-Reports. They can be ordered from the Office for Official Publications of the European Communities, 2 rue Mercier, L-2985 Luxemburg, Tel. 49 92 81, Telex PUBOF LU 1324 b

This report was compiled and edited by H.E. Schmidt, J. Richter, and L. Ruczka.

Inquiries for more details should be adressed to the Programme Office, Institute for Transuranium Elements, P.O. Box 2340, D-7500 Karlsruhe, Phone 07247-84386, FAX 07247-4046

For further information concerning JRC programmes please contact the Directorate General Science, Research and Development of the Commission of the European Communities, 200 rue de la Loi, B-1049 Brussels, Belgium.